Capacity of the Hyperspectral Satellite Mission EnMAP for the Multiseasonal Monitoring of Biophysical and Biochemical Land Surface Parameters in Agriculture by Transferring an Analysis Method for Airborne Image Spectroscopy to the Spaceborne Scale

Dissertation der Fakultät für Geowissenschaften

der Ludwig-Maximilians-Universität München

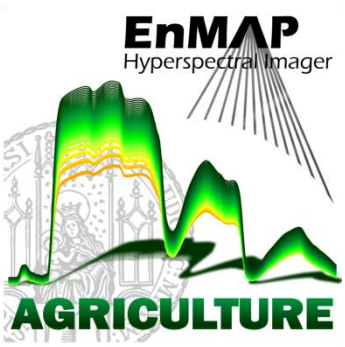

vorgelegt von:

Matthias Locherer

aus München

Eingereicht am 24.07.2014

1. Gutachter: Prof. Dr. Wolfram Mauser
2. Gutachter: Prof. Dr. Ralf Ludwig

Tag der mündlichen Prüfung: 04.11.2014

“Und, was macht die Diss?”

ALLE FREUNDE

Acknowledgements

Sincere thanks are conveyed to my supervisor, Prof. Dr. Wolfram Mauser, for giving me the opportunity and the funding to get involved in this fascinating project, for not only supporting me in the analysis of the AVIS data, but for the confidence placed in me, to single-handedly acquire these data in the airborne field campaign, and for his forbearance in awaiting the thesis submission.

Special thanks are extended to co-supervisor, Dr. Tobias Hank, for the extensive advice provided and for broadening my scope in stimulating discussions. Thank you for your unending support and infectious passion for this field of study. I cannot imagine a more motivating person.

I am very grateful to Dr. Katja Richter for introducing me to the topic of canopy reflectance models and for the scientific advice along the way.

Particular thanks are due to my colleagues and "co-combatants", office-mate Toni Frank, former office-mate Dr. Florian Schlenz, and to David Gampe and Philipp Klug, who shared my enthusiasm for FC Bayern and for the good times we shared; and to Franziska Koch, who has repeatedly accompanied me and brightened my path since our sojourn in New Zealand in 2007.

To the student team, for their commitment during the field campaign and for the support in preprocessing the vast amount of AVIS data, facing many unforeseen challenges: Martin Danner, Verena Huber Garcia, Sandra Dotzler, Ariane Hartmann, Raul Wood, Christina Obster, Johannes Mitterer, Leonie Keil, Andreas Suess, and Yueli Bettina Chen.

I am very much indebted to Dr. Dieter Hausamann, head of the DLR_School_Lab in Oberpfaffenhofen, for introducing me to the field of applied remote sensing in 2003 and for his encouragement in many ways ever since.

Sincere thanks are extended to Susan Braun-Clarke for applying her considerable language skills to the proof-reading and editing of the text.

My deepest gratitude is expressed to Juliana Braun, for her selfless dedication, for giving me strength and sustaining the vision throughout the duration of this study.

Many thanks also to the "crew", for persistently asking, when the thesis will finally be finished.

And to my family, Iris, Manuel and Poldi Pretzl, to Ursula Locherer and the late Franz Locherer, for their enduring support and for encouraging me to get involved in this project in the first place.

This thesis is dedicated to my father, whom I miss very much.

Table of Contents

List of Figures

List of Tables

List of Equations

List of Acronyms

a.s.l.	Above Sea Level
ALA	Average Leaf Angle
ANN	Artificial Neural Network
AOT	Aerosol Optical Thickness
APEX	Airborne Prism Experiment
ASE	Advanced Statistical Evaluator
ASI	Analysis of Spectral Integral
ASTER	Advanced Spaceborne Thermal Emission and Reflection Radiometer
AVI	Agricultural Vegetation Indices
AVIRIS	Airborne Visible / Infrared Imaging Spectrometer
AVIS	Airborne Visible and Near Infrared Spectrometer
b	Intercept of Theil-Sen regression
BRDF	Bidirectional Reflectance Distribution Function
BRF	Bidirectional Reflectance Factor
CASI	Compact Airborne Spectral Imager
CCC	Canopy Chlorophyll Content
CCD	Charge-coupled Device
CO_2	Carbon Dioxide
CRM	Canopy Reflectance Model
CWC	Canopy Water Content
CWV	Columnar Water Vapor
DC	Dark Current
DEM	Digital Elevation Model
DLR	German Aerospace Center
DN	Digital Number
EeteS	EnMAP End-to-End Simulation Tool

EnMAP	Environmental Mapping and Analysis Program
EO	Earth Observation
ESU	Elementary Sampling Unit
ETM	Enhanced Thematic Mapper
EWT	Equivalent Water Thickness
fAPAR	Fraction of Absorbed Photosynthetically Active Radiation
FF	Flat-Field
FOV	Field of View
FWHM	Full Width Half Maximum
GCP	Ground Control Point
GMT	Greenwich Mean Time
GPS	Global Positioning System
GSD	Ground Sampling Distance
H_2O_2	Hydrogen Peroxide
HSI	Hyperspectral Imager
HYMAP	Hyperspectral Mapper
IFOV	Instantaneous Field of View
IMU	Inertial Measurement Unit
LAD	Leaf Angle Distribution
LAI	Leaf Area Index
LCC	Leaf Chlorophyll Content
LIDF	Leaf Inclination Distribution Function
LUT	Look-Up Table
m	Slope of Theil-Sen regression
MLP	Multilayer Perception
MTF	Modulation Transfer Function
NDVI	Normalized Difference Vegetation index
NIR	Near Infrared
NSE	Nash-Sutcliffe Efficiency

O_2	Oxygen
OEC	Overexposure Correction
OLI	Operational Land Imager
PAR	Photosynthetically Active Radiation
PROMET	Process of Radiation Mass and Energy Transfer Model
PROSPECT	Model of Leaf Optical Properties Spectra
QE	Quantum Efficiency
R^2	Coefficient of Determination
RGB	Red-Green-Blue
RMSE	Root Mean Squared Error
RRMSE	Relative Root Mean Squared Error
RTM	Radio Transfer Model
SAIL	Scattering by Arbitrary Inclined Leaves
SLC	Soil-Leaf-Canopy
SNR	Signal-to-Noise Ratio
SVR	Support Vector Regression
SWIR	Short-Wavelength Infrared
SZA	Solar Zenith Angle
TM	Thematic Mapper
TOA	Top of Atmosphere
VNIR	Visible and Near Infrared

1 Introduction

In order to face the challenges of the 21st century, such as a growing world population, global food supply and ongoing climate change resulting in a progressive burden on the ecosystems, there is a strong need for products and methods that can provide information for advanced analyses of these effects. On a global level, agricultural land resources are limited and also endangered by land degradation due to faulty management decisions. To ensure the food supply of the world population in the future, one option would be to expand agricultural land, which is only possible by clearing even more forests. Since this is neither an appropriate nor a long-term solution, the demand can only be met by a sustainable increase in agricultural productivity and an associated reduction in the yield gap, that is, in the difference between potential and actual yield. This necessitates the introduction of agricultural management strategies, such as the selection of suitable plants and cultivars, improved water productivity, organic farming, fertilizer and pesticide management, soil conservation, and irrigation (KAUFMANN ET AL., 2012). The spatial variability in the landscape due to different climate conditions, varying soils, and topography likewise requires accurate spatial information for the monitoring of crop and soil characteristics. Since landscape-scale vegetation mapping requires expensive and time-consuming field surveys, the remote sensing technique offers an alternative which is both time- and cost-effective (GOVENDER ET AL., 2007). The German satellite mission EnMAP (Environmental Mapping and Analysis Program), to be launched in 2017, has the strong potential to provide spatial information products that are relevant to agricultural issues. According to KAUFMANN ET AL. (2012) the major scientific goals of the EnMAP mission are to study environmental changes, investigate ecosystem responses to increasing human activities, and monitor the management of natural resources. For this purpose, EnMAP will provide high-quality calibrated hyperspectral data enabling the development of novel methodologies for the accurate retrieval of geochemical, biochemical and biophysical parameters, analyses of ecological processes and the provision of information products that can serve as input for advanced ecosystem models.

1.1 Challenges of Agriculture in the 21st century

Within the last decades remote sensing has proved its potential to provide information on a full range of agricultural issues. According to HABOUDANE ET AL. (2002) the benefits of this technique have been shown for crop classification, crop forecasting, yield prediction, mapping of crop status and condition and, last but not least, crop disease and micronutrient deficiency.

Yet traditional farming methods are being stretched to their limits. This has led to an enhanced interest in products supporting precision farming and the development of smart systems for agricultural resource management, which takes the land heterogeneity into account and has progressed towards a site specific management that targets spatial variability in soils and vegetation performance (PINTER ET AL., 2003). Precision farming aims to boost productivity and to optimize profitability in a sustainable way. To achieve these objectives, image-based remote sensing offers a technique that supplies spatial information on agricultural fields based on its potential by retrieving the biophysical and biochemical compounds of the plants growing there. This information can be used in early stages of the growing period to serve the quantification of adequate fertilizer demand, enabling ideal growth of the crops, which depends in particular on nitrogen supply. Since nitrogen content is directly related to chlorophyll content and therefore to photosynthesis, its supply is most important for crop growth and productivity. If nitrogen supply is too low, chlorophyll becomes ineffective and decreases, which leads to a reduced yield and thus to an economic loss. By contrast, if nitrogen supply is too high, it is washed out and infiltrates water bodies, which leads to eutrophication of aquatic ecosystems as well as economic loss (WOOD ET AL., 1993). In consequence, knowledge about the chlorophyll concentration in the canopy is of high relevance for assessing nitrogen variability and stress (BLACKMER ET AL., 1996).

Once agricultural plants reach an advanced development stage, the focus is on health monitoring and estimation of yield. For this purpose, agro-ecological land surface process models are used to allow the explicit simulation of crop growth. Plant parameters retrieved from hyperspectral image data thereby serve as input for these models (e.g., PROMET-V (SCHNEIDER & MAUSER, 2001)), resulting in site-specific information on key parameters which are not directly observable by remote sensing, such as biomass, plant height, crop yield, and nitrogen content. Dynamic vegetation models help to deepen process understanding as they are based on eco-physiological processes and feedbacks during the growing period (KAUFMANN ET AL., 2012). When linked with agricultural management models (e.g., PROMET (HANK, 2008)) and canopy models describing the distribution of assimilates within the canopy, valuable and reasonable results can be achieved (e.g., BACH ET AL., 2003; HANK ET AL., 2012). In future, the frequent availability of high-quality data provided by EnMAP will support further developments and will help such coupled model systems to reach an operational stage (KAUFMANN ET AL., 2012). In the context of global agriculture and food supply, these models can provide valuable information for reducing the yield gap, especially in regions with low-efficiency farming systems.

1.2 Airborne and Spaceborne Imaging Spectroscopy

The surface of the earth interacts with incident radiation in the form of absorption, reflectance and transmission as a function of the wavelength, and is dependent on surface characteristics, such as roughness, physical state or color. The absorption features are thereby defined by the chemical bonds, harmonics and overtones of vibrational electronic transitions of the material. Thus, the different surfaces have individual spectral signatures, i.e., specific reflection and absorption characteristics over the electromagnetic spectrum. Imaging spectroscopy focuses on the 400 to 2500 nm range of the spectrum because solar radiation shows the highest intensity in this range (Figure 1-1) (KAUFMANN ET AL., 2012).

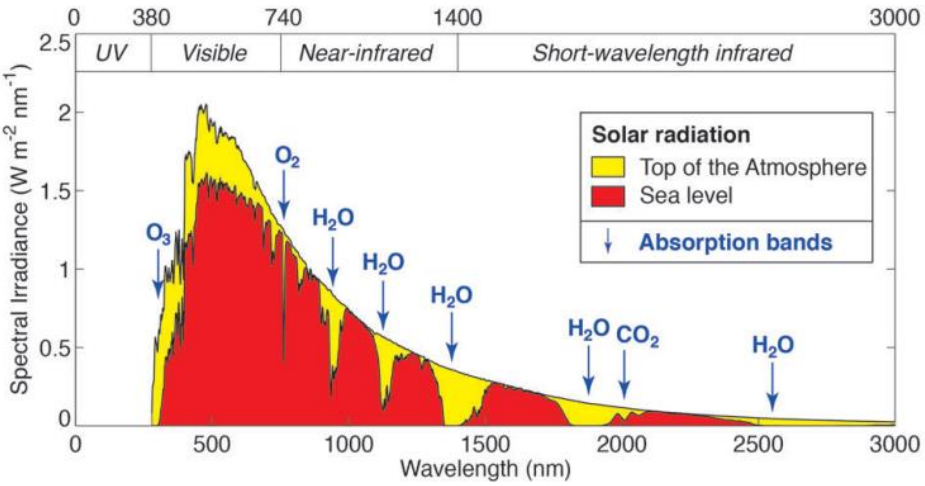

Figure 1-1: Solar radiation spectrum of top of the atmosphere radiation and global radiation at sea level (composed of incoming, diffuse, and reflected radiation) with major atmospheric absorption bands (KAUFMANN ET AL., 2012; based on data derived from the American Society for Testing and Materials (ASTM) Terrestrial Reference Spectra).

Passive remote sensing sensors measure the reflected signal from the surface, which can be divided into radiance and reflectance. These can be defined as follows:

(1) Radiance is the part of incident radiation that is reflected from the surface. It describes the energy flux leaving the surface and has a physical unit (W / m² sr nm).

(2) Reflectance is the dimensionless ratio of reflected to incident radiation, thus it can be seen as a pure surface property, which is dependent on illumination and viewing geometry if it has no Lambertian properties (ideal diffusely reflecting surface).

Imaging spectroscopy, which is also known as hyperspectral imaging, acquires simultaneous images in a high number of spectral bands, so that for each pixel of the resulting multichannel image a contiguous reflectance spectrum can be derived (e.g., GOETZ ET AL., 1985). Figure 1-2 gives an overview of different types of surfaces and the various spectral signatures within the main part of the solar domain.

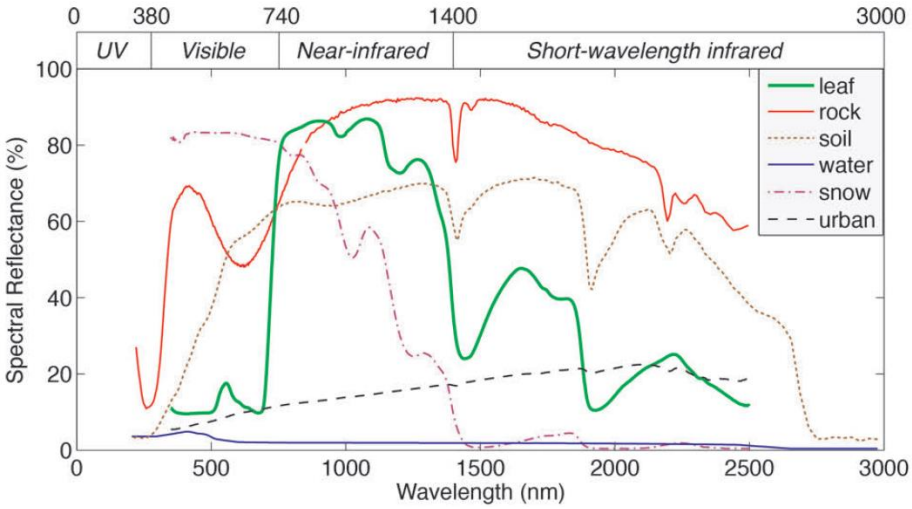

Figure 1-2: Reflectance spectra of selected Earth's surface components (KAUFMANN ET AL., 2012; based on data derived from the USGS Digital Spectral Library). The laboratory measurements represent samples of an oak leaf from Colorado (leaf), Aventurine quartz from India (rock), Montmorillonite and Illite from Virginia (soil), seawater from the Pacific Ocean (water), fresh snow from Colorado (snow), and black road asphalt from Colorado (urban).

Hyperspectral imaging has its origin in the application of multispectral imagery with airborne and spaceborne sensors since the 1960s. Multispectral systems were developed for the gathering of information in various scientific fields, such as agriculture, geology and urban spaces (LANDGREBE, 1999). These kinds of sensors collect data only with a small number of broad and discrete wavelength bands in the visible (380 – 740 nm), near infrared (NIR) (740 – 1400 nm) and short-wavelength infrared (SWIR) (1400 – 3000 nm). It should be noted that the spectral regions of visible and NIR often are summarized as VNIR. Advances in sensor technology in the 1980s have led to the first hyperspectral sensors typically containing more than 200 contiguous bands, which allowed the construction of quasi-continuous reflectance spectra. This enabled far greater in-depth examination of surface features in contrast to the relatively coarse bandwidths of multispectral sensors. Hence, the term 'spectral resolution' is defined by the number and width of wavelength ranges that can be measured separately by a sensor. The higher the number of available bands and the lower the width of these bands, the higher the spectral resolution (GOVENDER ET AL., 2007), which enables a finer discrimination of unique spectral features.

Hyperspectral imagers were first established in aircrafts as airborne sensors, such as AIS (VANE ET AL., 1984), DAIS (COLLINS & CHANG, 1990), CASI (GOWER ET AL., 1992), AVIRIS (VANE ET AL., 1993), HyMap (COCKS ET AL., 1998), AVIS (OPPELT & MAUSER, 2007), APEX (ITTEN ET AL., 2008) and HySpex (BAUMGARTNER ET AL., 2012). In addition to the very successful multispectral systems in space, such as the Landsat program (TM, ETM, OLI) and ASTER, hyperspectral spaceborne sensors initially came up in the year 2000 with the Hyperion program by the National Aeronautics and Space Administration (NASA) (PEARLMAN ET AL., 2003), followed by CHRIS / PROBA by the European Space Agency

(ESA) in 2001 (BARNSLEY ET AL., 2004), HJ-1A by the China Aerospace Science and Technology Corporation (CASC) in 2008 (WANG ET AL., 2010) and HICO by the NASA in 2009 (CORSON ET AL., 2008).

However, these pioneers of spaceborne spectrometers have certain limitations, since some of them serve primarily as technology demonstrators (Hyperion, CHRIS), others cover only the VNIR range (CHRIS, HJ-1A, HICO) or have a low signal-to-noise ratio (Hyperion) (KAUFMANN ET AL., 2012). The German Environmental Mapping and Analysis Program (EnMAP) strives to overcome these limitations. From 2017 on, EnMAP will provide high-quality hyperspectral data on a regional scale. The present study is embedded in the scientific preparation of the mission, whose background is described in the following section.

Apart from the EnMAP mission, further hyperspectral imagers are currently in preparation: PRISMA (PRecursore IperSpettrale della Missione Operative) by the Italian Space Agency (ASI), HISUI (Hyperspectral Imager Suite) by the Japanese Aerospace Exploration Agency (JAXA), HyspIRI (Hyperspectral Infrared Imager) by the NASA and, last but not least, HYPXIM by the Centre National d'Études Spatiales (CNES) (KAUFMANN ET AL., 2012).

1.3 The EnMAP Mission

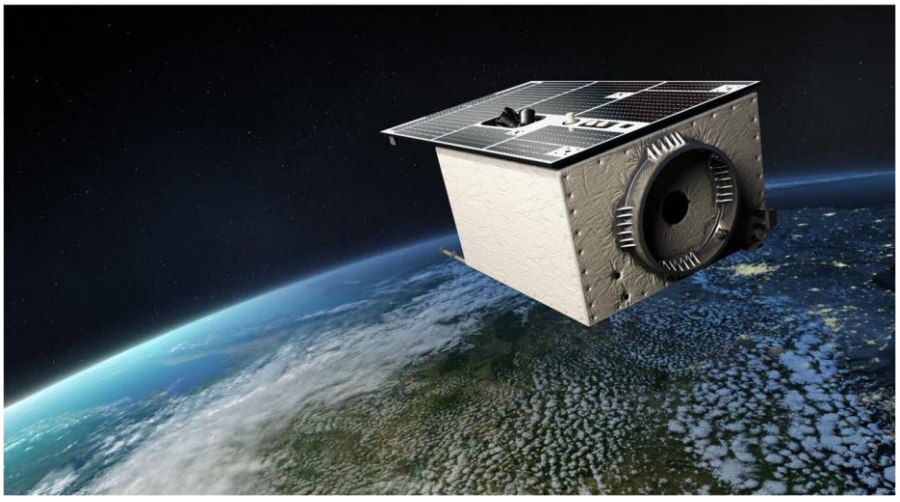

Figure 1-3: Illustration of EnMAP (KAUFMANN ET AL., 2012).

Hyperspectral remote sensing provides technology to derive biophysical land surface parameters, which are vital for improved land surface management, more precisely compared to multispectral methods (STAENZ, 2009). From 2017 onwards, the upcoming German satellite mission EnMAP (Figure 1-1) will deliver high-quality hyperspectral data with a spatial resolution of 30 meters (KAUFMANN ET AL., 2012). EnMAP will be launched in a sun-synchronous orbit at a height of 653 km (at 48 °N) and an inclination angle of 97.96°, allowing the satellite a revisit time of 23 days. Furthermore, in particular cases, the revisit

time can be increased up to four days due to the across-track off-nadir pointing ability of ± 30°. With a designated lifetime of five years and the frequent revisit time, EnMAP will not only enable hyperspectral monitoring on the regional scale, but will also allow for the multiseasonal monitoring of dynamic vegetation development. The specifications of the satellite can be taken from Table 1-1.

Table 1-1: EnMAP satellite characteristics.

Parameter	Performance
Orbit	Sun-synchronous
Altitude	643 km
Inclination	97.96°
Weight (payload + bus)	1000 kg
Size	3.1 m × 1.9 m × 1.7 m
Target Revisit Time	23 days (VZA ≤ 5°) / 4 days (VZA ≤ 30°)
Equator Crossing Time	11:00 h ± 18 min (local time descending node)
Average Ground Speed	6.9 km / s
Along-track Exposure	4.3 ms

The centerpiece of the satellite is the Hyperspectral Imager (HSI), which is a push-broom sensor recording the earth in a range of 420 to 2450 nm with 242 contiguous bands. The sensor carries two spectrometers covering two ranges of the electromagnetic spectrum: the VNIR with 88 bands and a spectral resolution of 6.5 nm, and the SWIR with 154 bands and a spectral resolution of 10 nm. Its major specifications can be seen in Table 1-2.

Table 1-2: EnMAP hyperspectral imager (HSI) specifications.

Sensor characteristics	Performance	
Imaging Principle	Push-broom, two prism imaging spectrometers	
Spectral Domain	VNIR	SWIR
Number of Spectral Bands	88	154
Spectral Range	420 – 1000 nm	900 – 2450 nm
Sampling Interval	6.5 / 10 nm	10 nm
Spectral Bandwidth (FWHM)	8.1 ± 1.0 nm	12.5 ± 1.5 nm
Signal-to-Noise Ratio (SNR)	> 500:1 (at 495 nm)	> 180:1 (at 2200 nm)
Ground Sampling Distance (GSD)	30 m (at Nadir, sea level)	
Swath Width	30 km (Field of View = 2.63° across-track)	
Swath Length	1000 km / Orbit – 5000 km / day	
Pointing Angle	± 30°	

Because EnMAP will be able to provide data frequently covering large areas, evaluation methods have to be developed for a full exploration of the satellite's potential for an application in a regional and also global scale. Thus it is necessary to adapt and enhance existing data analysis methods, which are based on established sensor systems such as airborne spectroscopy, to the spaceborne EnMAP scale.

Furthermore, the Department of Geography of the LMU Munich is involved in the preparation of algorithms that are designed to fully exploit these special capabilities of EnMAP for innovative agricultural applications of earth observation data. Some of the algorithms developed in this context are and will be published within a software product called EnMAP-Box, entirely dedicated to the use of the EnMAP data. The EnMAP-Box is a platform-independent software interface designed to process hyperspectral remote sensing data. It is intended to enable scientists interested in working with EnMAP data to perform basic but nonetheless state-of-the-art image operations. Some of the methods used in this study are also implemented to the EnMAP-Box.

1.4 Motivation and Goals of this Thesis

The scientific aim of this study is the investigation of two major objectives: data supply and data analysis. Since EnMAP data is not yet available, alternative ways must be found to acquire hyperspectral data, which then is used to simulate EnMAP data. Before the challenge of acceptable data provision is discussed, the aim relating to the second objective of data analysis is defined. The capabilities of EnMAP for the periodic monitoring of vegetation

parameters lead to the following question: Is it possible to gain multiseasonal information about biophysical and biochemical land surface parameters from spaceborne imaging spectroscopy without being dependent on in-situ data?

As part of this study, it is examined whether the retrieval of biophysical and biochemical parameters is possible throughout the growing period, and valid for different crops by the use of a unified method, which must not be adapted to the individual time steps of measurements. Further, a main objective must be to derive this information without depending on a-priori information in the form of in-situ data, as an implementation of corresponding field measurements in the context of EnMAP would not be viable.

Consequently, this study focuses on the retrieval of leaf area index and chlorophyll content, as they are important variables for the monitoring of the current status of plant and of canopy physiology, respectively. Leaf area index describes the size of the producing layer (WEISS ET AL., 2001) and is important for the estimation of foliage cover, as well as for forecasting crop growth and yield. It promotes the understanding of biophysical processes in canopies (HABOUDANE ET AL., 2004). Chlorophyll content is of particular significance as it indicates photosynthesis activity. As described above, it is directly related to nitrogen concentration and thus can serve as a measure of the crop response to nitrogen application (HABOUDANE ET AL., 2002). These two variables occur on different scales; chlorophyll content as chemical compound takes place at the leaf level, while leaf area index is a structural variable describing a canopy property.

The challenge of estimating these parameters from hyperspectral data without the use of in-situ data leads to the application of physically-based methods. For this purpose, the widely accepted coupled leaf optical properties model (PROSPECT-5b) and canopy bidirectional reflectance model (4SAIL) PROSAIL (JACQUEMOUD ET AL., 2009) were applied, which simulates realistic reflectance data for homogeneous vegetated surfaces (JACQUEMOUD ET AL., 1995). In contrast to empirical-statistical models, such as vegetation indices which have to be calibrated against in-situ data if they are to be used for the derivation of actual vegetation variables, physically based methods can be applied without in-situ data available. Due to their intrinsic dependency on in-situ data, empirical models may deliver high-quality results, but at the same time suffer from a very limited transferability. In addition, vegetation indices are limited due to the fact that they are not a measure for a specific variable, such as chlorophyll content, since the reflected signal is influenced by the interaction of several biophysical and biochemical components (e.g., HABOUDANE ET AL., 2004). The inversion of a reflectance-generating physically based model, by contrast, enables the determination of several biophysical parameters. Furthermore, empirical methods are sensitive to anisotropy effects that result from a variable sun-sensor-target geometry within the airborne data. This fact is also of importance in regard to the ± 30° pointing capability of EnMAP. Physically based approaches may explicitly account for these anisotropies, so that illumination angle dependent

nonlinearities may serve as additional information instead of being an error source. This can be integrated into the retrieval strategy, thereby improving the overall retrieval quality. Such models have previously been applied to field crops and grasslands (e.g., JACQUEMOUD ET AL., 2000; VERHOEF & BACH, 2003).

To counteract the non-availability of EnMAP data until 2017, an alternative database was necessary for the implementation and examination of retrieval strategies. Hence airborne spectroscopy was widely used for the development of these methods. Applying commercially available imaging spectrometers, however, is limited by the sensor availability and often involves high costs, which makes it almost impossible to generate a multiseasonal dataset for a specific test area based on commercial sensors alone. To overcome this limitation, a cost-effective series of airborne imaging spectrometers called AVIS (Airborne Visible and Near Infrared Spectrometer) has been developed at the Department of Geography of the LMU Munich (OPPELT & MAUSER, 2007). The goal of obtaining a multiseasonal database which is able to project the vegetation dynamics over the growing period was thus achieved by the use of the third-generation sensor, AVIS-3. Therefore, four data acquisitions were successfully performed during the course of the vegetation period of 2012 over a 12 km² large test site in Southern Germany (Neusling, Lower Bavaria). Because AVIS-3 is an experimental sensor, the elaborate preprocessing steps are an essential part of this thesis. Furthermore, the multiseasonal campaign was complemented by two additional acquisitions from the airborne sensor HySpex, which is operated by the German Aerospace Center (DLR). In order to accurately validate the methods developed for the retrieval of biophysical and biochemical parameters an extensive field campaign was carried out alongside the airborne data acquisitions.

Since the retrieval strategies applied to the multiseasonal database were based on the spectral properties of the airborne sensors, which differ from those of EnMAP, and were validated on field measurements which reflect a comparatively higher spatial resolution of the very same, these methods are neither valid nor easily transferable to the properties of the satellite. To test the applicability of the analysis procedure on a spaceborne scale, both the database as well as the methods were consequently adapted to the properties of EnMAP.

1.5 Radiative Properties of Vegetation

For the retrieval of plant-physiological parameters from remote sensing data it is important to understand the biophysical and biochemical processes which regulate the radiative properties of leaves and vegetation canopies. While the radiative properties are, on the leaf level, mainly controlled by the biochemical composition of vegetation, reflectance is, on the canopy level, driven by biophysical or structural processes and properties. Although these effects relate to

two different scales and thus are described separately, it should be kept in mind that these processes are closely intertwined. An alteration of the biochemical compounds of leaves is often associated with alterations of the canopy structure, and vice versa.

1.5.1 Leaf Level Properties

The primary process driving plant growth is photosynthesis. Thereby, carbon dioxide (CO_2) is fixated from the atmosphere and converted to sugar serving as building blocks and as source of energy for the synthesis of complex organic molecules. During this process oxygen (O_2) is released as a secondary product. The process of photosynthesis can be separated into light reaction, which is the absorption of photosynthetically active radiation (PAR), and dark reaction describing the biochemical processes of CO_2 fixation and the production of sugar. The rate at which leaves fixate CO_2 depends on the diffusion rate of CO_2 from the atmosphere through the leaf boundary layer, stomata, and intercellular cells into the liquid phase of chloroplasts (JONES & VAUGHAN, 2010).

The way solar radiation interacts with vegetation depends not only on the wavelength of incident radiation but also on the structural and biochemical composition of leaves, such as pigment content, water content, leaf structure, leaf thickness and leaf age. The chemical and structural characteristics of leaves in turn are influenced by plant growth, phenological phase and specific stress. The most important substance in leaves is chlorophyll, a green pigment molecule located in the chloroplasts, which are organelles of the mesophyll. Mesophyll is the basic cell tissue in leaves and is protected by an epidermis, usually containing no chloroplasts. In most cases, the epidermis is covered by a waxy cuticle protecting the leaf from degassing water. Gas exchange takes place through the stomatal pores.

Chlorophyll, directly connected to nitrogen content (GITELSON ET AL., 2003), is the main component influencing reflectance in the visible spectral domain and gives plants the characteristic green color, as it is responsible for most of the absorption of radiation in the red but also in the blue wavelength ranges. In addition, there are other photosynthetic pigments influencing the reflectance predominantly in the visible domain, called accessory pigments. They are usually located on so-called thylakoid membranes of the chloroplasts. Together with chlorophyll they are responsible for the absorption of PAR, which excites electrons in the pigments. These electrons are also collected as well as regulated by carotenoids in their function as antenna pigments. Carotenoids extend the absorption to the blue-green wavelength range; they can be differentiated into two main groups: carotenes (e.g., β-carotene), which transfer a fraction of the absorbed energy to the chlorophyll, and xanthophylls (e.g., violaxanthin, zeaxanthin and lutein), which regulate the amount of excited electrons transferred to chlorophyll, thus protecting the plant from the harmful effect of photo oxidation. (GITELSON ET AL., 2002; MERZLYAK & GITELSON, 1995). Photo oxidation, resulting

in the generation of reactive oxygen species, e.g., hydrogen peroxide (H_2O_2), indirectly influences fluorescence of the leaf. Fluorescence is caused by excited chlorophyll molecules and describes the process of an immediate re-emission of around 2-5 % of the absorbed radiation (MERONI ET AL., 2009) at a longer wavelength than the exciting wavelength, with emission peaks at 690 and 735 nm. It should not to be confused with heat dissipation, a mechanism which xanthophylls induce to prevent photo oxidation. This process, however, leads to the elimination, also-called quenching, of the fluorescence signal. Thus, the detection of fluorescence shows high potential for the derivation of current status of photosynthesis process and leaf health (JONES & VAUGHAN, 2010).

While carotenes have a yellow appearance, xanthophylls are characterized by an orange color. Both become visible in autumn or under certain environmental conditions, when chlorophyll content decreases. Other important pigments are anthocyanins, which develop at the end of the growing period and support the protection of the leaf from high energy ultraviolet radiation. They are responsible for the reddish color in autumn leaves. Typical autumn colors occur due to the progressive process of senescence. This is triggered by a photoperiodic change, which generally occurs towards the end of the growing period. With ongoing senescence, even carotenoids and anthocyanins disintegrate and the typical brownish color (brown pigments) emerges.

While vegetation barely absorbs radiation energy in the NIR, cellulose, lignin and proteins induce increased absorption in the SWIR range. Furthermore, plant water causes the same broad absorption bands as atmospheric water vapor, especially around 1450, 1950 and 2500 nm. These absorptions are caused by rotation and stretching of chemical bonds between light atoms due to a lower energy content of lower wavelengths (CURRAN, 1989).

Since only a small fraction of incident radiation is reflected at the top surface of a leaf (cuticle), radiation interacts in the form of scattering, transmission and absorption processes at different levels and at air/water interfaces at the surface of cells within the leaves.

1.5.2 Canopy Level Properties

The reflectance of solar radiation does not solely depend on leaf properties, but also on the angle of the leaf to incident radiation. Different leaf angles thus result in different brightness levels registered throughout the whole solar range. Within a canopy, the leaf angle distribution (LAD) is often described by an average leaf angle (ALA), leading to a specific assumption on canopy density. This information alone is however less meaningful, since the distribution of the leaves may range from horizontal (planophile) to vertical (erectophile). To improve the specification of the current distribution, a leaf inclination distribution function (LIDF) can be defined, thereby taking into account that there are manifold leaf orientations within the canopy.

When radiation is incident on a canopy it is scattered by its different components, a process known as volume scattering. Apart from photosynthetically active leaves, these components include branches, stems and other plant material. In addition, the reflectance of the canopy is influenced by its architecture and spatial distribution as well as the underlying soil. These scattering effects can be compared to those caused within the leaf structure, but occurring on a larger scale. One of the most prominent descriptions of canopy density is the leaf area index (LAI). It is defined as the one-sided leaf area [m²] per unit ground [m²] (JONES & VAUGHAN, 2010).

Apart from structural parameters, e.g., LAD and LAI, the anisotropic behavior of canopies must be taken into account. Anisotropy originates from the fact that leaves are not Lambertian surfaces, which means they do not reflect incident radiation ideally diffusely. Moreover, and this has a far greater impact, an altering viewing angle implies a varying proportion of sunlit and shadowed parts within the canopy. This effect depends on the viewing direction of the observer: when the canopy is regarded in the same direction as the incoming solar radiation, mainly sunlit areas are within the field of view; when the observer faces the sun, however, the canopy shows far more shadowed sections. The first, i.e., when the view direction corresponds with the solar angle, leads to the hot spot effect, although it is not only influenced by the viewing direction but also by the shape of the leaves and canopy. Thus the reflected signal, and thereby the brightness of the canopy, depends both on the incident angle and the direction of view of the observer. A full description of this property is given by the wavelength-dependent bidirectional reflectance distribution function (BRDF), which is defined for all possible illumination and viewing angles. According to JONES & VAUGHAN (2010), the BRDF is defined by:

$$f(\theta_i, \varphi_i; \theta_r, \varphi_r) = \frac{dL_r(\theta_r, \varphi_r)}{dI_i(\theta_i, \varphi_i)} \qquad \textit{(Equation 1-1)}$$

where

Θ_i	illumination zenith angle
Φ_i	illumination azimuth angle
Θ_r	observer zenith angle
Φ_r	observer azimuth angle
dL_r	reflected spectral irradiance
dI_r	incident directional spectral irradiance

Since this definition allows the specification of infinitesimally small view and incident angles, which is a level of detail that imaging spectrometers, and sensors in general, do not supply, i.e., they have finite acceptance angles, the BRDF can be simplified to the bidirectional reflectance factor (BRF). The BRF is the ratio of actual reflected radiance in a certain

direction to the hypothetical reflectance of a Lambertian surface under the same geometric conditions (NICODEMUS ET AL., 1977). The BRF is theoretically symmetric, but it is influenced by structural properties, such as LAI, LAD and leaf size. It also is wavelength-dependent, since scattering and transmission amount differ within the solar spectral range. In vegetation surfaces, these effects are strongest in the near infrared at the red edge.

Knowledge of the potential variation of reflectance under several illumination and viewing conditions may serve as further information. When analyzing the reflectance properties of canopies, the processes and properties occurring in vegetation, which have been described here, must be taken into account. Consequently, an overview of different methods for the analysis is given in the following chapter.

1.6 Methods for the Retrieval of Biophysical Parameters from Remote Sensing Data

The measured reflectance signal is defined by the properties of the surface. Thus, in an agricultural context its purpose is to retrieve information about the canopy by analyzing this reflected signal. In general, two completely different approaches can be distinguished for the estimation of biophysical parameters from optical remote sensing data: empirical-statistical methods and the inversion of physically based models. Both methods are independent of the type of the sensor (spaceborne, airborne, spectroscopic field measurements) and are described in the following sections.

1.6.1 Empirical-statistical Methods

Empirical-statistical methods establish a relationship between the measured reflectance signal from the sensor and the sought biophysical information at the ground. Therefore these models rely to in-situ measurements, such as leaf area index or water content, because the output of these models is usually a dimensionless value. Using one of the numerous regression techniques which have been developed over the years these dimensionless values are related to the measured ground information of corresponding pixels. Among several approaches the use of vegetation indices is the most common and oldest method (GLENN ET AL., 2008). A spectral vegetation index is usually a combination of different spectral bands in a ratio, or the normalized form of this. The most famous among them is the normalized difference vegetation index (NDVI) defined by DEERING & HARLAN (1974), which has been applied in numerous studies and is still a powerful tool for the identification of vegetation and its vitality status. Moreover, several studies investigated the potential of the NDVI for the retrieval of biophysical parameters, such as leaf area index (e.g., BARET & GUYOT, 1991). Generally,

normalized indices have the advantage of being applicable to uncalibrated grey values as well as compensating for shadow effects in spectroscopic image data, since they are based on the brightness relationship of only a small number of bands. Within the last decades hyperspectral remote sensing has enabled the development of a whole range of narrowband vegetation indices, which serve for the determination of a variety of vegetation characteristics.

Given the availability of ground truth information, indices represent a sophisticated technique for the retrieval of vegetation characteristics, as they are in most cases based on simple equations and deliver prompt results through fast calculation time. Therefore, a module called AVI (Agricultural Vegetation Indices) containing a collection of 65 hyperspectral vegetation indices which were selected in an extensive literature survey, was implemented in the EnMAP-Box. The indices of the module are grouped according to their primary purpose: estimation of structural (N=13) characteristics, chlorophyll (N=26), carotenoids (N=5), leaf water (N=8), dry matter (N=9) and fluorescence (N=4).

A more recent method is based on the concept of continuum removal, an approach commonly applied in chemical sciences for the determination of mixture component concentrations. This approach has been developed as an alternative to simple vegetation indices. In contrast to narrowband indices, which only use discrete wavelengths, this approach makes use of a predefined range in a quasi-continuous dataset, as it is given by hyperspectral sensors, and thereby of the full spectral information available from a specific wavelength region. Thus it is potentially more sensitive compared to narrowband indices and more suitable for the analysis of hyperspectral data. The algorithm compares integrated areas enclosed below the spectrum and below an envelope line which is spanned as a spectral hull between two bordering wavelengths. It was first used for the retrieval of chlorophyll content by integrating the chlorophyll absorption range from 550 to 760 nm (OPPELT, 2002). Compared to conventional indices this approach proved superior in that study. Recently, the algorithm was transferred to another spectral range and demonstrated high potential for the estimation of canopy water content (HANK ET AL., 2010a). However, further biophysical variables, which are particularly sensitive in certain regions of spectral absorption, can be estimated as well.

This method, due to its flexibility, was also realized in the EnMAP-Box. The ASI module (Analysis of Spectral Integral) was implemented in a dynamic fashion, which allows the user to determine subjectively the extent of the absorption range by changing the border wavelengths of the spectral range to be integrated.

Although empirical-statistical retrieval strategies lead to valuable and satisfactory results (e.g., ATZBERGER ET AL., 2003; PRICE & BAUSCH, 1995), they are limited mainly in three main ways:

(1) The spectral signal measured by the sensor is usually influenced by multiple surface properties, which may impede an isolated derivation of a specific land surface parameter. In addition, only parameters measured in-situ could be retrieved;
(2) The derivation of an empirical relationship requires the collection of corresponding measurements of the requested land surface parameter at the ground, which is often very time-intensive or even impossible in poorly accessible areas;
(3) The transferability of an empirical model, which is based on the relationship of a sensor signal to the ground measurement, is severely limited due to varying sensor properties, illumination and viewing geometries as well as time of recording. This makes the site- and sensor-specific empirical-statistical models unsuitable to be applied to other datasets, regardless whether they stem from a different sensor or represent seasonal data recorded with the same sensor, as these datasets may be subject to a significantly different sun-target-sensor geometry (e.g., CURRAN, 1994). It is thus also not possible to apply these models to data of a large areal extent.

These limitations make empirical-statistical models most unsuitable for the multiseasonal parameter retrieval from future EnMAP data, as it is planned to (i) retrieve multiseasonal information, (ii) of large areas and (iii) without the dependence on in-situ data.

1.6.2 Physically based Models

In contrast to empirical-statistical methods, physically based models follow a completely different approach. As already mentioned, these models have the advantage of being independent of in-situ measurements. Furthermore, while empirical methods suffer from anisotropy effects, physically based models explicitly account for bidirectional reflectance caused by specific sun-target-sensor geometries. In general, the physically based models discussed in this study can be described as radiative transfer models, since they try to calculate reflectance, absorption and transmittance of leaves and canopies from biophysical plant characteristics. These models can be used in two directions: in forward operation mode, where the radiative properties are calculated as a function of the underlying physics of the individual components of the leaf or canopy, resulting in a predictive reflectance signal. In the other direction, inverse operation mode, biophysical and biochemical parameters are retrieved from a measured reflectance signal. Since the inversion process is an important and complex matter, it is described in the following chapter in more detail.

Radiative transfer models which calculate the properties of a leaf are called leaf optical properties models, while those addressing whole canopies are called canopy reflectance models (CRMs). Since a hyperspectral sensor usually images the surface of the earth and thus vegetation canopies, CRMs are used in inverse operation mode to retrieve the respective parameters. There are several CRMs described in the literature which differ in architecture

and complexity. According to JONES & VAUGHAN (2010), four types of canopy reflectance models can be distinguished, which are presented in the following.

Turbid-medium models describe the canopy as one-dimensional layers of a horizontal slab with infinite small elements that follow a statistical distribution. They are based on the same theory that describes radiation transfer in gases. Although these models generate bidirectional reflectance they are not able to directly simulate the hotspot effect. To counteract this, *turbid-medium models* have been extended to so-called hybrid models, considering a finite leaf size defined by an empirical correction, which allows the hot spot effect to be calculated. These models are most suitable for the description of plant populations within a homogenous surface, as they occur in agricultural canopies. The theory of this approach is described in more detail in Chapter 3.1.2, as the SAIL model, based on the turbid-medium concept, was used in this study.

Geometrical-optical models, by contrast, assume the canopy to be an array of geometrical objects. These objects have defined shapes and optical properties that follow a statistical distribution. The model calculates radiation interaction and reflectance analytically, considering light interception and shadowing defined by the geometry of the canopy. The overall reflectance of the canopy is thus calculated as a weighted average of the single area fractions, such as sunlit and shaded leaves/soil. This is possible for any viewing angle. These models are in general used to describe forest canopies as Lambertian cones (OTTERMAN & WEISS, 1984; LI & STRAHLER, 1985 and 1992).

Monte-Carlo ray-tracing models simulate how a defined number of light rays emitted by a light source would interact with each of a canopy's elements. A probability density function calculates how these rays are absorbed, transmitted and reflected at the single elements of a canopy (GOVAERTS & VERSTRAETE, 1998). A single ray is thus either reflected between the elements until it leaves the canopy, or its energy level falls below a defined energy threshold due to absorption processes. Since only a minimum part of rays would reach a sensor in this model, such a theoretical calculation would be very computationally intensive. Consequently, many models calculate the pathway of the ray of light inversely, which means the ray starts at the sensor and traces back through the canopy to the light source. Ray-tracing models impress with their potential for comprehending the way of direct radiation, and because they do not rely on analytical solutions of the radiation-transfer equations of canopies (JONES & VAUGHAN, 2010). However, when calculating diffuse irradiance, the computation time may become excessively long. Closely related to this approach are three-dimensional radiosity models that treat the canopy as a number of diffuse reflecting surfaces and calculate the energy flux from (in theory diffuse) surfaces, whether it is reflected, transmitted or emitted (e.g., BOREL ET AL., 1991). The exchange of radiation between the different surfaces is regulated by a view factor, describing the fraction of energy leaving and received by two infinitesimal surfaces. In comparison to backward ray-tracing models, radiosity models are

more suited for the calculation of diffuse radiation, since they consider radiation from all directions. The calculation of the view factor matrix, which describes all possible factors, may be, however, time-consuming.

The last type comprises *kernel-driven semi-empirical models* that differ significantly from the other approaches. These models use the sum of three kernels representing isotropic scattering, volume scattering from homogenous canopies and geometrical scattering for the description of three-dimensional objects including shadowing effects and consider the hot spot effect (e.g., ROUJEAN ET AL., 1992)). Using empirical definitions they have the advantage of being much faster and easier to invert than the models described above.

Most canopy reflectance models are not suitable for considering the biochemistry of the canopy. By contrast, leaf optical properties models take these into account to determine the reflectance behavior. JACQUEMOUD & USTIN (2001) categorize four classes of models, which are presented only briefly here since they have much in common with the CRMs described before.

Plate models (e.g., ALLEN ET AL., 1969) describe the leaf as an absorbing plate with a rough diffuse reflecting surface. Extending this approach to a *N-flux model*, the internal leaf structure is separated into N homogenous compact layers and N-1 cell-to-air layers (e.g., ALLEN ET AL., 1970). A popular version of this approach is the PROSPECT model (JACQUEMOUD & BARET, 1990), which is used in this study. A detailed description of this approach can be found in Chapter 3.1.1.

Furthermore, *stochastic models* separate the leaf into different tissues, by which the optical properties are simulated by a Markov chain (e.g., TUCKER & GRANT, 1977; MAIER ET AL., 1999). Last but not least, *ray-tracing models* are used as well to describe the internal leaf structure, although a detailed characterization is necessary (e.g., ALLEN ET AL., 1973; GOVAERTS ET AL., 1996).

1.6.3 Inversion of Canopy Reflectance Models

To estimate biophysical parameters from spectral reflectance data, physically based radiative transfer models generally have in common that they must be inverted (DARVISHZADEH ET AL., 2008), which means that for a measured reflectance spectrum the parameter configuration of a corresponding, in an ideal situation identical, modeled spectrum is derived. The quality of the parameter estimation from physically based models depends on three factors (JACQUEMOUD ET AL., 2000):

(1) The access to a comprehensive model which is able to generate reflectance data based on the physics of biophysical and biochemical parameters at leaf as well as at canopy level considering the complex influence of different illumination and viewing angles;

(2) The availability of high-quality, calibrated reflectance data;
(3) An appropriate inversion procedure.

There are several inversion techniques described in the literature, which differ in computation speed, robustness and performance. The most common inversion techniques for parameter retrieval are numerical optimization algorithms, artificial neural networks (ANN) and look-up tables (LUT) (RICHTER ET AL., 2009). In the following the architecture, advantages and disadvantages of these techniques are presented. Subsequently, the comparatively new inversion concepts of support vector regression (SVR) and Bayesian inversion are summarized in Chapter 1.6.3.4.

1.6.3.1 Numerical Optimization Algorithm

Numerical or iterative optimization algorithms have the longest history in the field of inversion methods (KIMES ET AL., 2000). The optimization algorithm identifies the minimum of a function by applying the model iteratively in forward mode, under a given initial parameter setting. Within a certain parameter range this process continues until a cost function between measured data and modeled data is minimized. One of the most prominent optimization algorithms in remote sensing applications is the quasi-Newton method (e.g., KIMES ET AL, 2000, COMBAL ET AL., 2002 & MERONI ET AL., 2004) which is constrained by fixed upper and lower boundaries of independent variables using function values only (subroutine E04JAF, NUMERICAL ALGORITHMS GROUP, 2012). It approximates a Hessian matrix, which describes a square matrix of second-order partial derivatives, at each iteration of the function (KIMES ET AL., 2000). JACQUEMOUD ET AL. (2000) as well as KIMES ET AL. (2000) list and describe a selection of frequently used algorithms, among them also comparatively common algorithms such as the downhill simplex method (NELDER & MEAD, 1965) or the conjugate direction set method (e.g., subroutine POWELL from PRESS ET AL., 1986).

However, iterative optimization methods hold the risk of being trapped in local minima (MERONI ET AL., 2004). Another disadvantage of iterative optimization algorithms is that they are very time consuming in processing the high-resolute spectral information of imaging spectroscopy with its substantial number of bands and several thousands of pixels (DARVISHZADEH ET AL., 2012).

1.6.3.2 Artificial Neural Network

In theory, neural networks assume that there is an optimal mathematical relationship between a set of input parameters and a corresponding set of output parameters. Reflectance spectra thereby act as input parameters whereas biophysical parameters act as the output. The stronger the mathematical relationship, the better are the results of the output (KIMES ET AL.,

2000). Neural networks must be trained with examples which are provided by a CRM to approximate a relation between a spectral reflectance of a canopy and its structural and optical parameters.

A commonly used method for this is the back-propagation multilayer perception (MLP). A multiple number of nodes connect the input information to the output. The nodes represent a simple processing element responding to a weighted input from other nodes (ATKINSON & TATNALL, 1997).

The feed-forward neural network in general consists of three layers: a single input layer, a multiple hidden layer and a single output layer. The first layer represents the spectral information. The number of nodes at the input layer is equivalent to the number of used spectral wavelengths. The nodes of the input layer are fully connected to the nodes of the hidden layer(s) which respond to a weighted input from the previous ones in a characteristic way. Each node in the hidden layer is a nonlinear processor which produces a new output signal from the incoming information by weighting it differently. It is not revealed how this weighting decision is made, i.e., it is hidden. Thus, the signal which is sent to subsequent nodes is hidden too. Finally, the signal reaches the output layer which represents the output data, i.e., the biophysical parameters (KIMES ET AL., 2000).

During the training process the produced network output is compared to a desired output and the error is computed. When using the physically based, modeled spectra the output of the network is compared to the parameter specification of the RTM. The error then is back-propagated through the network which leads to an alteration of the weights of the connections between the nodes in the hidden layer. This process is carried out iteratively until the error is minimized (ATKINSON & TATNALL, 1997).

To guarantee that the neural network is able to yield consistent results with unknown data, several factors can be considered. They include the number of nodes and the architecture of the network, the size of the training dataset and the training time. Generally one can say that the higher the number of hidden layers, the better the network is able to solve complex problems. On the other hand, if the network is too much aligned to the training data due to a high number of nodes or an extensive training time, resulting in too-strongly minimized errors, it lacks the capability of generalization when confronted with unknown data. The network then is overfitted (ATKINSON & TATNALL, 1997).

Other major disadvantages of neural networks are the exhaustive training times and the lack of transparency due to the unexplained decisions in the hidden layer. The neural network can thus be described as “black box”.

The advantages of neural networks include the fact that, once they are trained, they perform much faster than other inversion techniques, even faster than a look-up table (VUOLO ET AL., 2010). Accordingly, neural networks are in general suitable for the processing of large

amounts of image data. Furthermore, they are independent of any initial parameter settings (KIMES ET AL., 2000).

1.6.3.3 Look-Up Table

In the look-up table (LUT) approach the applied model precomputes, in forward operation mode, spectral reflectances based on a specific range of predefined parameter combinations. It thus produces a multidimensional table of outputs with a certain amount of spectra and their corresponding parameter configuration. Based on a cost function, which searches for the lowest distance between two spectra, the measured reflectance of a pixel is assigned to the reflectance of the LUT which it resembles the most. As a consequence, the underlying parameter setting behind the modeled spectrum is assumed to be valid for the measured spectrum and thus represents the biophysical variables to be retrieved. The quality of a LUT depends on the range, discretion levels, number of parameter configurations as well as an optimal search strategy (e.g., KIMES ET AL., 2000). If the distance between the discretion levels is too great or the dimension is too low, the LUT inversion may lead to suboptimal solutions (RICHTER ET AL., 2009).

Similar to neural networks, an advantage of the LUT is that a large amount of the computing time is completed before the inversion is carried out (KIMES ET AL., 2000). In contrast to numerical optimization and ANN, the LUT approach however admits a global search and is in this way not in danger of being trapped in local minima (DARVISHZADEH ET AL, 2011)

Numerous studies, e.g., from COMBAL ET AL. (2002) or VUOLO ET AL. (2010), show that the LUTs are often more robust and generate higher accuracies than other approaches. Moreover, LUTs have the advantage that they represent a relatively simple method, their content being precisely defined (KIMES ET AL., 2000). In this way, intermediate results can also be considered as comprehensive, while neural networks are often criticized as being black boxes. Compared to iterative optimization algorithms, the LUT method is significantly less time consuming (e.g., DARVISHZADEH ET AL., 2012). However, it is not as fast as a neural network.

A feature that the LUT has in common with the other approaches is the ill-posed nature of inversion. This means that different parameter settings of the model may lead to nearly identical spectra. There are different ways to solve the ill-posed problem, for example by averaging the parameters of a specific number of best fits. The ill-posed problem and the solution approach are described in detail in Chapter 3.2.3.4.

Due to its simplicity, transparency and robustness the LUT approach was chosen to serve as the inversion technique for this study. Its transparency in particular was a crucial criterion, as it facilitates a deeper understanding of canopy reflectance processes, model output and behavior, and the identification of potential weak spots in the data applied, for example

minimal atmospheric distortions. A detailed description of the applied LUT can be found in Chapter 3.2.

1.6.3.4 Other Inversion Techniques

A comparatively new inversion method is the support vector regression (SVR), which is based on the theory of statistical machine learning and was developed by VAPNIK (1995). SVR, which is a variation of the support vector machine (SVM) approach, is capable of identifying a solution through the construction of a so-called optimal hyper plane in a high-dimension feature space. The hyper plane separates two classes and is defined by a kernel and a regulation parameter. For the retrieval of LAI, DURBHA ET AL. (2007) used the SVR approach to perform a feature extraction by a kernel principal component analysis (KPCA), which represents a non-linear extension of the classical PCA. The application of SVR has proven to lead to respectable results, since it features good capabilities for generalization and is able to handle linearly non-separable data by the use of multiple hyper planes. However, the SVR method is excluded from application in the context of this study, since only one parameter can be retrieved at a time.

Other alternative inversion techniques include Bayesian methods, which are based on the Bayes' theorem, a mathematical theorem from probability theory, which describes the calculation of conditional probabilities. Bayesian methods, for example Monte-Carlo Markov Chains and Importance Sampling (e.g., MAKOWSKI ET AL., 2006), approximate the posterior distribution. This means that the probability distribution of the parameters can be determined when the measured reflectance is known (BARET & BUIS, 2008). Nevertheless, similar to numerical optimization algorithms, there is a risk of trapping into local minima. This necessitates the careful choice of starting conditions, e.g., the choice of considered values or an optimization of the number of sample angles used.

2 Generation of a Multiseasonal Database

The implementation of the objectives of the thesis requires a fundamental data base, on which multiple demands are made:

(1) Hyperspectral quality: methods and algorithms presented in this study must correspond to the technical specifications of EnMAP, especially regarding the spectral quality. Thus, the database should at least offer spectral properties corresponding to EnMAP.
(2) Multiseasonality: to capture the wide range of vegetation dynamics occurring within a vegetation period, a minimum number of datasets must be defined and acquired.
(3) Extensive validation fundament; to validate methods a sufficient and independent reference database is needed.
(4) Transferability: methods should be applicable to every type of agricultural land and to different kinds of crops.

To fulfill point (1), methods must be developed and tested on an alternative database, since EnMAP data will not be available until 2017, Unfortunately, other already existing spaceborne hyperspectral sensors, e.g., Hyperion, do not offer the potential to deliver data in an adequate spectral quality and temporal frequency, a prerequisite for item (2). However, airborne image spectroscopy is a cost-efficient, flexible and efficient alternative that fulfills both demands. For this reason, two airborne sensors were used to provide the required database: AVIS-3, operated by the Ludwig-Maximilians-University, and HySpex, operated by the German Aerospace Center. To fulfill point (3) an extensive field campaign was carried out parallel to the flights, measuring a set of biophysical parameters in-situ. The test site was carefully chosen to offer a representative cross-section of important crop types cultivated in Germany, Europe and also worldwide.

This chapter introduces the implementation and data acquisition of the substantial multiseasonal campaign carried out in 2012 (Chapter 2.1) including a description of both the test site and the airborne and in-situ data collection. This is followed by the specification of the hyperspectral sensor systems and complex (pre-)processing steps of the data (Chapter 2.2). To conclude, the essential transfer process of the airborne data to a simulated EnMAP-scale is explained (Chapter 2.3).

2.1 Field Campaign 2012

From April until September 2012, a multiseasonal campaign meeting the requirements defined above was conducted with a total of six data acquisitions using airborne image spectrometers. During the flights, five different biophysically relevant parameters were gathered in-situ at more than 500 sampling points. Furthermore, the in-situ database was extended by spectroscopic field measurements of defined reference targets, which served for calibration purposes. In a predominantly agricultural region in the southeast of Germany an investigation area of 12 km² (3x4 km) was identified as offering the necessary diversity of crop types. The geographical setting of the study site and the measuring techniques of this extensive field campaign are described below.

2.1.1 Study Site Neusling, Lower Bavaria, Germany

The study site around the village of Neusling in Lower Bavaria, Germany, is located about 110 km northeast of Munich and about 50 km southwest of the Bavarian Forest. The region is also known as the ‘Gäuboden’, a German expression describing the markedly fertile soils in Lower Bavaria. This area was chosen since it offers a representative sample of important agricultural crops cultivated in Bavaria, Germany and Central Europe.

The region is characterized by a humid climate all year round with an average annual temperature of 7.4 °C and an annual rainfall amount of 750 – 850 mm. The main geological feature in this region is the extensive glacially shaped loess area, partially interrupted by older gravel cover originating from the Danube and Guenz glacial periods as well as by upper freshwater molasses from the Tertiary. The soil types dominating the area are brown earth and luvisol, partially pararendzina, gleyed brown earth and pseudogley (INT 1).

Figure 2-1 shows the result of the land use examination of the test site, conducted in April and August 2012. The dominant crop types in the area are winter wheat, winter barley, potatoes and maize, followed by rapeseed, sugar beet and cucumber. The figure reveals that the winter crops, such as winter wheat or rapeseed, had already been harvested by the time of the second land use recording in August.

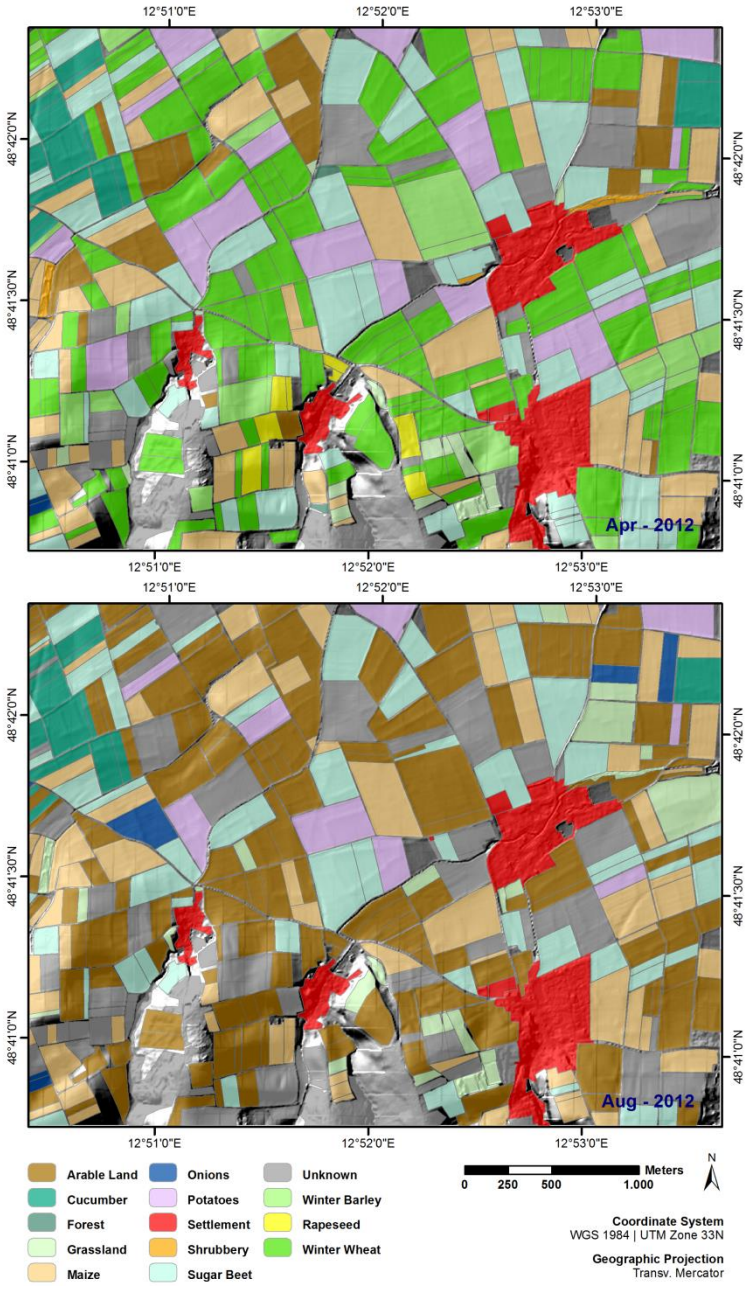

Figure 2-1: Land use map for spring (April) and late summer (August) in the test site.

2.1.2 Airborne Image Data Acquisition

Unquestionably, the basis of this multiseasonal campaign was formed by hyperspectral image data from airborne sensors. Besides the data acquired as part of this thesis with LMU's proprietary AVIS-3, further recordings were sourced from the HySpex sensor, operated by the German Aerospace Center (DLR). According to HANK ET AL. (2013), at least four flights are required to enable the monitoring of the physiological dynamics of a vegetation period. To minimize the risk of unforeseen acquisition failures which may occur during the period of the campaign due to unfavorable weather conditions or technical complications, and because of

the tight schedule of HySpex operations for other research institutes, it was planned to carry out at least four flights with AVIS-3. Due to restrictions imposed by the airport from which the aircraft that served as platform operates, flights were possible only on weekends and public holidays. Although it was planned to operate the flights at regular intervals from April to September, scheduling had to be adapted depending on adequate weather conditions, which significantly limited the number of potential flight dates. Nevertheless, four acquisitions with AVIS-3 were successful and could be complemented by image data from two HySpex flights. A third HySpex flight, scheduled for June 29th, had to be cancelled at short notice due to rapidly changing weather conditions, although the field team had already started to collect data. Another problem occurred when, despite the good weather forecast, convective clouds partially disturbed the flyover on May 25th. The consequences are described in Chapter 2.2.4. Table 2-1 gives an overview of all acquisition dates, including HySpex data.

Table 2-1: Data acquisitions of the 2012 campaign. The table contains information on sensor type, actual date, planned date, average flyover time, resulting average solar zenith angle (SZA) and final result.

Flight Nr.	Sensor	Actual Date	Planned Date	Avg. Time (CET)	Avg. SZA [°]	Result
1	AVIS-3	Apr 28th	Apr 21th	11:05	42	Flight & field data collection successful
2	HySpex	May 08th	-	10:18	45	Flight & field data collection successful
3	AVIS-3	May 25th	Jun 02th	15:22	39	Flight partially (clouds) & field data collection successful
4	AVIS-3	Jun 16th	Jul 07th	12:06	28	Flight & field data collection successful
-	HySpex	Jun 29th	-	-	-	Flight cancelled, field data collection successful
5	HySpex	Aug 14th	-	11:05	43	Flight & field data collection successful
6	AVIS-3	Sep 08th	Sep 8th	11:59	45	Flight & field data collection successful

In order to ensure efficient data acquisition with AVIS-3, a flight plan was developed prior to the flyover. For this purpose, the total size of the test site (3x4 km) was divided into six flight strips, which were to be flown individually. With respect to the field of view (FOV) of the two sensor systems within AVIS-3 (see Chapter 2.2.1.1), this step was necessary to obtain full coverage of the test site. The narrower FOV of 20° of the SWIR camera was the decisive factor in this process for the determination of the flight altitude and the number of required flight strips. The altitude was set to 2620 m a.s.l. (corresponds to flight level 86), which resulted in an effective swath width of 800 m at the ground (mean elevation: 320 m). To prevent sun squint effects in the data the flight direction was set to N-S and vice versa. Thus six flight strips distributed over the test site allowed an overlap of almost 130 m, or 65 m per

site. The details of the resulting GSD can be found in the description of the camera system in Chapter 2.2.1.1. Unfortunately, the analysis of the image data of the first three acquisitions revealed that six flight strips were not enough for full coverage by the SWIR camera, due to the underestimated intensity of flight movements in transverse direction. In consequence, the number of required flight stripes was raised to eight at a later date. All flight strips were defined by means of three GPS points, whereby the first point served as a point of orientation for turning the aircraft to a correct approach angle, and the other two points marked the intended beginning and end of the strip for recording purposes. Altogether, 52 separate flight strips were recorded using AVIS-3. A detailed specification of both AVIS-3 and HySpex, as well as the complex preprocessing of the AVIS-3 data, is described in Chapter 2.2.

2.1.3 In-Situ Measurements

Field or in-situ measurements are of great relevance, since they fulfill two important purposes. First, reflectance measurements using a field spectrometer at the ground are essential for the transformation of airborne raw data to radiance and reflectance. Since they serve to remove the influence of the prevailing atmospheric conditions at the time of the airborne data acquisition, and to ensure identical sun geometry, the spectrometer measurements were performed simultaneously to the flyover. In order to exclude the possibility of the calibration process being falsified due to brightness differences and angle-dependent anisotropies effects the measurements were taken at unalterable sites, e.g., at extensive asphalt surfaces. The second purpose of in-situ measurements is the generation of an exhaustive database, which serves for the validation of the subsequent analysis methods. For that reason, biophysically relevant variables were measured. Besides leaf area index and leaf chlorophyll content, on which this study focuses, three further plant physiological variables were collected: status of phenology, stand height and soil moisture content.

2.1.3.1 Spectral Reflectance and Radiance

In order to ensure a descriptive data basis for the calibration of the airborne sensor’s signal, potential reference targets need to meet certain requirements. The reference should be a homogenous, non-alterable and flat surface to guarantee availability and comparability over all data acquisitions. Ideally, the reference target should feature Lambertian properties, which means it is almost ideal-diffusely reflecting, to be independent from the influence of different viewing angles to the signal and resulting BRDF effects. In addition, it should reflect solar radiation uniformly over all relevant wavelengths. Furthermore, the size of the target should be at least twice the size of a pixel, to ensure that the airborne sensor receives an undistorted signal which stems only from the reference target. In regard to the intended AVIS-3 ground resolution of 4 m, the reference target therefore should cover at least an area of 8x8 m. Given

that the demand for an absolutely ideal reference target are unrealistic, in particular with regard to it being a Lambertian reflector, asphalted areas are considered suitable. These areas, e.g., at crossroads or parking sites, are sufficiently large, homogenous and they reflect the radiation for the most part uniformly. Thus, seven different reference targets in the study area were identified and measured during the data acquisition phase of each flight. Both radiance and reflectance were collected using a calibrated ASD FieldSpec 4 from Sphere Optics. The main specifications of the field spectrometer are listed in Table 2-2.

Table 2-2: ASD FieldSpec 4 spectrometer specifications.

Sensor characteristics	Performance	
Detectors	VNIR detector (350-1000 nm): 512 element silicon array SWIR 1 detector (1000-1800 nm): Graded Index InGaAs Photodiode, TE Cooled SWIR 2 detector (1800-2500 nm): Graded Index InGaAs Photodiode, TE Cooled	
Spectral Bands	2151	
Spectral Range	350 – 2500 nm	
Sampling Interval	1.4 nm @ 350-1050 nm	2 nm @ 1000-2500 nm
Spectral Resolution	3 nm @ 700 nm	10 nm @ 1400/2100 nm
Radiometric Resolution	16 bit (65536:1)	
Scanning Time	100 milliseconds	

At each reference target a sample of single measurements was taken at five locations, to ensure coverage in the 4 m scale of AVIS-3. Starting from a center spot, four further locations were identified at a distance of two meters from the center and at an angle of 90° to each other. At each location, 30 consecutive measurements were averaged and saved to file. This step was repeated five times. All in all, 750 single measurements were averaged to represent the target's spectral properties in a 4 m scale. To convert the signal to absolute reflectance, a calibrated white reference was used (Spectralon ®, Labsphere), to which the spectrometer was calibrated before each single location acquisition. This procedure ensured an exclusion of the influence of an altered sun angle to the measurement. Figure 2-2 gives an overview of all reference targets, taken on September 8th during the fourth flight. The averaged spectra are plotted with their corresponding standard deviations. As can be seen both by the varying reflectance properties and the variance of the spectra, which is expressed through its standard deviation, the targets show major differences. These differences are the reason that seven potential reference targets are required, since their spectral properties were previously unknown. Furthermore, more options offer alternatives for calibration, in case the chosen reference target is unsuitable, e.g., due to clouds or a disturbed data recording.

A further evaluation of the quality of the reference target is carried out in Chapter 2.2.2.3.1, where reflectance calibration is discussed.

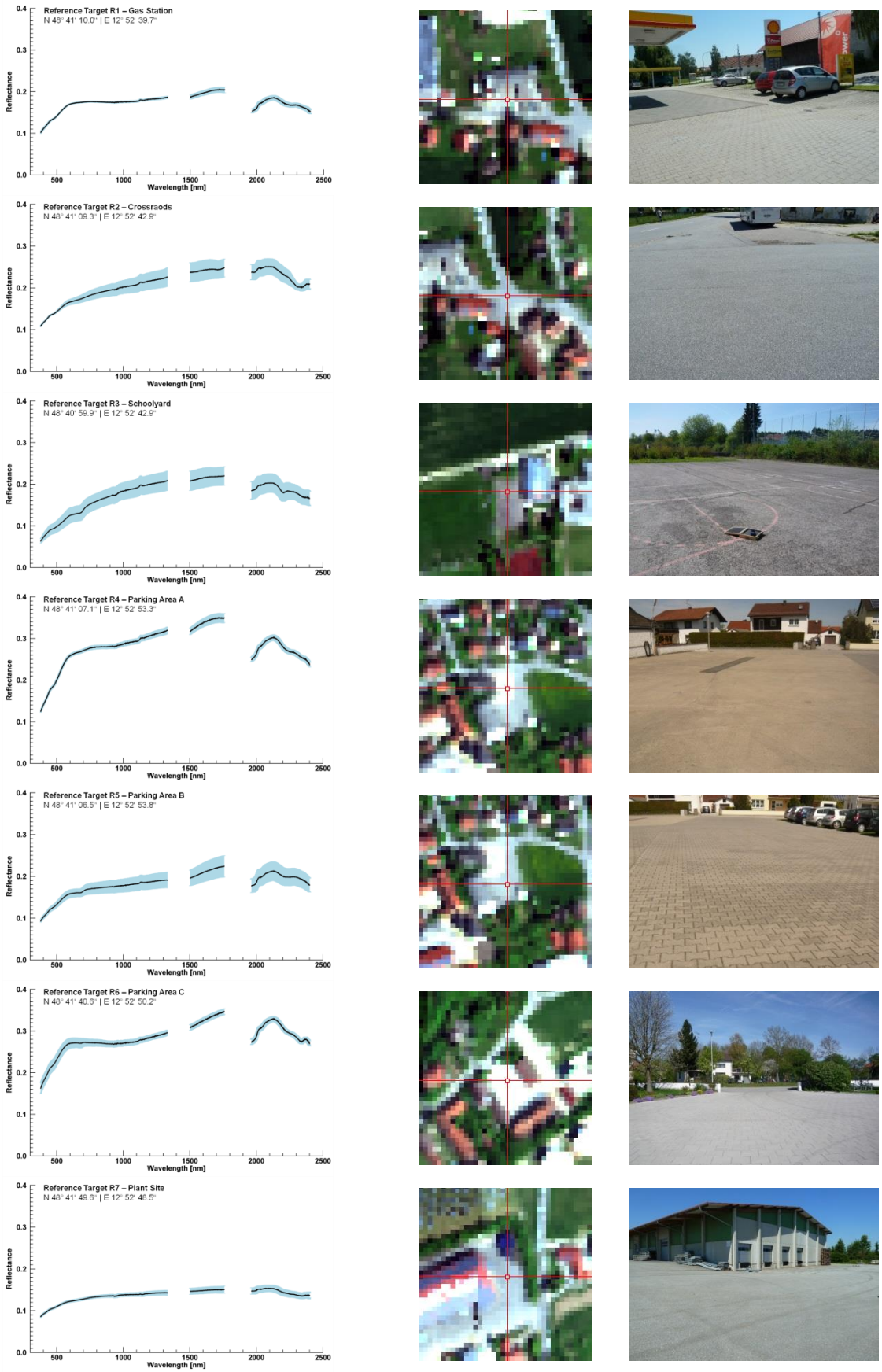

Figure 2-2: Radiometric reference targets presenting reflectance with corresponding standard deviation, localization in AVIS-3 image (true color) and photo on site.

2.1.3.2 Biophysical Parameters

During the 2012 field campaign a total of 565 in-situ measurements or rather elementary sampling units (ESUs) were measured on seven different dates. Within each ESU, five variables, i.e., leaf area index (LAI), leaf chlorophyll content (LCC), status of phenology, stand height and soil moisture, were measured - each by means of an individual sampling strategy. Although phenology, stand height and soil moisture are not essential for the goal of this thesis, these variables were measured as well for two reasons. First, phenology and stand height serve as additional information about the canopy, allowing valuable consistency checks on LAI or LCC level at a specific site, and on their coherence. This is, for example, useful for detecting senescent canopies in the data, as they deliver high LAI values in the field, while showing low LCC since they are no longer active in photosynthesis processes. They are therefore also difficult to identify by the physically-based model. Second, the data of the campaign including soil moisture may serve as a basis for future studies, e.g., as input for land surface process models. Table 2-3 gives an overview of the number of all ESUs, categorized by crop type and acquisition date. Focusing on important crops cultivated in Germany, data was collected for three types of winter crops (rapeseed, winter wheat, winter barley) and two summer crops (sugar beet and corn), the latter beginning to germinate from late spring on. Compared to the rest of the acquisition dates, the number of ESUs is significantly lower on June 29th and Aug 14th. On the first date, airborne data acquisition was cancelled at short notice, so the field measurement was aborted. On the second date the number of in-situ measurements was restricted by the limited availability of the field team.

Table 2-3: Number of all ESUs, divided into crop type and date. The cancelled flight on June 29th is marked in red.

Date	Rape-Seed	Winter Wheat	Winter Barley	Sugar Beet	Corn	Total
Apr 28th	12	45	29	-	-	86
May 08th	6	79	23	-	-	108
May 25th	5	76	20	-	-	101
Jun 16th	6	76	23	-	-	105
Jun 29th	-	35	-	-	8	43
Aug 14th	-	-	-	19	19	38
Sep 08th	-	-	-	44	40	84
Total	29	311	95	63	67	565

The locations of the ESUs are presented In Figure 2-3. In order to gain a representative sample, emphasis was placed on a meaningful distribution of the sampling points, which should ideally allow the detection of potential heterogeneities within a field, on the one hand, while trying to capture as many fields as possible on the other hand. Moreover, a distance of

at least 20 m between each ESU was assigned in order to prevent the recording of redundant information when allocating the in-situ to the airborne data.

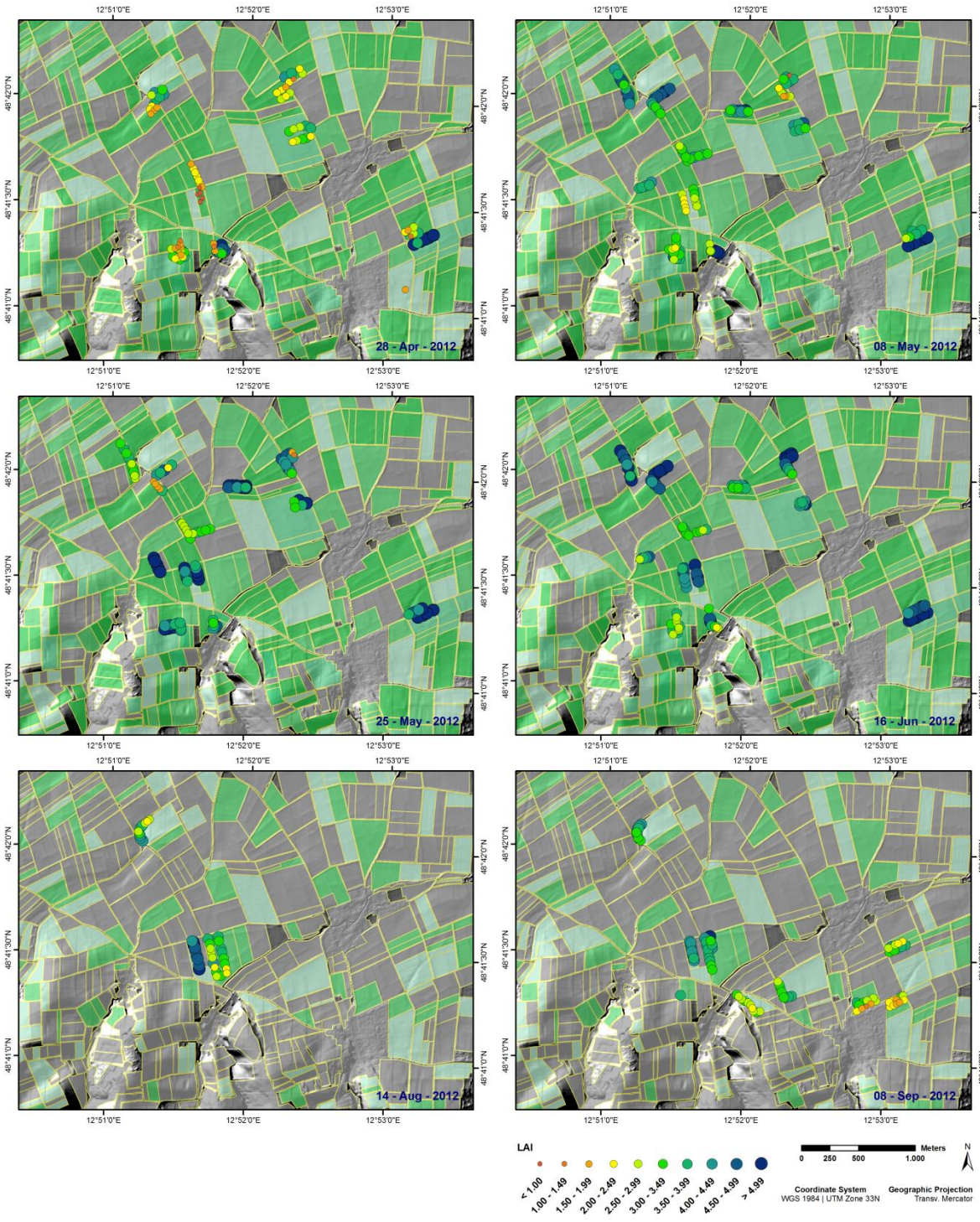

Figure 2-3: ESU locations, presented as collected LAI values, for all successful flyovers. Relevant fields containing rapeseed, winter wheat, winter barley, sugar beet or maize are highlighted in greenish colors. Field boundaries are displayed in yellow.

In the following section the measuring methods and the corresponding sampling strategies of LAI, LCC and phenology are explained in detail. Mean plant height was comparatively

simple to measure and was averaged over ten measurements within a four-meter range of an ESU using a folding meter stick. Since soil moisture measured with a time-domain reflector probe is not of relevance for this study, the description of this method is not included here.

Leaf Area Index

Data on leaf area index was collected by means of a Li-COR LAI-2200. According to BREDA (2003), it is the most widely used instrument for non-destructive determination of LAI in agricultural and silvicultural disciplines. Based on hemispherical photography, the device determines LAI using the inversion of the gap fraction; this method estimates the probability of a ray of light passing through the canopy having no contact with plant material and thus quantifies the fraction of visible sky (JONES & VAUGHAN, 2010). Consequently, the LAI-2200 measures the incident diffuse radiation below the stock and hence its transmission. Radiation recordings above the canopy serve as reference. During the measurement, a fish-eye-shaped lens with a zenithal field of view of 148° detects radiation of five different concentric sky sectors separated by several silicone rings. The measurement is based on the following assumptions (LI-COR, 2010): (1) the foliage is black; it neither transmits nor reflects incident radiation. Therefore, an optical filter rejects radiation > 490 nm. (2) The foliage is randomly distributed within certain foliage-containing envelopes and there are no clumping effects. (3) The foliage elements are small compared to the viewing surface of each ring. (4) The foliage is azimuthally randomly oriented, and its inclination has no direct effect. All these conditions are rarely met in reality because, for example, foliage within a canopy usually tends not to be randomly distributed; it is clumped along branches and stems. As a result of the measuring technique, these branches and stems in addition directly affect the recorded radiation, so the expression ‘leaf area index’ is not really applicable, plant area index (PAI) or green LAI, if referred only to photosynthetic leaves (HABOUDANE ET AL., 2004), would be more appropriate (BRÉDA, 2003). Further sources of error for the collection may be the influence of direct sunlight due to lack of shading or a high proportion of senescent leaves.

The sampling strategy involved a randomly distributed repeat of eight canopy and two reference measurements per ESU, the latter taken under the open sky. During this process, all employable standards of measurement conditions were applied, including use of the 180° view cap to prevent falsified measurements by the operator, and avoidance of direct sunlight and uniform azimuthal orientation of the device throughout the repetitions.

Leaf Chlorophyll Content

Leaf chlorophyll content was derived through the employment of a SPAD-502Plus from Konica Minolta, which is, similar to the Li-COR LAI-2200, a non-destructive measurement

instrument. The handheld device with a 2x3 mm large sensor measures the transmitted energy, which is emitted by two LEDs at peak wavelengths of 650 and 960 nm (MINOLTA, 1989). The device therefore uses the spectral properties of the red edge to derive chlorophyll content. Before and during the actual measurement a self-calibration of the device is carried out. By pinching the plant leaf, the relative amount of chlorophyll content is calculated and stored as an internal SPAD value, which is proportional to the relative optical density of the material. Although this value seems to be in a realistic range for LCC (µm cm^{-1}), it has to be calibrated to absolute LCC based on individual calibration curves. Many studies examined those relationships for several crops (e.g., MARKWELL ET AL., 1995, MONJE & BUGBEE, 1992 and UDDLING ET AL., 2005). In this study the polynomial regressions from MARKWELL ET AL. (1995) and MONJE & BUGBEE (1992) were tested (see Chapter 3.3.3.2).

Data on chlorophyll content was collected by averaging four single measurements at different positions of a sampling leaf. This step was repeated five times for each ESU. Here, equally important aspects pertaining to quality assurance were considered, e.g., a uniformly distributed measuring of the leaves at different plant height.

Phenology

Since there is no technical measuring instrument for capturing phenology, it is determined by means of a visual and qualitative description. For this purpose, morphological aspects of individual plants are compared to characteristic values of a reference table and assigned a scaled number indicating the stage of phenological development. The most common reference table is the Zadoks Scale (ZADOKS ET AL., 1974), which is widely accepted among different scientific disciplines examining the development of crops. It is based on the scale by Feekes (LARGE, 1954) and was prepared by Zadoks, who simplified the code to two digits and added addtional features to enable worldwide application. His goal was to create a method that can be used at any given location, and any given level of prior knowledge of plant physiology. At the beginning of the 1990s the Zadoks Scale was enhanced to allow its use on a variety of different crops. This was done in a cooperative effort of the former German Federal Biological Research Centre for Agriculture and Forestry, the German Federal Plant Variety Office, both now part of the Federal Ministry of Food, Agriculture and Consumer Protection, and the German Agrochemical Association, together forming the BBCH (Biologische **B**undesanstalt, **B**undessortenamt und **CH**emische Industrie) (HACK ET AL., 1992). Phenological status here is defined in a macro scale for the development stage from 0 (germination) to 9 (senescence) and a micro scale from 0 to 8, which represents a percentage associated with a characteristic value. The macro stadia are listed in Table 2-4.

Table 2-4: Macro stadia of the BBCH scale.

Stage	Description
0	Germination / sprouting / bud development
1	Leaf development (main shoot)
2	Formation of side shoots / tillering
3	Stem elongation or rosette growth / shoot development (main shoot)
4	Development of harvestable vegetative plant parts or vegetatively propagated organs / booting (main shoot)
5	Inflorescence emergence (main shoot) / heading
6	Flowering (main shoot)
7	Development of fruit
8	Ripening or maturity of fruit and seed
9	Senescence, beginning of dormacy

Figure 2-4 shows the crop specific averages obtained from the measurement of the five variables at each acquisition date. In addition, the standard deviations are displayed to allow an estimation of the underlying measurement uncertainty. The change over time in the variables mostly follows an expected pattern. First, the leaf area index increases throughout all crops and reaches its maximum in the crop-specific, highest development stage (e.g., rapeseed at BBCH 65, winter wheat and maize at BBCH 79). With first senescence, both LAI and LCC values decrease, although LCC may be influenced by other factors as well, e.g., nitrate content. The development of plant height provides a good visual indication of the growing period and, in most cases, maximum plant height coincides with the maxima of LAI. It can be assumed that soil moisture values are primarily affected by local rainfall events and thus do not allow conclusions to be drawn concerning the status of plant physiology.

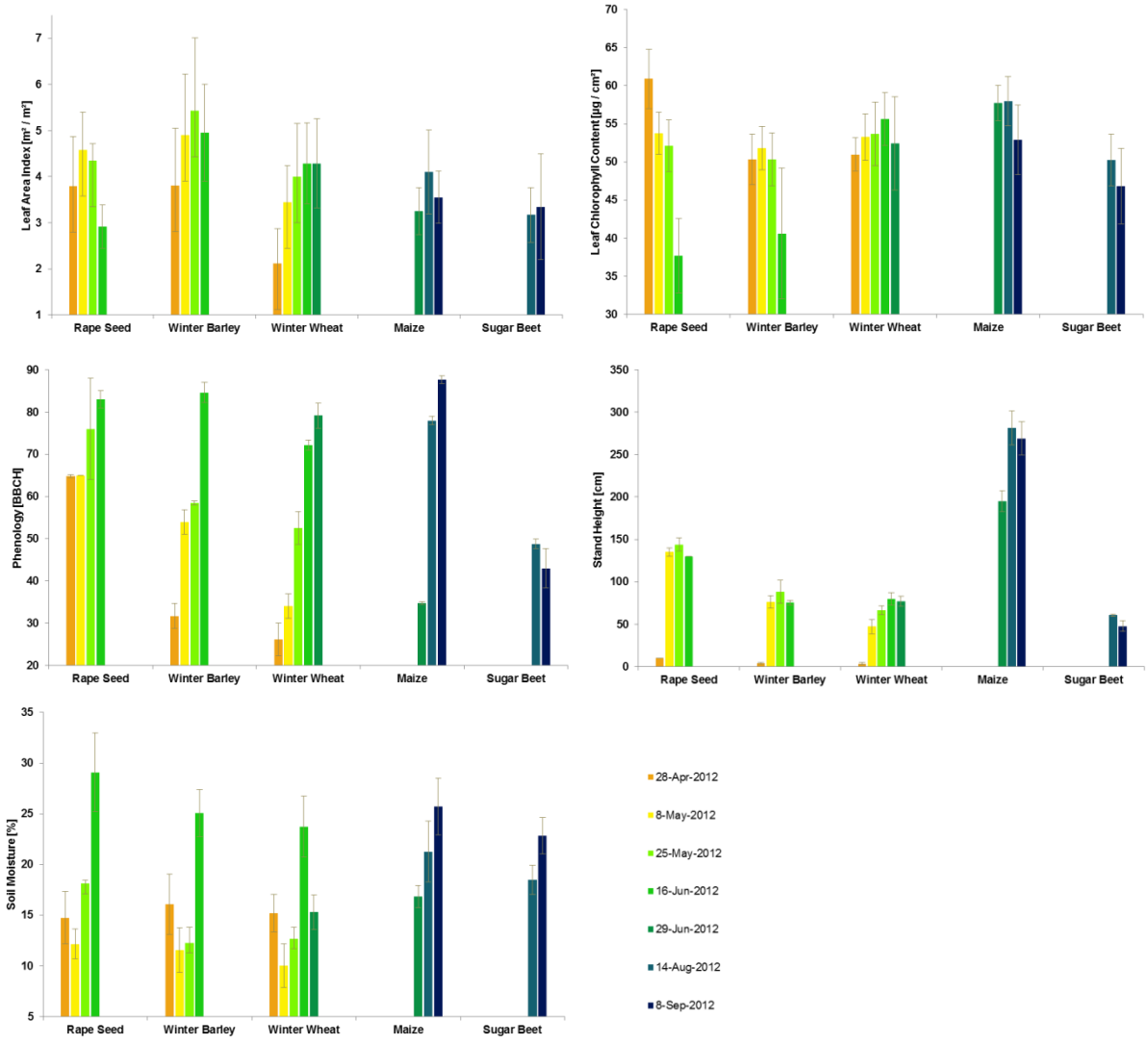

Figure 2-4: Crop specific measurement averages of leaf area index, leaf chlorophyll content (SPAD value), status of phenology, stand height and soil moisture for each acquisition date. The error bars represent the standard deviation.

Although the field campaign was carefully planned, measurement errors cannot be excluded, especially given the wealth of data collected in the 565 ESUs. In individual cases, this added uncertainty may lead to measurement averages not being representative for the entire field. A critical examination of the quality of the in-situ data was carried out during validation (Chapter 3.3.1).

2.2 The Airborne Image Spectrometer AVIS-3

Having its origin in geological applications in the early 1980s (GOETZ ET AL., 1985), hyperspectral imaging spectroscopy became more and more popular in a variety of earth sciences, such as those investigated within the EnMAP context: geology, forestry, agriculture,

coastal zones and inland waters, urban systems and ecosystems (KAUFMANN ET AL., 2012). Besides well-known airborne sensors like AVIRIS (Airborne Visible / Infrared Imaging Spectrometer), CASI (Compact Airborne Spectral Imager) and HYMAP (Hyperspectral Mapper) (OPPELT & MAUSER, 2007), a comparatively modern generation of hyperspectral imagers, such as HySpex (BAUMGARTNER ET AL., 2012) and APEX (Airborne Prism Experiment) (ITTEN ET. AL, 2008) serves an increased demand within the user community. Nevertheless, availability through dedicated programs is limited, particularly when multitemporal data is needed. However, plant-physiological studies are by nature dependent on a high frequency of data acquisitions, since all relevant biophysical processes of agricultural crops usually take place within one growing period. Because commercial sensors are cost-intensive, the Department for Geography of the Ludwig-Maximilians-University in Munich (Germany) started with the development of a proprietary airborne hyperspectral system, which was designed to be both cost-efficient and to provide some independence concerning flight scheduling. It was introduced in the year 1997, when the first generation of AVIS, the **A**irborne **V**isible and Near **I**nfrared Imaging **S**pectrometer, was designed. AVIS, operating in the years 1999 and 2000, covered a spectral range from 550 to 850 nm with its 74 bands (OPPELT, 2002). The availability of enhanced technical components led to the development of AVIS-2 in the year 2001. Covering a range from 450 to 880 nm within 64 bands, the sensor had an improved signal-to-noise ratio and a higher sensitivity in the NIR spectral domain. The geometrical correction was enhanced by adding an inertia navigation system (INS) to the dGPS system, which was already employed in AVIS. Furthermore, the system was now able to record along track multi-angular images between +55 and -55 degrees (OPPELT & MAUSER, 2006). Starting in 2006, a third-generation – AVIS-3 – was developed, with the intention of increasing the spectral resolution and implementing a wider measurable spectral range to the SWIR spectral domain. While the VNIR sensor was designed to cover a range of 400 to 1000 nm, the new construction added a second spectrograph unit, which is sensitive from 900 to 1750 nm. All AVIS sensors have in common that they are designed in lightweight construction and are platform-independent, which allows operation in different aircrafts, even microlight aircrafts. Figure 2-5 gives a sense of the size of AVIS-3.

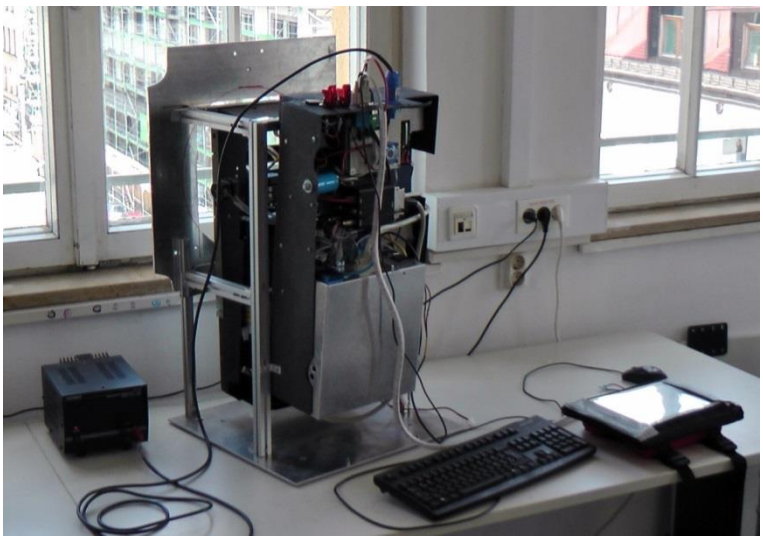

Figure 2-5: AVIS-3 running in test mode during a trial measurement out of the window.

2.2.1 System Description

The AVIS-3 is characterized in the section which follows. It contains a description of the camera system, which represents its centerpiece, and its spectral properties. These properties were analyzed in the laboratory prior to any data acquisition, in order to determine the actual spectral range, the spectral responsivity and the spectral resolution of the spectrometer. In addition, the navigation system consisting of an inertial measurement unit and a differential GPS for the determination of the systems position is introduced, followed by a description of the aircraft, which served as a platform during the 2012 multiseasonal campaign.

2.2.1.1 Camera System

AVIS-3 is an earth observation device that combines two different sensors within one compact system. In its function as an imaging spectrometer, AVIS-3 records the land surface using a silicon-based VNIR detector covering a spectral range from 400 to 1000 nm. In addition, an indium-gallium-arsenide-based SWIR detector takes records in the spectral range from 900 to 1700 nm. Table 2-5 shows the spectrometer specifications of the AVIS-3 sensor system.

Table 2-5: AVIS-3 image spectrometer characteristics.

Sensor characteristics	VDS Vosskühler CCD-1020	Xenics-Xeva 1.7-LVDS
Spectrograph	SpecIm IMSPECTOR V10 E	SpecIm IMSPECTOR N17 E
Number of Spectral Bands	398	257
Spectral Range	400 – 1000 nm	900 -1700 nm
Sampling Interval	1.7 nm	3.1 nm
Spectral Resolution	2.8 nm	5.0 nm
Radiometric Resolution	12 bit (4096:1)	12 bit (4096:1)
Geometrical Resolution (IFOV)	1.2 mrad	1.1 mrad
Maximum Sampling Rate	15 pic/s	60 pic/s
Swath Width (FOV)	45°, 640 pixels	20°, 320 pixels
Along Track Swivel Range	-55° > +55°, 0.18 increment	-55° > +55°, 0.18 increment

The sunlight reflected from the surface of the earth and reaching the detectors is redirected by a rotatable mirror to the spectrographs, which are mounted on the photosensitive cameras. This design allows for quick and precise (0.18° per 20 ms) swinging of the camera angle in flight direction (along track) which facilitates the recording of multiangular image data. The internal structure of the camera system can be seen in Figure 2-6 and Figure 2-7.

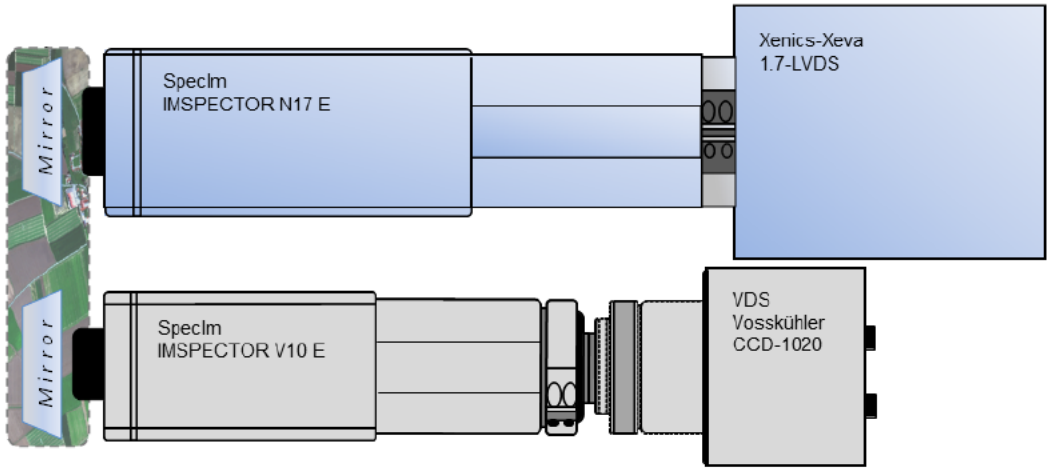

Figure 2-6: Internal structure of the AVIS-3 sensor from above, including the VNIR (below) and SWIR (top) spectrographs with the associated cameras. The sensors monitor the land surface through openings on the underside of the casing. The horizontal visual axis is redirected to the bottom by a highly reflective aluminum mirror (HANK ET AL., 2010b, modified).

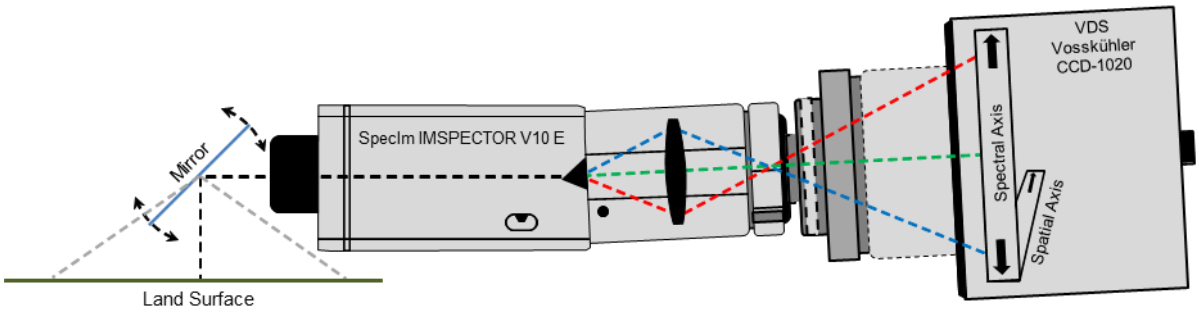

Figure 2-7: Side view of the internal structure of the AVIS-3 sensor. It illustrates the different visual axes of the spectrometer, the pivotable mirror and the perpendicular axis of the spectral dimension at the CCD (HANK ET AL., 2010b, modified).

The signals from the cameras are transmitted by means of two PLEORA iPORTs PT1000-LV via TCP/IP and a GigE protocol over a gigabit network connection to the industrial PC (INONET Conception bX Embedded PC). Besides the 40 GB S-ATA data storage device, the PC has an additional 30 GB solid state data storage device which can handle the strong shocks which the system is exposed to during the flight. This guarantees a constant writing of the recorded data even under harsh flight conditions (up to 80 MB/s).

With respect to the geometrical properties of the components (see Table 2-5), AVIS-3 can achieve different spatial resolutions. The across-track resolution is defined by the altitude above ground, while the along-track resolution is determined by the aircraft speed. A limiting factor for the geometric resolution in across-track direction is the number of image columns in each CCD, while in the along-track direction it is limited by the writing rate. The spatial resolution ultimately achieved thus depends mainly on the required spatial coverage of the study site.

To ensure the target geometric resolution of 4 m, a swath width was specified of approximately 1880 m, resulting in a spatial resolution of 2.94 m based on the VNIR spectrometer (swath width = 45°, 640 pixels). As already mentioned in Chapter 2.1.2, this was achieved at flight level 86 (2620 m above sea level, 2300 m above ground). Since the final spatial resolution was targeted to be 4 m, a higher flight level was theoretically possible and also desirable, because fewer strips would have been necessary to cover the study area and thus would have led to decreased processing runtimes. However, a higher flight level was not possible due to the maximum flight height of the aircraft (see Chapter 2.2.1.4). Because of its lower swath width (20°, 320 columns), this adjustment led to an effective swath width of approximately 800 m for the SWIR spectrometer, resulting in a spatial resolution of 2.5 m. Consequently, the SWIR spectrometer was the limiting factor for the number of necessary flight strips to cover the test site.

Finally, to adapt the along-track resolution, an airspeed of 42 m/s (151 km/h) was intended. With an adjusted frame rate of 14 for both cameras this resulted in an along-track resolution of 3 m.

2.2.1.2 Spectral Properties

Before the digital numbers of the raw data can be transformed into radiance and reflectance, the spectral properties of the spectrometer must be known. This is because the properties specified by the manufacturer may differ from the actual properties of the sensor. It is further advisable to analyze the spectral responsivity, which enables the identification of bands with a lower sensitivity. Finally, the sampling interval may be adapted as appropriate with respect to the actual spectral resolution.

2.2.1.2.1 Actual Spectral Range

According to the manufacturer (Table 2-5) the two sensors cover the following wavelength ranges:

CCD-1020	400 – 1000 nm
Xenics-Xeva	900 – 1700 nm

To ensure that the subsequent calibration of raw data to radiance and reflectance (see chapter 2.2.2.3) is successful, the exact wavelength of each sensor's band was examined in the laboratory. For this purpose, the radiation of a calibration light source was measured with both CCD-1020 and Xenics-Xeva and with an additional field spectrometer (ASD FieldSpec 4), covering the spectral range from 450 to 2500 nm. A Model SP-200 Spectrum Tube Power Supply from Electro-Technic was used as a light source, which has an integrated krypton gas lamp. Krypton shows discrete emission bands from the visible red (~ 630 nm) to the short wave infrared (~ 2400 nm) (KELLY & PALUMBO, 1973) and is thus suitable for both cameras. Since the ASD FieldSpec 4 is a calibrated instrument, the emission maxima occurring in the spectra of all sensors can be assigned to specific wavelengths. Consequently, the choice of two wavelength maxima for each sensor allows it to interpolate and extrapolate, respectively, the true wavelength for each given band of both sensors. For the CCD-1020 the emission maxima were identified at 764 and 913 nm, corresponding to the bands 204 and 307. For the Xenics-Xeva the wavelength maxima at 1147 nm (band 74) and 1694 nm (band 239) served for the estimation via interpolation /extrapolation. The results of the spectral fit can be seen in Figure 2-8 and Figure 2-9.

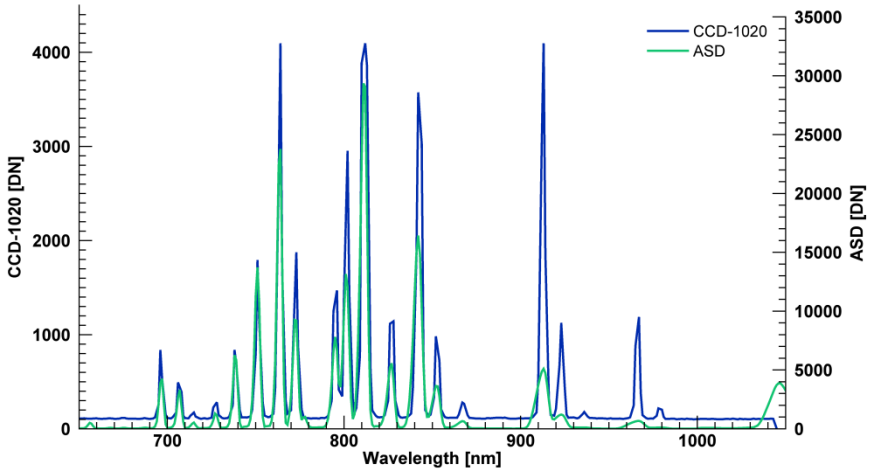

Figure 2-8: Krypton emission bands measured with CCD-1020 compared to ASD FieldSpec 3Jr.

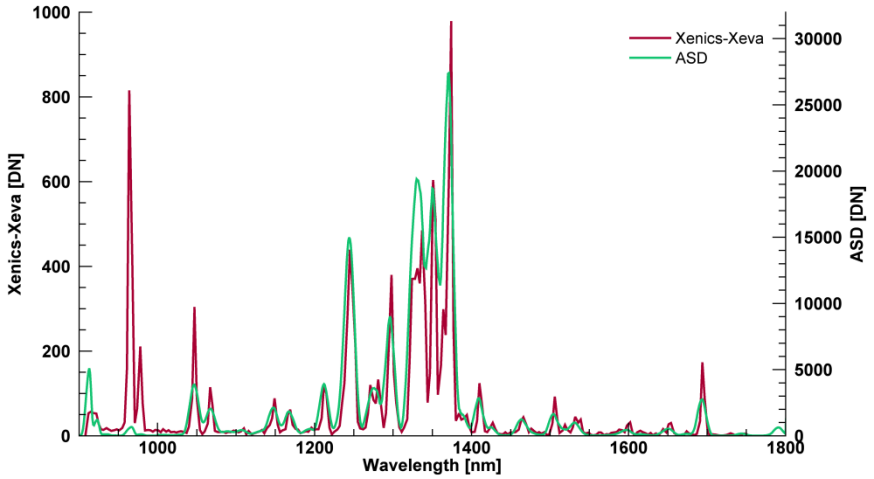

Figure 2-9: Krypton emission bands measured with Xenics-Xeva compared to ASD FieldSpec 3Jr.

The figures prove the success of the determination, as the remaining emission maxima show conformity between the measurements with the AVIS-3 sensors and the field spectrometer. As a result of this evaluation, a partially significant deviation of the spectral range from the manufacturer's specifications was identified, which led to the determination of the actual spectral ranges of the spectrometers as follows:

CCD-1020	471 – 1045 nm
Xenics-Xeva	908 – 1753 nm

The most striking finding was the anterior shift of the CCD-1020 range, which actually does not start at a wavelength of 400 nm, but at 471 nm, underlining the necessity of the wavelength analysis.

2.2.1.2.2 Spectral Resolution

Based on the technical specifications of its components, the VNIR spectrometer records spectral reflectance in 398 bands, covering a range from 471 to 1045 nm, the latter identified by the analysis discussed in the previous section. That implies a sampling interval of 1.45 nm (manufacturer: 1.7 nm). The SWIR spectrometer segregates the rectified spectral range from 908 to 1753 nm into 257 bands and thus has a sampling interval of 3.28 nm (manufacturer: 3.1 nm). Due to the effective spectral resolution of both spectrometers, which is lower than the actual spectral sampling interval in both cases (VNIR 2.8 nm, SWIR 5.0 nm), the system is oversampled. To counteract this, the number of bands is linearly downsampled by the factor 4 for CCD-1020 and factor 2 for Xenics-Xeva. Table 2-6 gives an overview of the spectral specifications before and after band merging.

Table 2-6: Spectral specifications of the CCDs before and after band merging.

Spectral characteristics		**CCD-1020**	**Xenics-Xeva**
	Spectral resolution	**2.8 nm**	**5.0 nm**
Before band merging	Sampling interval (manufacturer)	1.7 nm	3.1 nm
	Sampling interval (evaluated)	**1.45 nm**	**3.28 nm**
	Number of bands	397	257
After band merging	Sampling interval	**5.8 nm**	**6.6 nm**
	Number of bands	99	128

Several tests with linear and Gaussian averaging methods revealed that linear factors of 4 for the CCD-1020 and 2 for Xenics-Xeva show the best combined result in eliminating oversampling and reducing noise while at the same time retaining special spectral features in the data, e.g., the discrete oxygen absorption at 760 nm. Figure 2-10 exemplarily shows the influence of band merging to the signal of the VNIR spectrometer applied to actual measurements from the campaign.

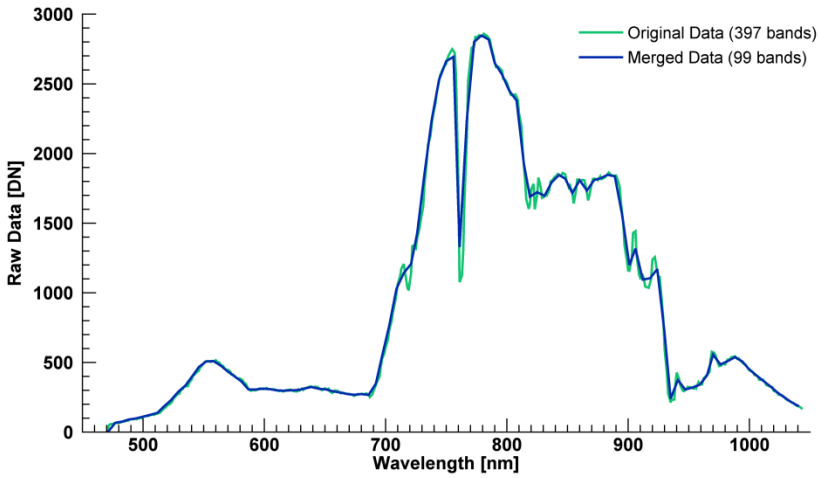

Figure 2-10: Band merging of CCD-1020 with a linear factor of 4. Noise is reduced, but the oxygen absorption feature at 760 nm is still visible.

2.2.1.2.3 Spectral Responsivity

The spectral responsivity is a measure of the wavelength-dependent sensitivity of a CCD. It results from the responsivity of each of the sensor's light passing components (spectrograph, lens, filter and camera) (OPPELT & MAUSER, 2007). For the calculation of the spectral responsivity of the AVIS-3 sensors, the signal of an integrating sphere containing a halogen calibration lamp (OCEAN OPTICS HL-2000) as illumination source was used for both CCD-1020 and Xenics-Xeva. At the same time, radiance of the integrating sphere was measured with the calibrated ASD FieldSpec 4, from which correction factors were calculated to simulate a constant illumination source over all wavelengths. The DNs of the AVIS-3 spectrometers were multiplied by these factors and normalized. Figure 2-11 shows the relative responsivity of both spectrometers under theoretical wavelength-independent and constant light conditions.

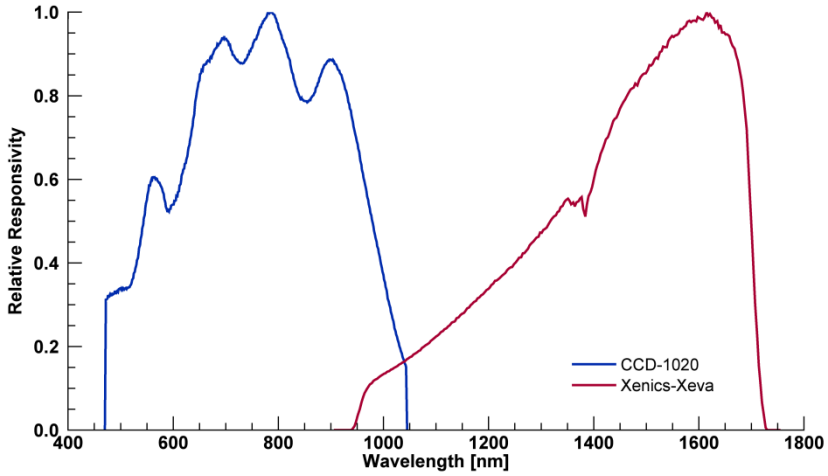

Figure 2-11: Spectral responsivity of CCD-1020 and Xenics-Xeva.

As expected the responsivity is lowest in the spectral periphery of both sensors. The responsivity of CCD-1020 is highest in the NIR region, while it is low in the visible spectrum, especially up to 520 nm. Xenics-Xeva shows a behavior that is skewed to longer wavelengths with a maximum around 1600 nm and is therefore weakest in its lowest wavelengths. Moreover, the first and last bands of each sensor are not usable for any analysis, since they do not receive any radiation. Knowledge of the spectral responsivity is valuable for later analyses of the data, since bands with a lower responsivity are more susceptible to noise and uncertainties during calibration of raw data to radiance and reflectance.

In addition to defining the responsivity of the entire CCDs, the spectral response function of each band should be analyzed as well. This may be of importance when adapting bands of another instrument to artificial AVIS-3 data. However, this analysis could not be performed, since an adequate and calibrated measuring device, operating in a sub-nanometer range, was not available. Nevertheless, the need for this step may be considered as negligible for the following reasons. Compared with a multispectral system, the spectral resolution of a hyperspectral sensor is much higher. In the case of AVIS-3, the resolution encompasses not more than 2.8 nm (Xenics-Xeva: 5.0 nm) with a sampling interval of 5.8 nm (Xenics-Xeva: 6.6 nm) after band merging. Hence, variations in intensity in the scale of some nanometers do not carry much weight. It is therefore assumed that the spectral response function corresponds to a Gaussian distribution around the center wavelength of each band. Thus, the resulting full width half maximum (FWHM) of that distribution is assumed to equal the sampling interval of the particular sensor.

2.2.1.3 Navigation System

In light of the limited stability of aircraft platforms, the geometric correction of the images is of particular importance. Since AVIS-3 is a push-broom sensor, which records individual

image rows synchronously, each pixel along a row can be associated with a certain constant recording angle. Depending on the current altitude a.s.l., flight situation (roll, pitch and yaw, see Figure 2-12) and ground elevation, an individual target-sensor distance and a comprehensible camera angle results for each pixel.

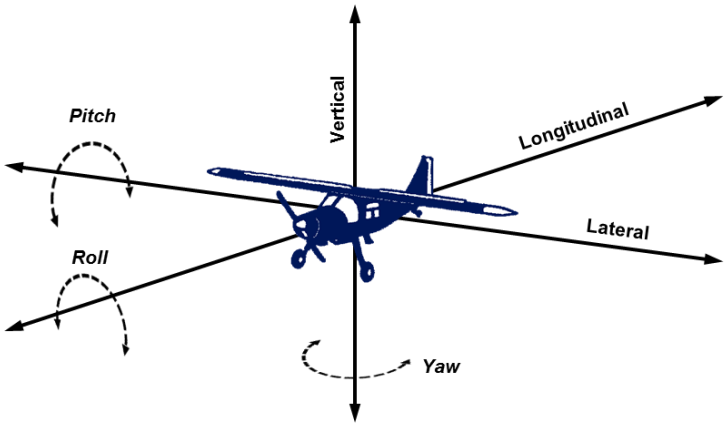

Figure 2-12: Aircraft movement caused by roll, pitch and yaw.

Based on this, the distortion of position can be calculated and corrected for each pixel. To reproduce the flight movement and geographical location, a high-frequency GPS (GNSS Trimble BD982, GPS L1/L2/L5, GLONASS L1/L2, maximal 50Hz, by extrapolation of FMS 100Hz) and an inertial measurement unit (IMAR INAV-FMS) are integrated in AVIS-3. During data acquisition this data is written in the last column of each CCD. Table 2-7 shows, by way of example, the extraction of an AVIS-3 navigation file, taken during the 2012 data acquisition. Besides the geographical location measured via the dGPS, and the angles of roll, pitch and yaw measured via IMU, the file also contains information about heading and speed of the aircraft as well as the time step for each row. The way in which the navigation information is used for the geometric correction is described in Chapter 2.2.2.2.1.

Table 2-7: Extraction of an AVIS-3 navigation file.

Parameter	Measurement reading				
Image row	1	2	3	4	1105
Year	2012	2012	2012	2012	2012
Month	9	9	9	9	9
Day	8	8	8	8	8
Second	42969	42969	42969	42970	43035
Longitude [°]	12.8577443	12.8577418	12.8577415	12.8577386	12.8563106
Latitude [°]	48.6747628	48.6748019	48.6748063	48.6748497	48.7093248
Altitude [m]	2569.69	2545.84	2548.00	2569.65	2575.66
Roll [°]	5.082	5.126	5.130	5.160	0.961
Pitch [°]	-4.055	-4.055	-4.030	-4.042	-4.806
Yaw [°]	-86.604	-86.653	-86.662	-86.704	-86.259
Heading [°]	-1.612	-1.615	-1.615	-1.615	-1.617
Speed [km/h]	147.54	147.54	147.66	147.66	143.87

2.2.1.4 Platform

For the flights carried out within the framework of this study, a propeller-driven Dornier Do 27 served as platform, which was provided by the BW aviation group of Fürstenfeldbruck, Germany. Originally designed for aerial photography, this aircraft offers optimal conditions for the installation of the AVIS-3 sensor. Placed into an aluminum rack, the sensor can be installed exactly onto the bottom flap of the Do-27 aircraft (Figure 2-13).

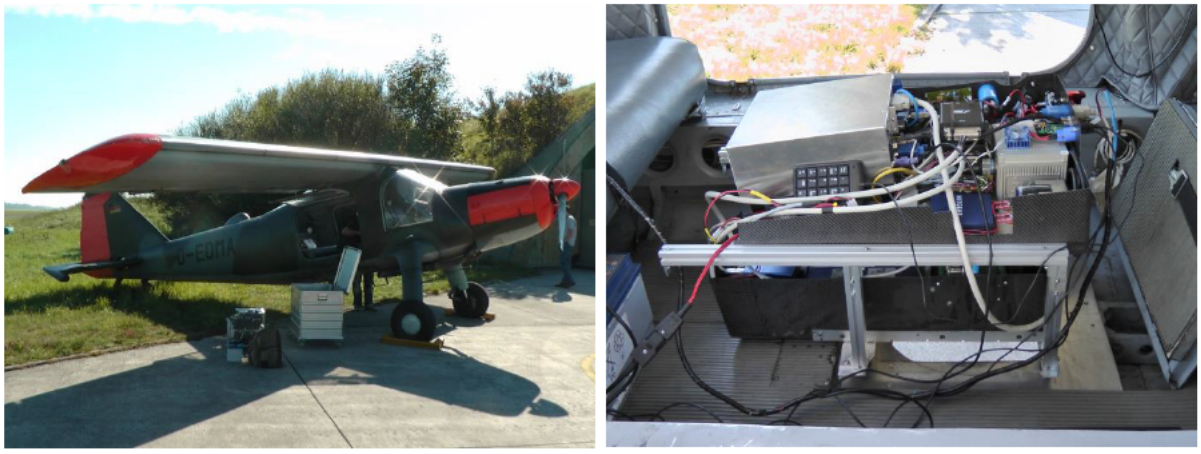

Figure 2-13: Aircraft Dornier Do 27 (left), and AVIS-3 attached above the bottom flap (right).

Power is supplied by two 12V car batteries, thus rendering the system independent of the platform generator and thereby preventing any electrical disturbances that might evolve from

a direct electrical connection between sensor and platform. An advantage of the Do 27 is its minimum flight speed of less than 150 km/h. This ensures that the images are not disturbed by data gaps which can occur when the flight speed exceeds a certain limit during data acquisition.

2.2.2 Data Preprocessing

Before the acquired image data could be analyzed the 52 flight strips had to be preprocessed in three major steps. In general, this included sensor calibration to clean the raw data from systemic noise and deficiencies, geometric correction to equalize aircraft motions during recording, as well as ortho-rectification and radiometric calibration to convert the non-dimensional grey values to radiance and reflectance. Furthermore, several smaller steps of data fusion and preparation were necessary for the final generation of four high-quality hyperspectral data cubes of the entire test site. The several stages of preprocessing are described in the following section.

2.2.2.1 Sensor Calibration

In a first step before any geometric or radiometric calibration is performed, the sensor properties must be analyzed and, if necessary, noise effects reduced and systemic inhomogeneities accounted for. In particular, these are dark current and flat-field effects. Their rectification requires two correction matrices with the column and row size of the CCD of each camera which are then applied to the raw data. This ensures homogenous conditions among all pixels of both CCDs and thus allows the subsequent geometric and radiometric correction steps. Flat-field gain and dark current offset correction is calculated by

$$DN = \left(DN_{raw} - DC_{i,j}\right) * FF_{i,j} \qquad \textit{(Equation 2-1)}$$

where

DN	grey value
DN_{raw}	grey value of raw data
$DC_{i,j}$	dark current offset for each pixel in column i and row j
$FF_{i,j}$	flat-field gain for each pixel in column i and row j

Within the flat-field analysis, the so-called smile effect is analyzed as well. Finally, impractical columns in the data which originate from limitations of the aperture angle are removed. The sensor calibration is executed with original data before band merging.

2.2.2.1.1 Dark Current Correction

Besides triggering electrons induced by the internal photoelectrical effect, the rigid crystal lattice of a charge-coupled device (CCD) provokes inelastic collisions which may trigger free carriers. Consequently, these electrons trigger off a signal at the sensor, even without being illuminated. As this signal noise is generated thermally, dark current depends strongly on the temperature of the sensor (WIDENHORN ET AL., 2002). The total amount of dark current aggregates from three different sources: the surface of the Si-SiO2 interface, within the bulk region and the depletion region of the CCD, whereas the majority of thermally generated electrons originate at the surface (HOLST, 1998).

As dark current depends on temperature as well as on material properties, it can be measured by closing the shutter of the lens. This ensures that no light reaches the CCD and only dark current is recorded. Figure 2-14 shows a segment of dark current measurement of the CCD 1020 sensor, carried out on 1000 rows. The image was recorded in a laboratory with a sensor temperature of around 18°C, as this corresponds to flight conditions with AVIS-3. For dark current measurements, it is also important to take the integration time as well as the mean duration of a typical recorded flight strip above the test site into account, since dark current is time-dependent and increases along with the continued duration of the recording.. For this reason, a dark current measurement of 1000 rows was taken.

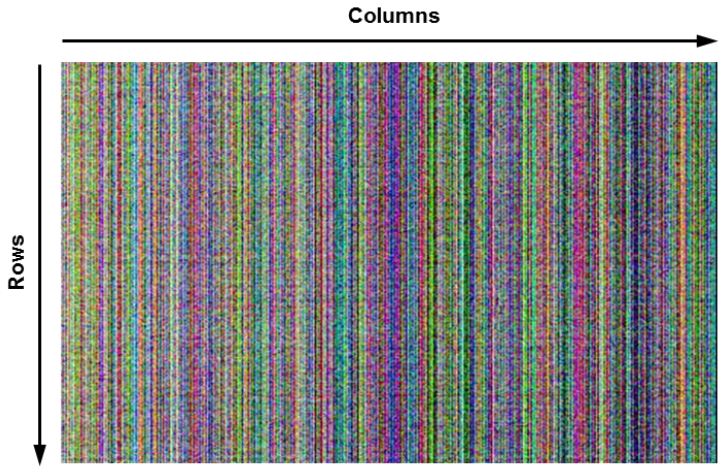

Figure 2-14: Segment of dark current measurement, displayed in RGB (bands 130-51-19).

For the elimination of the influence of random noise and systemic fluctuations, a correction matrix was calculated by averaging the measurement over all rows, resulting in an offset value for each column and each band. In Figure 2-15 the histogram proves that, as expected, the dark current data is almost normally distributed.

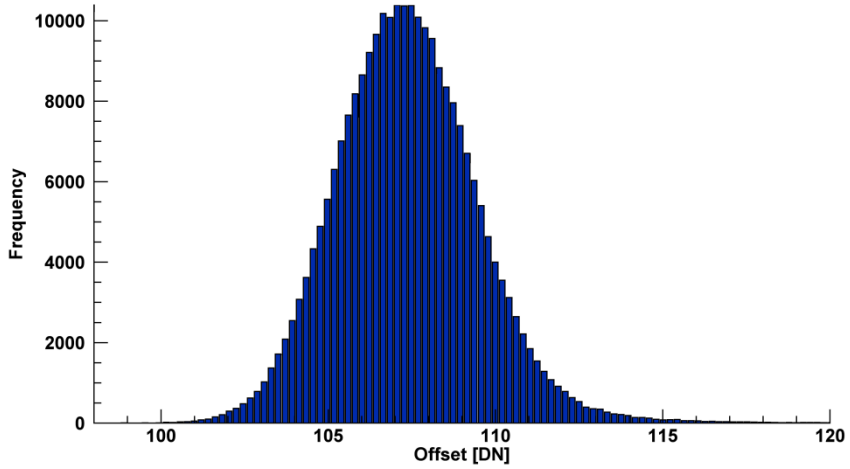

Figure 2-15: Histogram of dark current frequency distribution of CCD-1020.

A correction matrix with offset values for each pixel was calculated on the basis of this data (Figure 2-16). It seems that there are two hot spots with higher values of dark current; nonetheless a trend of increasing values from the lower right side to the upper left side is visible. This can be explained by the direction of current flow from upper right to lower left and an associated accumulation of carriers at lower left.

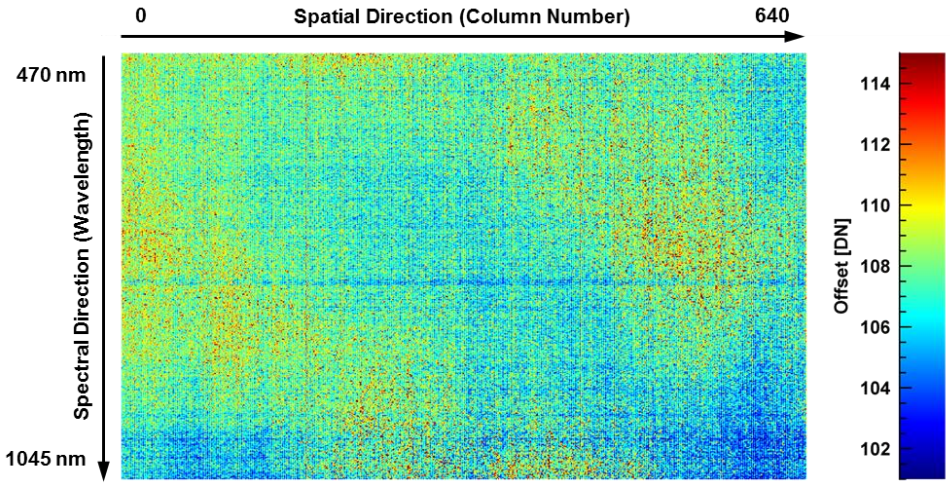

Figure 2-16: Dark current offset matrix of CCD-1020.

Applying the offset matrix to the recorded data leads to a reduction in image strips, however the visible effect is not that distinct as after flat-field correction (see following Chapter 2.2.2.1.2).

Apart from their use in the correction of image data, dark current measurements were also applied for the determination of the Signal-to-Noise ratio (SNR), which is a measure of the efficiency of the sensor. The SNR is the ratio of the measured signal to the variation in systemic noise (e.g., OPPELT, 2002) and is defined as a function of exposure time, illumination conditions and the reflectance properties of the target. The SNR thus depends on

the brightness of the surface in each wavelength. It uses the standard deviation (sigma) of dark current measurements of the CCD and is calculated by the following equation:

$$SNR = \frac{DN_i}{\sigma_{DC,i}} \qquad \textit{(Equation 2-2)}$$

where

DN_i measured signal (dark current corrected) at band i [DN]

$\sigma_{DC,i}$ standard deviation of dark current at band i [DN]

Although the ideal SNR may be defined in the laboratory with the integrating sphere, the conditions during data acquisition are more realistic when trying to evaluate the quality of the data and the SNR. This is due to the fact that during data acquisition, the brightness of the surface does not meet the same ideal reflection conditions as those which occur when using an integrating sphere. Therefore, a raw signal from a representative vegetation surface, taken during the fourth flight on September 8th, was examined for its SNR. Figure 2-17 shows the measured grey values of that pixel and the corresponding SNR: the higher the signal from the raw data (blue), the higher the SNR (green). The standard deviation of dark current is displayed in red and demonstrates the varying behavior of wavelengths-dependent dark current sigma.

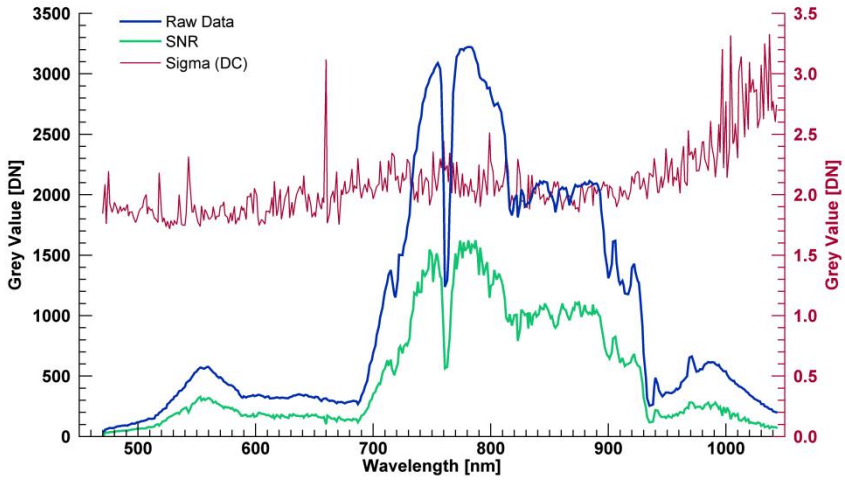

Figure 2-17: SNR analysis of CCD-1020. Sigma is the wavelength-dependent standard deviation of dark current and refers to the second y-axis.

In order to calculate the maximal SNR, the ratio of the band with the maximal grey value and the corresponding sigma was taken into account as defined by Equation 2-3. The maximal SNR of the CCD-1020 was thus determined to amount to 65 dB (1743:1).

$$SNR = 20log\left(\frac{DN_{max}}{\sigma_{DC}}\right) \qquad \textit{(Equation 2-3)}$$

where

DN_{max} measured maximum signal (dark current corrected) [DN]

σ_{DC} standard deviation of dark current at the corresponding wavelength [DN]

Dark current correction is necessary only for the CCD-1020 device, as the SWIR-sensor Xenics-Xeva is equipped with an integrated Peltier device, a thermoelectric cooler which lowers the sensor's temperature to 263K by pumping the heat from the CCD to a heat sink electrically (HOLST, 1998). At this temperature, dark current is significantly lower but still of relevance. A manual correction is nevertheless not necessary, because it is corrected internally by the device. Consequently, the determination of the SNR of Xencis-Xeva is not possible here.

2.2.2.1.2 Flat-Field Correction

In addition to the signal noise caused by dark current, there are two further major sources of artifacts which affect the electro-optical performance of the CCD: the vignette effect resulting from the architecture of the optical aperture on the one hand, and a non-uniform quantum efficiency (QE) among the CCD cells on the other (OLSEN ET AL., 2010).

Vignetting refers to a reduction in brightness from the center of an image to its edges. It occurs due to light obstruction by blockage at the frame of the lens, filters and neutral glasses, as well as due to different light path lengths and incident angles (LELONG ET AL., 2008). Since manifold CCD detectors are rarely identical, each cell inside the CCD has an individual quantum efficiency (QE). The QE is the ratio of incident photons to triggered electrons and thus is a measure of the electrical sensitivity of a CCD (JANESICK, 2001).

These effects can be corrected by flat-fielding, a process by which a matrix of gain factors generated from a homogenous reference image compensates for the illumination differences. Usually an integration sphere serves for the generation of an image under homogenous conditions. Due to size of the lenses and the complicated device setup consisting of two cameras, it was, however, not possible to ensure identical light conditions among all columns of both cameras. Instead, a different correction approach was tested using the images taken during the field campaign.

The flat-field correction was performed based on the assumption that starting from a certain length of data recording, i.e., the number of image rows collected in along-track direction, the fractions of the different landscape types occurring within the study site, e.g., forest, several crops and bare land, will eventually be equally distributed within each image column and can

then be averaged to one single image row reflecting the study sites mean landscape characteristics in across-track direction. The averaging of the image rows leads to a (theoretically) uniform brightness distribution over all 640 columns (Xenics-Xeva: 320), with individual characteristics for each band, and thereby makes the formerly heterogeneous landscape appear homogeneous. The resulting matrix, which only in theory comprises uniform brightnesses throughout all columns, consequently reflects the electro-optical inequalities of the CCD and can, when applied to the original flight strip, correct its flat-field effect.

It has been shown that this method is successful when averaging a minimum of 5000 image rows. In the case of the AVIS-3 data collected in 2012, a single flight strip consisted of about 1000 rows. For this reason, all of the strips recorded on an acquisition date were used to compute the flat-field gain matrix. The result for the CCD-1020 can be seen in Figure 2-18.

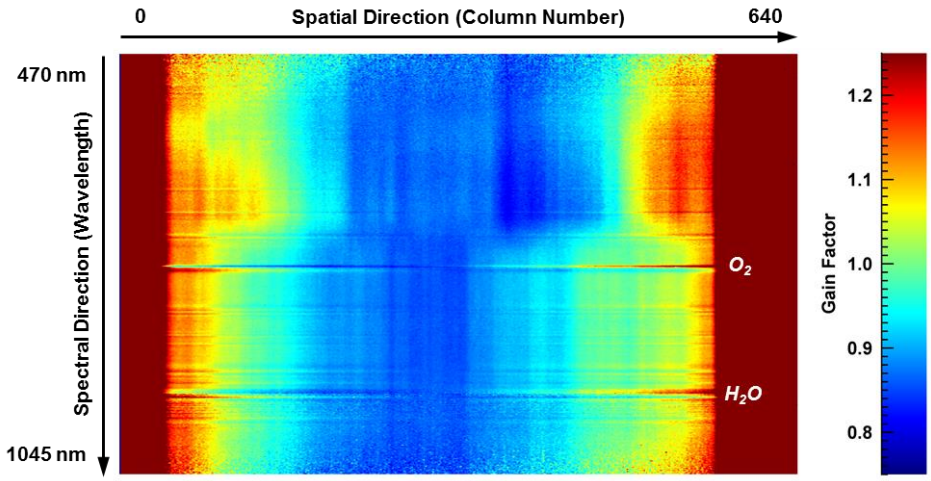

Figure 2-18: Flat-field gain matrix of CCD-1020. The two conspicuous line structures are caused by atmospheric absorption due to oxygen and water vapor.

The most notable features in the gain matrix are the homogenous areas with a correction factor of 1.3 at the left and right border. Although the correction factors in this area are in some cases much higher, all values > 1.3 are bound to this value for reasons of contrast enhancement. This massive deviation is due to limitations of the optical aperture of the sensor and is described at the end of this chapter. Apart from this fact, the matrix shows the expected trend of higher gain values from the middle to the margins of the CCD. Variations in this main trend caused by vignetting can be attributed to the photosensitivity of the CCD cells. Further, a couple of rows at the bottom and the top of the image appear to be slightly noisy; this is due to the lower responsivity (see Figure 2-11) of the silicon-based CCD-1020 at lower (< 520 nm) and higher wavelengths (> 1000 nm).

Moreover, it must be noted that the flat-field gain matrix also contains atmospheric features since it is based on real data acquisitions from the aircraft. Especially the strong oxygen

absorption at 760 nm (GREENBLATT, 1990) and the atmospheric water vapor absorption around 930 nm (JONES & VAUGHAN, 2010) appear as different-coloured row structures among all columns. However, the presence of atmospheric features is an advantage, since they can be used to reveal the smile effect. The smile or frown effect describes non-uniformity in the wavelength by each row of the CCD (CUTTER & LOBB, 2004). It originates from a misalignment of the optical components on the one hand and light dispersion properties of grating spectrometers on the other, which may lead to a shift in the actual wavelength in a row from the center to the borders of the array (OPPELT & MAUSER, 2007). An analysis of the accurate position of the oxygen absorption band at 760 nm thus shows that there is no smile effect in the AVIS-3 data or that it is so slight that the deviation is considerably lower than the spectral resolution. This makes a correction of the effect redundant.

As can be seen in Figure 2-19 the CCD of Xenics-Xeva behaves differently. Compared to the CCD-1020 the gain factors are distinctly lower, which means the Xenics-Xeva is more homogenous. The vignette effect is not, or at best barely, visible and the array is predominantly influenced by its individual photosensitivity. The spectral responsivity (see Figure 2-11) of Xenics-Xeva is, in contrast to the CCD-1020, also at its margins (< 980 and > 1700 nm) very low and thus error-prone, which can be explained by the different behavior of the gain factors at the upper and lower areas of the array. The figure also shows that the water vapor absorption bands ranging from 1100-1170 nm and 1340-1490 nm (JONES & VAUGHAN, 2010) occur as different-colored structures, whereby the latter is far more distinct than the first.

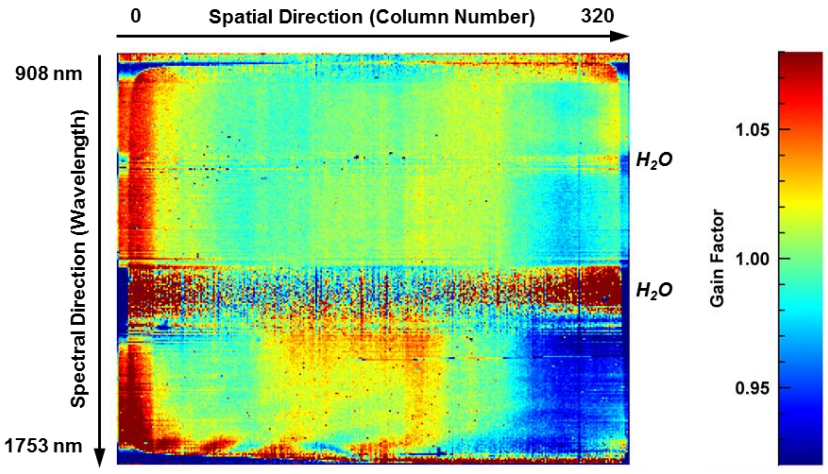

Figure 2-19: Flat Field gain matrix of Xenics-Xeva.

Figure 2-20 compares the raw data with the images received after they have been cleared from dark current and corrected for inhomogeneities. Clearly, the procedure resulted in a distinct image enhancement; in addition to the elimination of striations in the data, the images are of higher contrast now.

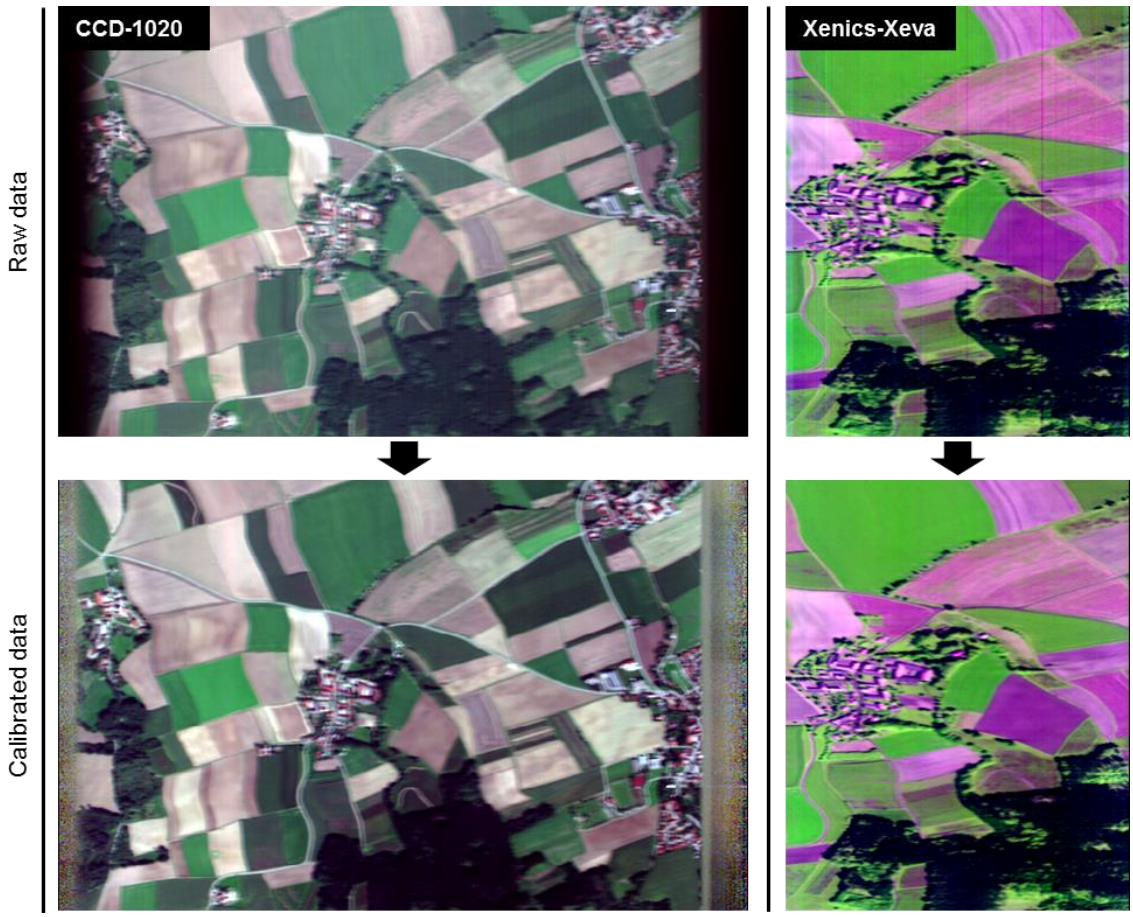

Figure 2-20: Raw and sensor-calibrated images of CCD-1020 (true color) and Xenics-Xeva (colored infrared).

Before the data can be corrected geometrically, the marginal areas at the images with bad values have to be removed. As can be seen in the Figure 2-18 and Figure 2-20 these areas of the CCD-1020 and its flat-field gain matrix appear corrupt. The reason for this is a limited opening angle of the bottom flap of the Do-27 aircraft. What the camera sees at the outer borders of the CCD are the flaps of the aircraft. This problem occurs only for the CCD-1020 as Xenics-Xeva has a lower FOV. Therefore the first 32 and the last 48 columns were detached.

To accelerate the processing time in the following stages, and because it is no longer essential or even reasonable to maintain the original number of bands the data will now be spectral downsampled, as described in Chapter 2.2.1.2.2.

2.2.2.2 Geometric Correction

To resample the data geometrically four steps are necessary: determination of the external orientation, analysis of image geometry, its backward transformation to the target geometry and the resulting final resampling. Figure 2-21 gives an overview of the geometrical process chain by which the raw image was transformed to a rectified image. The different steps are further specified in the following sections.

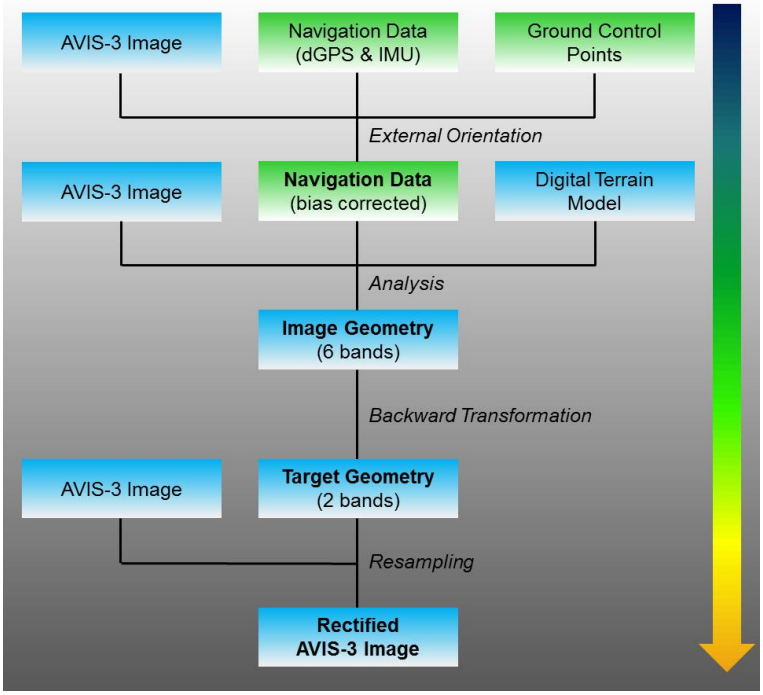

Figure 2-21: Organogram of the geometrical process chain. Input / output data differs in image data (blue) and meta data (green).

2.2.2.2.1 External Orientation

The exact position of each pixel can be determined by means of the navigation information registered by the dGPS and the IMU. Figure 2-22 shows the recordings of the navigation components for a single strip flown from South to North, consisting of 927 rows. The record was taken with the Xenics-Xeva camera, during the fourth flight with AVIS-3 in 2012 (Sept 8th). The graphs for roll, pitch and yaw (Figure 2-22, right) reflect the instable conditions and turbulences during the flyover, to which the pilot has to counteract in order to remain in track. Even then the resulting flight track does not draw a perfect line from south to north; it should be noted that divergences are comparatively slighter in east-west direction than they appear in Figure 2-22 (left), due to the different scaling of the two axes.

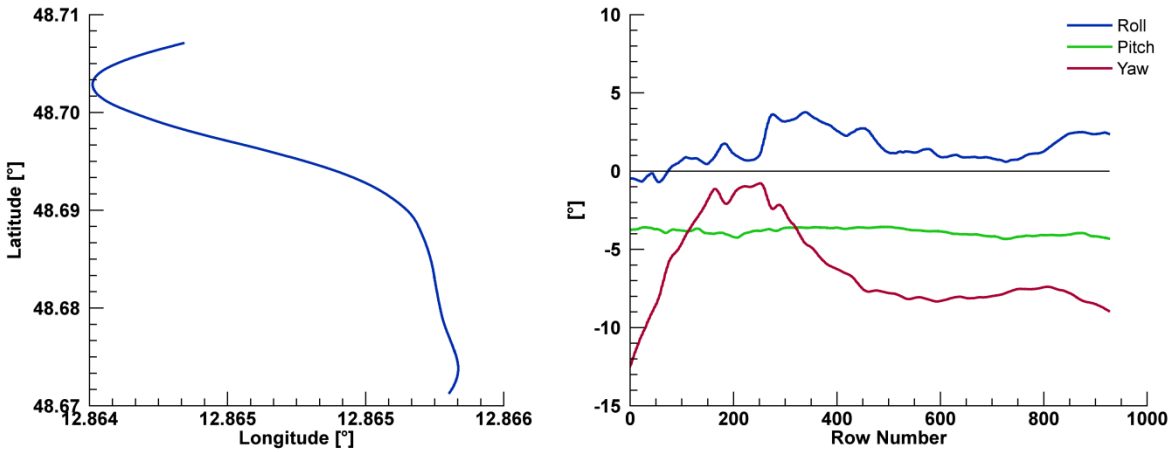

Figure 2-22: Recordings of position, measured via dGPS (lef), and roll, pitch and yaw, measured via IMU (right), for a single flight line.

Before the data can be used it is necessary to determine the external orientation of the sensor. This is due to the fact that the data of the inertial measurement unit is oriented to an internal reference. The installation position of the two dGPS antennas may vary with each flight, so the sensor is distorted in all three spatial directions. To calculate the exact external orientation a ground control point file (GCP), containing latitude, longitude, elevation, column number and row number, is required in addition to the navigation recordings. By combining the GCP file with the image data and the navigation information the rotation angle can be determined. The result is corrected angle information for the navigation data. Based on the true external orientation, the image geometry can be analyzed in the next step.

2.2.2.2.2 Analysis of Imaging Geometry

The exact position of each pixel on the surface of the earth can be traced back by applying the now-known bias of the external orientation, the navigation information as well as a high resolution digital elevation model (DEM). For this purpose a six-band output image was calculated, comprising easting, northing, altitude a.s.l., terrain elevation, zenith angle and azimuth angle for each pixel. Figure 2-23 shows the result of the analysis for the exemplarily stripe, based on the recordings of the Xenics-Xeva camera. The bands containing zenith and azimuth angle information are of special interest, as they are an important information source for sun-target-sensor geometry during later data analysis. Their variation traces the flight track. The zenith angle here ranges from less than -10° up to more than +10°. The values of the azimuth angle thereby switch along the absolute zenith track between approximately 60° to 0° and < 360° to 300°, which is an indication that the flight direction extends from south to north. It can be assumed that the zenith values of the same strip recorded with the CCD-1020 camera are of a higher range, since the VNIR spectrometer has a larger swath width.

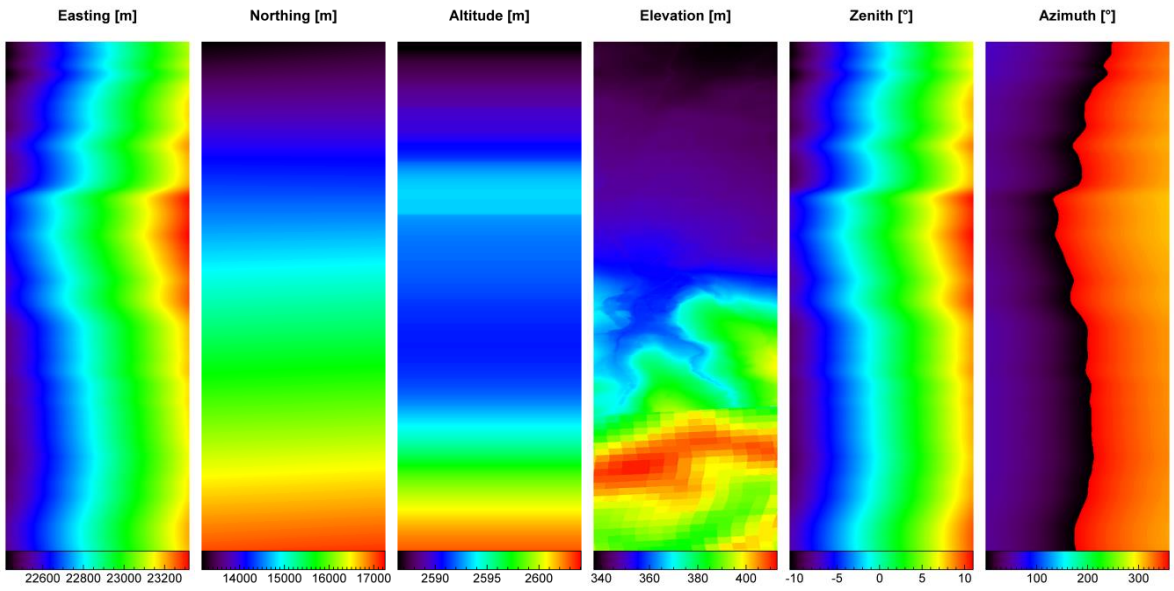

Figure 2-23: Analysis of the image geometry. The data is based on the navigation recordings of Xenics-Xeva.

The elevation band output shows a special feature in the lower section of the image, where it seems to be pixelated. This stems from the lower resolution of the ASTER-DEM which was used to fill in the gaps of the high resolution DEM in areas outside of the 3x4 km sized study area around Neusling.

2.2.2.2.3 Target Geometry and Resampling

A two-band image of the target geometry was calculated by the process of backward transformation. As part of this step the final spatial resolution was defined. For this purpose each pixel in the resulting image was matched to the pixel of the original image which was closest based on its geographical location. The two bands contain information on the column and the row number, respectively, of the original image (Figure 2-24). Compared to the layers of the image geometry (Figure 2-23), the spatial extent of the target geometry appears to be much narrower than one would be expected when the underlying aim is only to correct distortions. This can be explained by the fact that the Xenics-Xeva camera has a comparatively higher spatial resolution in across-track direction than in along-track, due to its narrow FOV (20°, 320 columns). By setting the final resolution to 4 m and calculating the target geometry, these inequalities of the Xenics-Xeva were compensated for.

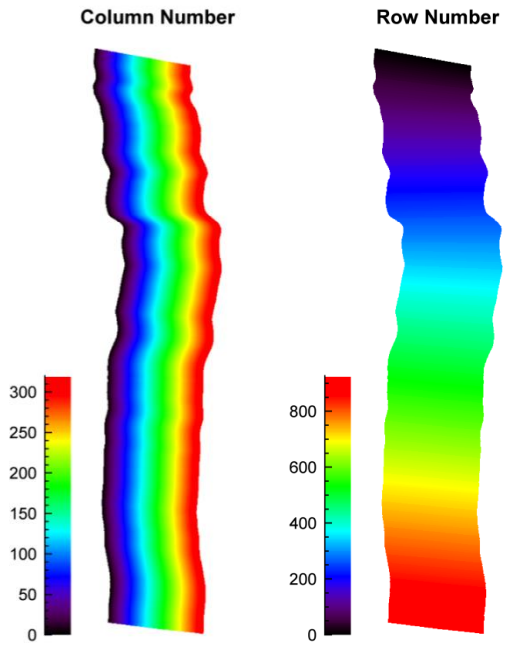

Figure 2-24: Target geometry with the column (maximal 320) and row number (maximal 927) of the original image.

Geometric correction was finalized by resampling the image data, whereby the cubic convolution method was found to perform best. Figure 2-25 illustrates the final resampling step of the identical flight strip for both cameras. The success of the geometric correction becomes evident when regarding the borders of agricultural fields, which now appear straight where they were formerly curved.

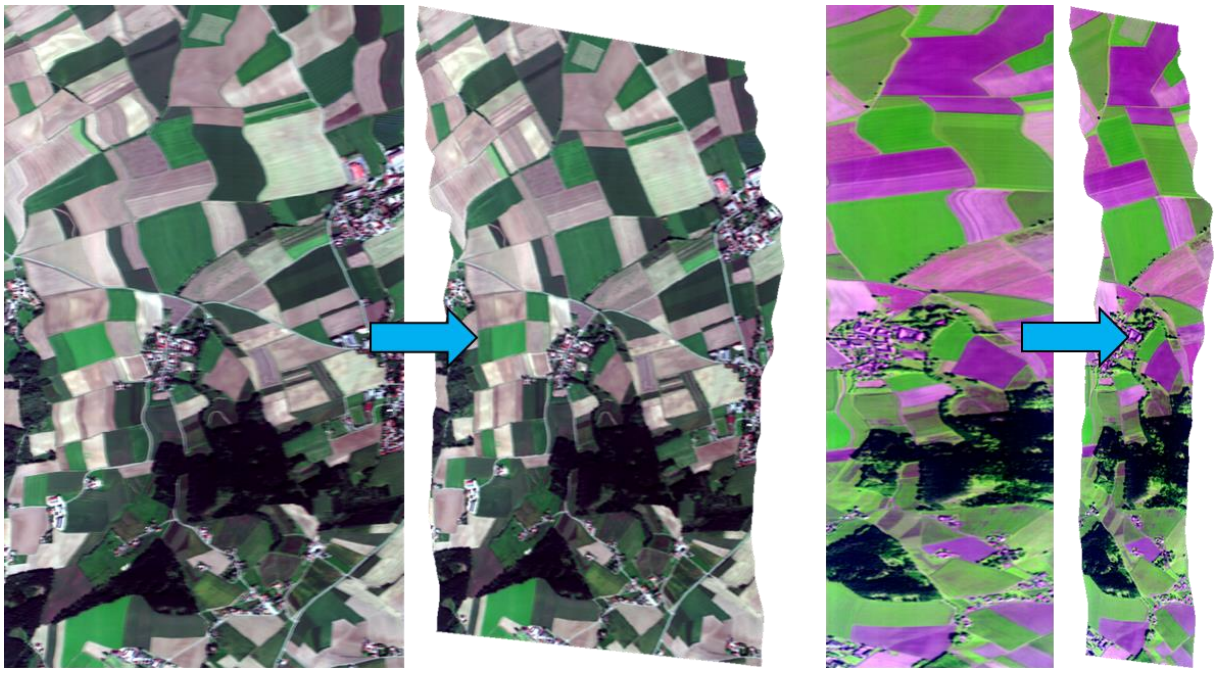

Figure 2-25: Final resampling step from only sensor calibrated to geometric corrected images of CCD-1020 (left, true color) and Xenics-Xeva (right, colored infrared).

2.2.2.2.4 Image Mosaicking

After all of the 52 image strips were processed by means of sensor calibration and geometric correction, in a next step the data was layered and mosaicked. For that purpose, the Xenics-Xeva data (128 bands) was co-registered to the CCD-1020 data (99 bands), since there were minimal deviations between the two sensor recordings, even after geometric correction. To allow a pixel accurate evaluation of the very important sun-target-sensor geometry during later analysis, the previously extracted information on zenith and azimuth angle was resampled as well and stacked to the other layers as additional bands. Figure 2-26 gives an overview of the data layers. To prevent errors in the wavelength-dependent analysis to come, the wavelengths of the new bands of zenith and azimuth were set to 9998 and 9999 nm, respectively.

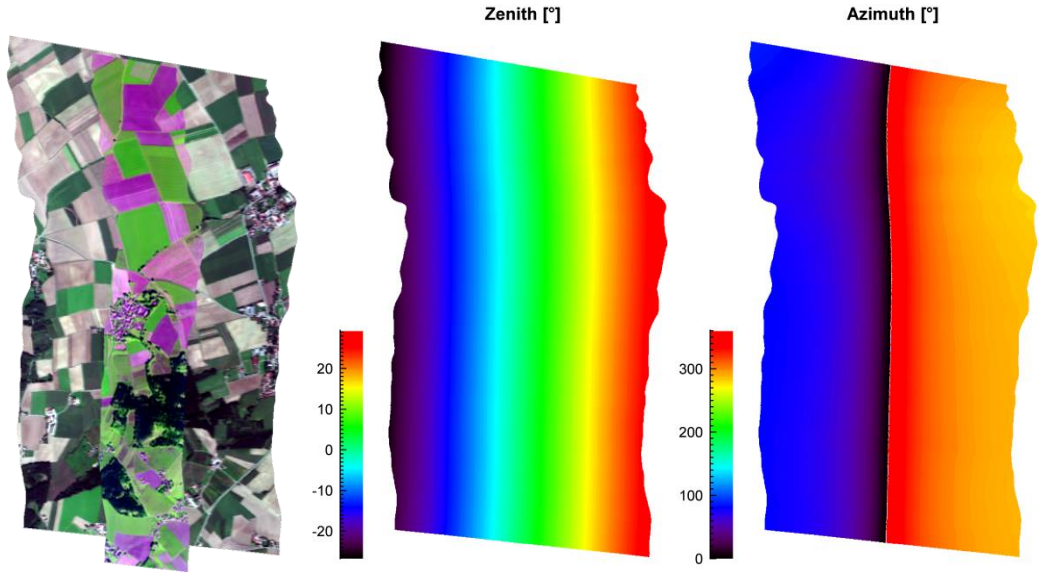

Figure 2-26: Image layers to be stacked:CCD-1020 bands (true color, left below), Xenics-Xeva bands (colored infrared, left above), zenith angle (middle) and azimuth angle (right).

As a result, the new data cube now consisted of 229 bands. It should be noted, however, that the actual number of bands had to be reduced due to the overlapping of the spectral ranges of both cameras. The reduction was carried out after radiometric calibration (see Chapter 2.2.2.3).

Before image mosaicking was carried out, the images were ortho-rectified to a high-resolution aerial photo of the study area in order to ensure that the flight strips among all scenes are geometrically absolutely congruent to each other. This is necessary due to potential geometrical divergences in the resampled image stripes, which may originate from minimal measurement inaccuracies of the IMU and the dGPS as well as from recording errors.

During image mosaicking, the components of the final mosaic are merged based on their spatial extent. Here, it was necessary to consider that the strip widths of the CCD-1020 and the Xenics-Xeva data differ and should be merged based on the spatial properties of the latter,

since it has a lower spatial coverage. When consecutively merging the images over the full spectral range, this would, however, lead to the loss of large parts of SWIR information, even if they are merged based on the spatial extent of the Xenics-Xeva data. This is due to the fact that areas lying outside the Xenics-Xeva extent but inside the CCD-1020 extent of the next image strip, holding solely information in the VNIR domain, would replace the SWIR information of the previous strip. To prevent this kind of data loss the mosaicking was carried out in two steps. First, the extent of the Xenics-Xeva bands served as a mask for the full dataset, including CCD-1020 bands and sensor angles. The image mosaic was composed on the basis of this segment. Since this mosaic showed data gaps originating from an insufficient number of flight strips to achieve full spatial coverage over the whole study area in the SWIR domain (see Chapter 2.1.2), another mosaic was calculated based on the full extent of the CCD-1020 data, in order to at least gain full coverage in the VNIR domain. The second mosaic was then used to fill in the data gaps of the full spectral range mosaic. Figure 2-27 visualizes the resulting mosaic for the fourth flight on September 8th. The position of field boundaries on the hyperspectral image proves the quality of ortho-rectification. Further, it is shown that even with eight flight strips data gaps in the SWIR may occur. This problem is reviewed in chapter 2.2.4.

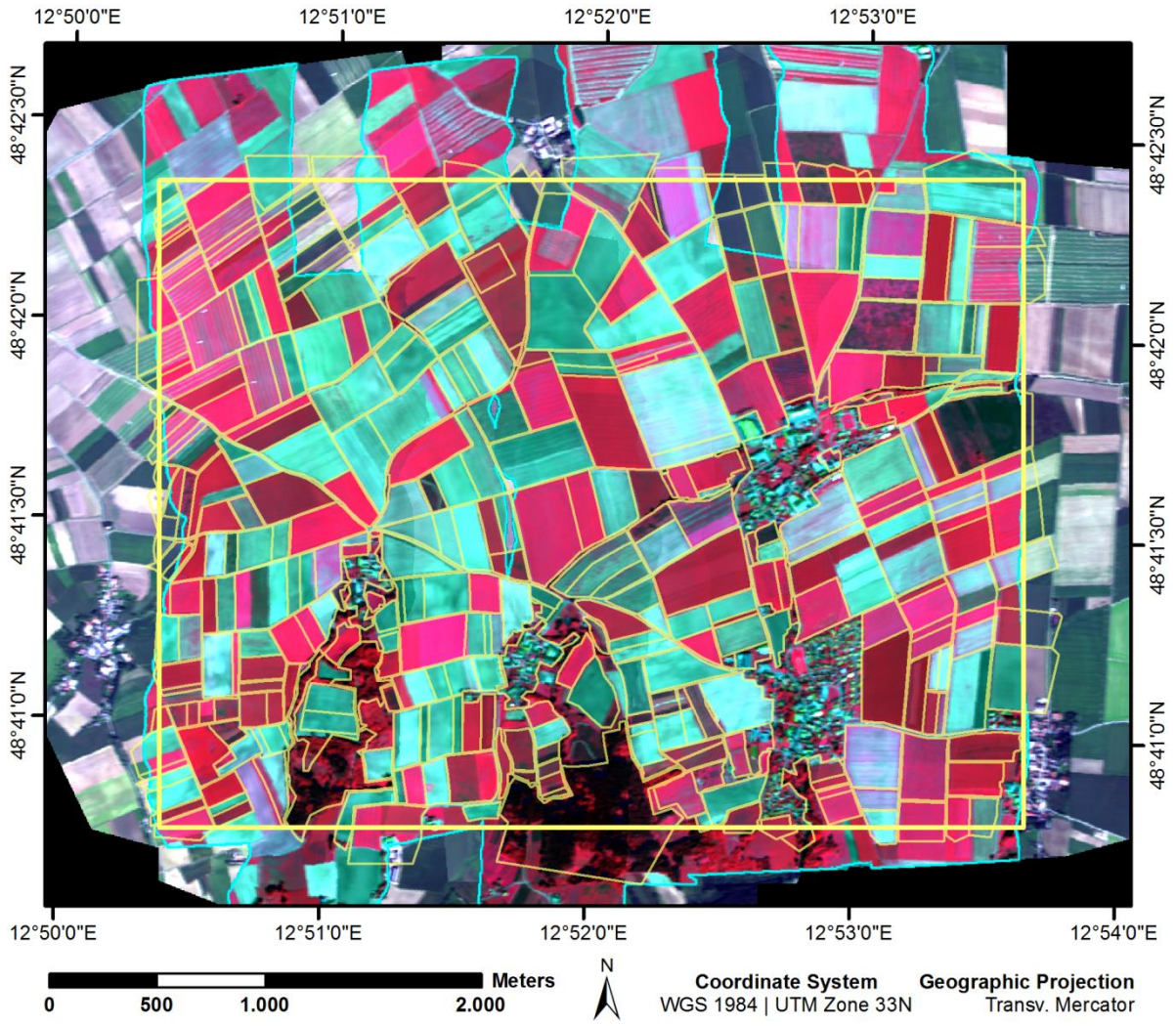

Figure 2-27: Ortho-rectified image mosaic of the fourth AVIS-3 flight consisting of eight single flight strips. The extent of the SWIR-based mask is shown in colored infrared (framed in blue), compared with the underlying VNIR extent in true color. The test site extent and field boundaries are displayed in yellow.

2.2.2.3 Radiometric Calibration

During radiometric calibration the dimensionless grey value signal is transferred to radiance and reflectance. While radiance is the physical amount of energy that actually reaches the sensor, reflectance is the fraction of incident radiation that is reflected from the surface. Reflectance is driven here by color, physical state, surface roughness and illumination conditions and thus can be seen as surface property. Consequently, the derivation of reflectance data is the major goal of this calibration step, because, from a plant-physiological perspective, reflectance allows direct conclusions to be made about the controlling elements within vegetation and its state. However, radiance data is of importance too, since it supports the interpretation of the strength and width of atmospheric absorption bands, which may disturb a later analysis of the data.

In contrast to other studies (e.g., OPPELT, 2002; BACH, 1995) in which spectral reflectance was derived by the use of an atmospheric radiative transfer model, an empirical alignment approach was applied in this study. To support this, spectroscopic field measurements of defined reference targets were collected during the flyovers of the field campaign (see Chapter 2.1.3.1). Because the field spectrometer has a higher spectral resolution (3 nm with a sampling interval of 1 nm) than the airborne AVIS-3 record, the spectral resolution of the in-situ data was reduced according to the center wavelengths of AVIS-3 bands. Thereafter, a correction file was calculated based on the ratio of the AVIS-3 record to its corresponding reference measurement and then applied to the full dataset to obtain reflectance and radiance.

Compared to the inversion of an atmospheric model, this procedure has some advantages, but also some limitations, which arise from the method of calibration. An advantage of field measurements is the fact that they allow a far more accurate characterization of the atmospheric conditions at the time of the flyover than an atmospheric model could ever deliver. However, this method is not flawless. Since atmospheric conditions as well as the influence of the sun zenith angle can change significantly within minutes, a precise calibration of all image strips would require measurements to be collected for each image strip, at representative, non-alterable sites, at the exact time of the airborne data recording. These requirements cannot be met for both logistical reasons and because of the lack of suitable reference targets at the ground. In addition, they are far more time-intensive than the use of an atmospheric model. However, the advantages of field measurements outweigh the disadvantages since they lead to higher data quality.

Calibration is essential to ensure comparability between different datasets. This comparability is not given for the raw data, since several substances within the atmosphere as well as changing atmospheric conditions at each data acquisition influence the signal received by the sensor. First, there are absorption processes which are caused by different molecules in the atmosphere, such as ozone, oxygen, water vapor and carbon dioxide (e.g., OPPELT, 2002). This absorption effect cannot be corrected, since solar radiation in the affected wavelengths reaches neither ground nor sensor. Fortunately, this is only the case for specific wavelengths. When the absorption effects are too strong, these ranges are in general excluded from the analyses of the airborne datasets. Second, there are scattering effects in the atmosphere, which can in turn be corrected by calibration. Specifically, these effects are Rayleigh and Mie scattering (SCHANDA, 1986). Rayleigh scattering, caused by air molecules whose diameters are much smaller than the wavelength, is inversely proportional to the 4th power of the wavelength. Mie scattering, by contrast, is caused by particulate matter similar in size to the wavelength, such as water vapor, smoke and dust particles. Scattering effects disturb the signal that reaches the sensor in two ways. First, they cause path radiance, which is radiation scattered in the atmosphere and reaching the sensor without being reflected by the ground (OPPELT, 2002). Second, scattering effects lead to overexposure in the data, which is the result

of direct and diffuse radiation reflected from surrounding pixels (BACH, 1995). This effect is also called ‘adjacency effect’ (VERHOEF & BACH, 2003)

Since adjacency radiation depends, above all, on the brightness of the immediate surroundings in each wavelength, it cannot be calibrated using field measurements. As a consequence, a different approach needs to be adopted. In contrast, path radiation is a purely atmospheric property. Hence its influence can be eliminated by calibration against field measurements. It is based on the assumption that the field measurements register the reflectance, taken at a height of about one meter above the ground and calibrated using a white reference, free of atmospheric effects; thus it can be used to correct the airborne image data. Although an atmospheric influence in an atmospheric layer thickness of one meter may be detectable when analyzed, it can nevertheless be neglected here.

To efficiently calibrate the data into reflectance and radiance values, it is advisable to start with the removal of the adjacency radiation from the raw data before correcting the effect of path radiance. Adjacency radiation depends on the heterogeneity of the reflection properties of the surroundings and its impact is becomes more pronounced, the closer the adjacent pixels are to the center pixel. KAUFMANN (1995) quantified the sphere of influence of adjacency radiation for spaceborne sensors to 2 km around the center. BACH (1995) investigated the possibility to correct the adjacency effect, referring to two studies in which the spatial distribution of overexposure influence had been modelled (TANRE ET AL., 1981 and 1987). The model calculations revealed that 50% of overexposure is caused within 1 km of the pixel. To clear images of this effect, a filter matrix is calculated based on a weighting function (TANRE ET AL., 1981) which takes the spatially distributed influence of overexposure into account. Nearby pixels are thereby weighted to a higher degree than those lying farther away. Based on the weighting function, BACH (1995) found that, in order to consider the adjacency effect in its entirety, the filter size should be at least 2 km. If applied to the AVIS-3 data, which has a ground resolution of 4 m, the resulting filter box would contain at least 250,000 singular weightings, which would then have to compute the amount of background radiation for each pixel. This would entail a long computation time. In addition, it would make little sense to use a 2 km filter at a large, 3x4 km test site. However, the models developed by TANRE are designed in particular for spaceborne data. Airborne systems differ not only in the reduced operation height, which reduces the size of an influencing neighborhood, but also in the smaller-scale distribution of reflection elements (BACH, 1995). Because of these two facts, an iterative approach was tested to calculate the optimal size of the filter matrix, which in this case is a Gaussian kernel. The kernel is defined by its size in column and row direction and the width of the standard deviation (sigma) of the Gaussian function. Different combinations of size and sigma of the Gaussian function were tested. Several iterations were required in order to obtain the most efficient combination. During each iteration, the current Gaussian kernel was tested on the radiometric raw data whereby an offset for each pixel was calculated.

This offset represents the overexposure and was subtracted from the original data. In a following step, the effect of path radiance was removed from the data and calibrated into reflectance. Overexposure correction (OEC) was applied to the raw data and thus before the step of reflectance calibration. Due to the iterative approach of the OEC and because it is based on the interpretation of reflectance, the derivation of radiance and reflectance is described at first. An overview of the whole procedure of radiometric calibration is shown in Figure 2-28.

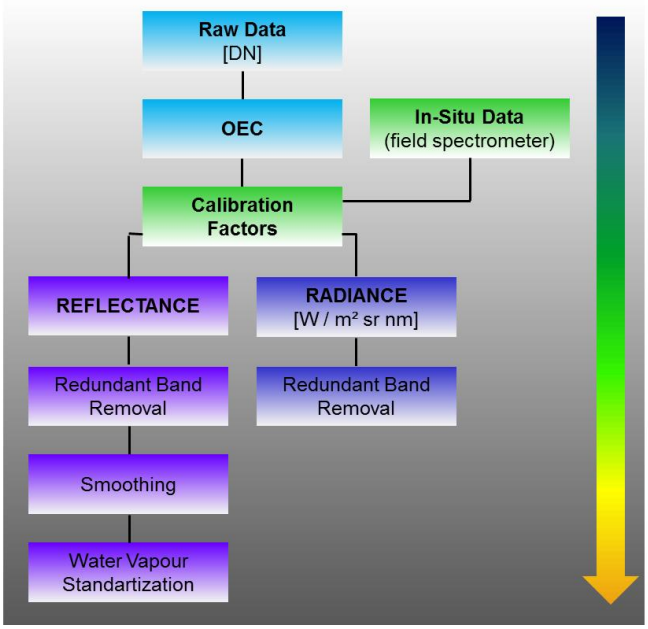

Figure 2-28: Organogram of radiometric correction.

2.2.2.3.1 Derivation of Radiance and Reflectance

Once the influence of adjacency radiation is removed, the only remaining source of error in the data is path radiance. This is corrected by the calibration of the dimensionless digital numbers of grey values.

The evaluation of all reference targets identified the asphalt surface of the plant site (R7) to the north of the village of Neusling as the most suitable for calibration, since its asphalt surface is relatively new and thus very homogenous, and free of any coarse damage. The surface reflects radiation quite uniformly over all wavelengths and the standard derivation is acceptably small (see Figure 2-2). Nevertheless, the total amount of reflected radiation is low. For this reason, the reference target of R6 (Parking Area C) was tested too, as it offers a comparatively high reflectance and is thus less susceptible to noise and more suitable for the deduction correction factors. The standard deviation of that target is acceptably small as well. Although the reflectance below 500 nm is significantly lower than in the rest of the wavelength spectrum for reference target R6, a characteristic that is not as distinct in the

spectral signature of reference target R7, the first is a more appropriate target, because it allows a more precise calibration.

For the generation of a correction file for AVIS-3, both reflectance and radiance data (collected in-situ), first had to be sampled down to the band specifications of the airborne sensor. This was done based on the spectral response function of AVIS-3, which was defined as normal distribution with a FWHM corresponding to the sampling interval around each center wavelength (see Chapter 2.2.1.2.3). Next, a ratio of the down-sampled data to the AVIS-3 spectrum of the reference target pixel was formed. This resulted in a correction factor for each band, which then was applied to the full AVIS-3 dataset. The following Figure 2-29 shows the raw signal of a sample vegetation surface.

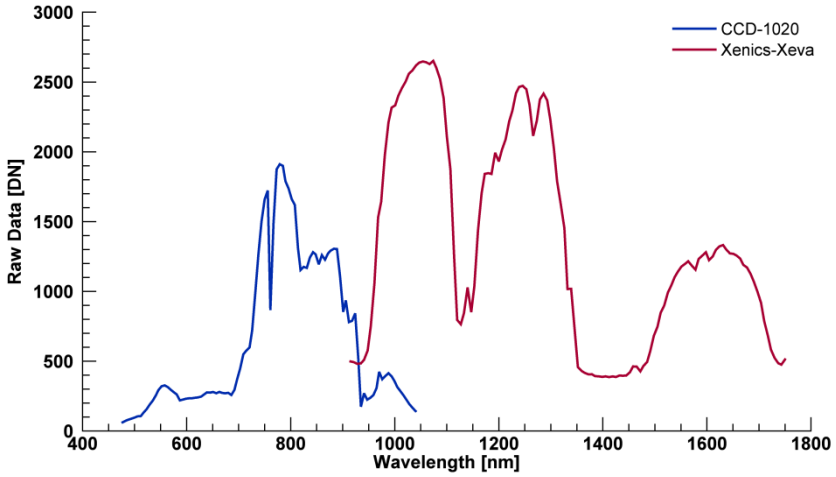

Figure 2-29: AVIS-3 raw data, containing the signals of both the CCD-1020 and the Xenics-Xeva. The spectrum is from a sample vegetation surface, taken during the data acquisition on September 8th.

In a first step, the dimensionless grey values registered by the AVIS-3 sensor were converted to physical radiance (W / m² sr nm). Only one calibration file was necessary to derive radiance from all four datasets, since both the airborne sensor as well as the field spectrometer register atmospheric influences, and the correction factors obtained for the individual flights were thus very similar. In a final step, the CCD-1020 and the Xenics Xeva data were merged. Because there is a spectral overlap of the two sensors (see Figure 2-29), duplicate bands were removed from the data. This resulted in a VNIR sensor coverage from 471 to 994 nm, while the SWIR sensor covers the range from > 994 to 1750 nm. However, due to the low sensor responsivity at the spectral margins of the CCD-1020 and the Xenics-Xeva (see Chapter 2.2.1.2.3) which could lead to an error-prone calibration affected by noise, these outer bands had to be removed as well. Thus, only 197 of the original 227 spectral bands remained, covering the range from 477 to 1704 nm. The final result can be seen in Figure 2-30. The figure also shows the position of the absorption bands due to oxygen (O_2) and water / water vapor (H_2O).

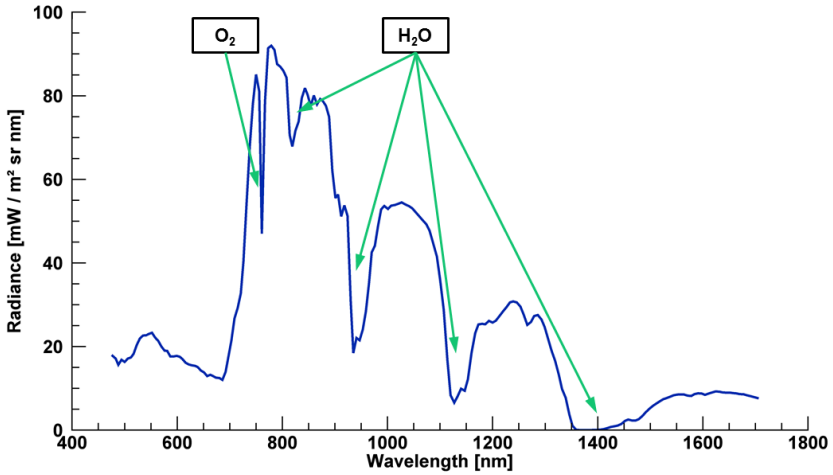

Figure 2-30: AVIS-3 radiance after redundant band removal. The absorption ranges of O_2 and H_2O are illustrated too.

Neither oxygen absorption at 760 nm nor the first (~ 820 m) and second (~ 930 nm) water vapor absorption bands were expected to adversely affect a later analysis of reflectance in those spectral areas, because the signal in the local minima is still strong enough for valid calibration. Rather, the absorption of H_2O in these ranges can be attributed to plant cell water and therefore represents valuable information. In the third (~ 1125 nm) water vapor absorption range, however, the reflected radiance may be too slight to efficiently support the use of this spectral area, while this is definitely the case in the fourth absorption range at approximately 1400 nm.

The retrieval of reflectance, which can be stated as a surface property, involved the generation of a correction file for each flight which was then applied to the corresponding dataset. Redundant bands were removed, likewise, but in contrast to the retrieval of radiance, the calibrated reflectance data had to be further enhanced since the spectra still appeared slightly noisy. A modest averaging filter (size=3) was used to smooth the data.

Since the spectral range affected by water vapor varied between the different data acquisitions, a uniform regulation had to be found, to ensure a full comparability of all scenes when excluding those spectral ranges. Guided by the outermost areas affected, the borders were set to 1120 and 1160 nm and to 1300 and 1500 nm, for the third and fourth absorption band, and the gaps linearly closed. When analyzing the resulting data, it should be considered that sections of the spectral signature no longer provide valid information.

The result of reflectance calibration can be seen in Figure 2-31. The figure shows the untreated reflectance calibrated for the two sensors and the final result after redundant band removal, smoothing and water vapor standardization. For a better overview, the two absorption ranges affected most are highlighted in grey.

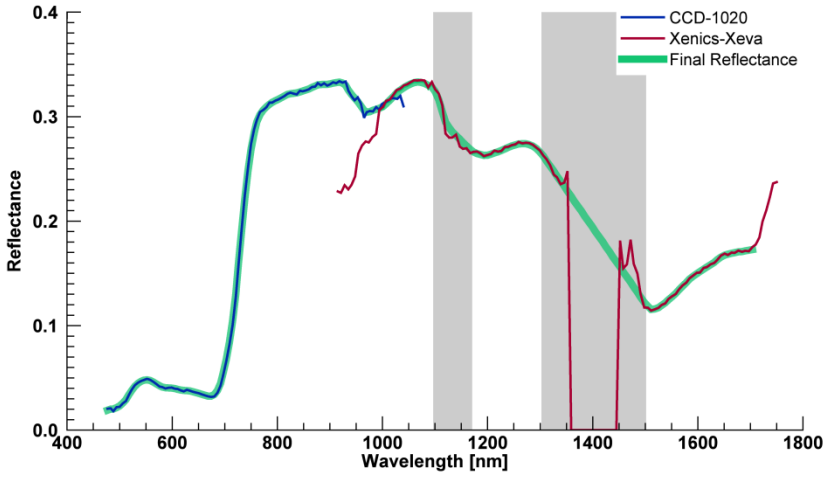

Figure 2-31: AVIS-3 reflectance of CCD-1020 and Xenics-Xeva before and after band removal, smoothing and water vapor standardization. Ranges of the latter are marked in grey. The green plot shows the spectrum after data fusion.

2.2.2.3.2 Overexposure Correction

Overexposure was corrected prior to the processing steps by which radiance and reflectance are derived, but since the success of its elimination can be assessed far more precisely after the conversion of the grey values to reflectance, it is listed afterwards in this study. The OEC was based on a Gaussian kernel which is defined by the sigma of a Gaussian function over a specified amount of pixel. Different sigma values, ranging from 0.8 to 20, were tested for various filter sizes, ranging from 20 to 400 pixels, and led to the filter matrix finally applied to the image data (Figure 2-32). This Gaussian kernel was generated with a sigma of 1.8 and a width of 40 pixels, which corresponds to a filter size of 160 m.

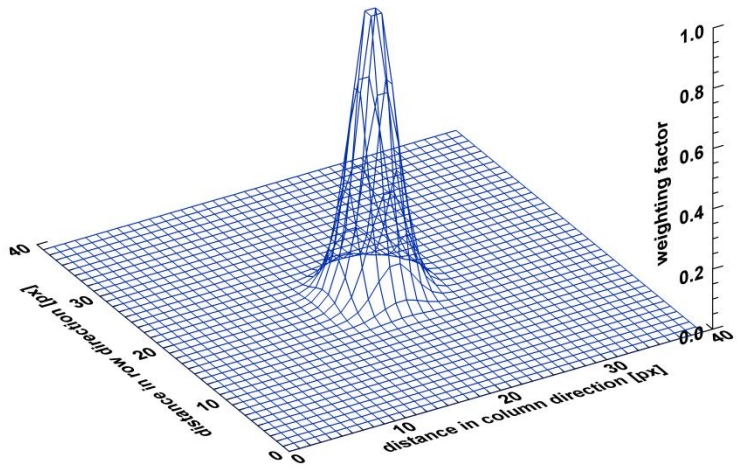

Figure 2-32: Gaussian kernel (Sigma = 1.8, Width = 40 Pixel) for overexposure correction.

For validation purposes, the filter's influence on the reflectance of three different surface types was examined: water, bare soil and vegetation. Their characteristic spectral features

were to be at least as, but ideally even more, distinct after the OEC, compared to their initial spectral signature. Since overexposure has a more pronounced effect on a pixel's reflectance the closer it is situated to an area of a different land cover, the control pixels were chosen in boundary areas. The position of the validation pixels can be taken from Figure 2-35.

A pond to the south of the test site served for the investigation of the filter's effect on water reflectance. Characteristically, an open water surface absorbs radiation in the SWIR up to nearly 100%. In the control pixel, however, the reflectance in this spectral domain was significantly higher due to the adjacency effect. The OEC thus aimed to reduce the signal in the long-wave range, i.e., for radiation with a wavelength > 1100 nm, without leading to negative reflectances, since this would mean the exposure filter was too strong. Figure 2-33 compares the uncorrected reflectance of the pond with its reflectance after overexposure correction. The result is satisfactory, since reflectance in the SWIR is nearly zero. Although some peaks remained in the SWIR range of the data, this fact could be ignored as they occurred in the water vapor absorption ranges and were consequently excluded from the later analysis.

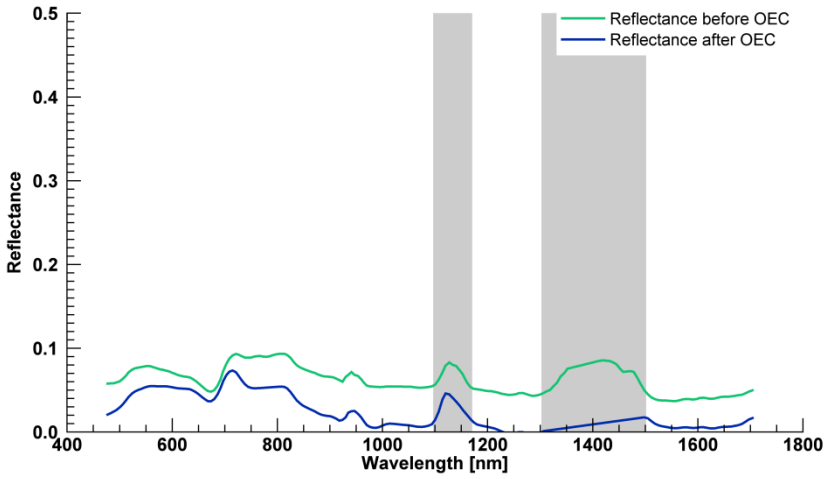

Figure 2-33: Impact of OEC on reflectance of water. The range of atmospheric water vapor absorption is highlighted in grey and is therefore not to be considered.

Figure 2-34 shows the impact of the correction on the spectra of bare soil and vegetation. The uncorrected soil spectrum showed an increase in reflectance around 720 nm, which was attributed to the red edge, a characteristic feature in vegetation spectra, although the sample represents an absolutely fallow field. With the successful application of the overexpose filter, the red edge could be eliminated. In the vegetation spectrum the OEC acted in a contrast-enhancing way. In spectral ranges of absorption, e.g., in the visible and the SWIR region, the signal was cleared from the comparatively high reflectance of surrounding bare soil pixels in that spectral range. In contrast, high reflecting areas of the spectrum, e.g., in the NIR-plateau, had been underestimated due to the lower reflectance properties of soil in this specific range.

Through the OEC the reflectance was thus increased. Again, negative reflectance values would have led to the rejection of the filter but were not found throughout the whole dataset.

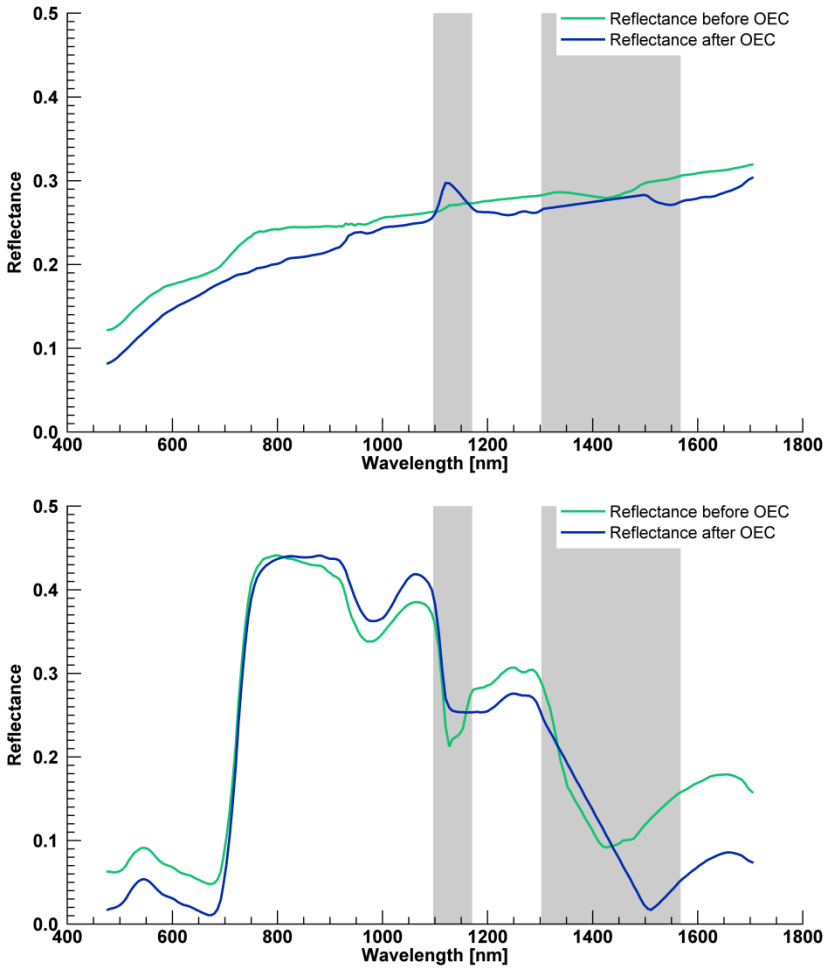

Figure 2-34: Impact of OEC to reflectance of soil (top) and vegetation (bottom). The range of atmospheric water vapor absorption is highlighted in grey, since the signal in the affected range tends to be noise.

Figure 2-35 shows an image section of the AVIS-3 flight on September 8th before and after OEC. The enhancement concerning image sharpness and clarity is clearly visible. As mentioned above, the figure also contains the positions of the three sampling spectra. The completion of sensor calibration, geometric correction, radiometric calibration and all data merging steps enabled the meaningful analysis of the AVIS-3 datasets which is discussed in Chapter 3.

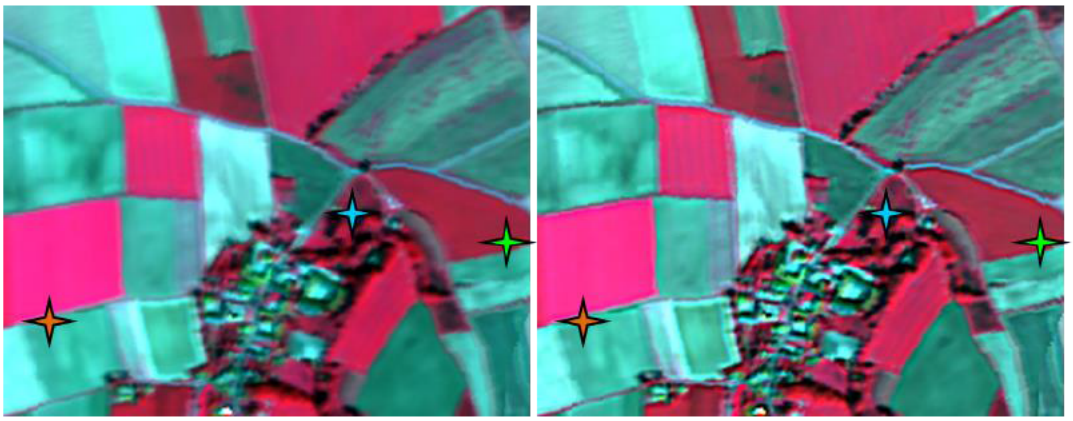

Figure 2-35: Image section (colored infrared) before (left) and after (right) overexposure correction. The stars mark the positions of the validation spectra of water (blue), bare soil (orange) and vegetation (green).

2.2.3 Extension of the Database with HySpex

As already mentioned in Chapter 2.1.2, the hyperspectral image database consisting of four AVIS-3 recordings could be extended by HySpex imagery, supplied by the German Aerospace Center, resulting in a total of six separate scenes for the test site. The HySpex flights took place on May 8th and August 12th. HySpex is a hyperspectral push-broom sensor developed and manufactured by NEO (Norsk Elektro Optikk A/S) and consists in the current specification operated by DLR of two camera systems. The sensor properties can be taken from Table 2-8 (BAUMGARTNER ET AL., 2012).

Table 2-8: HySpex image spectrometer characteristics.

Sensor characteristics	VNIR-1600	SWIR-320m-e
Spectral Bands	160	256
Spectral Range	410 – 1000 nm	1000 – 2500 nm
Sampling Interval	3.7 nm	6.0 nm
Radiometric Resolution	12 bit	14 bit
FOV / Swath Width	17°, 1600 pixels	14°, 320 pixels
Min. GSD	0.3 m	0.6 m

The HySpex data was acquired and preprocessed by the DLR, and delivered with a GSD of 4 m, equal to the AVIS-3 data. Since the image data for each acquisition date consisted of three separate flight strips of the test site, it was sufficient to perform an image mosaicking. In addition, the spectral properties of HySpex were adapted to those of AVIS-3, according to the spectral response functions described in 2.2.1.2.3. Further, sensor zenith and azimuth information was added as separate bands to the HySpex data in order to conform to the

specifications of the processed AVIS-3 data. Consequently, the adapted HySpex data comprised 197+2 bands, covering the same range from 477 to 1704 nm.

2.2.4 Résumé and Results of Preprocessing

In retrospect, the acquisition and preprocessing of AVIS-3 data brought some unexpected challenges, which could be solved in most cases, but were much more time-consuming than originally anticipated. One of the greatest challenges was the data acquisition itself, which was explicitly dependent on adequate weather conditions and thus turned out to be a limiting factor for the creation of a solid image database. The range of potential acquisition days was limited further by restrictions imposed by the airport, allowing motorized flights only on weekends and holidays. In addition, unexpected weather changes during data acquisition, e.g., on the second flight with AVIS-3 at May 25th, rendered some in-situ measurements useless since the collected imagery data was partly covered by clouds and thus had to be removed from the later analysis.

Further problems arose during data preprocessing, such as the lack of an integrating sphere that is large enough for the sensor to carry out a flat-field correction. This could be addressed by calculating a correction matrix from the image data acquired.

During geometric analysis, problems occurred due to the partly disturbed navigation data of some flight strips. Fortunately, all files could be reconstructed. However, some image areas in the scenes still appeared distorted. Moreover, the inertial measurement unit was not able to measure intense and quick flight movements, as occurred especially during the third flight. The movements of the aircraft thus could not be traced back and made it impossible to correct the image data from this effect. Since it was a small-scaled phenomenon, usually in a range of only a few pixels, it could be neglected.

The radiometric calibration must be viewed critically as well. Although the method of empirical alignment by the use of field spectrometer data worked very well and led to coherent spectra, it cannot be overlooked that due to the time difference, and thus varying sun position between the airborne data recording and the acquisition of reference spectra of the corresponding location at the ground, some spectra are minimally corrupted.

During preprocessing it was discovered that the original flight plan of six overlapping strips for covering the test site was not enough to guarantee full coverage by the Xenics-Xeva SWIR sensor. Due to the high frequency of the flights and the time-consuming activity of preprocessing, this issue was unfortunately only revealed after the third data acquisition had taken place on June 16th. The gaps were caused by the underestimation of the intensity of compensation movements, especially those induced by rolling, that the aircraft had to absolve to keep on track. Generally, these movements led not only to gaps between several strips, but also to the loss of data at both ends of the flight strips in some cases. This occurred when

pitch angles were too large despite a spatial buffer included in the calculation of the necessary length of the flight strips. For the fourth flight on September 8th at least, the number of strips was increased to eight, but even then some small gaps appeared. Figure 2-36 shows the four AVIS-3 scenes. The images each contain a true color visualization of the data taken with CCD-1020, which provides full coverage, and are overlaid by a colored infrared band combination that shows the full scope of data gaps in the SWIR range. The different patterns of the SWIR extents in the images are the result of varying flight conditions. For example, the second data acquisition was much more disturbed by turbulences than the first one due to midsummer weather conditions. This is in line with the spontaneous convective cloud formation that can be seen in the south and northeast of the second scene. The patchy data gaps in the image acquired on June 16th were the result of the lower navigational skills of the less experienced reserve pilot who replaced the otherwise booked proficient pilot during the third flight.

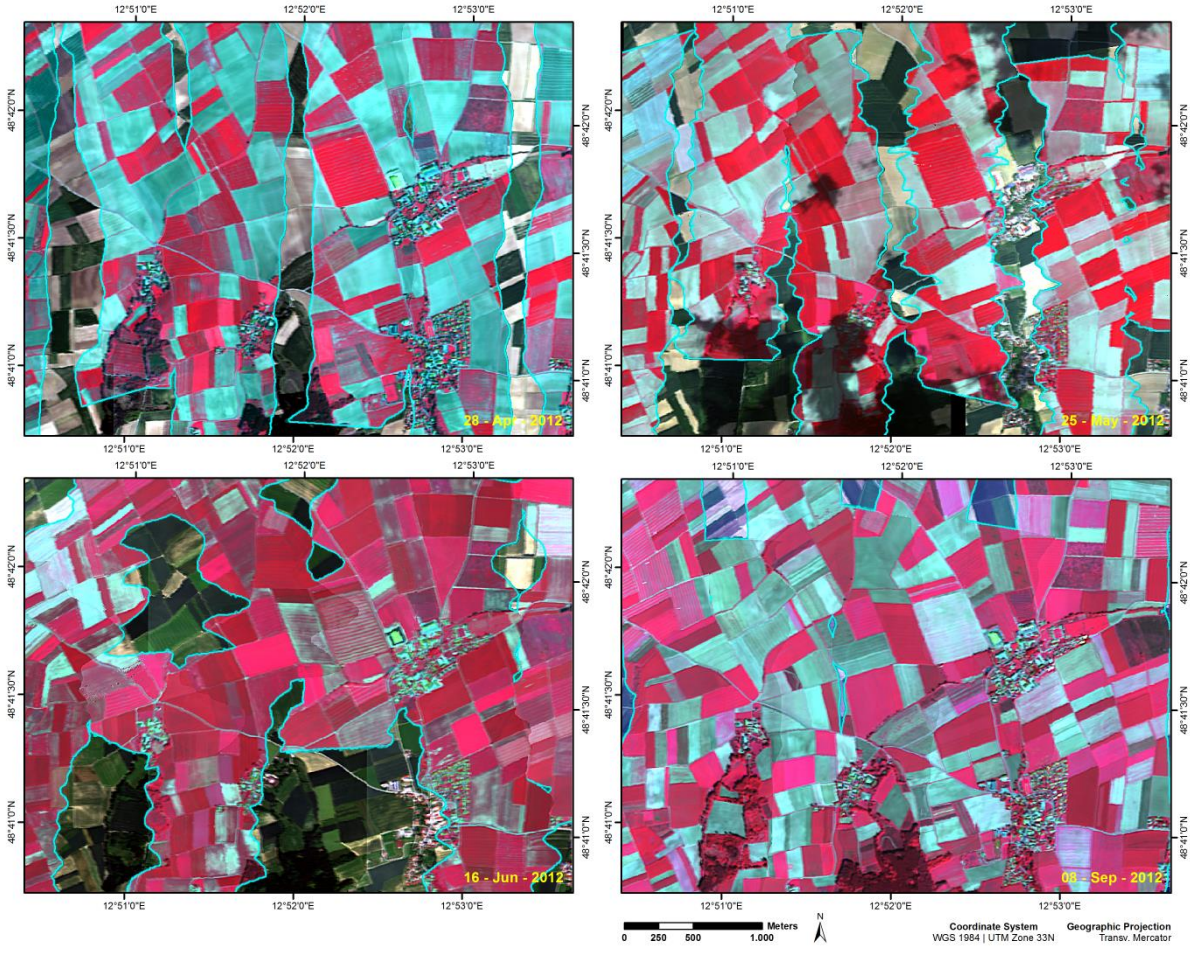

Figure 2-36: AVIS-3 data mosaics. The coverage of the SWIR data (colored infrared), which is framed in blue for better visibility, is layered on top of the VNIR extent (true color).

A malfunction of the CCD-1020 sensor, which was encountered in the data after the first flight, was a further problem that had to be addressed. In high-contrast areas, e.g., at roads and edge areas of agricultural fields, a kind of squint effect appeared within the data. This effect

caused a sort of overframing from brighter to darker areas with an offset of three to four pixels. Since this effect did not occur in test data of the years 2011 and 2010, it was initially attributed to an incorrect focusing of the lens. In the laboratory, however, this error was identified as being systemic, since no improvement was achieved when modifying the focus. Figure 2-37 shows the impact of the effect on an image section of roads with surrounding agricultural fields in five different wavelengths from the visible blue (477 nm) to near infrared (750 nm). Two arrows mark roads which are along-track or across-track to the flight direction.

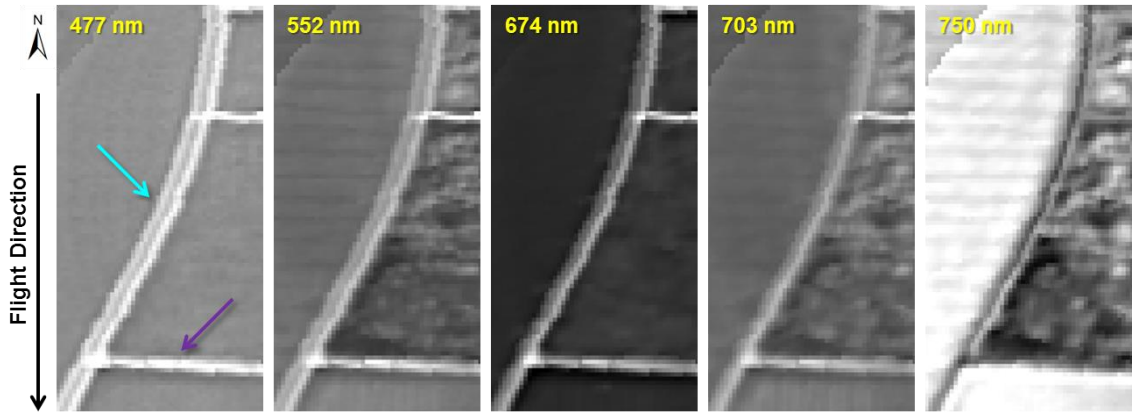

Figure 2-37: Squint effect of CCD-1020, taken with AVIS-3 on September 8th. The arrows mark roads along (blue) and transverse (purple) to the flight direction.

A closer examination of this issue led to three main findings. First, the squint effect only appeared on the along-track road in the across-track direction. Second, the second road which then appeared was always situated to the right of the flight direction. Third, the effect is wavelength-dependent and most distinct in the short-wave bands. Thus, the effect was no longer visible in the last image (750 nm). It seems that the lens or a part of the spectrograph was damaged, possibly due to harsh flight movements. Although this effect disturbs the spectral quality of the data, it is only critical in areas where two contrasting land covers occur in high proximity to each other.

Despite all difficulties mentioned, the acquisition and preprocessing of AVIS-3 data can be considered a success. This is because the AVIS-3 records covering both VNIR and SWIR, complemented by two HySpex datasets, provide an extensive database for the evaluation of methods for the retrieval of biophysical surface parameters throughout the growing season 2012, when combined with the corresponding field measurements. Figure 2-38 shows the four AVIS-3 and two HySpex scenes in the correct timely order and nicely illustrates the dynamics of the vegetation period.

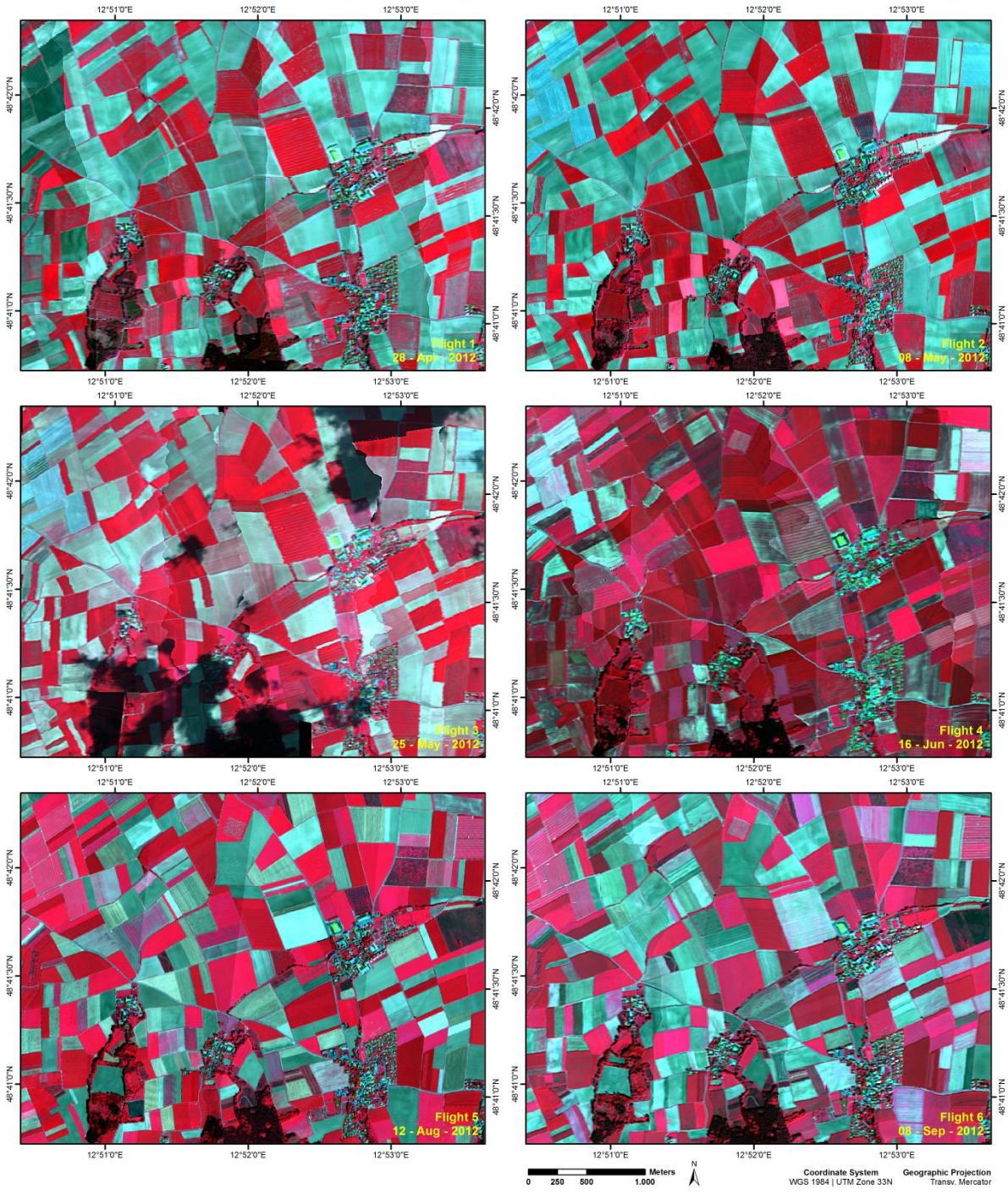

Figure 2-38: Final data mosaics of all acquisitions with AVIS-3 and HySpex (colored infrared).

2.3 Data Transfer to EnMAP Scale

To examine the applicability of the methods investigated in this study to the upcoming EnMAP-HSI, the airborne hyperspectral datasets of the study site had to be transferred to meet the spatial and spectral properties of the satellite. However, it is not sufficient to simply

resample the airborne data taken with AVIS-3 and HySPEX spatially and spectrally. Due to the lower ground sampling distance (GSD) of 30 m, at least 49 spectra would need to be averaged to represent an EnMAP pixel. This would lead to an unrealistic, almost noise-free reflectance signal and thus prevent an appropriate analysis of the potential of the spaceborne mission from being made. For that reason, SEGL ET AL. (2012) developed the EnMAP End-to-End Simulation Tool (EeteS), the image data from the multiseasonal campaign was transferred to EnMAP scale using EeteS, with the support of Karl Segl from the GFZ German Research Centre for Geosciences in Potsdam, Germany. The steps of the conversion, described in detail in SEGL ET AL. (2012), are summarized in the following section.

As can be seen in Figure 2-39, the EeteS first converted reflectance data to raw sensor data, i.e., Digital Numbers (DN), in its forward simulation module, and then further processed the raw data in the backward simulation module. There it was subjected to a simulated on-board calibration as well as all of the data preprocessing steps that will be integrated in the EnMAP image generation process.

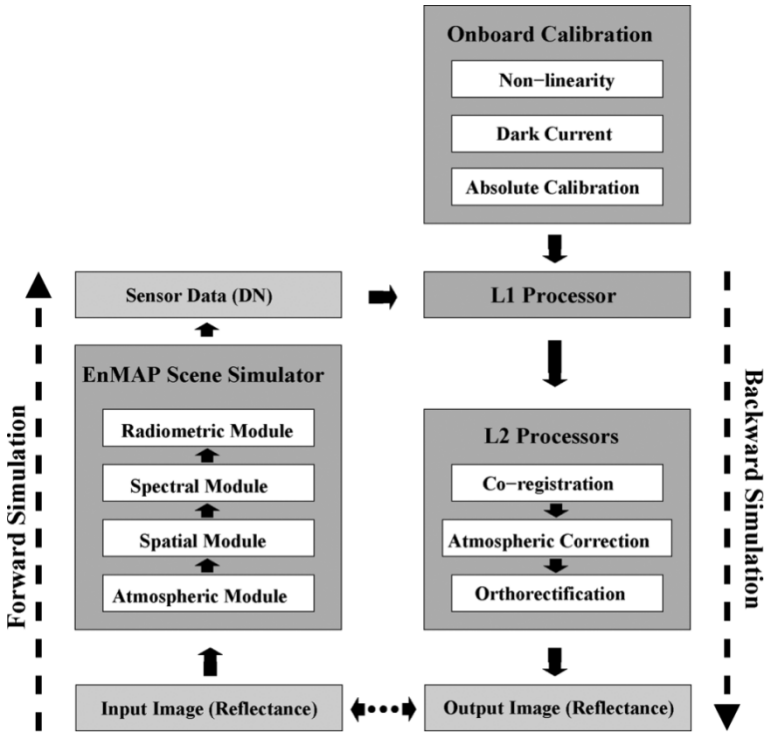

Figure 2-39: Organogram of the entire EeteS processing chain (SEGL ET AL., 2012).

The forward simulator consists of four independent parts in the sequential processing chain: an atmospheric, spatial, spectral and radiometric module. It is coupled with the backward simulation tool encompassing on-board L1-calibration of non-linearity and dark current correction as well as absolute radiometric calibration. The subsequent L2-processors of co-registration, atmospheric correction and ortho-rectification complete the tool. This allows the generation of artificial EnMAP data, which incorporates the instrumental and environmental configurations of the HSI.

In the first step L0 raw data [DN] is generated, for which reflectance data and a digital elevation model (DEM) are needed. With respect to the final EnMAP sampling interval the data is spectrally and spatially oversampled. The *atmospheric module* then converts the reflectance to TOA radiance by the use of horizontal distributions of aerosol optical thickness (AOT), pixel-wise columnar water vapor, surface elevation and an optional cloud cover/shadow. The *spatial module* simulates the spatial recordings, as produced by EnMAP, by the use of both a geometry and an optical-sensor model. The geometry model is defined by the pointing vector for each detector element, while the optical-sensor model is characterized by the modulation transfer function (MTF) of the sensor. After that the *spectral module* executes a spectral resampling, accounting for the spectral response function of all 244 EnMAP bands as well as non-uniformities in the spectral domain, such as the smile/frown effect and the spectrometer shift in the spectral dimension. In a final step, the *radiometric module* converts the data from at-sensor radiance to digital numbers by taking into account a range of influence parameters, such as integration time, QE, different kinds of noise, infrared background signal, high / low gain modes for the VNIR detector, variable offsets and gains, as well as an individual non-linear response for each detector element. This is an important step, because these parameters define the sensor-dependent noise, as specified by the detector manufacturer. Table 2-9 gives an overview of the individual steps involved in forward simulation.

Table 2-9: Adjustable sensor parameters of the modules of the EeteS software (SEGL ET AL., 2012).

Module	Sensor parameters
Atmospheric Module	• Geographic latitude and longitude • Month, day and GMT • Aerosol optical thickness (AOT) • Columnar water vapor (CWV) map • Cloud patterns • DEM
Spatial Module	• Geographic latitude (defining altitude, speed of satellite and earth rotation) • Sensor rotation (roll, pitch, yaw) • Pointing of detector elements incl. keystone and optical properties • Point-Spread-Function (PSF) (modelled by 6 different MTFs)
Spectral Module	• Spectral response functions • Spectral smile and shift
Radiometric Module	• Quantum efficiency (QE) • Optical transmission • Read noise • ADC noise • Dark signal • IR-background signal • Full well capacity • Number of bad and dead pixels

Once the L0 data is calculated, the on-board calibration can be simulated. On board the EnMAP-HSI two Focal Plane Assembly (FPA) LEDs, which provide an almost uniform illumination to all detector elements, measure (non-) linearities under 40 different integration time settings. From these measurements, which are simulated by EeteS, a correction factor is calculated for each detector element. To simulate dark current, the TOA radiance is set to zero and an offset is defined by averaging 256 measured lines. Within the HSI, dark current measurement will be carried out by closing a shutter. For the calibration to absolute radiance a diffuser panel is installed in front of the instrument aperture and illuminates the FOV. The panel itself is illuminated by the sun, which serves as reference light source. Due to the complexity of influences of the optical components to the passage of radiation, a precise simulation of the absolute radiometric calibration is not possible. Thus, a simplified version is implemented to EeteS. A solar radiance model (FONTENLA ET AL., 1999) provides the input to the tool, from which the reflectance of the diffuser panel is simulated. A total of 1024 lines is corrected from dark current and non-linearities. From the ratio of the input radiance and the resulting DN values a gain is estimated, which allows the conversion of the raw radiance to absolute radiance.

Backward simulation is then performed by the L1 and L2 processors. The L1 processor is based on the on-board calibration and converts raw DN to TOA radiances. This step is comparable to the sensor calibration of AVIS-3 and leads to an enhancement of the images. In the following co-registration, the spectral shift of both spectrometers is corrected. Due to the separate scanlines of the sensor, the shift amounts to 20 pixels in along-track and to 1.3 pixels in across-track direction. The shift correction is conducted without resampling, as this is carried out by the L2geo processor in the ortho-rectification module. The L2atm processor converts the TOA radiance to reflectance data, accounting for columnar water vapor (CWV) maps and AOT, which are estimated automatically from the raw data. Smile effect is analyzed by the location of the O_2-absorption feature at 760 nm for the VNIR sensor and 1140 nm for the SWIR sensor. Finally, the L2geo processor uses the pointing characteristics of each detector element, the sensor position and a DEM for the ortho-rectification of the image.

In an extensive validation of radiance, reflectance and geometry, the authors proved that EeteS simulates realistic EnMAP data in line with the expectations (SEGL ET AL., 2012). Figure 2-40 presents the data mosaics of the multiseasonal campaign after they have been processed by the EeteS software.

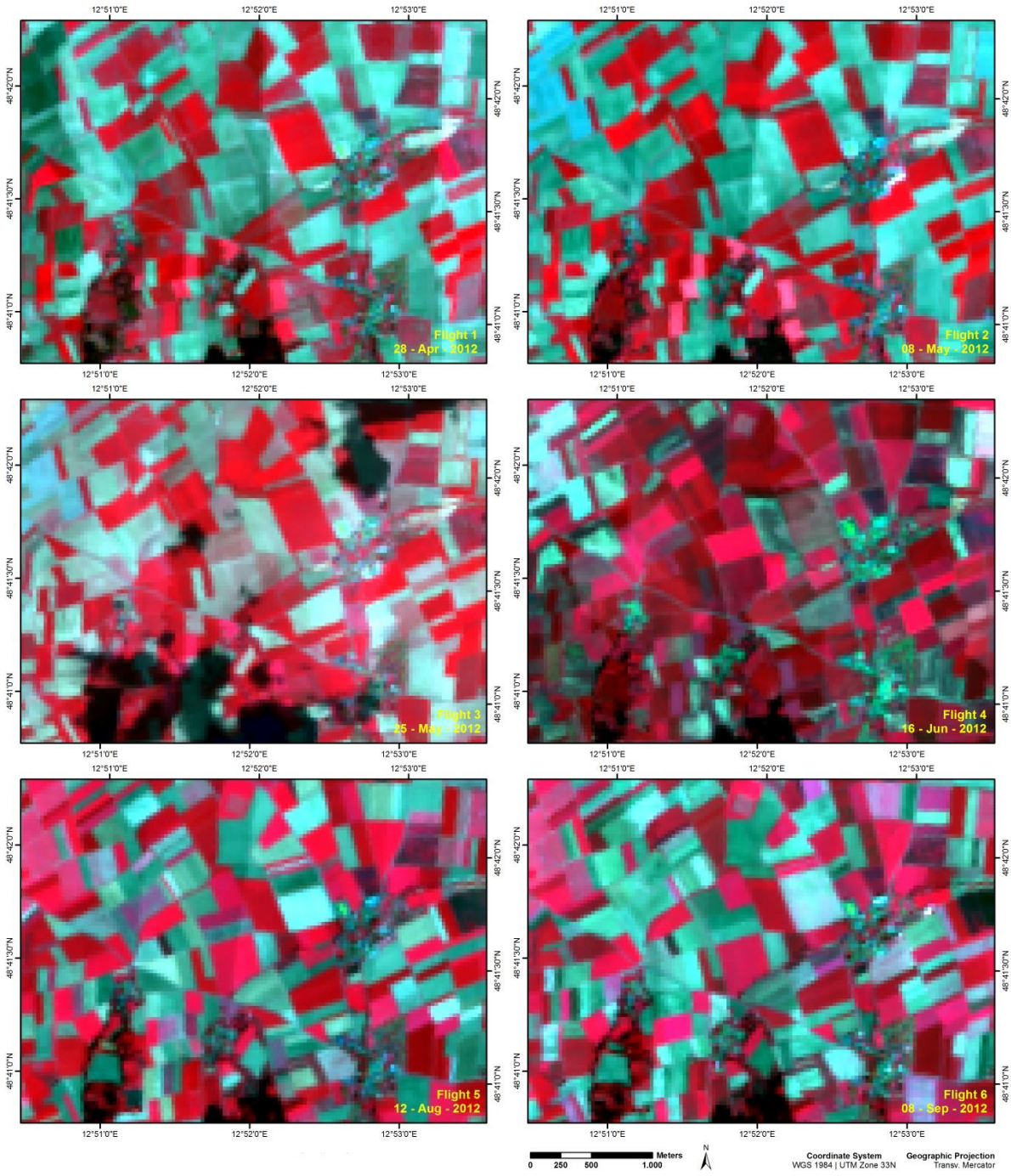

Figure 2-40: EnMAP simulations of the six scenes of the campaign 2012 (colored infrared).

In Figure 2-41, a comparison is made of the different scales of AVIS-3 and EnMAP in order to illustrate the spatial and spectral differences between the two sensors. The images show the same sample section of the scene from September 8th. Of particular note is, of course, the large difference in the GSD at 4 m and at 30 m. With regard to the spectral differences, a minimum of 49 pixels forms the basis of an EnMAP pixel, depending on the resampling strategy. For this reason, these 49 spectra of the AVIS-3 image and the EnMAP reflectance of one corresponding pixel are displayed in one plot. It shows that the EnMAP spectrum does

not behave as if it were just averaged from the 49 spectra. There are certain forms of noise occurring especially in the NIR plateau around 800 nm, which can be attributed to properties of EnMAP-HSI. In addition, the overlap of the two spectral sensors of EnMAP-HSI between 900 and 1000 nm is visible.

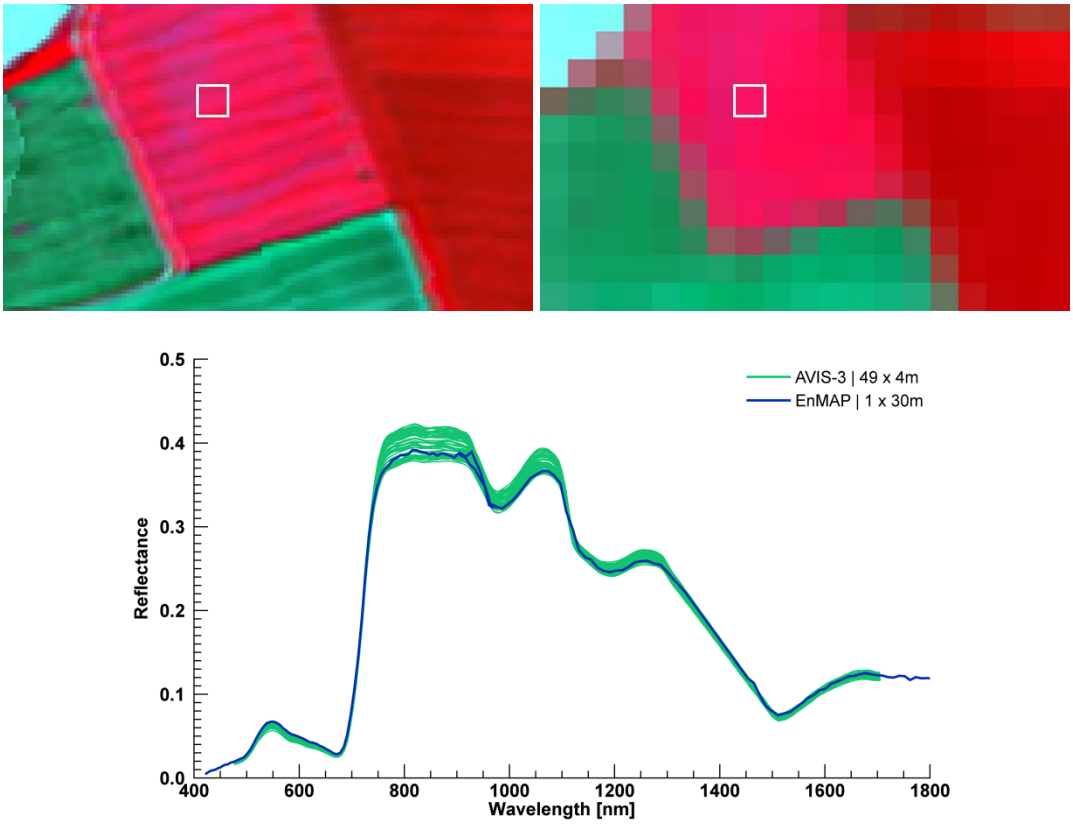

Figure 2-41: Comparison of AVIS-3 and EnMAP scale. The CIR image section of the scene of September 8th shows the spatial differences of AVIS-3 (above, left) and EnMAP data (above, right). The spectra plot (below) involves 49 AVIS-spectra and a corresponding EnMAP spectrum of the same region, which is marked in white above.

It should be noted that the EnMAP simulations could obtain spectral information only in the range of AVIS-3, that is, from 471 to 1753 nm. Although the simulation includes the full EnMAP spectral range, all bands beyond 1753 nm are of no value here. This constraint is also valid for the SWIR data gaps in some areas of the scenes of AVIS-3.

3 Estimation of Biophysical Parameters

This chapter explains the choice and the benefits of the PROSAIL model, the definition of the input criteria that generated the LUT and the implemented program sequence of the inversion, which allowed a flexible variety of settings, and an extensive analysis of the retrieval accuracy. For this study, the coupled PROSPECT leaf optical properties model and SAIL canopy bidirectional reflectance model, also referred to as PROSAIL, was used to generate a comprehensive Look-Up Table containing reflectance spectra including the information on the corresponding parameter settings. This library thus served for inversion of the observed hyperspectral data collected with both AVIS-3 and HySpex airborne sensors to retrieve several biophysical parameters, with its focus to leaf area index and chlorophyll content.

3.1 The PROSAIL Model

The choice of a suitable radiative transfer model was subject to certain requirements. In view of the future data that will become available through the EnMAP HSI and its anticipated high temporal frequency, the model to be chosen had to be able to project the reflectance of agricultural crops throughout the entire annual growing period. Under normal conditions, agricultural crops have the advantage of forming a homogenous canopy, a characteristic found in most reflectance models. Further, the model chosen must allow the retrieval of multiple biophysical variables, such as photosynthetic light absorbing pigments or water content on a leaf level, as well as components describing canopy architecture, e.g., leaf area index, average leaf angle and the amount of soil reflectance on a canopy level. Since the influence of different illumination geometries is of high importance to the reflectance properties, the model should also offer the possibility to process information on a solar zenith angle as well as on an observer zenith and relative azimuth angle, especially with regard to the potential side-looking mode of the EnMAP-HSI. For these reasons, and since it is widely accepted in the literature, the combined optical leaf level and canopy reflectance model PROSAIL was chosen, which combines two independent models: PROSPECT (*A Model of Leaf Optical **Pro**perties **Spect**ra*) and SAIL (***S**cattering by **A**rbitrary **I**nclined **L**eaves*). According to JACQUEMOUD ET AL. (2009) PROSPECT and SAIL are the most popular among a range of different radiative transfer models published during the last two decades. The success of PROSAIL is based partly on the extensive testing of the principles on which the model is founded. In their review of the model, JACQUEMOUD ET AL. (2009) give an overview of the validation of both PROSPECT and SAIL, performed extensively in several studies. Within

those studies, the model outputs were either validated against direct measurements, or compared to the outputs of other radiative transfer models or results derived from inversion processes.

In general, PROSPECT performs well on broadleaves and even does well in its prediction capability of needles, although the model was not designed specifically to account for these optical properties (see following chapter). SAIL was validated against direct measurements of the canopy of crops. Commonly, the studies proved a good agreement of the model results with observed data. The combined model PROSAIL was tested likewise in several studies, e.g., ANDRIEU ET AL. (1997) and DANSON & ALDAKHEEL (2000).

To ensure an accurate validation of the models even after they are tuned, their output can be compared to the results of other radiative transfer models, which then serve as a reference. By this means, SAIL was successfully tested against other 1-D and 3-D models for homogenous canopies, e.g., from WEISS ET AL. (2000) or WIDLOWSKI ET AL. (2007). The development and enhancements of both models in the last decades and their characteristics are described in the following two chapters.

3.1.1 Leaf Optical Properties Model – PROSPECT

PROSPECT simulates bidirectional-hemispherical reflectance and transmittance based on the optical properties of plant leaves in the solar spectrum from 400 to 2500 nm (JACQUEMOUD & BARET, 1990). These optical properties are defined through the interaction between incident radiation and leaves, which depends to a large extent on the chemical and physical characteristics of the latter (VANE & GOETZ, 1988). JACQUEMOUD & BARET (1990) describe the absorption process in leaves as a function of changes in the spin and angular momentum of electrons, transitions between orbital states of electrons in particular atoms and vibrational-rotational modes within the molecules. While the absorption properties of different photosynthetic pigments within the leaf, such as chlorophyll a and b, carotenoids (xanthophylls and carotenes) and brown pigments mainly affect the spectral signature in the visible range, leaf water and dry matter are the determining factors in the near and middle infrared (HODÁŇOVÁ, 1985).

PROSPECT was developed in 1990 and based on the *plate model* developed by ALLEN ET AL. (1969), which describes the plant leaf as a compact medium of a transparent plate with rough plane parallel surfaces. The *plate model* was specified based on a refractive index and an absorption coefficient. The refractive index is influenced by various plant biophysical parameters. It is subject to a theoretical distribution within the leaf and regulates reflectance, especially by a low absorption of the near infrared (JACQUEMOUD & BARET, 1990). Since the model was not able initially to describe complex leaf structures of non-monocotyledonous, an improvement in the approach was published one year later, in which the model had been

expanded by a pile of homogenous N layers describing the number of N-1 cell-to-air layers within the mesophyll (ALLEN ET AL., 1970 and GAUSMAN ET AL., 1970).

The initial version of PROSPECT, which incorporated the enhanced version of the *plate model*, described the reflectance spectrum based on three parameters: pigment concentration, water content and the structural parameter N, the latter being a continuous, non-integer variable in the model. With its growing popularity as key model for the simulation of leaf directional-hemispherical reflectance and transmittance, several versions of the model were developed following 1990 (FERET ET AL., 2008). Besides an extension for the description of dry matter (cellulose and lignin), which absorbs radiation especially in the SWIR (e.g., BARET & FOURTY, 1997, FOURTY ET AL., 1996, and JACQUEMOUD ET AL., 1996), and an increase in the spectral resolution from 5 nm to 1 nm (LE MAIRE ET AL, 2004, unreleased version), PROSPECT was updated to consider leaf surface directional reflectance (BOUSQUET ET AL., 2005). In 2008 FERET ET AL. (2008) released the PROSPECT versions 4 and 5 comprising a refined average refractive index of the leaf interior, which incorporated a more realistic leaf surface roughness parameter, and an updated specific absorption coefficient for each biochemical constituent. While the first version of PROSPECT by JACQUEMOUD & BARET (1990) assumed that chlorophyll is the only relevant absorbing pigment in the visible spectrum, and senescent leaves were consequently removed for the calculation and calibration of the specific absorption coefficient of chlorophyll, PROSPECT-5 enabled a separate description of chlorophyll (a+b) and carotenoids (carotenes and xanthophyll).

In PROSPECT-5b, which is used in this study, a brown pigment parameter was introduced, based on tannin and anthocyanins, to take senescence status into account. Brown pigment content is, however, implemented in the form of internal arbitrary units and thus not truly retrievable. The influence of the five reflectance-building input parameters can be taken from Figure 3-1. It shows the specific absorption coefficients, which were normalized for a better overview.

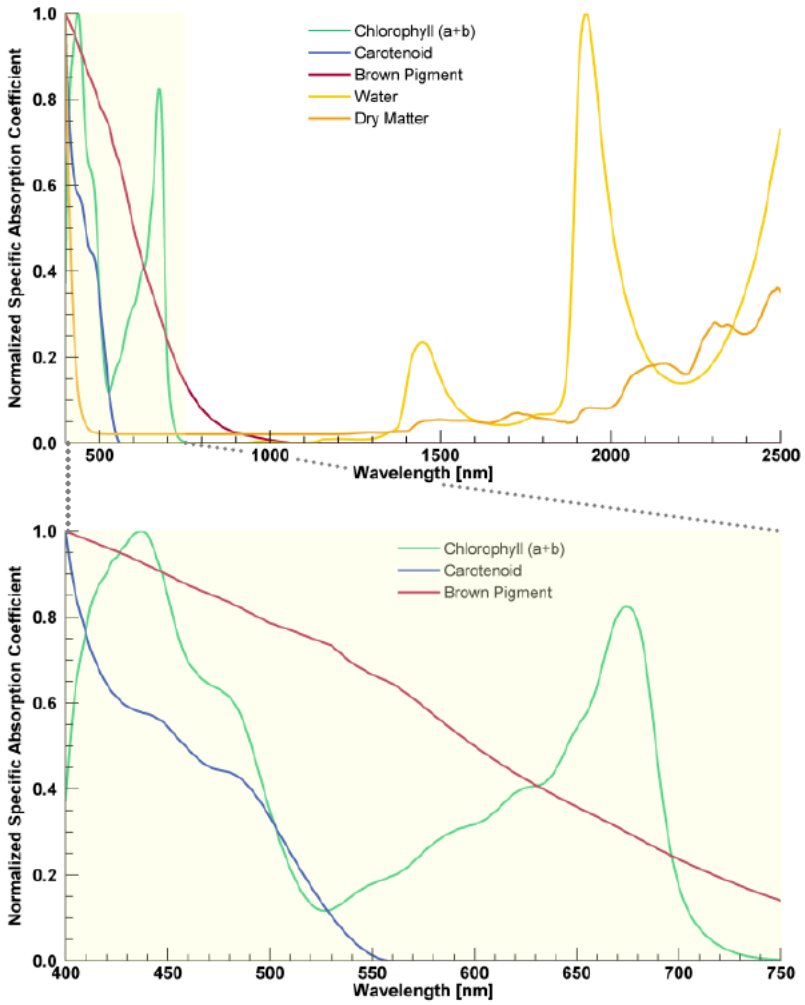

Figure 3-1: Normalized specific absorption coefficients of chlorophyll, carotenoids, brown pigment, water and dry matter, implemented in PROSPECT-5b.The top figure shows the coefficient over the whole spectral domain of PROSPECT, the bottom one is an enlargement of the visible range (400-750 nm) to give a better overview of the absorption behavior of chromorphic pigments.

For chlorophyll (a+b), the characteristic absorption maxima at 450 and 680 nm are visible, while carotenoids only absorb in the visible blue and green below 550 nm. Brown pigments also show a behavior as expected with a decreasing absorption to longer wavelengths. Water, as well as dry matter, are responsible for the absorption in the SWIR, although it can be assumed that water is the prevailing absorber in this range. The high absorption rate of dry matter below 450 nm can be explained by polyphenols or phenolic compounds in certain flavonols (CEROVIC ET AL., 2002). In the latest update of PROSPECT called *FluorMODleaf*, PEDROS ET AL. (2010) incorporated steady-state fluorescence caused by chlorophyll into the model.

3.1.2 Canopy Reflectance Model – SAIL

SAIL was one of the first radiative transfer models published, and was developed by VERHOEF (1984, 1985). Belonging to the class of turbid-medium models, the first version of

SAIL incorporates the same theory for radiation transfer through canopies as it was developed for the transfer of radiation in gases (JONES & VAUGHAN, 2010). One of the first theories of radiation flux in turbid-media is the general theory of KUBELKA & MUNK (1931), which describes the flux vertically to the medium. Besides the upward/downward diffuse energy flux in vertical direction, the model of SUITS (1972) also takes directional solar irradiation and radiance in viewing angle direction into account, rendering it a *four-stream* radiative transfer model (VERHOEF, 1984). Thus, SAIL, as it is based on the *Suits* model, calculates the interaction of these fluxes with a system of four linear differential equations. For the interaction with vegetation the following assumptions are made:

(1) The canopy is represented by an infinite and horizontal plate;

(2) Its individual elements are infinitely small and are only leaves; thus stems, branches, sprouts and other plant component are non-existent;

(3) The layer is homogenous and the leaves are homogenously distributed within the canopy.

Since these models were developed for application on homogenously distributed vegetation, they are most suited for use in the agricultural field. The concept of the four-stream turbid-medium is presented in Figure 3-2.

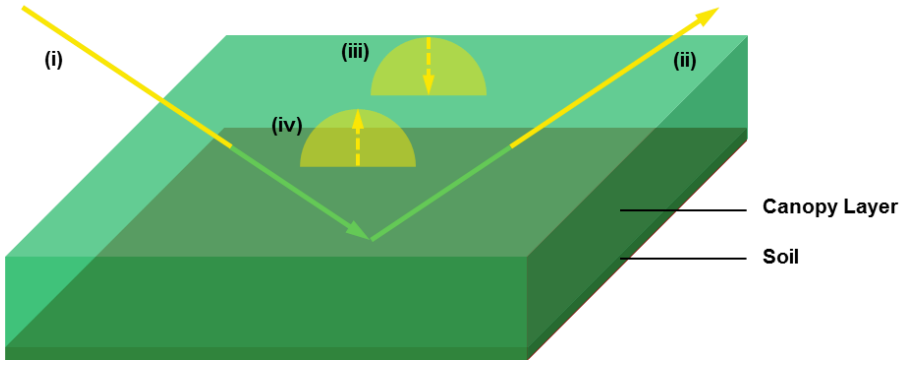

Figure 3-2: Illustration of the canopy as a four-stream turbid-medium model. The canopy is a homogenous, uniformly distributed medium with infinitely small and randomly distributed leaves. The energy flux is separated into solar incident flux (i), observer radiance (ii), diffuse downward flux (iii) and diffuse upward flux (iv).

The position of the leaves follows a statistical distribution (JONES & VAUGHAN, 2010). Since the *Suits* model takes into account only the projected area of horizontally and vertically inclined leaves, SAIL uses a probability density function to describe the distribution of the leaves' inclination angle as additional input. The azimuth angle of the leaves is, however, ignored, since their distribution is considered to be random (VERHOEF, 1984). The resulting leaf inclination distribution function (LIDF) is usually described through defined characteristic representatives, e.g., by the well-known canopy type-specific functions by GOEL & STREBEL (1984). The LIDF, the angular geometry and the leaf area index (LAI), representing canopy density, thus describe scattering and extinction coefficients of the canopy

(VERHOEF ET AL., 2007). In addition, solar and observer zenith angle as well as a relative azimuth angle are taken into account for the calculation of the radiation fluxes. This information is used to calculate absorption and scattering of incident light as a function of canopy geometry by the four differential equations. Direction and intensity of reflectance are thereby based on the bidirectional reflectance distribution function (BRDF) as defined by NICODEMUS (1970). Diffuse incident radiation has, in this context, only a very small influence on the canopy reflectance (CLEVERS & VERHOEF, 1993).

Following the first version of SAIL, several updates have extended the model family. Although SAIL generates bidirectional reflectance, the hot spot effect cannot be simulated, since the turbid-medium model assumes that leaves are infinitely small and homogenously distributed in uniform layers. Therefore, KUUSK (1991) added the hot spot parameter in SAILH, which is based on his own theory (KUUSK, 1985), as a function of the ratio of the average leaf size and the canopy height. Since then, SAILH and all later versions can be considered as hybrid models, because of the connection of the hot spot effect to a finite size of leaves (VERHOEF & BACH, 2007). GeoSAIL then, as further developed by VERHOEF & BACH (2003), was able to simulate vertically heterogeneous canopies using a dual-layer approach. This enabled the description of a vertical leaf color gradient, as is for example often seen in wheat canopies. With the release of SAIL++ (VERHOEF, 2002) and 4SAIL (VERHOEF ET AL., 2007) numerical robustness and speed performance were optimized. In addition, 4SAIL was capable of calculating internal flux and thermal emission. VERHOEF & BACH (2007) recently developed 4SAIL2, which combines GeoSAIL and SAIL++ and also considers the forest-typical effect of crown clumping. Together with PROSPECT and a modified non-Lambertian soil BRDF model (HAPKE, 1981), 4SAIL2 was combined to an integrated radiative transfer model called SLC (**S**oil-**L**eaf-**C**anopy). Table 3-1 gives an overview of the different SAIL versions and their properties.

Table 3-1: Overview of SAIL versions of canopy reflectance models (VERHOEF & BACH, 2007, modified).

Property / Model	SAIL	SAILH	GeoSAIL	SAIL++	4SAIL	4SAIL2
Year of development	1981	1989	1999	2000	2003	2003
Type	Turbid medium	Hybrid	Hybrid	Hybrid	Hybrid	Hybrid
Hot spot effect	No	Yes	Yes	Yes	Yes	Yes
Number of canopy layers	1	1	2	1	1	2
Singularity removal	No	No	No	Yes	Yes	Yes
Numerical precision	Single	Single	Single	Double	Double	Single
Speed optimization	No	No	No	Yes	Yes	Yes
Number of diffuse streams	2	2	2	72	2	2
Internal flux profiles supported	No	No	No	No	Yes	No
Thermal application supported	No	No	No	No	Yes	No
Non-Lambertian soil BRDF	No	No	No	No	No	Yes
Crown clumping effects	No	No	No	No	No	Yes

3.1.3 Coupling PROSPECT-5b and 4SAIL to PROSAIL

Running a leaf optical properties or canopy reflectance model in the forward mode leads to an output of radiation fluxes as a function of the individual parameters for each wavelength. The inversion of such models by contrast leads to the retrieval of biophysical parameters, which is mathematically non-trivial. GOEL (1988) stated that complex models require a large number of different parameters to be able to reproduce realistic outputs. With the number of parameters to be estimated, the demand for individual measurements increases as well. Because of the non-linearity of many processes, the number of measurements far exceeds the number of retrieved parameters. In this context JACQUEMOUD ET AL. (2009) defined the problem for the inversion of multi- and hyperspectral satellite data with SAIL, where the increase in wavelengths/bands leads to an under-determined system. Leaf reflectance and transmittance as well as soil reflectance thus form three wavelength-dependent input variables for SAIL. For parameter retrieval under a defined illumination and viewing geometry, at least three times as many variables as given wavelengths would be necessary, which makes an inversion impracticable, in the event of a lack of multiple recordings from different viewing angles. In order to address the inverse problem corresponding to the (multi-)dimensionality, and to determine the biochemistry within leaves, SAILH was coupled with PROSPECT resulting in a model called PROSAIL (BARET ET AL., 1992). In the forward mode, the output of the leaf reflectance and transmittance of PROSPECT serves as direct input to SAIL, which then calculates the total reflectance of the canopy. For the inversion, the process is reversed,

so that the output parameters of SAIL act as input to PROSPECT, which then calculates the missing biochemical parameters.

The PROSAIL version used in this study is freely available and was downloaded from *http://teledetection.ipgp.jussieu.fr/prosail/* on October 9th 2010 in the programming language IDL (Interactive Data Language). It couples PROSPECT-5b and 4SAIL. Some facts should be noted: the LIDF integrated in 4SAIL is ellipsoidal (CAMPBELL, 1986), thus the program expects only input in the form of an average leaf angle (ALA). In contrast to the further developed SLC model (VERHOEF & BACH, 2007), PROSAIL, as it is used in this study, is still based on a Lambertian soil background. Further, only the standard soil reflectance is used in this study, in order to make the application independent of in-situ information. The input parameters of the model applied in this study are shown in Table 3-2.

Table 3-2: Configurable input parameters of PROSAIL.

Model	Parameter	Symbol	Unit
PROSPECT-5b	Leaf chlorophyll content	LCC	[µg / cm²]
	Leaf carotenoid content	Car	[µg / cm²]
	Brown pigment content	Cbrown	[arbitrary units]
	Equivalent water thickness	Cw	[cm]
	Leaf mass per unit leaf area	Cm	[g / cm²]
	Structure Coefficient	N	-
4SAIL	Average leaf angle	ALA	[°]
	Leaf area index	LAI	[m² / m²]
	Hot spot	Hspot	-
	Soil coefficient	Psoil	-
	Solar zenith angle	Tts	[°]
	Observer Zenith Angle	Tto	[°]
	Relative Azimuth	Psi	[°]
	Ratio of diffuse to total incident radiation	skyl	-

3.2 Look-Up Table Inversion

Because of the benefits of the look-up table inversion explained in Chapter 1.6.3.3, this method was identified as fulfilling the requirements of the study. This section contains the definition of the LUT dimension as well as its input parameter setting, which is essential for a successful retrieval of biophysical parameters. Further, the manner in which the inversion was implemented, enabling several differences in illumination geometry to be taken into account,

is presented. Based on a range of criteria, which directly influence the quality of the inversion, a strategy is defined for a systematical examination of its potential for multiseasonal analyses.

3.2.1 Input-Parameter Setting

Before the LUT was generated by the model running in forward operation mode, its dimension had to be defined. This decision affected the number of parameters both in column and in row direction of the LUT. The number of columns is thereby defined by the number of simulated spectral bands and by the number of parameter specifications that lead to the generated reflectance values stored in the first, while the rows are defined by the number of spectra within the LUT.

In order to enable the highest possible flexibility in the determination of an optimal band combination for the inversion process, the LUT was designed to contain all the bands available in the AVIS-3 data, excluding only the bands affected by water vapor absorption in the range of 1300 – 1500 nm. Consequently, 167 bands ranging from 477 to 1299 nm and 1505 to 1704 nm were calculated by PROSAIL. The model wavelengths of the simulated bands correspond to the center wavelengths of the AVIS-3 data. In addition to the 167 reflectance values stored in column direction of the LUT and the corresponding input parameters by which the modeled reflectance spectrum is generated, the LUT also includes the modeled fraction of absorbed photosynthetically active radiation (fAPAR) and the fraction of vegetation cover (fCover). The fAPAR is useful for the quantification of the photosynthetic capacity of green vegetation, while fCover corresponds to the gap fraction of green vegetation in the nadir viewing direction and is therefore useful for decoupling vegetation and soil in energy balance processes (BACOUR ET AL., 2006). In summary, the LUT consists of 179 columns containing the essential reflectance information (n = 167), the input parameter setting (n = 10) and the simulated parameters (n = 2).

Subsequently, the size of the LUT in row direction was specified, defining the number of reflectance spectra available for the comparative analysis with measured reflectance signals. If the size is too small, the estimation accuracy may suffer. By contrast, a too large number of modeled spectra would lead to an increase in computation time, without adding value in terms of accuracy after a certain accuracy level has been reached. WEISS ET AL. (2000) investigated the effect of the LUT size on the accuracy of canopy variables. They tested several LUTs ranging from 25 000 to 280 000 in row size and found that an LUT based on 100 000 modeled spectra provides an optimal compromise between model accuracy and required computer-resources. Based on this finding, in the present study the input parameters to the model were randomly combined in 100 000 instances, each following a distribution within a specific range. Instead of using a uniform distribution, the input parameters were defined to follow a Gaussian distribution according to their most probable incidence. This procedure has

the advantage that the most likely variable values can be distinguished in finer steps, which increases model accuracy. However, the accuracy for less likely variable values may suffer from less frequent cases. The Gaussian distribution was chosen over other distribution functions, since the aim of this study is to estimate parameters within a growing period. It is thus not expected that the variables under examination, e.g., LAI, show very rapid increases, or even extreme values, but rather that they develop gradually. Table 3-3 shows the range and distribution of each PROSAIL input parameter as defined in this study. The individual settings are based on experiences and empirical values from several studies (BACOUR ET AL., 2006; BARET ET AL., 2007; VERGER ET AL., 2011) which were subject to minor adjustments to incorporate site-specific characteristics of this study. It should be noted that during this step, parameters describing the illumination geometry were fixed and are therefore identical in each of the 100 000 combinations. Furthermore, the ratio of diffuse to total incident radiation was due to its negligible effect constantly set to 10%.

Table 3-3: Distribution of PROSAIL input parameters for the generation of the LUT.

Model	Parameter	Minimum Border	Maximum Border	Mean	Standard Deviation
PROSPECT-5b	LCC [µg / cm²]	0	90	50	40
	Car [µg / cm²]	0	20	10	7
	Cbrown [arbitrary units]	0.0	1.5	0.2	0.8
	Cw [cm]	0.00	0.05	0.02	0.025
	Cm [g / cm²]	0.00	0.02	0.01	0.01
	N	1.0	2.5	1.5	1.0
4SAIL	ALA [°]	30	80	60	20
	LAI [m² / m²]	0	7	3.5	2.5
	Hspot	0.0	1.0	0.45	0.6
	Psoil	0.0	1.0	0.5	0.5

Figure 3-3 displays the frequency distribution of the different input parameters. While defining the individual settings, care was taken to adequately represent even the less probable extreme values, so that all values could be estimated to a satisfactory degree.

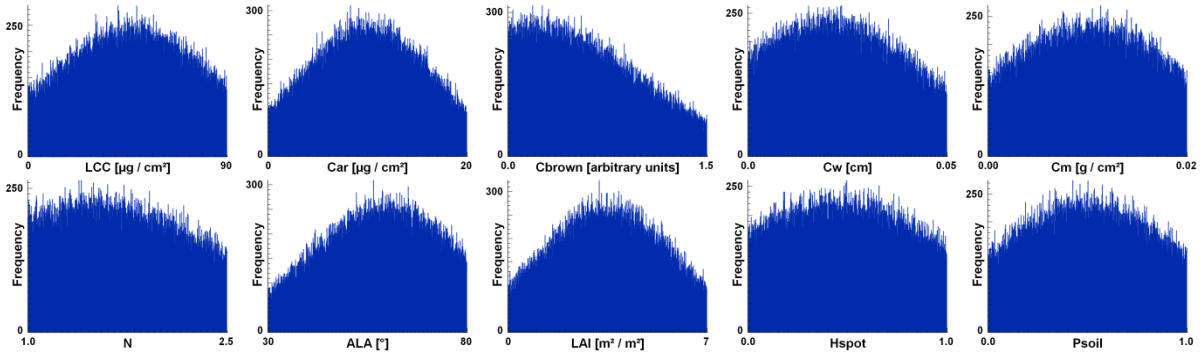

Figure 3-3: Histograms (500 bins) of PROSAIL input parameters.

Figure 3-4 (leaf level) and Figure 3-5 (canopy level) illustrate the effects of varying parameter settings on the simulated reflectance and absorption processes within the spectral range of AVIS-3, by successively altering only one input parameter within its defined range, while keeping the others at a fixed value. However, this behavior may be unrealistic under natural conditions, because biophysical vegetation variables usually co-vary (JACQUEMOUD ET AL., 2009).

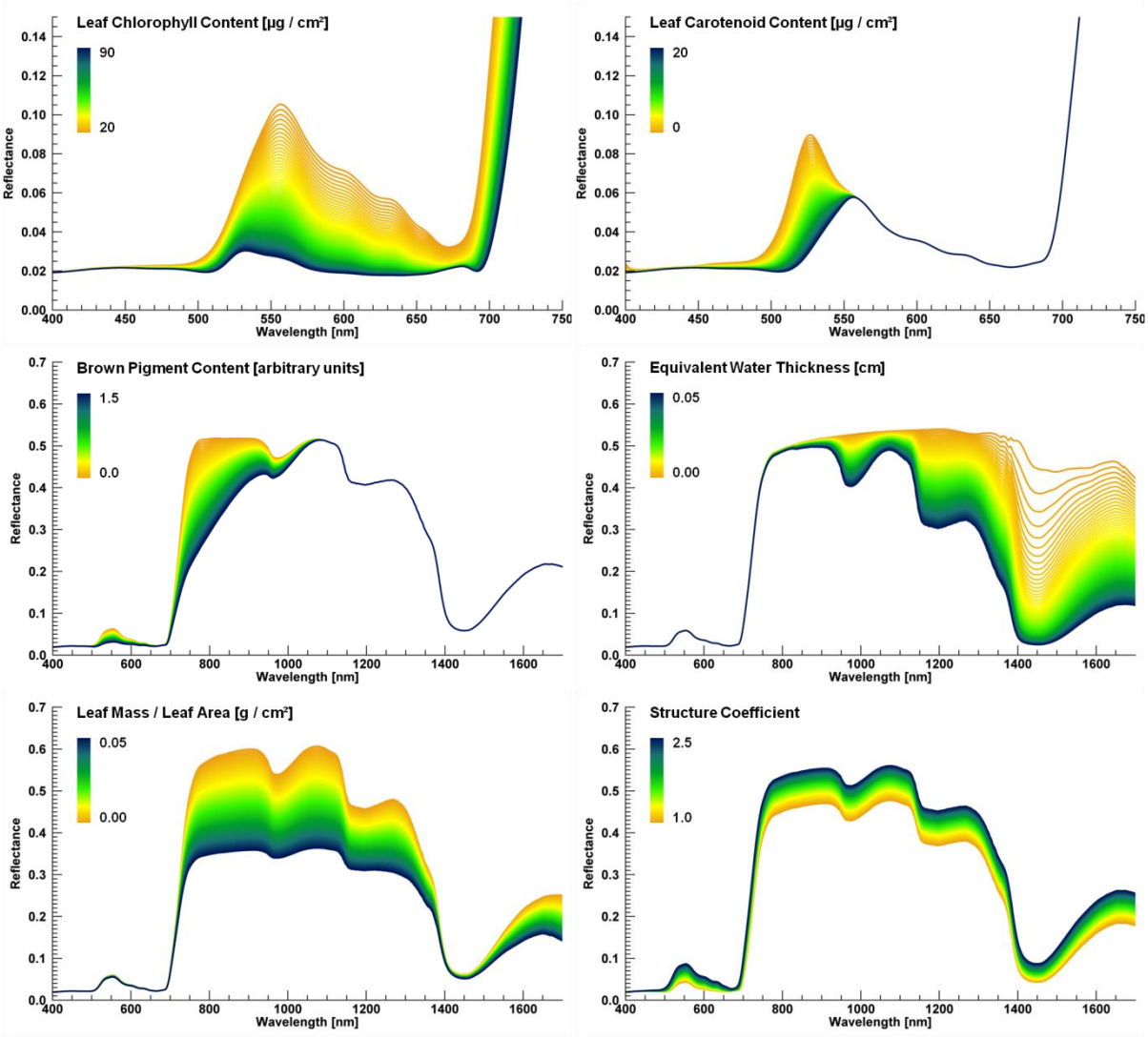

Figure 3-4: Impact of leaf input parameters on the reflectance simulated by PROSAIL, varying within their defined range. The respective uninvolved parameters are defined by their mean value.

The figures clearly demonstrate that the alteration of some of the leaf parameters affects only limited parts of the spectrum, such as the pigments which particularly influence in the VNIR or water thickness in the SWIR, while others, e.g., leaf mass and the structure coefficient, involve a change over the whole spectral domain. Above all, the magnitude of the influence that different parameter settings can induce, as caused by, for example, varying leaf mass values, emphasizes the difficulty in accurately estimating the parameters focused on in this study.

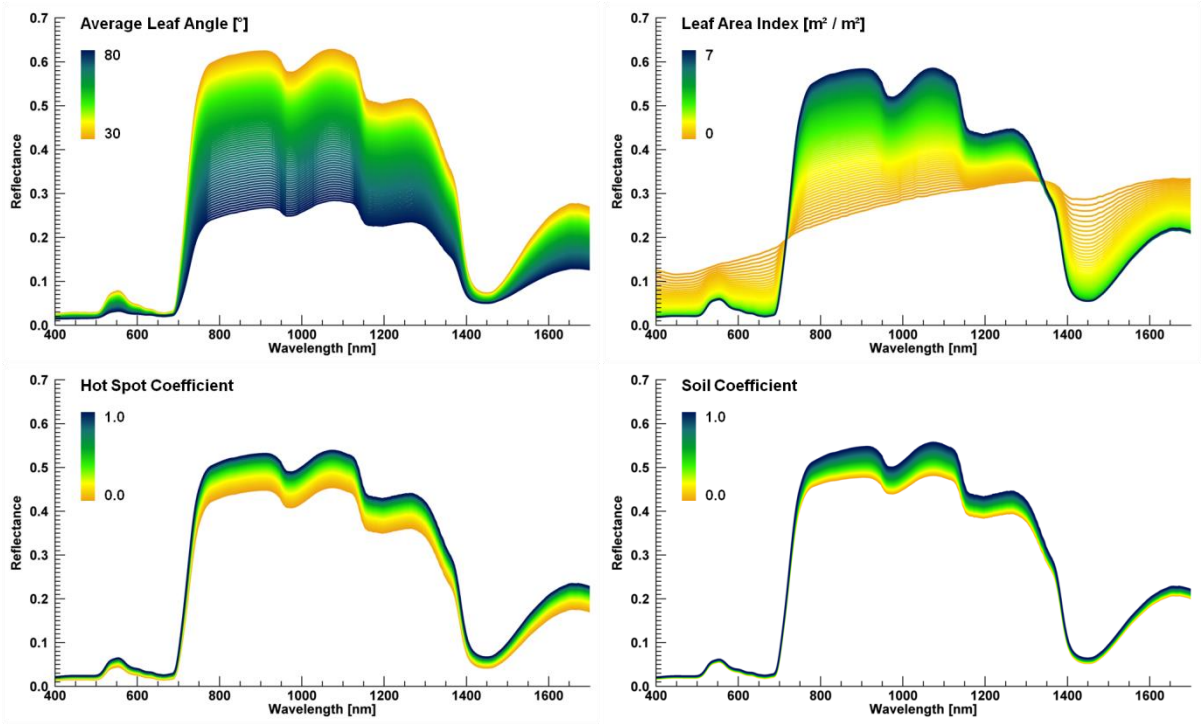

Figure 3-5: Impact of canopy input parameters on the reflectance simulated by PROSAIL, varying within their defined range. The respective uninvolved parameters are based on their mean value.

All of the canopy parameters affect the reflectance over the whole spectral domain. However, it is striking that LAI and especially average leaf angle cause a far more obvious change when varied. By contrast, varying hot spot and soil coefficients exert comparatively low influence on the reflectance spectrum. In the case of the soil coefficient this behavior is not surprising, since the reflectance represents a standard canopy, not allowing soil to have a greater influence.

As mentioned above, the parameters describing illumination geometry, i.e., solar zenith angle, observer zenith and azimuth angle, are fixed for the generation of the 100 000 spectra. Nevertheless, due to varying viewing angles in the 2012 images, caused by the broad FOV of the sensor, and different solar zenith angles during the six flights, the anticipated BRDF effects must be taken into account. This is necessary because different angle settings also affect the reflectance in a non-negligible fashion. Figure 3-6 shows the significant changes in reflectance induced by varying observer zenith and azimuth angles.

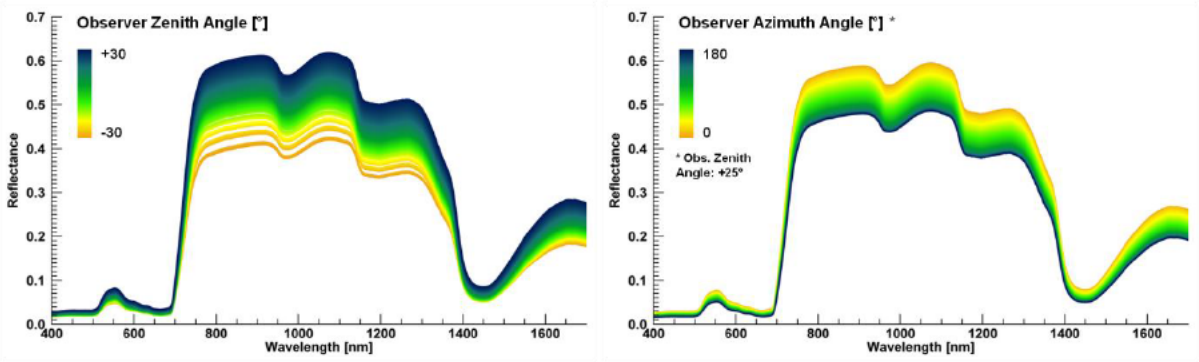

Figure 3-6: Impact of varying observer zenith and azimuth angles on the reflectance simulated by PROSAIL. The fixed leaf and canopy input parameters are based on their mean value. It is noted that for azimuth variation the zenith angle was set to +25°, since a varying azimuth angle does not have any influence when the observer is nadir-looking.

To solve this problem, the LUT was generated repeatedly for several classes of observer zenith and azimuth angles. The step size of zenith angles was set to 5°, covering a range from -25° to +25°. The required range was determined by the highest and lowest observer zenith angles in all available images of the 2012 campaign. For the relative azimuth angle, a step size of 10° in a range from 0° to 180° was chosen in order to cover all potential observer angles occurring in the image data. In order to take the solar zenith angles of the several flights into account, the steps of calculating the LUT for each possible observer angle class combination were repeated once more, this time considering the respective solar zenith angle of each of the six flights. However, four iterations were sufficient, because for the first and fifth as well as for the second and sixth flights the solar zenith angles were almost identical (see Table 2-1 on page 25). Table 3-4 lists the different classes, taking into account the illumination geometry.

Table 3-4: Overview of the different classes for the LUT generation describing the illumination geometry.

Characteristics	Observer Zenith Angle Classes		Relative Azimuth Angle Classes		Solar Zenith Angle Classes	
Number of classes	11		19		4	
Input	Min	-25°	Min	0°	Class 1	28° (Flight 4)
	Max	+25°	Max	180°	Class 2	38° (Flight 3)
	Step Range	5°	Step Range	10°	Class 3	42° (Flights 1 and 5)
					Class 4	45° (Flights 2 and 6)

As a consequence, the dimension of the generated LUT library is defined by the product of the biophysical input parameters (n = 100 000), the observer zenith angle classes (n = 11), the observer azimuth classes (n = 19) and the solar zenith angle classes (n = 4), resulting in a total of 83 600 000 reflectance spectra including their corresponding parameter specifications.

3.2.2 Inversion Sequence

For the LUT inversion an algorithm was constructed that explicitly takes illumination geometry into account. Furthermore, the aim was to allow several selection criteria settings, which are explained in the following chapter. The main features of the algorithm performing the inversion sequence is described in the following.

When applying the inversion sequence to an image, the algorithm starts with the identification of the respective solar zenith angle. This information, including the input of the corresponding solar azimuth angle for the time of the flyover, is entered manually by the user and reduces the amount of potential spectra within the LUT from over 83 million to 20 900 000. Following this step, the algorithm was designed to continue independently. The program identifies the first pixel and extracts the observer angle information which is stored in the additional bands 198 (zenith) and 199 (azimuth) of the AVIS-3 data. The relative azimuth is calculated based on the latter and on the manually supplied solar azimuth angle. According to the now specified angle information, the corresponding table, equaling the size of the initial LUT of 100 000 spectra, is loaded from the LUT library. In a next step, the information stored in the LUT is split up into the simulated reflectance data and the corresponding metadata (input and simulated parameters). The measured reflectance signal is then multiplied 100 000 times and individually compared to the simulated data. Based on a cost function, a curve fitting is subsequently performed, whereby best match(es) are identified. When completed, the algorithm collects the corresponding metadata of the best fit(s) and stores it with the equivalent pixel of the output image, then continues with the second pixel. Since the loading of the LUT from the library is one of the most time-consuming steps during computation, the algorithm checks if the observer angle setting of the current pixel requires the same LUT information as the previous pixel. If so, the table which was loaded for the former pixel is used again.

The result is a comprehensive multiband output image including information on all biochemical and biophysical input parameters as well as on simulated fAPAR and fCover. Furthermore, since chlorophyll and water content values are often not very meaningful on a leaf level, the corresponding canopy products, i.e., canopy chlorophyll content (CCC) and canopy water content (CWC) which are calculated by multiplying the above parameters with LAI, are stored to the output image as well. The background to this step is discussed in the validation section of the retrieved chlorophyll content in Chapter 3.3.3.2.

The success of the parameter retrieval depends on certain important selection criteria at various steps within the inversion sequence. The most critical are the precise choice of the data ranges that are compared, the cost function applied in the curve fitting process, and the management of the result of the curve fitting. These criteria are discussed in the following chapter.

3.2.3 Selection Criteria

3.2.3.1 Band Selection

The first criterion is the selection of bands to be used for the comparison of the measured and simulated reflectance. Since the quality of reflectance data might differ among the available bands due to noise, and some spectral ranges simulated by PROSAIL might be modeled poorly, they must be selected wisely to avoid potentially corrupt results. Many studies (e.g., MERONI ET AL., 2004; LAVERGNE ET AL., 2007; SCHLERF & ATZBERGER, 2006;) found that an appropriate band selection, or alternatively, a specific weighting of different spectral bands, leads to an improvement in the inversion quality and prevents biases in the parameter estimation. Making an informed selection is, however, not trivial. A strategy to consider is the one proposed by DARVISHZADEH ET AL. (2011) who suggested discarding those wavelengths that are not well simulated by PROSAIL using an iterative approach, starting with the elimination of the worst modeled spectral band among all sample plots. The LUT inversion is repeated until all bands show acceptable accuracies within a user-specified threshold.

In view of the capacity of EnMAP, a different approach was applied in this study. Since EnMAP will provide contiguous data, it was assumed that the curve fitting will lead to increasingly precise results, the higher the number of spectral bands included. Figure 3-7 gives a sense of a continuous reflectance spectrum compared to the multispectral coverage given by the future Sentinel-2 satellite. It is obvious that the contiguous spectrum contains much more information, e.g., on specific absorption ranges, than the multispectral dataset.

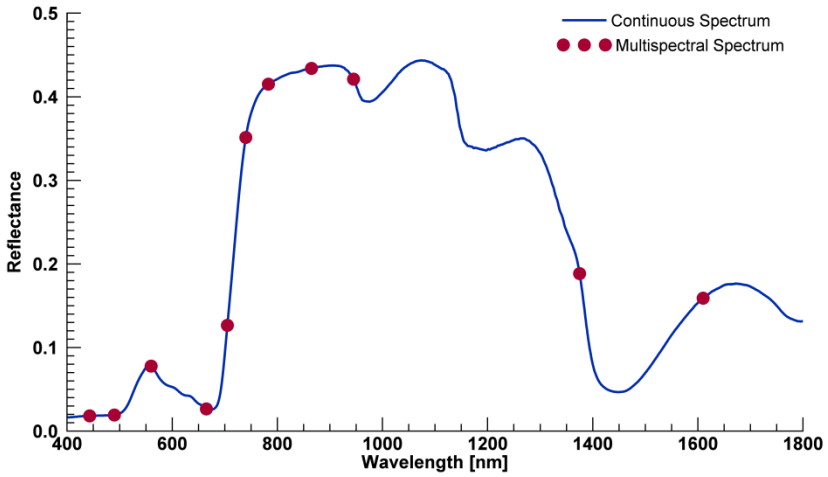

Figure 3-7: Comparison of a contiguous (hyperspectral) with a multispectral reflectance within the spectral range of AVIS-3, simulated with PROSAIL. The multispectral reflectance points refers to the center wavelengths of Sentinel-2.

Although the use of all available bands may provide redundant information when trying to retrieve individual parameters, e.g., LAI, this method has the advantage that some surface

parameters, affecting reflectance in different, in some cases very small wavelength ranges, can be derived by a uniform method. In the case of the AVIS-3 data, it was however found that not all of the initial 197 bands can be used successfully in the inversion, for two main reasons: first, bands covering the water vapor absorption ranges from 1120-1160 and 1300-1500 nm hold no relevant information, since these ranges were so strongly affected by errors that the measured values were replaced with values stemming from a linear interpolation between the bordering values, unaffected by water vapor, in order to retrieve a smooth spectrum (see Chapter 2.2.2.3.1). The first water vapor absorption range was consequently excluded from the LUT, while the second range had never been included due to the very large deviation of the measured reflectance from the reflectance received after preprocessing (compare Figure 2-31). Second, bands with a reduced sensitivity, located at the marginal areas of the CCD devices, were equally excluded in order to ensure the use of high-quality bands only. Thus, bands below 477 and above 1704 nm were removed. This resulted in 146 bands that were, in the end, used in the inversion process.

To examine the value added by the use of (contiguous) hyperspectral data, two additional, merely multispectral, band combinations were tested. The first one corresponds to the center wavelengths of the upcoming Sentinel-2 instrument (INT 2), given by nine bands within the spectral range of AVIS-3. The second band combination refers to the Landsat-TM specification, which encompasses distinctly broader wavelength ranges within its bands. In contrast to the simulated Sentinel-2 combination, the spectral bands in AVIS-3 corresponding to these wavelength ranges were consequently averaged according to the spectral responsivity functions of Landsat TM, resulting in four simulated Landsat bands within the spectral range of AVIS-3.

Furthermore, since the AVIS-3 data has spatial data gaps in the SWIR sensor coverage, a setting containing only the 88 bands of the VNIR range (477 – 988 nm) was tested as well. Table 3-5 gives an overview of all four examined band settings.

Table 3-5: Selection of band settings, which were considered by the LUT inversion.

Band setting	VNIR	SWIR	Number of bands
Full-range	477 – 1094 nm (contiguous)	1173 – 1299 nm (contiguous) 1571 – 1704 nm (contiguous)	146
VNIR	477 – 988 nm (contiguous)	-	88
Sentinel-2	490 nm 740 nm 560 nm 783 nm 665 nm 865 nm 705 nm 945 nm	1607 nm	9
Landsat-TM	506 – 628 nm (averaged) 634 – 686 nm (averaged) 779 – 895 nm (averaged)	1564 – 1704 nm (averaged)	4

3.2.3.2 Artificial Noise

A fundamental difference between simulated and measured reflectance gathered using AVIS-3 and HySpex is the fact that the latter is affected by uncertainties originating from the measurement inaccuracies and the preprocessing steps of sensor calibration, geometric correction and radiometric calibration. These uncertainties differ in type; geometric correction often leads to additive uncertainties in the signal, whereas radiometric calibration predominantly introduces multiplicative uncertainties. Sensor calibration and atmospheric correction induce both types. However, the model might produce uncertainties as well, which are associated with its complex architecture for the calculation of canopy reflectance (VERGER ET AL., 2011).

To take these uncertainties into account, artificial noise is often added to the simulated reflectance data, providing more flexibility in finding the optimal solution and allowing the incorporation of inadequacies between simulated and measured data. The type and amount of noise introduced differs in studies found in the literature. BACOUR ET AL. (2006), e.g., added a 4% white Gaussian noise with no bias to the data. White Gaussian noise thereby is a mathematical model for the description of random variation phenomena implying that the statistical noise is randomly distributed according to the probability density function of a Gaussian distribution. BARET ET AL. (2007), by contrast, added a white Gaussian noise to the reflectance values, which has an absolute value of 0.04. A combination of both with an additive level of 0.01 and a multiplicative level of 4% was used by VERGER ET AL. (2011). In a study by VERRELST ET AL. (2014), a systematic approach was pursued which examined the effect of adding 0% to 30% Gaussian noise to the data in 1% steps. A modified approach was investigated by RIVERA ET AL. (2013) in which the influence of a multiplicative noise ranging from 0% to 50%, in 2% steps was tested.

Similar to the latter two studies, an approach combining different noise types was adopted to identify the noise level leading to the best possible results in this study. In this approach, both additive and multiplicative Gaussian noise as well as a combination of both was used. Of decisive importance for the amount of noise is the variance (σ^2) in the Gaussian distribution, which corresponds to a percentage of the reflectance. In case of additive noise, the variance refers to a theoretical reflectance value of 1. This means that a variance of 0.04 (4%), for example, is applied to all bands, independent of the wavelength. In the case of multiplicative noise, the variance value is wavelength-dependent and refers to the respective reflectance value. For example, for a single band with a reflectance value of 0.5, a variance value of 0.04 leads to an actual variance of 0.02 (2%).

Since the impact of multiplicative noise on the reflectance depends on the individual value of each band, high reflectance values, for example those occurring in the red edge, obtain higher noise values than low reflectances. However, low reflectance values are typically more prone to noise due to a lower light intensity reaching the sensor, which results in a low SNR for the affected band. Therefore, an inverse form of multiplicative noise, having a stronger impact on low reflectance values than on high values, was tested as well. This is achieved by simply subtracting the simulated reflectance value at the given wavelengths, which can range from 0 to 1, from the highest possible reflectance value of 1. The impact of this approach is shown in Figure 3-8, in which two different levels (1% and 5%) of the inverse multiplicative Gaussian noise are presented. As clearly visible in the figure, the amplitude of the noise is decisively higher in low reflectance ranges than in high reflectance ranges.

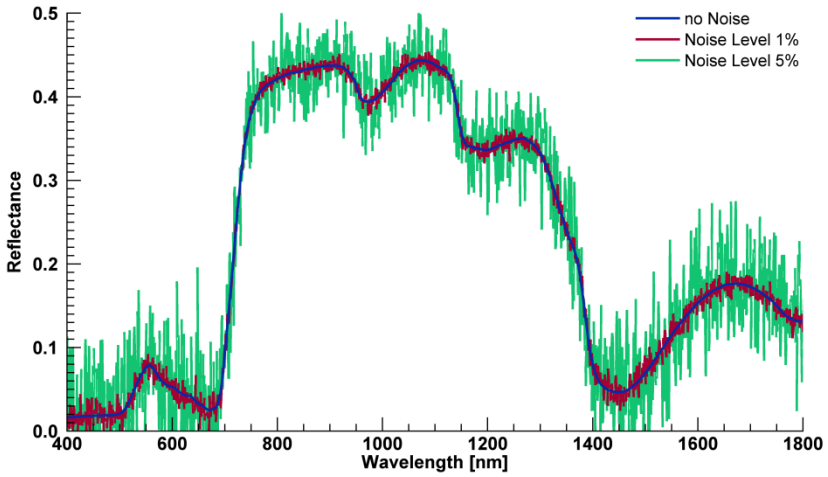

Figure 3-8: Impact of different noise levels (inverse-multiplicative) compared on an un-noised reflectance in a 1 nm resolution, simulated with PROSAIL. The noise levels are defined as an amount of the variance of a Gaussian distribution that corresponds to a defined percentage of reflectance.

A total of five types of noise were defined for this study and tested concerning their performance. They are described by:

1) Additive noise

$$R_{ns}(\lambda) = R_{sim}(\lambda) + \chi(0, \sigma(\lambda)) \quad \textit{(Equation 3-1)}$$

2) Multiplicative noise

$$R_{ns}(\lambda) = R_{sim}(\lambda) * [1 + \chi(0, \sigma(\lambda))] \quad \textit{(Equation 3-2)}$$

3) Inverse-multiplicative noise

$$R_{ns}(\lambda) = 1 - \{[1 - R_{sim}(\lambda)] * [1 + \chi(0, \sigma(\lambda))]\} \quad \textit{(Equation 3-3)}$$

4) Combined noise

$$R_{ns}(\lambda) = R_{sim}(\lambda) * \left[1 + \chi\left(0,2\sigma(\lambda)\right)\right] + \chi(0, \sigma(\lambda)) \quad \textit{(Equation 3-4)}$$

5) Inverse-combined noise

$$R_{ns}(\lambda) = 1 - \{[1 - R_{sim}(\lambda)] * [1 + \chi(0,2\sigma(\lambda))]\} + \chi(0, \sigma(\lambda)) \quad \textit{(Equation 3-5)}$$

where

$R_{ns}(\lambda)$	simulated reflectance value for band λ with noise
$R_{sim}(\lambda)$	simulated reflectance value for band λ
$\chi(0,\sigma)$	Gaussian distribution (mean value 0 and variance σ^2)
$\sigma(\lambda)$	uncertainties within the Gaussian distribution for band λ

In order to account for the fact that a given variance value has a less pronounced effect when applied as multiplicative noise, it is double-weighted compared to the additive noise factor in the combined methods.

3.2.3.3 Cost Function

The cost function measures the discrepancies between observed and simulated reflectance values (JACQUEMOUD ET AL., 2009) and therefore serves for the purpose of identifying the combination by which the error between the simulated data provided by the LUT and the measured reflectance is minimized. One of the most common measure in this context is the root mean square error (RMSE), which has been applied in several studies (e.g., COMBAL ET AL., 2002; BACOUR ET AL., 2006; RICHTER ET AL., 2009). For this reason, it was chosen as one

of the cost functions applied in this study and is also used for validation purposes. It is described in detail in Chapter 3.3.2.

Recently, several studies have investigated the potential of alternative cost functions for the retrieval of best fits between measured and simulated data (e.g., LEONENKO ET AL., 2013; RIVERA ET AL., 2013; VERRELST ET AL., 2014). In this context, LEONENKO ET AL. (2013) classified the statistical measures under examination as information measures of divergence, M-estimates, and minimum contrast methods. The first class of information measures tries to minimize the distance between two probability functions. The second class of M-estimates (*M* stands for *maximum likelihood-type*) is described through a nonlinear regression function seeking to find a relationship between independent and dependent variables (RIVERA ET AL., 2013). The last class of minimum contrast methods assumes spectral domain and reflectance as a spectral density function of stochastic processes (LEONENKO ET AL., 2013; RIVERA ET AL., 2013). However, many of the cost functions within the three groups are highly complex and, in some cases, require expert knowledge in order to ensure for the accurate specification of some of the parameters.

Therefore, only M-estimates were focused upon, as they exhibit certain robust properties and offer comprehendible regression functions. The widely used least-square estimators (L_2-estimators) produce good results when the underlying assumptions, such as noise is Gaussian, are true (RIVERA ET AL., 2013). In addition to the RMSE, which belongs to this group, two further L_2-estimators, i.e., Nash-Sutcliffe Efficiency (NSE) and Geman & McClure Estimator, and a L_1-estimator (absolute value), which is represented by the Laplace Distribution, were tested.

The Nash-Sutcliffe Efficiency (NSE) is a measure of the mean square error to the observed variance, and is sensitive to large errors (WAINWRIGHT & MULLIGAN, 2005). In this study, the NSE is not only used as a cost function, it also supports model validation and is for this reason further described in Chapter 3.3.2. Among all cost functions, the very general Laplace Distribution represents the simplest one. The L_1-estimator calculates the distance, or in other words the area, between two spectra. As a result of its design, outlier values, which in general produce the largest errors, exert a less pronounced influence on the overall result when compared to the NSE. This advantage is also the case for the Geman & McClure Estimator. However, this last measure cannot guarantee the identification of a unique best fit (RIVERA ET AL., 2013), which is a general requirement of a robust M-estimator. The cost functions are described by:

1) Root Mean Square Error (RMSE)

$$RMSE = \sqrt{\frac{1}{n}\sum_{\lambda=1}^{n}(R_{sim}(\lambda) - R_{msd}(\lambda))^2} \qquad \textit{(Equation 3-6)}$$

2) Nash-Sutcliffe Efficiency (NSE)

$$NSE = 1 - \frac{\sum_{\lambda=1}^{n}(R_{msd}(\lambda) - R_{sim}(\lambda))^2}{\sum_{\lambda=1}^{n}(R_{msd}(\lambda) - \overline{R}_{msd})^2} \qquad \textit{(Equation 3-7)}$$

3) Geman & McClure Estimator (GM)

$$GM = \sum_{\lambda=1}^{n}\frac{(R_{msd}(\lambda) - R_{sim}(\lambda))^2}{(1 + (R_{msd}(\lambda) - R_{sim}(\lambda))^2)} \qquad \textit{(Equation 3-8)}$$

4) Laplace Distribution (LP)

$$LP = \sum_{\lambda=1}^{n}|R_{msd}(\lambda) - R_{sim}(\lambda)| \qquad \textit{(Equation 3-9)}$$

where

$R_{msd}(\lambda)$ measured reflectance at band λ

$R_{sim}(\lambda)$ simulated reflectance at band λ

3.2.3.4 Ill-Posed Problem & Averaging Method

COMBAL ET AL. (2002) declared that for an exact solution of the model inversion, the inversion problem must be well-posed. In the sense defined by Jacques Hadamard, a physically based model problem is well-posed if (i) a solution exists, (ii) the solution is unique, and (iii) the solution depends continuously on the data (GARABEDIAN, 1964). If one of these conditions is not met, the problem is ill-posed. The ill-posed nature of radiative transfer models is caused by the fact that different parameter settings can produce equal spectra. Consequently, the inversion of these models holds the risk that the resulting parameter specification does not match the parameters that in fact lead to this reflectance in reality, although this specification might have produced a reflectance spectrum which corresponds very well to the measured one. Figure 3-9 displays an example of an ill-posed problem,

showing two spectra simulated with PROSAIL. Although the input parameters of both settings differ greatly, especially concerning the LAI, the resulting spectra are almost equal.

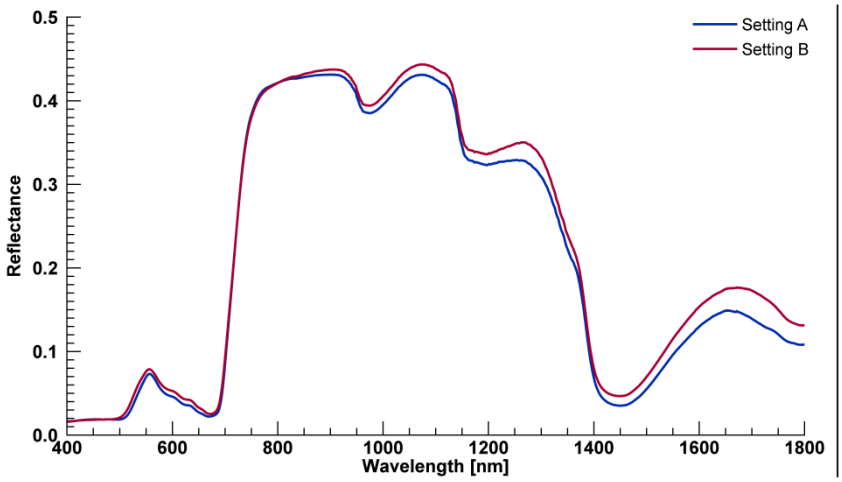

SETTING	A	B
Chlorophyll	21.1	29.9
Carotenoid	10.9	13.3
Brown Pigment	0.058	0.115
EWT	0.020	0.029
Leaf Mass	0.009	0.004
Structure	1.03	2.20
Leaf Angle	66.3	57.7
LAI	6.8	2.9
Hot Spot	0.67	0.02
Solar Zenith Angle	35.0	35.0
Obs. Zenith Angle	15.0	15.0
Obs. Azimuth Angle	42.0	42.0
Soil	0.687	0.345

Figure 3-9: Ill-posed problem, displayed with two PROSAIL-generated spectral reflectances (left), which are based on highly different input parameter settings (right).

Further reasons for the ill-posed problem are uncertainties of the model and of the reflectance data they are compared to. While physically based models may be quite sophisticated, all models remain a mathematical abstraction and thus a simplification of reality. For CRMs that means that complex reflectance and scattering behavior at leaf level cannot be considered by the model in its entirety (yet). Calibration errors and sensor noise in the reflectance data can lead to additional uncertainties (ATZBERGER, 2004).

As a consequence, the best fit of the model inversion might not lead to a correct parameter specification (e.g., VUOLO ET AL., 2010). In contrast to a well-posed problem, a major consequence of model and reflectance uncertainties in ill-posed problems is that these lead not just to uncertainties regarding the solution, but even more likely to outright errors. This is due to the fact that the solution space is very widespread and not centered around one true solution (ATZBERGER, 2004).

Regularization strategies must be formulated in order to solve the ill-posed problem. COMBAL ET AL. (2002) used a priori information which can be separated into three categories. The first category is the knowledge of in-situ data or products provided by another sensor. The second category is the knowledge of the type of canopy architecture that defines the class of the CRM. The third category stands for the knowledge of the typical distribution of canopy biophysical variables which are used as a parameter setting for the CRM. This information can be crop-specific and/or include the phenological status. The application of a priori information to the model inversion was realized in two steps. First, only the pure reflectance data was considered. In a second step, all parameter configurations resulting in an error lower than in-situ measurement uncertainty were extracted. In doing so, only the reduced LUT was applied to the data, hence only the best fit between the measured data and the reduced LUT

was considered to be the best estimate. In this way, the widespread solution space was distinctly minimized. Other a priori information can be given by using growth models, whereby vegetation growth is described by a specific curve, which also reduces possible solutions (JONES & VAUGHAN, 2010).

By contrast, ATZBERGER (2004) investigated an object-based approach taking not only the spectral signature of the pixel of interest into account, but also its neighboring pixels. Using image segmentation, classifications or digitized field boundaries, pixels can be grouped to represent distinct objects. This could improve the accuracy of inversion.

Many studies (e.g., RIVERA ET AL., 2013; DARVISHZADEH ET AL., 2008; COMBAL ET AL., 2002) have shown that the single best fit calculated by the cost function does not necessarily lead to the best accuracy. This can be addressed by taking a certain number of best fits between measured and modeled reflectance signatures into account, rather than just one single best fit. A threshold is defined based on the best fit determined by the cost function. Within the resulting range, each given input parameter is averaged. To define the threshold, RICHTER ET AL. (2009) used the root mean squared error (RMSE) as cost function and considered all combinations lying within the range of less than 10% of the lowest RMSE value.

Alternatively, a predefined number of best fits can be used instead of a percentage weighting, which was applied in this study, testing various different amounts. The consideration of a certain amount of best fits potentially mitigates the influence of wrong parameter configurations. In addition, the effect of averaging the corresponding input parameters of the resulting spectra selected from the LUT by both mean and median were examined. This was also investigated by DARVISHZADEH ET AL. (2011), who tested the influence of the above mentioned averaging methods on the best 10 and 100 simulations, respectively.

3.2.4 Analysis Strategy

In view of the multiple options and potential combinations of selection criteria, a strategy had to be defined for a systematical examination of the best fit(s). The in-situ measurements of LAI and chlorophyll content served here as reference, enabling validation by comparing the field measurements to the retrieved information of the corresponding pixels. In order to incorporate as many of the above listed selection criteria as possible, an inversion loop was implemented, which is described in the following sections.

The hyperspectral band setting containing 146 AVIS-3 bands served as a basis for the inversion loop. In a first step, the artificial noise was added to the LUT reflectances for all five types defined in Chapter 3.2.3.2. To find the ideal amount of noise for each type, the variance of the Gaussian distribution describing the noise was set to 21 different values, beginning with 0 %, which means that no noise was added, up to a maximum of 5, 10 or 20 %, depending on the noise type. Various ranges were chosen to take into account the different

weighting the variance has in each noise type. In the next step, all four cost functions (Chapter3.2.3.3) searched for the best fit between the measured and the (noisy) simulated data. To find the best solution for the ill-posed problem, a total of 21 solutions incorporating multiple solutions (best fits) were defined and averaged. The first solution represents only the overall best fit, the second solution represents the average of the best 50 fits. This is continued, with step sizes of 50 additional spectra per solution, until the last step, the 21st solution, is reached, incorporating 1 000 spectra, i.e., 1% of the complete LUT. When averaged, both mean and median were used.

Since every possible criteria combination within the defined range was calculated, the total number of single inversions is the product of different noise types (n = 5), various noise amounts (n = 21), different cost functions (n = 4), number of best fits (n = 21) and the two separate averaging methods (n = 2). Consequently, a total of 17 640 singular inversions were conducted, which were executed by means of an inversion loop. The algorithm performing the loop was configured to store the parameters of interest, i.e., LAI, leaf chlorophyll content and canopy chlorophyll content, of every possible combination in a file in order to enable the later evaluation. Given the high number of 17 640 inversion processes, this method could not be applied to the whole dataset of six images, each containing more than 750 000 pixels, because it would have been beyond the scope of what is technically feasible with the available computing capacity in this study. Therefore, based on all six images, a new image was constructed containing only those pixels, for which in-situ data was available. The requirements of the in-situ data serving for validation are further discussed in Chapter 3.3.1. The newly constructed dataset included both the reflectance information as well as the two bands with the corresponding observer zenith and azimuth angles. The algorithm performing the inversion loop was applied to this dataset, automatically considering the specific solar zenith angle of each pixel. This ensured the respective illumination setting to be considered and thereby the correct choice of the corresponding LUT.

Moreover, the method was applied, in a modified form, to the three other band settings (VNIR, Sentinel-2, Landsat TM) based on the noise type that was identified to be the most successful for the full-range hyperspectral setting (see Chapter 3.3.3.1).

Table 3-6 gives an overview of the entire setup of selection criteria for the inversion loop.

Table 3-6: Selection criteria setting for the inversion loop. It is noted that all five noise types were applied only to the hyperspectral full-range (146 bands) setting. For the settings of hyperspectral VNIR, Sentinel-2 and Landsat-TM, only one noise type was added to the LUT data.

Criterion	Specification						Quantity of Settings
Band selection	• Hyperspectral full-range (146 bands) • Hyperspectral VNIR (88 bands) • Sentinel-2 (9 bands) • Landsat-TM (4 bands)						4
Noise type	• Additive noise (AN) • Multiplicative noise (MN) • Inverse-multiplicative noise (IMN) • Combined noise (CN) • Inverse-combined noise (ICN)						5
Noise variance	*Noise type*	*AN*	*MN*	*IMN*	*CN*	*ICN*	21, per noise type
	Min	0 %	0 %	0 %	0 %	0 %	
	Max	10 %	20 %	20 %	5 %	5 %	
	Step range	0.5 %	1.0 %	1.0 %	0.25 %	0.25 %	
Cost function	• RMSE • NSE • Laplace • Geman % McClure						4
Number of solutions (best fits)	*Min* 1 *Max* 1000 *Step range* 50						21
Averaging method	• Mean • Median						2

3.3 Model Evaluation

3.3.1 Preparation of In-Situ Data

As described in Chapter 2.1.3.2, a total of 565 in-situ measurements were gathered during the field campaign in order to support the validation of the model results. However, the measurements had to be critically rated before their use. In addition to the removal of systematic errors, it had to be considered that the whole dataset is influenced by uncertainties originating from several sources.

The validation is based on the assumption that the collected parameter values represent the state of the canopy of the corresponding pixels in the 4 m spatial resolution of the airborne data. However, they are merely point measurements, leading to a potential source of

uncertainty. The more heterogeneous the canopy, the less probable is the accurate representation of the measurements in regard to the 4 m scale of the image data. This problem often occurs where crops grow in row structures and thus a large amount of soil visible. Further, it has been shown that the in-situ data is error-prone itself due to measurement inaccuracies, resulting from a different usage of the field instruments by various users. Unstable weather conditions, e.g., caused by a brief presence of fair-weather clouds during the measurement process, can also distort the data quality.

Other inaccuracies originate from a wrong localization of both the ESUs and the airborne data. The geocoding of the ESUs was conducted using handheld GPS devices (Garmin GPSmap 60). Although these devices have a high positioning accuracy in the open field and benefit from the almost ideal weather conditions during the data acquisitions, an inaccuracy of a few meters cannot be ruled out. Further, the accurate geometrical correction of the airborne data depended, on the one hand, on the quality of the navigation data provided by the inertial measurement unit, leading to faulty results when strong flight movements occurred and caused distorted pixel areas (see Chapter 2.2.4). On the other hand, the process of ortho-rectification is also somewhat error-prone and may have had led to an unprecise localization of the corresponding pixels in the image.

However, as described in Chapter 2.1.3.2, several sampling strategies aimed at addressing, and ruling out these uncertainties. It was still necessary to clear the data from unsuitable or corrupt measurements. This entailed the removal of all field measurements gathered on June 29th (n=43), which became useless due to the short-term cancellation of the airborne acquisition. Unfortunately, all measurements gathered in ESUs that correspond to pixels that contain no SWIR information due to the Xenics-Xeva data gaps, had to be excluded as well (n=67) in order to enable a validation of the inversion method based on the full spectral range of AVIS-3. In addition, the ESUs corresponding to pixels that were affected by cloud cover in the second flight had to be dismissed (n=27). With respect to the properties of SAIL as a turbid-medium model, which was developed for a homogenous canopy cover, ESUs in areas of high heterogeneity were removed as well (n = 34). With regard to the squint effect (see Chapter 2.2.4), all ESUs were excluded that are located too close to high-contrast areas (n=21). In a few ESUs (n=10), very high LAIs with values > 6.5 were measured. Since the input parameters of the LUT were set based on a Gaussian distribution in order to distinguish moderate values occurring within the growing period more precisely, the model quality suffered when estimating extreme values. Consequently, these measurements were excluded too. Finally, measurements of senescent vegetation (n = 33) were dismissed, since the model is not able to project this status.

This led to the final number of 330 ESUs which were identified to hold valid information and could thus be used for the validation of the LAI values retrieved by the inversions methods performed. The validation of the chlorophyll content was based on 304 ESUs, their number

diminished in comparison to LAI measurements by the field team (n=26). Table 3-7 shows the number of ESUs that were selected for the validation of LAI and chlorophyll content compared to the total number of field measurements. The table shows that all data acquisitions are still represented by a sufficient number of field measurements.

Table 3-7: Total number of ESUs compared to the valid number that served for evaluation of LAI and chlorophyll content.

Date	Total number of ESUs	Valid ESUs for evaluation of LAI	Valid ESUs for evaluation of chlorophyll content
Apr 28th	86	58	36
May 08th	108	77	73
May 25th	101	46	46
Jun 16th	105	55	55
Jun 29th	43	-	-
Aug 14th	38	30	30
Sep 08th	84	64	64
Total	565	330	304

3.3.2 Statistical Measures

For the accurate evaluation of the inversion results, a range of several statistical measures was used, which had to fulfill certain requirements. For the definition of an ideal statistical set for the validation of vegetation parameters, RICHTER ET AL. (2012) analyzed the main terms and concepts for the quantitative assessment of model performance in the context of biophysical parameter retrieval from EO data, in an exhaustive literature review. The most common measures that were used within the reviewed studies can be grouped into four main categories:

(1) Error indices (residual-based)
(2) Correlation-based measures (association-based)
(3) Dimensionless indices
(4) Pattern indices

The groups differ in general advantages and drawbacks of the respective measure. Error indices quantify the deviation of estimated and observed values, describing the offset of the estimations to the expected values. However, since they measure a displacement, they are not bounded and consequently dependent on the data scale. By contrast, correlation-based measures are bounded and therefore independent of the scale. This group provides dimensionless indices, similar to the measures from the third category, but in addition, they are capable of explaining the correlations between the variables. The last group, the pattern

indices, compares residuals of model estimations to an independent variable. For the purpose of estimating biophysical parameters, pattern indices are usually not suitable due to the lack of an independent variable.

In regard to these advantages and drawbacks, the use of just one measure often insufficiently describes the model's accuracy. For the selection of adequate statistical measures, RICHTER ET AL. (2012) recommended the indicator set to meet following essential model validation criteria:

(1) Non-dimensionality, to avoid influence from the magnitude of the values;
(2) Normalization, i.e., the measures are bounded, for an effortless comprehension of their meaning (e.g., between 0-no agreement and 1-perfect agreement);
(3) Symmetry, i.e., datasets should be interchangeable since the assumption of "ground truth" is unrealistic in remote sensing applications;
(4) Dimensionality, i.e., the measurement of the actual differences, supplied in the unit the data is measured in, in order to understand the magnitude of the error;
(5) Model prediction capability compared to measurement statistics (e.g., observed mean value).

Based on to these guidelines, a statistic set of five measures was defined, including root mean square error (RMSE) from the category of error indices; coefficient of determination (R^2), slope and intercept of Theil-Sen regression (FERNANDES & LEBLANC, 2005) from the category of correlation-based measures; relative RMSE (RRMSE), and Nash-Sutcliffe efficiency (NSE) index (NASH & SUTCLIFFE, 1970) from the category of dimensionless indices. They are described by the following equations. It is noted that although RMSE and NSE have already been presented as cost functions, they are here listed again in the context of validation measures.

1) Root Mean Squared Error (RMSE)

$$RMSE = \sqrt{\frac{1}{n}\sum_{i=1}^{n}(V_{est}^{i} - V_{obs}^{i})^2} \qquad \textit{(Equation 3-10)}$$

2) Coefficient of determination (R^2)

$$R^2 = 1 - \frac{\sum_{i=1}^{n}(V_{est}^{i} - \hat{V}_{est})^2}{\sum_{i=1}^{n}(V_{est}^{i} - \overline{V}_{est})^2} \qquad \textit{(Equation 3-11)}$$

3) Slope and intercept of Theil-Sen regression (m/b)

$$V_{est}^{i} = mV_{obs}^{i} + b \qquad \textit{(Equation 3-12)}$$

4) Nash-Sutcliffe Efficiency (NSE)

$$NSE = 1 - \frac{\sum_{i=1}^{n}(V_{obs}^{i} - V_{est}^{i})^2}{\sum_{i=1}^{n}(V_{obs}^{i} - \overline{V}_{obs})^2} \qquad \textit{(Equation 3-13)}$$

5) Relative root mean squared error (RRMSE)

$$RRMSE = \frac{RMSE}{\overline{V}_{obs}} \qquad \textit{(Equation 3-14)}$$

where

V_{obs} observed variables

V_{est} estimated variables

RMSE and R^2 are very common and therefore ensure comparability with previous studies. However, R^2 is not able to specify the absolute difference between observed and estimated data, whereas slope (m) and intercept (b) indicate their relationship and allow the localization of the regression line in a two-dimensional scatter plot. Slope further serves for the identification of asymmetry in the scale of both datasets, whereas intercept describes the main bias. These measures are of high relevance, since, in certain cases, all other statistical measures provide acceptable results and thus indicate good agreement, although slope and intercept values are poor. The NSE is very sensitive to changes in the mean and to variances in the observed and estimated values, thus, it is more meaningful than R^2. Further, the NSE is well suited to assess the predictive power of the model, as it indicates whether a model performs better than the mean of the observed data (i.e., NSE>0). However, the NSE is sensitive to outliers. Thus, the RRMSE was included in the analysis, since it is less sensitive to outliers and is also less bias-prone. Further, it is well-suited for comparing different values and scales. Table 3-8 summarizes the characteristics, advantages and drawbacks of the statistical measures that were applied for validation.

Table 3-8: Characteristics, advantages and drawbacks of the statistical measures serving for validation purposes (RICHTER ET AL, 2012; modified).

Indicator	Recommended range / value		Advantages and drawbacks	
RMSE	Generally:	Close to 0	+	Indicates magnitude of errors (in variable units)
	e.g., LAI		+	Symmetry is provided
	Excellent:	RMSE < 0.5	+	Frequently used in the literature
	Good:	0.5 ≤ RMSE < 1.0	-	Depends on data unit, range, and distribution of the variable value
			-	Not bounded
R^2	Generally:	Close to 1	+	Reflects spatial patterns
	Excellent:	$R^2 \geq 0.9$	+	Dimensionless & bounded
	Good:	$0.9 > R^2 \geq 0.5$	+	Symmetry is provided
			+	Frequently used in the literature
			-	Does not measure actual differences, therefore may impose an apparent good/high model accuracy where it is not the case
m / b	Generally:	m: Close to 1 b: Close to 0	+	Indicates model under-/overestimation for low/high values
	Excellent:	0.95 < m < 1.05	+	b indicates linear model biases
	Good:	0.80 < m < 1.20	-	Asymmetric for traditional OLS forms, therefore use of Theil-Sen or RMA forms recommended
NSE	Generally:	Close to 1	+	Indicates the predictive power of models
	Excellent:	NSE ≥ 0.9	+	Reveals, whether the model performs at least as accurate as the mean of observed data
	Good:	0.9 > NSE ≥ 0.5	-	Not bounded in negative direction
RRMSE	Generally:	Close to 0%	+	Suitable for comparisons between different variables or different ranges
	Excellent:	RRMSE ≤ 10%	+	Insensitive to the magnitude of values
	Good:	10% < RRMSE ≤ 20%	+	Less sensitive to outliers
			-	Not bounded

A wider acceptance and use of a set of these statistical measures would enable a better intercomparison of scientific results, urgently needed in times of increasing model development activities that are carried out with respect to the upcoming EnMAP and other EO missions. Therefore, the above listed statistical measures from the groups of error indices, correlation-based measures and dimensionless indices, as well as further indices, were implemented to the EnMAP-Box. The purpose of the Advanced Statistical Evaluator module (ASE) is to provide remote sensing practitioners (i.e., non-statisticians) guidance for model evaluation.

3.3.3 Validation of the LUT Inversion

In this section the performance of the LUT was examined with regard to its capacity to estimate leaf area index and chlorophyll content. The results of the inversion loop, which is

based on several combinations of selection criteria, were assessed and led to the identification of the ideal combination showing the highest accuracy of estimated parameters when compared to the observed in-situ measurements. This was, in a first step, conducted for the LAI. Although it was expected that the criteria combination that leads to the highest accuracy for estimation of chlorophyll would differ from the one identified for LAI (see Chapter 3.3.3.2), it was tested whether the latter, that is, the "LAI setting", could also be applied successfully for chlorophyll estimation. This is of importance, as it is a goal of this study to provide a consistent analysis method for hyperspectral data allowing several parameters to be retrieved.

3.3.3.1 Retrieval of Leaf Area Index

3.3.3.1.1 Validation of the Estimation Quality

The evaluation of the results of the inversion loop for the retrieval of LAI was conducted in two steps. First, based on the full-range band setting, the ideal combination of selection criteria, containing cost function, noise amount, number of considered best fits and averaging method, was identified for all five types of noise. Second, based on the most efficient noise type found for the full-range band setting, the evaluation was repeated for the other band settings, i.e., VNIR, Sentinel-2 and Landsat-TM, and then in a final step compared to the former one. This is described in the following chapter. Due to its good applicability for assessing model prediction, the Nash-Sutcliffe Efficiency was used as primary measure for the description of the estimation accuracy. The other measures were then used to identify weaknesses in the data that are not described by the NSE.

Since it was expected that the selection criteria with the greatest influence would be the amount of noise, i.e., the variance (σ), which was added to the simulated data, and the number of multiple solutions, i.e., best fits (n), which were considered and averaged for the parameter retrieval, Figure 3-10 shows the result of the inversion loop for the inverse multiplicative noise type. The figure contains eight accuracy (NSE) matrices, representing the combinations of the four cost functions and two averaging methods. Each of the 441 squares within a matrix thereby gives the accuracy for the corresponding noise (σ) and the number of considered fits, which were averaged.

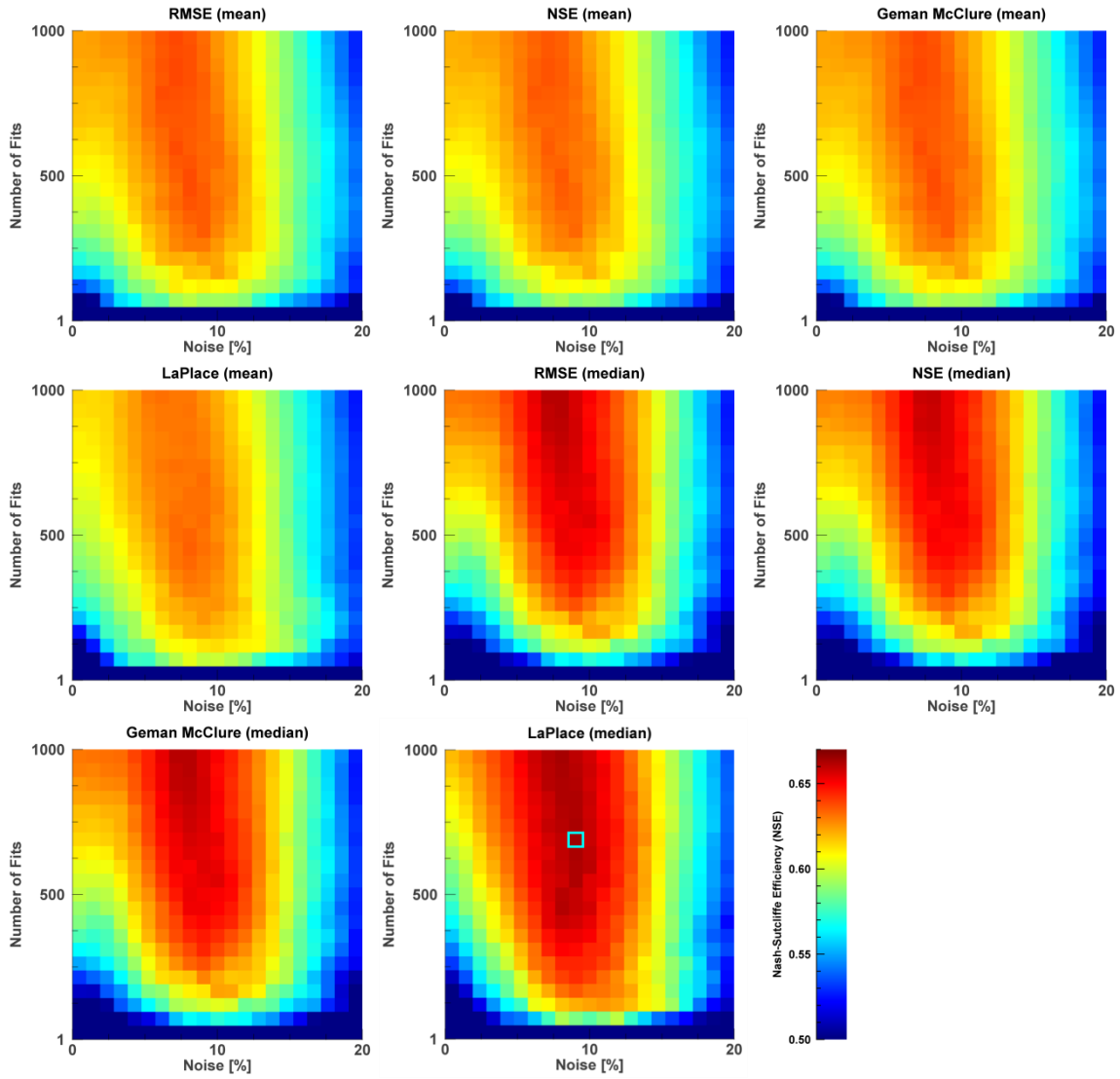

Figure 3-10: Accuracy matrices for the inverse-multiplicative noise type. The matrices are sorted by cost function/averaging method and show the estimation accuracy (Nash-Sutcliffe Efficiency) for each combination of noise variance and number of considered best fits. For a better contrast, the range of the scale bar is 0.50-0.67. The blue-marked square at the Laplace/median matrix represents the combination (σ=9%, n=700) with the highest accuracy among all possible combinations of selection criteria, including noise type.

As shown by the figure, several combinations result in NSE values of over 0.5. According to the recommended value range stated in Table 3-8, this indicates a good prediction accuracy of the model. It should be noted that for the purpose of contrast enhancement the range of the presented NSE values was set to be comparatively narrow (0.50.-0.67), allowing an easier interpretation of the results. The comparison of the eight matrices shows that they all feature similar patterns and that the ideal amount of noise lies between 7 and 12%. Concerning the number of fits, almost all matrices show an increasing accuracy with the increasing number of best fits included in the analysis. Some matrices indicate that the highest accuracy values are achieved by the use of 1000 solutions. This leads to the question, whether a higher number (>1000) than applied to the inversion would have led to even higher accuracies. The further evaluation discussed in this section will, however, negate this theory.

Due to the narrow range of displayed NSE values, which prohibits a differentiation of NSE values < 0.5 since these are, in this illustration, all set to 0.5, it is not apparent which NSE values are reached when only the absolute best fit (n=1) is used. In fact, NSE values < 0 occurred, regardless of the amount of noise applied to the data, which is directly attributed to the ill-posed problem and proves that a single fit potentially leads to a faulty parameter retrieval.

The evaluation of the different cost functions revealed that they all led to similar estimation accuracies. However, a striking difference in accuracy was caused by the choice of statistical method applied for the averaging of the simulated spectra, i.e., whether the mean or the median were used. Throughout all cost functions, the median provided higher accuracies. All in all, the cost function providing the best result (NSE=0.67) is the Laplace distribution, based on 9% noise and averaging the amount of 700 solutions by the median.

For the comparison of the other four noise types, Table 3-9 lists the highest estimation accuracy (NSE) for each noise type, averaging method and cost function among all 17 640 iterations, depending on a specific noise variance and the number of best fits that were considered. The equivalent accuracy matrices of the other noise types containing the detailed description can be seen in Appendix A.1 – A.4.

Table 3-9: Result of the inversion loop sorted by the five different noise types. Each table shows the highest estimation accuracy (NSE) based on a specific combination of noise variance (σ) and number of considered fits (n) for each averaging method / cost function.

Additive Noise

Avg. method	Cost function	n (best fits)	σ (noise)	Accuracy (NSE)
Mean	RMSE	850	3.5%	0.63
	NSE	850	3.5%	0.62
	GM	850	3.5%	0.63
	LP	1000	3.5%	0.62
Median	RMSE	350	6.5%	0.65
	NSE	1000	7.0%	0.65
	GM	350	6.5%	0.65
	LP	700	7.0%	0.66

Multiplicative Noise

Avg. method	Cost function	n (best fits)	σ (noise)	Accuracy (NSE)
Mean	RMSE	950	17.0%	0.63
	NSE	950	17.0%	0.63
	GM	950	17.0%	0.63
	LP	1000	19.0%	0.62
Median	RMSE	1000	19.0%	0.65
	NSE	1000	19.0%	0.65
	GM	1000	19.0%	0.65
	LP	1000	0.0%	0.62

Inverse multiplicative noise

Avg. method	Cost function	n (best fits)	σ (noise)	Accuracy (NSE)
Mean	RMSE	900	7.0%	0.64
	NSE	900	7.0%	0.64
	GM	900	7.0%	0.64
	LP	450	8.0%	0.63
Median	RMSE	1000	8.0%	0.66
	NSE	1000	8.0%	0.66
	GM	1000	8.0%	0.66
	LP	700	9.0%	0.67

Combined noise

Avg. method	Cost function	n (best fits)	σ (noise)	Accuracy (NSE)
Mean	RMSE	1000	0.5%	0.62
	NSE	1000	0.0%	0.62
	GM	1000	0.5%	0.62
	LP	1000	1.75%	0.62
Median	RMSE	1000	3.75%	0.65
	NSE	1000	3.75%	0.65
	GM	1000	3.75%	0.65
	LP	950	3.75%	0.64

Inverse combined noise

Avg. method	Cost function	n (best fits)	σ (noise)	Accuracy (NSE)
Mean	RMSE	1000	5.0%	0.65
	NSE	1000	5.0%	0.65
	GM	1000	5.0%	0.65
	LP	850	5.0%	0.64
Median	RMSE	1000	5.0%	0.64
	NSE	1000	5.0%	0.64
	GM	1000	5.0%	0.64
	LP	950	5.0%	0.66

The table shows that there is no significant difference in the model accuracies of the different noise types. The best results were obtained by *inverse-multiplicative noise* (NSE=0.67), followed by *additive* and *inverse-combined noise* (NSE=0.66). Despite the fact that the classical *multiplicative noise* performs worst, implying that the assumptions that led to the implementation of an inverse mode of this noise type were correct, the differences in the highest accuracy achieved by the different modes are too small to be of meaningful relevance.

The analysis of the accuracies achieved by the application of different cost functions shows a similar trend for all cost functions, and was already noted in the example of *inverse-multiplicative noise*: there are slight differences, which are, however, mainly caused by the averaging method. In 17 of 20 cases the median leads to significantly higher accuracies than the mean.

The amount of noise, by contrast, is more difficult to compare, since the noise ranges applied in the noise types differ. As listed in Table 3-6, identical ranges were applied to *multiplicative* and *inverse-multiplicative noise* (maximal 20%), as well as to *combined* and *inverse-combined noise* (maximal 5%), while the *additive noise* added to the simulated spectra ranges between 0 and 10%. The comparison of the first group (multiplicative methods) reveals that the best fits for *multiplicative noise* were provided through high noise values (17 to 19%), while its inverse counterpart (*inverse multiplicative*) leads to best results when 7 to 9 % noise is applied. This can be assigned to the fact the first noise type, due to its design, exerts a lower influence on the reflectance spectra than the inverse type, because reflectance values rarely exceed 0.5. This relation is reversed in the second group (combined methods): *inverse-combined noise* leads to best fits with noise values of 5%, whereas for *combined noise* the values range from 0.5 to 3.75%.

A possible explanation for the Laplace/median combination providing the three highest accuracies among all possible combinations is the fact that the Laplace Distribution is a L_1-estimator which is less prone to outliers than the L_2-estimators. Among these three combinations, the one based on *inverse-multiplicative noise*, a noise variance of 9% and a considered number of 700 fits, provides the best inversion method leading to the highest accuracy. This is valid at least when applying the NSE.

To evaluate this result in a wider range, further statistical measures, which have been defined in Chapter 3.3.2, were consulted, since the setting should provide robust values for these as well. For that purpose, Figure 3-11 shows the Laplace/median matrix of the inverse multiplicative noise, displayed as RRMSE, R^2, slope (m) and normalized intercept (b) instead of NSE. Since the values of intercept depend strongly on the absolute values of data in general, a normalized version was generated by dividing it by the standard deviation of the in-situ data. This ensures comparability and provides a more accurate assessment. Since the RMSE shows behavior almost identical to the RRMSE, it is not included in the figure.

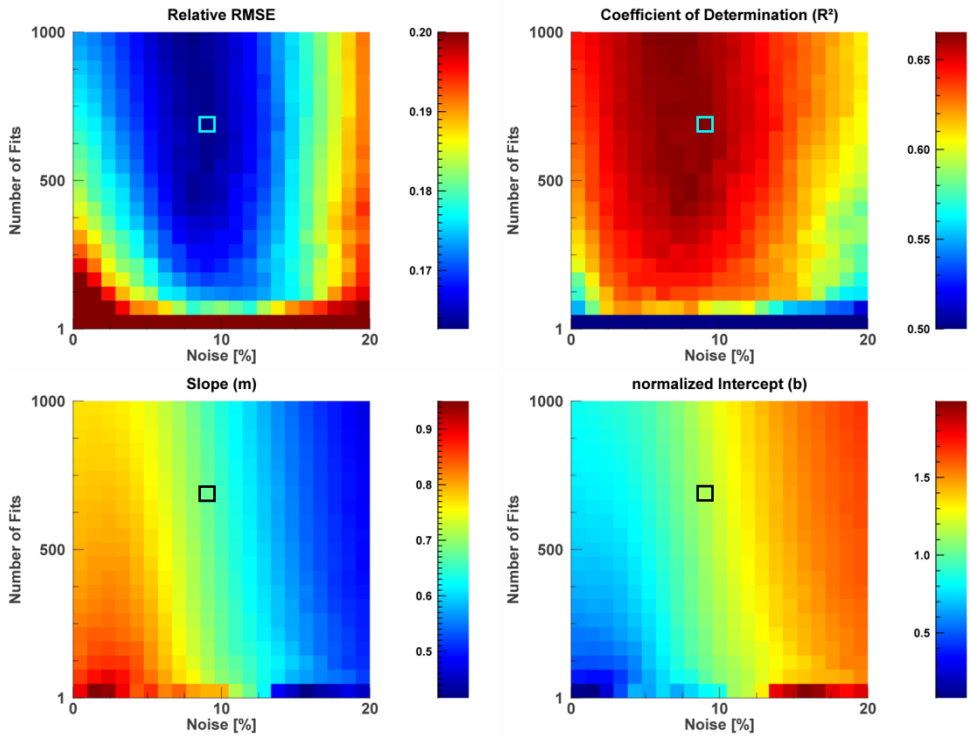

Figure 3-11: Alternative accuracy matrices (RRMSE, R², m, b) for the Laplace/median combination based on inverse-multiplicative noise, which has been identified as having the highest accuracy based on the NSE. The marked square shows the position of the best solution provided by the NSE.

The figure reveals that these measures partially result in different patterns. The matrices of RRMSE and R^2 show a comparatively similar behavior to the NSE matrix of Figure 3-10, which almost confirms the position of the best fit. By contrast, slope and normalized intercept show a distinct deviation to the NSE pattern. Furthermore, the slope value of 0.68 lies far outside the region of recommended values. As mentioned before, a divergent slope leads to an asymmetry between the observed and estimated data and therefore makes the former best fit combination inappropriate.

To counteract this, a slope/intercept rejection threshold was defined. This was applied to the accuracy estimation by the NSE and led to an exclusion of all combinations, where slope and intercept lay outside of the threshold. Following the recommendation of RICHTER ET AL. (2012), the slope (m) rejection threshold is defined by:

$$0.8 \leq m \leq 1.2$$

Since intercept depends on the absolute values of the underlying data, a general threshold could not be defined. By contrast, a threshold for the normalized intercept is fully transferable; consequently the intercept (b) rejection threshold was set to:

$$b \leq 1.00$$

This combination of both thresholds means that all combinations based on a slope, which is lower than 0.8 or greater than 1.2, and an intercept, which exceeds 100% of the standard

deviation of the observed data, are rejected. Figure 3-12 presents the NSE accuracy matrices for the inverse multiplicative noise type, after the slope/intercept rejection threshold was applied. All accuracies that are rejected as a result were excluded and set to zero.

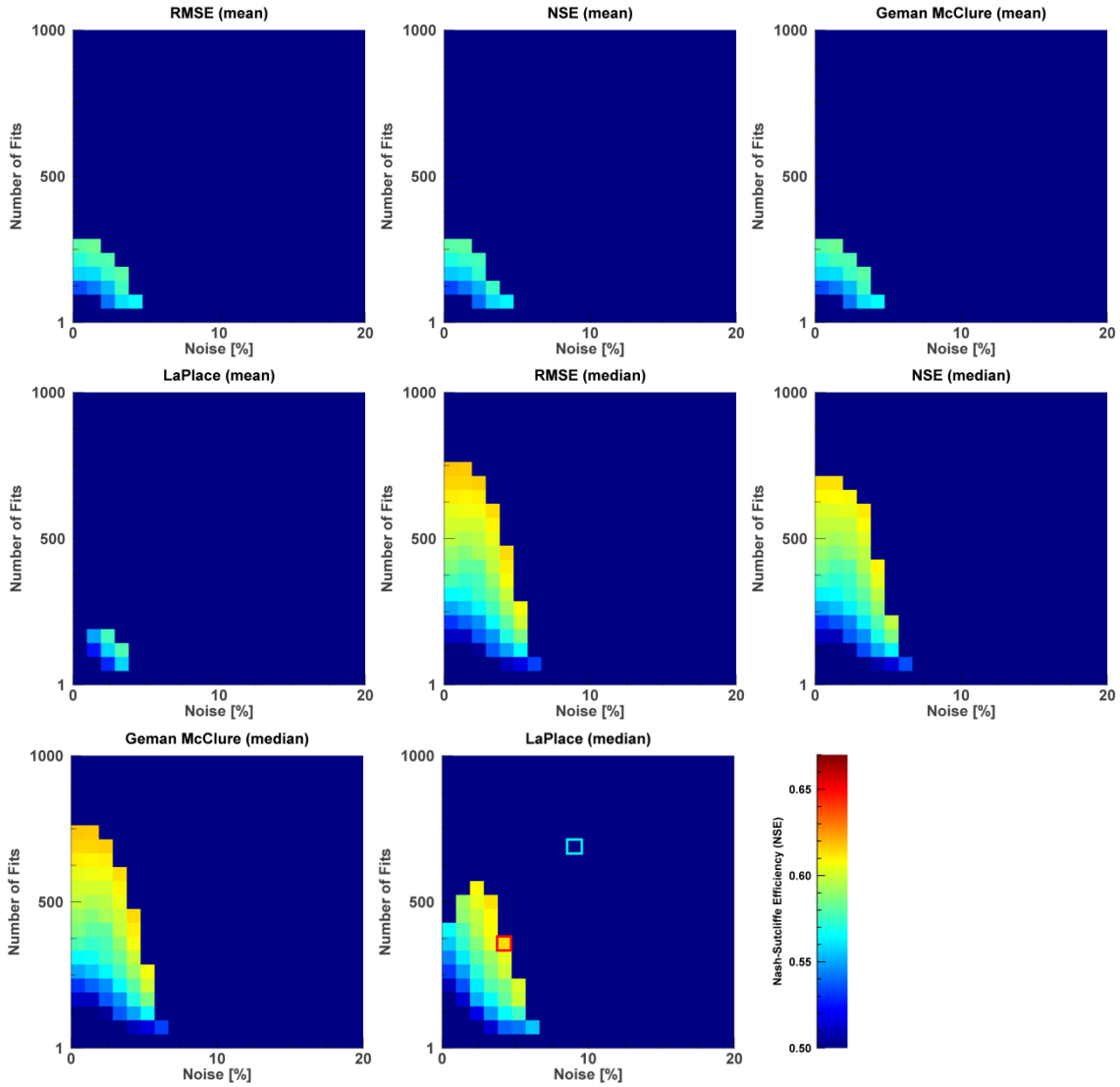

Figure 3-12: Accuracy matrices for inverse-multiplicative noise (see description for Figure 3-10) after a rejection threshold for slope ($0.8 \leq m \leq 1.2$) and intercept (≤ 1.00) was applied. The red-marked square shows the combination with the highest accuracy (σ=4%, n=350) after the exclusion of inappropriate combinations due to the threshold. For comparison, the blue-marked square shows the position of the former ideal criteria combination.

After applying the rejection threshold to the data, the matrices have distinctly changed in appearance. All higher noise levels as well as the higher numbers of considered solutions have been rejected. However, the median is still stronger than the mean among all cost functions. For the Laplace/median matrix, the best solution has moved to the bottom left, indicating a lower noise level and a reduced number of considered best fits compared to the former combination with the highest NSE accuracy. The new solution provides the best result with a NSE=0.62, which still is a valid value (>0.5), and is based on 4% noise and on the averaging

of 350 solutions by the median. To illustrate the impact of the modification, and in order to examine whether the statistical measures provide valid values, Figure 3-14 shows the scatter plots of the LAI estimation based on the best LUT selection criteria combination before and after the slope/intercept rejection threshold was applied.

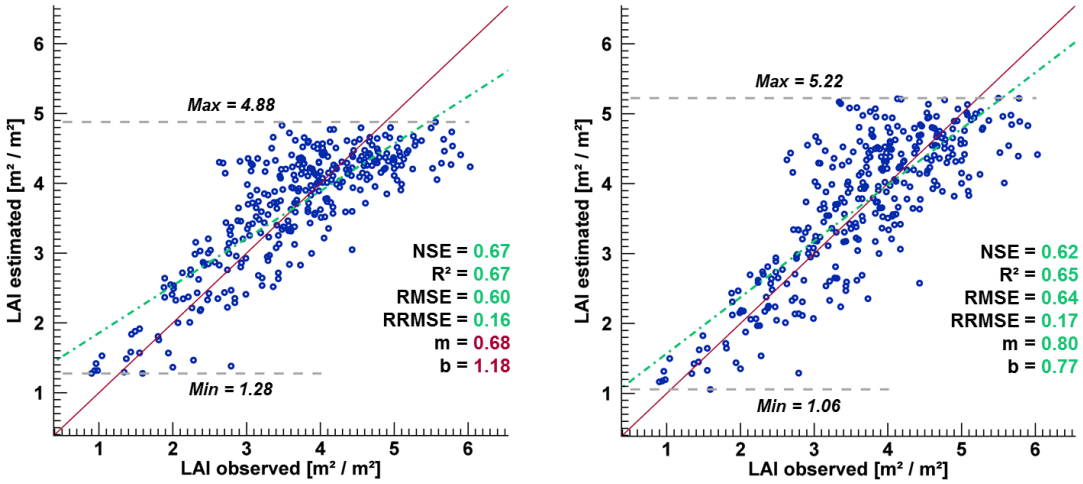

Figure 3-13: Correlation of observed and estimated LAI. The left scatterplot is based on the LUT criteria setting (Laplace/median, n=700, σ=9%, inverse-multiplicative noise) which resulted in the highest accuracy (NSE); the scatter plot to the right is based on the highest accuracy after the exclusion of inappropriate combinations based on the slope/intercept rejection threshold (n=350, σ=4%).

Although NSE, R², RMSE and RRMSE provided higher accuracies in the original LUT setting, the scatter plot (left) shows an asymmetry which is distinctly reduced after the application of the rejection threshold (right). It is assumed that the asymmetry, which is visible through a high minimum and a low maximum value in the estimated data, originated from the input parameter setting of the LUT following a Gaussian distribution. Since most LAI values of the input data scatter around values > 2.0 and < 5.0, a consideration of a high number of solutions leads to strong generalization and consequently to a loss of information. This is due to the fact that in addition to the LUT spectra that are based on matching LAI information, a high number of other spectra are considered, which are based on input parameters with the most common LAI values, i.e., > 2.0 and < 5.0. The amount of noise might have an influence as well, since all combinations based on higher values than > 5% were rejected also.

Consequently, the scatter plot incorporating the rejection threshold has a more common appearance, since it is not as clinched. The now adequate values of slope and intercept involved a slight deterioration of the other measures, which are, however, still in an acceptable range.

Figure 3-14 shows how the absolute best solution of the LUT (Laplace, inverse multiplicative noise, σ=4%, n=1) and an averaged LUT reflectance of multiple solutions (median, n=350)

are fitted to a corresponding, randomly chosen AVIS-3 reflectance (fourth flight). It should be emphasized that during the actual inversion, not the reflectance values of the considered fits of the LUT were averaged, but only the metadata containing the input parameters as well as fAPAR and fCover, as only these are of interest. The figure therefore merely serves as an illustration of the fitting process.

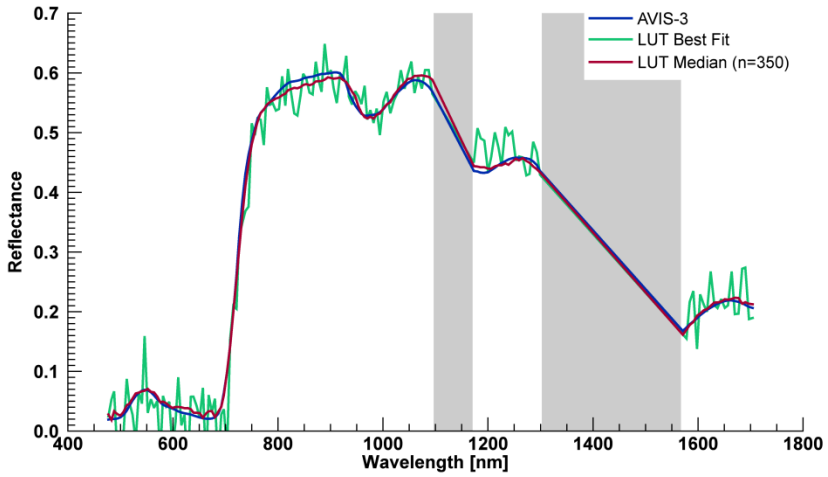

Figure 3-14: Comparison of a randomly chosen reflectance spectrum from AVIS-3 data (fourth flight) to the absolute best fit found by the LUT inversion solution (Laplace, n=1, σ=4%, inverse multiplicative noise) and to the averaged solution (median, n=350).

The figure also shows how the averaging of multiple solutions affects the fitted reflectance. While the singular LUT reflectance of the absolute best fit is clearly noisy, the median-averaged reflectance adapts to the measured reflectance of AVIS-3. This results from the fact that the median values of every band are combined.

3.3.3.1.2 Assessment of the Hyperspectral Band Setting

Following the determination of the Laplace/median method based on *inverse-multiplicative noise* as the most suited LUT inversion technique, at least for LAI estimation, the influence of the choice of considered bands on the estimation quality was examined, including a review of the value added by incorporating the full-range hyperspectral band setting, involving 146 bands, compared to the reduced hyperspectral setting of VNIR, using only 88 bands, and the multispectral settings, which correspond to bands of Sentinel-2 and Landsat-TM (see Chapter 3.2.3.1). Since it has been found that the influence of different noise types is rather negligible, the inversion loop based on the alternative band settings was performed only with *inverse-multiplicative noise*. The evaluation partially led to similar patterns concerning the combination of noise and multiple solutions for all cost functions. Further, for the Sentinel-2 and Landsat-TM band settings, the median also provided higher accuracies than the statistical averaging of the corresponding parameters by the mean. By contrast, the VNIR setting performed better when the mean was used. Because a detailed evaluation of these patterns is

not necessary, the accuracy matrices for the alternative band settings can be found in Appendix A.5 – A.7. However, the essential information is presented in Table 3-10. The table lists the highest NSE accuracies among all possible LUT criteria combinations for the three alternative band settings. In addition to the NSE, the corresponding values of the further statistical measures are listed as well. To rule out the issues related to slope and intercept, the table moreover features the highest accuracies after the rejection thresholds defined in the former section were applied.

Table 3-10: Highest accuracies of the LUT inversion loop for the alternative band settings of VNIR (band number = 88), Sentinel-2 (band number = 9) and Landsat-TM (band number = 4) before and after the application of the slope/intercept rejection thresholds. For VNIR and Landsat-TM the threshold criteria could not be fulfilled throughout all possible combinations. Alternatively, the estimation accuracy corresponding to their best slope value is listed. The Sentinel-2 band combination is not rejected by the application of the thresholds, its implementation, however, led to overall inacceptable accuracies.

Accuracy measure	Best criteria combination			Slope/intercept rejection threshold-adjusted best criteria combination		
	VNIR	Sentinel-2	Landsat-TM	VNIR	Sentinel-2	Landsat-TM
NSE (basis)	0.43	0.64	0.55	0.02	-0.31	0.43
R^2	0.45	0.64	0.63	0.32	0.34	0.54
RMSE	0.78	0.62	0.69	1.02	1.18	0.78
RRMSE	0.21	0.17	0.19	0.28	0.32	0.21
m	0.46	0.63	0.62	0.58 (max)	0.81	0.76 (max)
b	1.84	1.44	1.70	1.25	0.63	1.01

When exclusively considering the NSE of the best criteria combination, without the application of the rejection threshold, the band setting alone, according to Sentinel-2 (NSE=0.64), provides a similarly high accuracy compared to the full-range setting (NSE=0.67) examined in the previous chapter. By contrast, both the NSE of the Landsat-TM and the VNIR setting are significantly lower. While the Landsat-TM setting still shows an acceptable value (NSE=0.55), the result for VNIR is not satisfactory (NSE=0.43), which is also evident in a too high RRMSE of 0.21. The obvious inferiority of the VNIR setting for the retrieval of LAI, compared to the multispectral settings is attributed to the lack of bands in the SWIR.

All three settings have in common that the values of slope and intercept do not lie within an acceptable range and are inferior to the full-range setting. Consequently, the slope/intercept rejection threshold was applied to all three settings, which led to a drastic decrease in all corresponding NSE accuracies. Furthermore, the Sentinel-2 setting was the only one that provided slope values of >0.8. These valid slope values, however, led to the model no longer showing a predictive capability as can be seen by negative NSE values occurring, for example for -0.31. This is confirmed by the other measures (R^2, RMSE, RRMSE), which all lie outside

of the recommended range. In case of the settings of VNIR and Landsat-TM, none of the possible combinations fulfilled the slope/intercept condition. Hence, even by taking the best slope available into account, no acceptable combination could be identified, although the Landsat-TM setting succeeds in providing legitimate values for R^2 and RMSE. Even though the table may suggest that the Landsat-TM band setting provides better accuracies than the Sentinel-2 setting, the reduction in the rejection threshold applied to the Sentinel-2 setting to equal the slope of the Landsat-TM setting would provide a superior NSE value of 0.55 for the latter. However, this compromise would not really be satisfactory.

In Figure 3-15, the scatter plots for the highest accuracy of the Sentinel-2 setting before (RMSE/median, σ=3%, n=700) and after (σ=0%, n=50) the application of the threshold are presented. The scatter plots illustrate that the thresholds led to a dispersion of the estimated and observed LAI-values, which makes an inversion of the LUT based on this setting inappropriate.

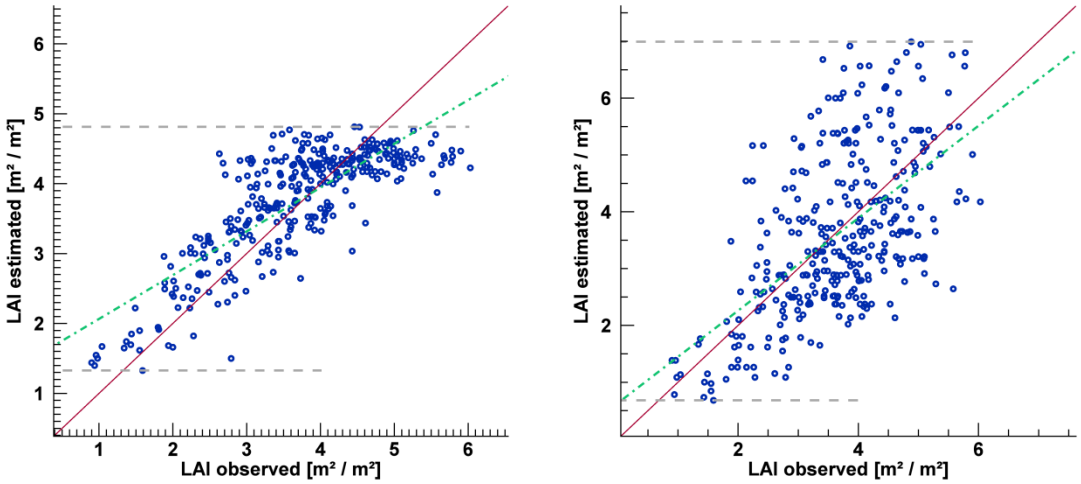

Figure 3-15: Scatter plot of LAI estimation for the Sentinel-2 band setting. The left scatter plot is based on the LUT criteria setting (RMSE/median, n=700, σ=3%, inverse-multiplicative) which resulted in the highest accuracy (NSE). The right scatter plot is based on the highest accuracy after the exclusion of inappropriate combinations due to the slope/intercept rejection thresholds (n=50, σ=0). The accuracies are listed in Table 3-10. The different scale of the axes between both plots should be considered.

3.3.3.2 Retrieval of Chlorophyll Content

In theory, the algorithm searches for the best fit of the modeled-to-measured reflectance among all simulated reflectance spectra stored in the LUT. Once it has been identified, this indicates that every individual parameter on which the generation of the modeled spectrum is based represents the canopy in a meaningful way. However, for several reasons, e.g., uncertainties in the model, the measured reflectance data and the in-situ data, the ill-posed problem, and the fact that chlorophyll content and LAI do not influence the same spectral

range, the LUT setting leading to the highest accuracy for chlorophyll might differ from the setting identified for LAI. This made it necessary to analyze the retrieval capability of the different LUT settings for chlorophyll as well.

Since the leaf chlorophyll contents, measured for validation purposes using a SPAD device (see Chapter 2.1.3.2), refer to an internal value, these values are usually calibrated, although the raw data also seems to provide realistic values. This is due to the fact that the SPAD assumes a linear relationship between measured values and actual chlorophyll content, which is only true if pigment concentration alone influenced the absorption. However, scattering effects at the boundary layers between cell wall and air spaces, reflection at the leaf surface and the distribution of pigments within the leaf play an important role in the absorption process as well (VOGELMANN, 1989). After a certain chlorophyll concentration (65 µg / cm²) has been reached, the relationship decreases, because it is no longer the number of chloroplasts, but only the chlorophyll density within the chloroplasts, which increases (TERASHIMA & SAEKI, 1983). Several studies investigated this behavior and tried to formulate a mathematical relationship between the SPAD values and the actual chlorophyll concentration. Polynomial formulas were defined, e.g., by MARKWELL ET AL. (1995) and MONJE & BUGBEE (1992). For the present study, these regression curves were applied to the SPAD values and used for the validation of the model results. They are defined by:

$$LCC_{Markwell} = 10.6 + x * 7.39 + x^2 * 0.114 \qquad \textit{(Equation 3-15)}$$

$$LCC_{Monje\ \&\ Bugbee} = 1.034 + x * 0.308 + x^2 * 0.11 \qquad \textit{(Equation 3-16)}$$

where

x	SPAD value
LCC	Leaf chlorophyll content [µg / cm²]

The curves are based on empirical studies, and showed good correlations when applied to specific crops within the corresponding studies, e.g., wheat, rice and soy bean in MONJE & BUGBEE (1992). Since absorption processes are also influenced by the crops' characteristic structures (DATT, 1998), a general transferability of these curves to all crop types must, however, be viewed critically. Hence, not only the calibrated leaf chlorophyll contents, but also the raw SPAD values were tested, assuming that they represent valid chlorophyll concentrations as well. This assumption is supported by the fact that the SPAD values increase linearly with increasing chlorophyll content as long as the latter does not exceed 65 µg / cm², which was the case for the measurements from the 2012 campaign. Thus these values provide a reliable measure of chlorophyll (GAO, 2006).

In Figure 3-16, the correlation between the modeled leaf chlorophyll content (LCC) and both the raw and the two calibrated SPAD values are presented in scatter plots. Each plot is based on the setting providing the highest accuracy (NSE) among all LUT combinations, given by the inversion loop.

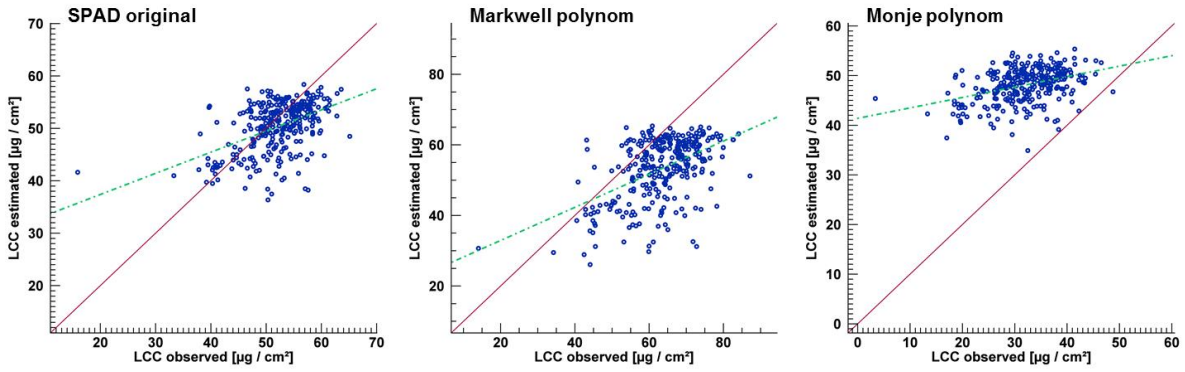

Figure 3-16: Correlation of measured and estimated leaf chlorophyll content, displayed for raw and calibrated SPAD values. Each scatter plot is based on the LUT setting providing the highest accuracy (NSE).

The figure shows that, on a leaf level, an accurate simulation of LCC is barely possible, regardless which SPAD configuration is used. This is not surprising, since the deduction of LCC is in general difficult, due to the fact that it is a very small-scale parameter that might vary within both the leaf and the canopy level. In addition, the missing information on the influence of soil reflectance and a potential disturbance by shadow and illumination effects hampers the ability to deduce the LCC.

The comparison of the three methods showed that the use of raw SPAD values leads to better correlations than the use of calibrated values, although the estimation accuracy is very low likewise, as can be seen in the accuracy matrix for the coefficient of determination (R^2) in Figure 3-17. The matrix is based on a Laplace/median setting with *inverse-multiplicative noise*.

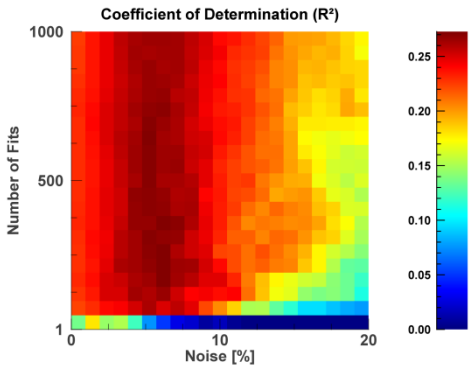

Figure 3-17: Accuracy matrix (R^2) for LCC, validated on the raw SPAD values, based on Laplace/median and inverse-multiplicative noise.

WEISS ET AL. (2000) found that for a more accurate LCC retrieval, several recordings, captured with different viewing angles, were necessary. This requirement is, however, not fulfilled in the data acquired for this study during the 2012 campaign. Since this is a well-known problem, LCC is often linked to LAI, allowing a more meaningful evaluation, since it is thereby related to the optical thickness of the (turbid) medium (WEISS ET AL., 2000). As a result of the high correlation found between LAI and LCC (e.g., BARET & BUIS, 2008), canopy chlorophyll content (CCC), which is obtained by multiplying LAI by LCC, is assumed to be a physically meaningful parameter.

In a next step, it was not intended to identify the potentially best solution for CCC estimation, but to examine whether the LUT setting used for LAI estimation leads to reasonable CCC estimates as well. The underlying intention of this is to investigate whether a universal and consistent estimation method, which is valid for both LAI and chlorophyll content, can be defined, even though the CCC could be estimated at a higher accuracy when it is not linked to the ideal setting for the LAI. However, the accuracy matrices based on the raw SPAD values can be found in Appendix A.8. Figure 3-18 shows the scatter plots including the corresponding accuracies for CCC estimation based on the LUT setting, which proved to be the best for the estimation of LAI, i.e., Laplace/median, *inverse-multiplicative noise*, σ=4%, n=350.

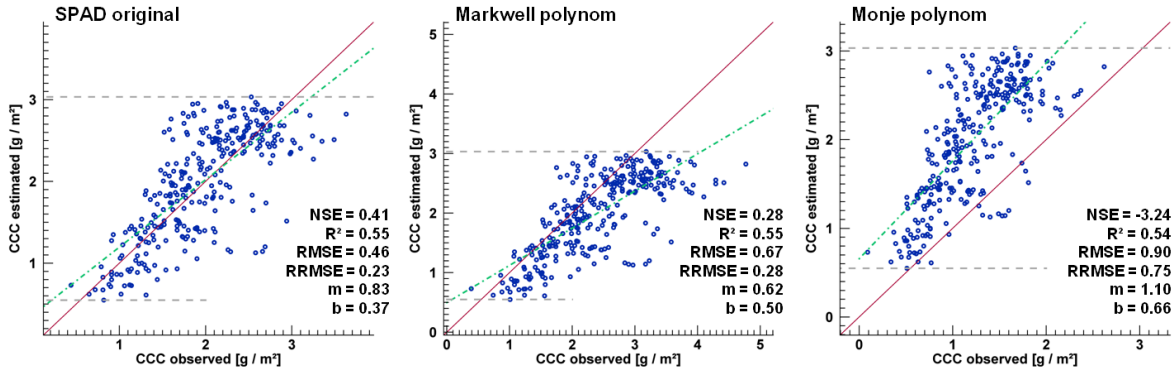

Figure 3-18: Correlation of measured and estimated canopy chlorophyll content, displayed for raw and calibrated SPAD values. Each scatter plot is based on the identical LUT setting that was identified as being most efficient for the estimation of LAI (Laplace/median, inverse-multiplicative noise, σ=4%, n=350). Note the different scales of the axes. The grey lines, denoting minimum and maximum of estimated CCC, refer to the same values in all three scatter plots and thus emphasize the massive deviation of the three plots.

By comparing the plots, which are based on the different SPAD configurations, it becomes quite evident that the only solution providing rather accurate results is based on the use of raw SPAD values. The results obtained for the calibrated versions prove that a transferability of the regression curves is not given, or at least not when applying the data from the 2012 campaign. This is in particular revealed through the bad values of NSE, RRMSE and intercept, especially for the Monje & Bugbee polynom. However, although a connection between estimated and observed CCC based on the raw SPAD values cannot be denied, the

overall result is only partly satisfactory. While R^2, RMSE, m and b lie within the recommended range, NSE and RRMSE provide values slightly below the recommended ones. With regard to the general difficulty in estimating chlorophyll contents and the limitation of applying the identical LUT setting as used for LAI, and not a setting which was explicitly optimized for LCC/CCC, this result can, nevertheless, be seen as acceptable.

4 Applicability, Transferability & Results

The evaluation of the LUT inversion with its manifold combination possibilities in different settings has shown that a multitemporal retrieval of vegetation parameters based on a consistent method is in theory possible. It has also been shown that the implementation of a number of different selection criteria led to an improvement in the estimation quality. In the first section of this chapter, the examined ideal LUT setting was applied to the multiseasonal dataset and thereby answers the initial question whether the dynamic of the growing period can be captured with hyperspectral data on an airborne scale. The second part then clarifies whether this analysis concept can be transferred to the spaceborne scale of EnMAP, which is defined by a much coarser spatial resolution and divergent spectral characteristics.

4.1 Applicability to Multiseasonal Data

Based on the best LUT setting (Laplace/median, inverse-multiplicative noise, σ=4%, n=350), which was identified to allow an accurate retrieval of both LAI and chlorophyll content, the inversion was repeatedly applied to a total of six hyperspectral scenes. However, since the high accuracy of this LUT setting was given only when taking the full hyperspectral range of the AVIS-3 data into account, the spatial data gaps, in which no SWIR data records exist, could not be considered equally. Therefore, the data gaps were masked out and are displayed in black in the resulting map of retrieved LAI (Figure 4-1). The figure features only the recordings conducted by AVIS-3, since these alone were affected by data gaps.

However, due to the data gaps, the result is not satisfying. To counteract this shortcoming, the LUT inversion was performed, for these data gaps, based on the VNIR band setting only, in full awarness of the less accurate results thereby supplied for these sections, a circumstance evidenced by lower estimation accuracies in Chapter 3.3.3.1.2. The retrieved information was nonetheless used to fill the data gaps.

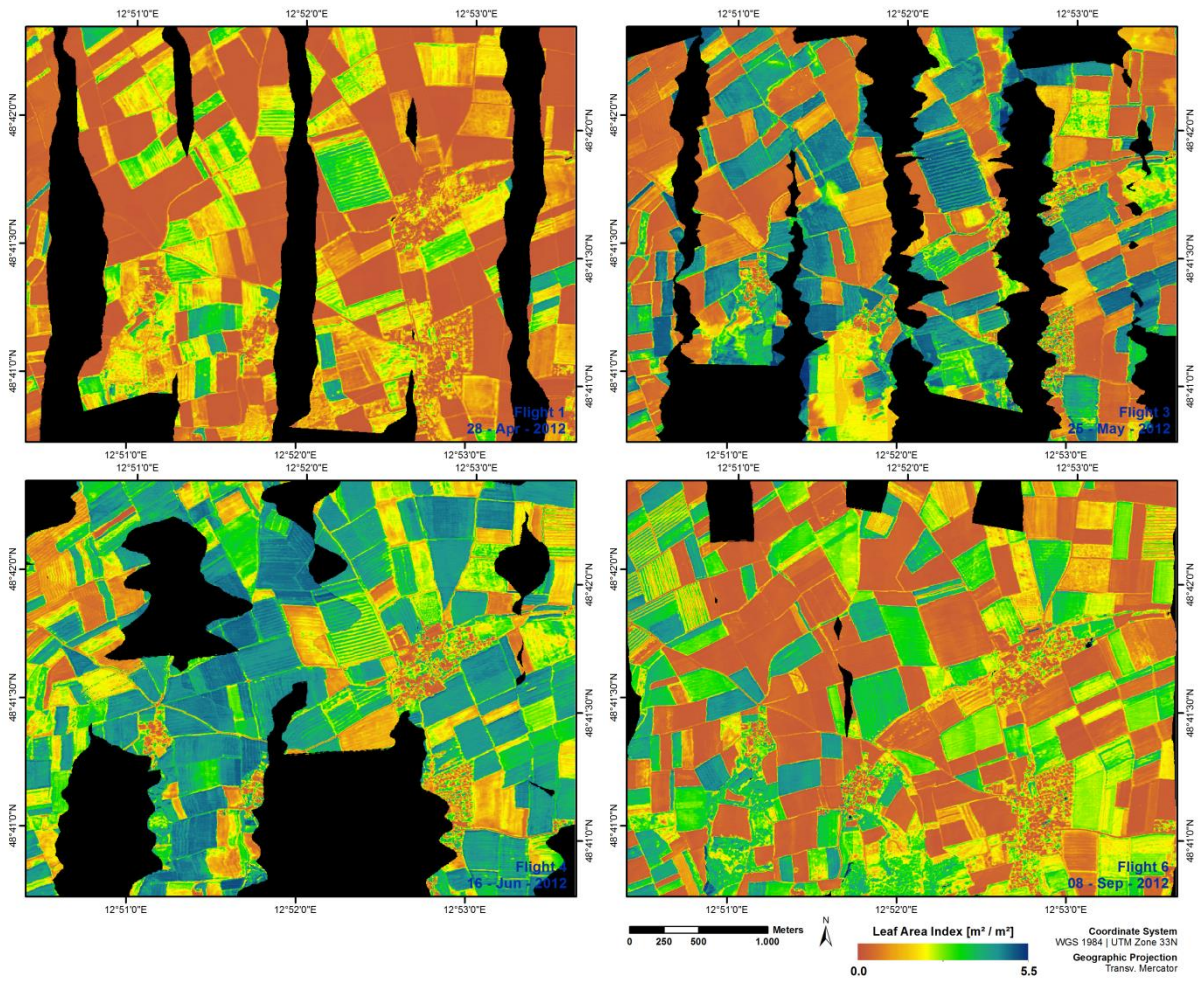

Figure 4-1: Result of the LUT inversion for leaf area index of the four AVIS-3 scenes, based on the determined ideal LUT configuration (Laplace/median, inverse-multiplicative noise, σ=4%, n=350).The method could be only applied to the areas in which a SWIR coverage was given.

In order to achieve a reasonable result with the VNIR setting, the amount of noise and the number of considered multiple solutions were chosen carefully. A compromise had to be found between acceptable values of NSE and slope, as these measures show an almost contradictory behavior (Figure 4-2).

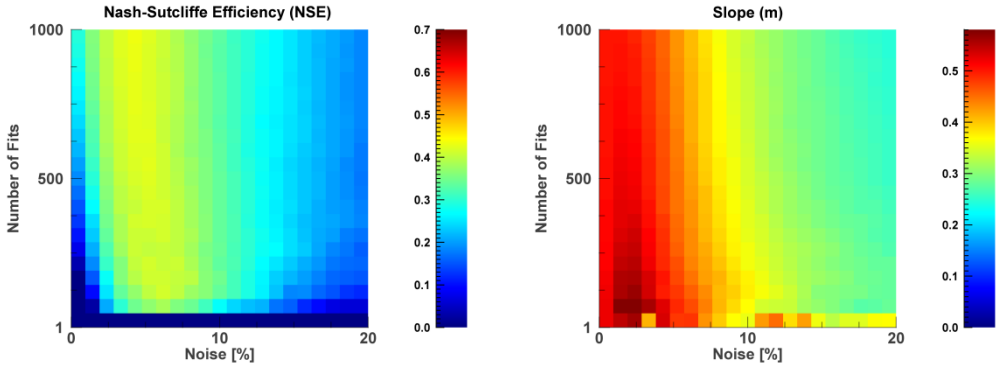

Figure 4-2: Comparison of NSE accuracy and slope accuracy for the VNIR band setting (Laplace/median).

Considering the different patterns of the matrices in the figure, a reasonable compromise was given by a noise amount of σ=3% and a number of solutions of n=100. The result with filled data gaps is given in Figure 4-3, which also includes the LAI estimates for the two HySpex flights and thus nicely illustrates the seasonal alteration of the landscape caused by varying LAIs.

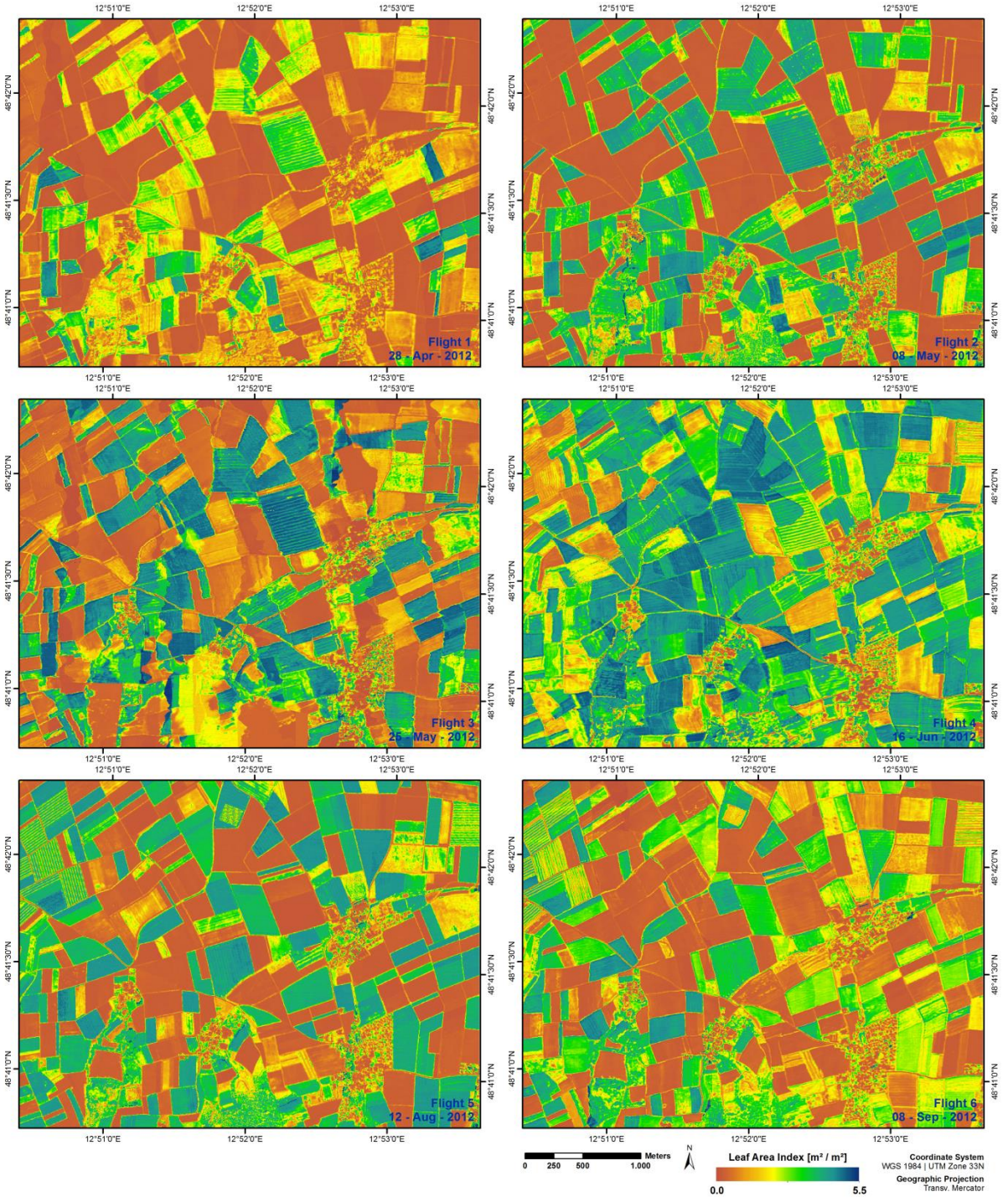

Figure 4-3: Result of LAI estimation for all six scenes acquired in 2012.

The same method was applied for the derivation of canopy chlorophyll content; the resulting images are presented in Figure 4-4. Since CCC is dominated by LAI values, the images show similar patterns as the former figure. Although the accuracy of CCC estimation was inferior to the accuracy achieved for LAI, the figure shows a clear distribution of CCC within the landscape.

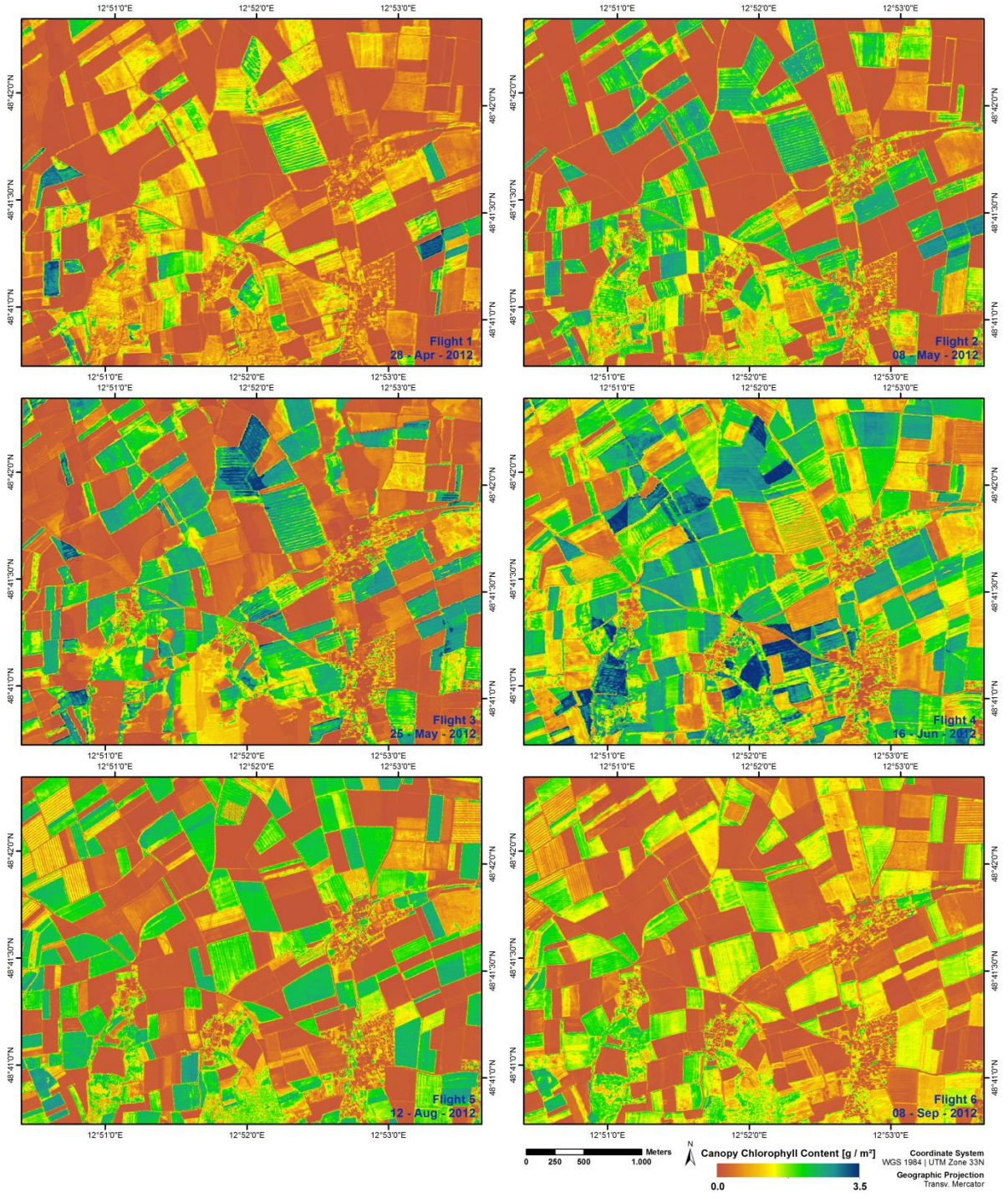

Figure 4-4: Result of canopy chlorophyll content estimation for all six scenes acquired in 2012.

It should be pointed out again that the estimation accuracy for the VNIR-based inversion is distinctly lower; hence, the areas affected by SWIR data gaps in both figures must be interpreted carefully. In such cases it appeared that both LAI and CCC tended to overestimation in these areas, a circumstance which can be identified by dark greenish or blue colors next to areas with lighter colors within field borders. However, the benefits of further available information outweigh this weakness.

Based on the estimated vegetation parameters, the progress of specific crops throughout the growing season could be analyzed. Figure 4-5 shows the development of LAI and CCC for winter wheat, winter barley, rapeseed, corn and sugar beet from April, 28th to September, 8th. The information was extracted from the retrieved parameter products by randomly choosing and averaging 30 pixels per scene and each crop type from the corresponding parameter.

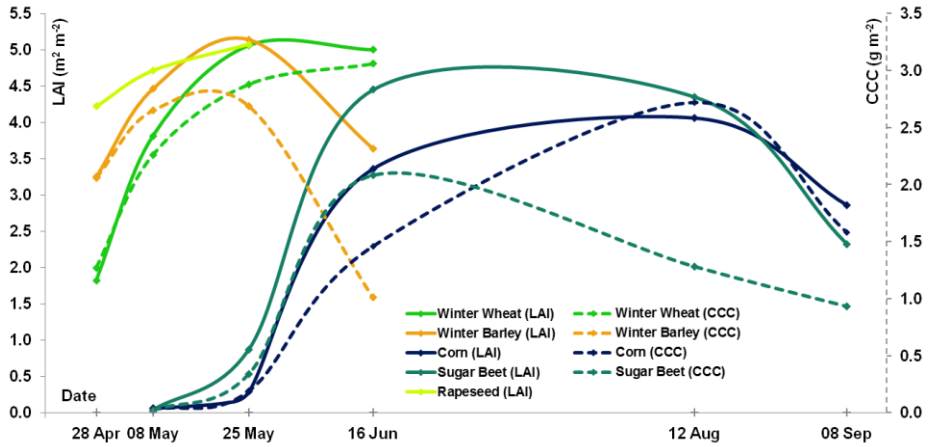

Figure 4-5: Development of LAI and CCC for the five investigated crops throughout the growing period, derived from six data acquisitions.

The figure traces the growth cycles of different crops from emergence until harvest. Rapeseed, which was harvested between May 25th and June 16th, winter wheat and winter barley reach maximal values of LAI and CCC already in late spring and early summer, which is typical for winter crops. According to the decreasing values of LAI and CCC, winter barley reaches maturity earlier than winter wheat. The development of corn and sugar beet shows the typical behavior of increasing LAI and CCC in spring and a maximum in mid-summer. Further, all crops show a decrease in these values after maturity, which can be related to senescence. However, the decrease in the actual LAI is overestimated compared to reality, mostly because the model is not able to simulate senescent vegetation, but rather simulates the spectral effects of green LAI, based on the amount of chlorophyll stored within photosynthetically active leaves.

4.2 Transfer of the Analysis Method to EnMAP Scale

The transfer of the retrieval method conducted by the LUT inversion to the EnMAP scale required an adjustment of the algorithm, since EnMAP will provide a deviant number of bands and spectral resolution compared to AVIS-3 data. The adaption process is described in the following chapter.

Further, the application of the inversion method to the simulated EnMAP data (see Chapter 2.3), requires validation as well. This, however, is not possible based on the in-situ measurements, since they are only representative for the spatial resolution for which they were gathered, and thus correspond to the 4m scale of the airborne data. Furthermore, since the in-situ data is based on point measurements, they are hardly suitable to serve for a validation of estimated parameters deduced from EnMAP data with a spatial resolution of 30m. Consequently, an alternative validation method was defined, which is described in Chapter 4.2.2.

4.2.1 Algorithm Sequence Adaption

For the application of the LUT sequence to the (simulated) EnMAP data, the program had to be modified, in the process of which it was enhanced to allow its application to the image data of several sensors.

The algorithm was designed in a way to process externally supplied image data, including multiple sensor specifications, e.g., EnMAP or Sentinel-2. Further, the amount of noise, the number of considered solutions, the cost function and the averaging method can be dynamically defined, serving the definition of the LUT setup.

Additionally, the input of the solar zenith and azimuth angle corresponding to the data is of decisive importance. Based on this information and the sensor type including the specification of the orbit inclination for the derivation of the sensor azimuth angle, the derived illumination geometry serves as input for PROSAIL, which then computes the LUT at a size of 100 000, by the use of the identical biophysical and biochemical input parameters as applied before. Further, the LUT is calculated corresponding to the specified sensor type, which means that the reflectance of only the available bands is simulated. Consequently, the parameter retrieval by the inversion process is based only on these bands.

The actual inversion was performed as described in Chapter 3.2.2, resulting in a multiband output image containing all relevant parameters. The inversion was now based on the EnMAP specific bands. However, the alternative validation method (see Chapter 4.2.2) was based on the use of the results obtained for the AVIS-3 scenes. Since the spectral range of AVIS-3 is smaller than of the upcoming EnMAP data, a meaningful comparison required the exclusion

of the spectral ranges which are not covered by AVIS-3, which, in any case, include no information, since AVIS-3 data served as data basis for the simulation of the EnMAP data. Therefore, a further setting was integrated into the program, which considers only EnMAP bands within the spectral range of AVIS-3.

4.2.2 EnMAP Scale Validation and Results

In order to evaluate the capacity of the analysis method for the retrieval of LAI and CCC from EnMAP data, the adapted LUT inversion was carried out on the simulated EnMAP data, based on the identical setting as used for the AVIS-3 data. Since the in-situ data could not be used for model validation on the 30 m spatial scale of the EnMAP data, another approach was chosen, which uses the results of the parameter retrieval based on the airborne image data. Since the estimation accuracy on the 4 m scale of AVIS-3 was proved to be acceptable by validation against in-situ data, the output images were scaled up to the spatial resolution of 30 m, thereby allowing direct comparison of the inversion results achieved with the simulated EnMAP data with the already validated AVIS imagery. However, due to the fact that the AVIS-3 scenes suffer from a lack of SWIR information in some areas, the HySpex scene, acquired at the second flight and covering the whole spectral range within the specification of AVIS-3, served as a basis for the comparison. It is noted that in the further course of the study the HySpex scene is referred to as AVIS-3, since it was spectrally and spatially adapted to the latter. In Figure 4-6, the retrieved LAI image of the EnMAP scene and the upscaled AVIS-3 scene are presented.

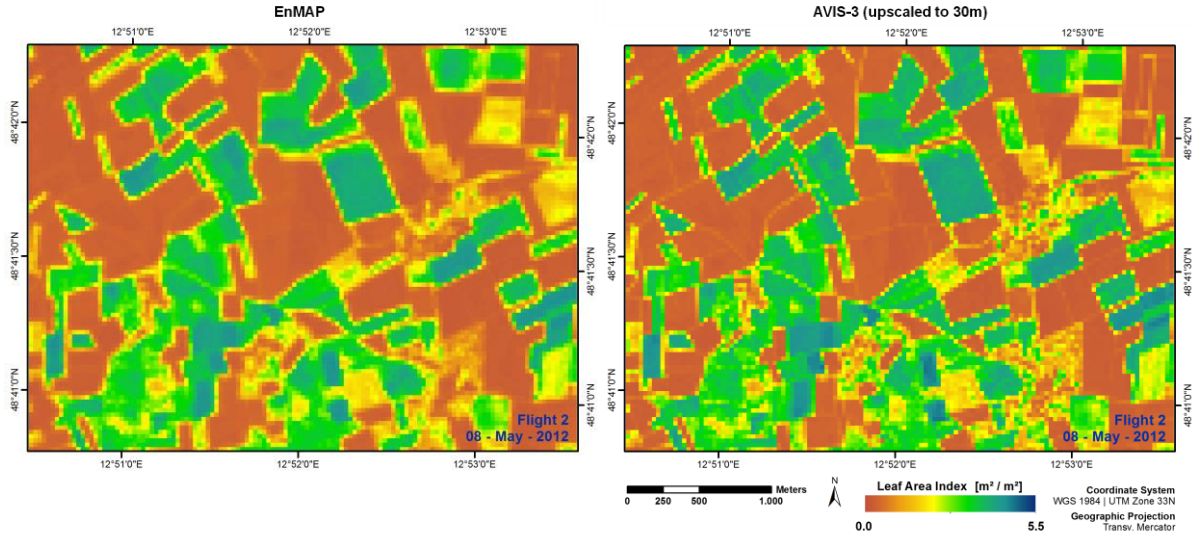

Figure 4-6: Comparison of estimated LAI (second flight), which was derived by the adapted LUT algorithm from the simulated EnMAP data (left) and the upscaled (30 m) LAI estimation based on the 4 m AVIS-3 data (right).

The visual interpretation of the figure shows that the estimations of LAI appear to have led to very similar results in both scenes. Using the set of statistical measures, the conformity

between both images was calculated by confronting each pixel of the LAI-EnMAP map to the corresponding one of the LAI-AVIS-3 map. Figure 4-7 illustrates the correlation between both retrievals and presents the accuracies that were found.

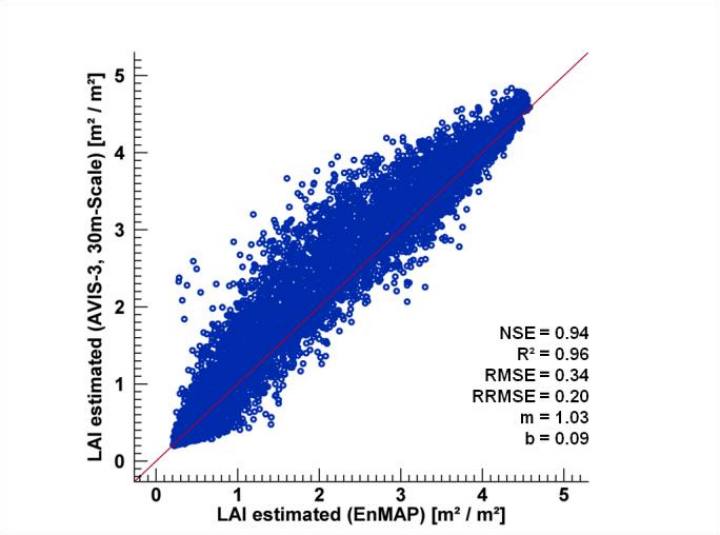

Figure 4-7: Scatter plot and accuracies of the retrieved LAIs of the full scene from May 8th, derived by the application of the LUT inversion to the simulated EnMAP scene and to the AVIS-3 scene, which had been upscaled after the inversion process.

The analysis shows that a very strong agreement exists, as evidenced by the consistently high values of the statistical measures. However, the question arises as to why a significant number of values would have a larger deviation. In order to examine whether these deviations follow a spatial pattern and, if they do, to identify these, a map was calculated showing the difference between the EnMAP and the upscaled AVIS-3 estimation. This is presented in Figure 4-8.

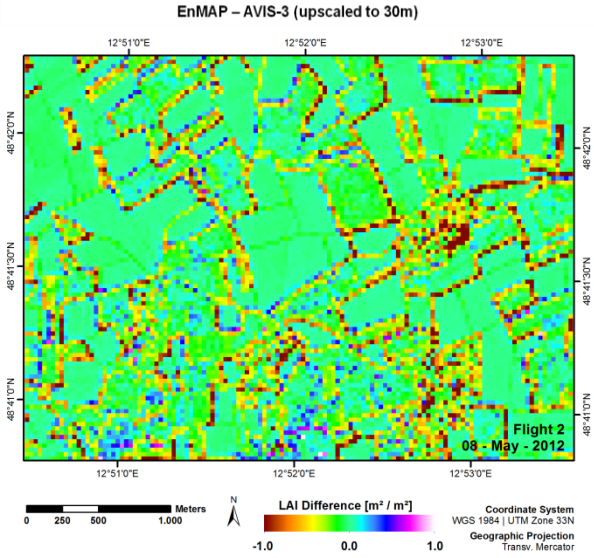

Figure 4-8: Difference map calculated from the LAI estimations of EnMAP and upscaled AVIS-3.

The figure clearly shows that strong difference values occur particularly in the marginal areas of fields, but also along streets and within developed areas such as villages. In these places, the LAI estimation of the airborne data generated almost consistently higher values than the one conducted using EnMAP data. This can be explained by uncertainties arising from differences in the incorporation of heterogeneities in the landscape of the two images, resulting from the different methodologies, by which the two underlying datasets were generated. While the LAI-EnMAP estimation was performed on a simulated dataset, which had been spectrally and spatially resampled prior to the LUT inversion, the LAI-AVIS-3 map was created based on the original dataset and spatially resampled to 30 m after the inversion. This means that, in the simulated EnMAP scene, small-scale heterogeneities had already been compensated for through the spectral redistribution of the nearly 200 reflectance values and the spatial upscaling of the image before the actual parameter retrieval was performed, which explains why the LAI values in these areas are lower. The parameter retrieval conducted on the 4 m scale (AVIS-3 image), however, explicitly took these spatial heterogeneities into account. When the latter was scaled-up afterwards, already existing high LAI values in the 4 m image had a stronger influence on the corresponding 30 m pixels than did the estimation based on the up-scaled reflectance value in the EnMAP scene. Conversely however, this means that for homogenous areas, this kind of scaling problem is not at all or barely existent. The figure shows that this assumption is correct, as hardly any deviation can be determined within the fields themselves. Last but not least, there are areas, especially in the southern part of the study area, in which a positive deviation prevails. Compared to the areas with negative deviation, these areas occur distinctly less often and follow less clear patterns. When compared to the land use map, these areas can be identified as being covered mainly by forest, and can, since they do not represent the agricultural areas focused on in this study, for this reason be ignored.

Nevertheless, in order to minimize the influence of the deviations, the application of a low pass filter to the upscaled LAI image is advisable, since this results in a smoothing of the image. Therefore, two Gaussian low pass filters were applied, based on kernel sizes of 3x3 and 5x5 pixels. Figure 4-9 illustrates the effect of the filters to the image.

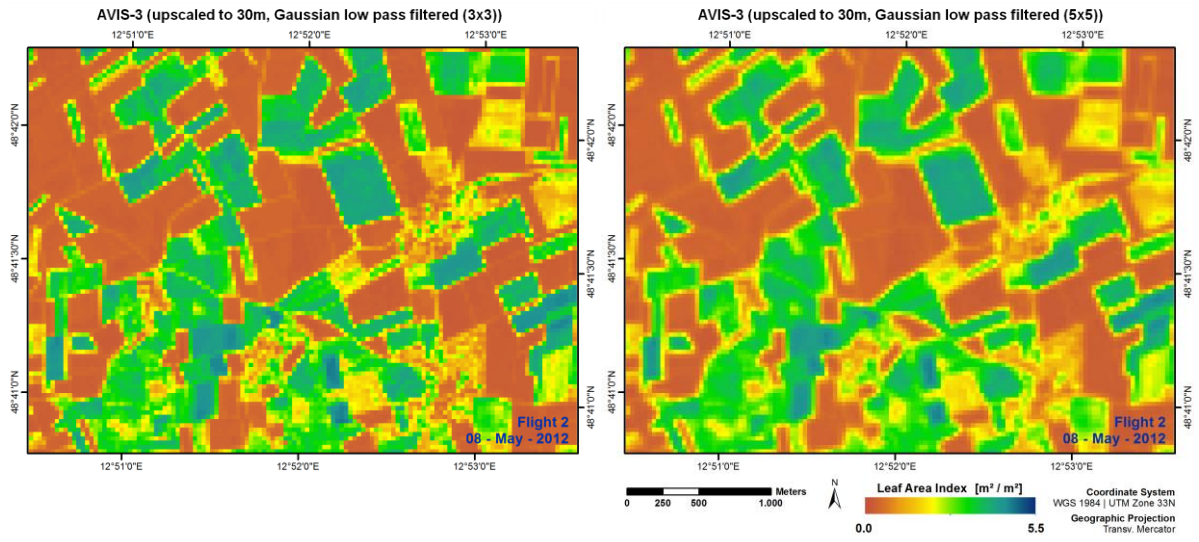

Figure 4-9: Upscaled LAI images after the application of a Gaussian low pass filter with kernel sizes of 3x3 (left) and 5x5 pixels (right).

Whereas the weaker 3x3 filter has only a minor effect on the appearance, the larger 5x5 filter causes a visible smoothing of the image. Both implementations were subtracted from the EnMAP-based LAI map, resulting in an improved conformity and an increase in the statistical agreement, which is presented in Figure 4-10.

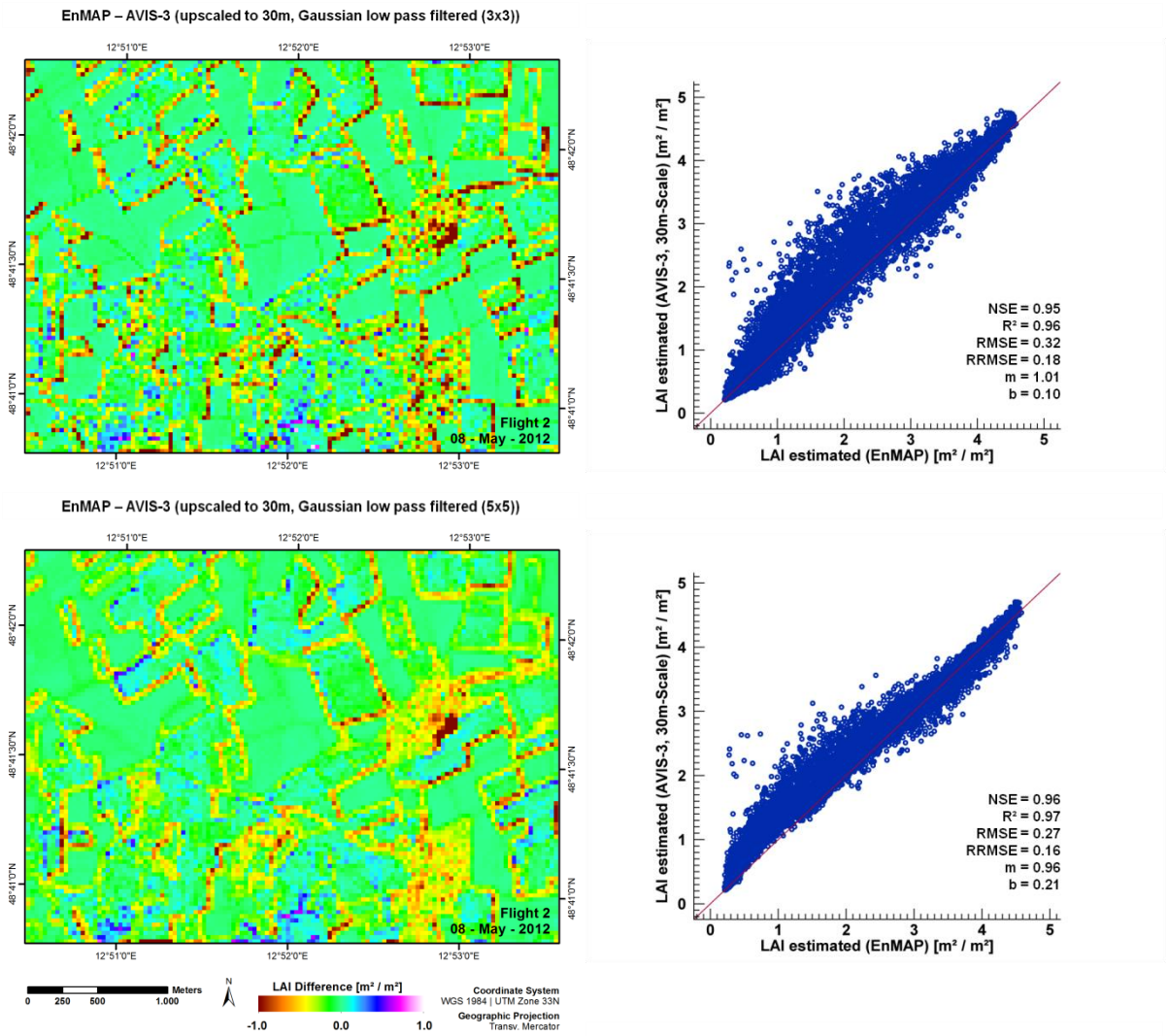

Figure 4-10: Difference maps calculated from the LAI estimations of EnMAP and the low pass filtered, upscaled AVIS-3 scenes (left). On the right side of the figure the corresponding correlation, illustrated by scatter plots, and the accuracies of the statistical measures is shown.

The analysis of the statistical conformity after the application of the low pass filter confirms that the lower filter causes only minor alterations. It does, however, succeed in raising the NSE, R^2, RMSE and RRMSE values. By contrast, the larger filter has a distinctly greater impact on the deviation map, and the statistical correlations thereby obtained. Randomly distributed, larger deviations within the image were to a major extent compensated for, which led to a further increase in accuracy and a visible alteration of the corresponding scatter plot, which is now in better agreement with the line of full conformity (red). The application of the low pass filter led to a reduction of the negative deviation, i.e., of the overestimation of LAIs estimated from the airborne AVIS-3 data compared to those estimated from the EnMAP data. The difference in statistical accuracy thereby achieved is very minimal, while leading to extraordinary good accuracies of NSE=0.96, R^2=0.97, RMSE=0.27, RRMSE=0.16, m=0.96 and b=0.21.

The same procedure was applied in order to examine the capacity for the retrieval of CCC. The results can be summarized by the following correlations and accuracies (Figure 4-11) between the EnMAP image and the three upscaled versions of the AVIS-3 image (original & Gaussian low pass filtered with the corresponding kernel sizes). For reasons of completeness it is noted that the both the estimation and difference maps of CCC can be found in Appendix A.9 and A.10.

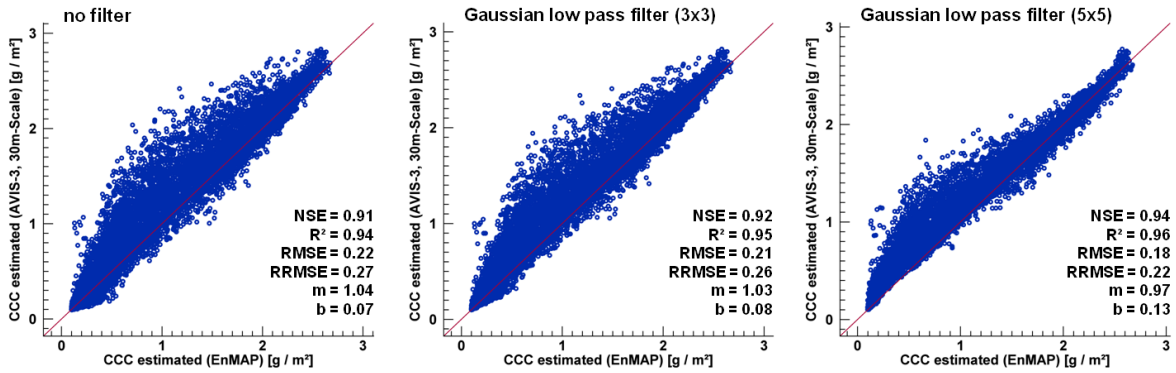

Figure 4-11: Scatter plot and accuracies of the retrieved CCCs of the full scene from May 8th, derived by the application of the LUT inversion to the simulated EnMAP scene and to the AVIS-3 scene, which was upscaled afterwards and to which in two cases (middle and right) a low pass filter was applied.

The scatter plots reveal that a comparable good agreement can be found for CCC as for LAI, even though the accuracy of the statistical measures is somewhat lower.

The results prove that a transfer of the hyperspectral LUT inversion to spaceborne images is possible, with minimal limitations which are mainly caused by the lower spatial resolution of these images. For homogeneous regions, the method showed very good agreement also on the spaceborne scale.

To emphasize the advantage of performing the parameter retrieval based on hyperspectral data as it will be provided by EnMAP, the analysis method for LAI retrieval was also tested on artificial, multispectral Sentinel-2 data. The image data, also simulated by the EeteS tool, provides realistic reflectance values which are based on the spectral responsivity function of the bands of Sentinel-2, which are broader than those of hyperspectral sensors. As described before (see Chapter 3.3.3.1.2), the implementation of an adapted LUT setting applied to the center wavelength of Sentinel-2 led to a lower estimation accuracy than for the full-range setting based on AVIS-3. However, the following analysis aimed at determining how a transfer of the identical analysis method, as applied to EnMAP, impacts the parameter estimation when only Sentinel-2 bands are used.

Consequently, the adapted LUT inversion was carried out on the simulated Sentinel-2 data of the corresponding AVIS-3 flight in the same manner described above. In addition, the retrieved LAI information of the 4 m scale was upscaled to 20 m, according to the spatial resolution of Sentinel-2. The resulting images were then compared to each other. Figure 4-12

shows the deviation between the LAI estimation with Sentinel-2 data and the upscaled LAI image of AVIS-3, which was considered both in original and low pass filtered version with the larger kernel size of 5x5 pixels. It is noted that the corresponding difference maps of CCC can be seen in Appendix A.11.

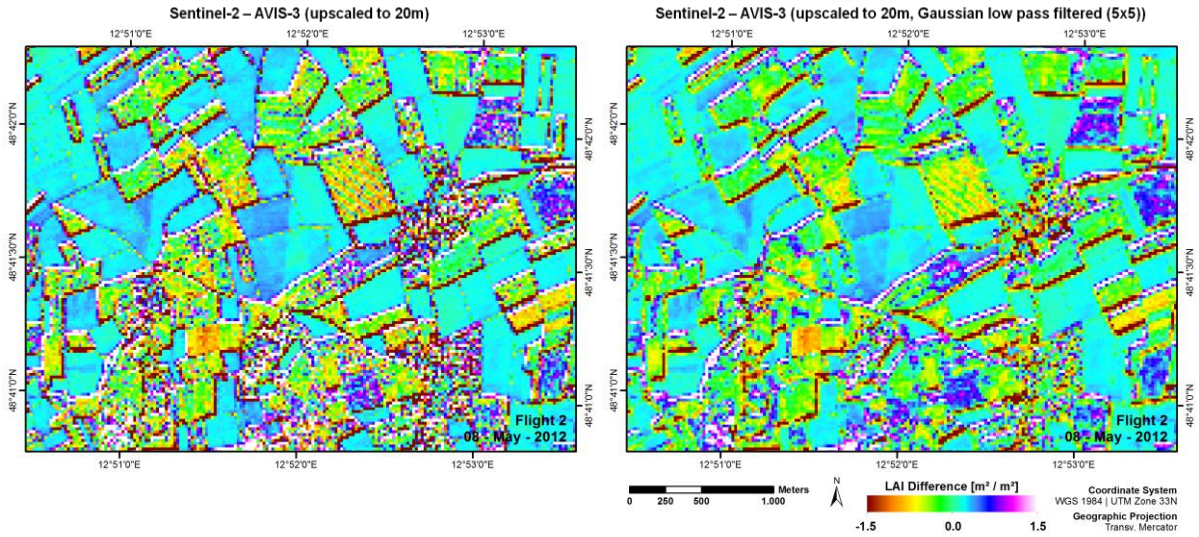

Figure 4-12: Difference maps calculated from the LAI estimations of Sentinel-2 and the original (left) and low pass filtered, and upscaled AVIS-3 scene (right). For the low pass filter the larger kernel size of 5x5 pixels was chosen. When compared to the deviation maps based on EnMAP data in Figure 4-8 and Figure 4-10, the different magnitude of the color bar should be considered.

Compared to the deviation maps based on EnMAP, the resulting images show a much higher deviation, which can also be seen by the difference in scale. The figures show similar patterns of a high deviation at the edge regions of fields and other heterogeneous areas, but in both negative and positive direction. Of substantial relevance, however, is the high deviation also in homogenous, mostly vegetated areas. This persists even after low pass filtering of the upscaled image and is also expressed by the scatter plots given in Figure 4-13.

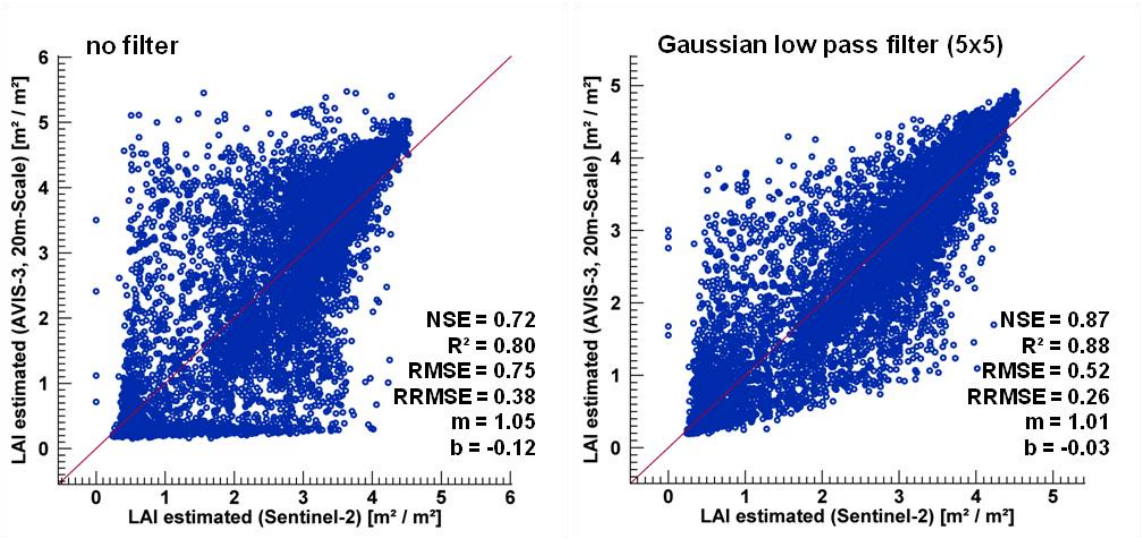

Figure 4-13: Scatter plots and accuracies of the retrieved LAIs of the full scene from May 8th, derived by the application of the LUT inversion to the simulated Sentinel-2 scene and to the AVIS-3 scene, which was up-scaled after the inversion and to which, in the case of the plot to the right, a low pass filter was applied.

The plots show a distinctly higher scattering, which results in lower accuracies among almost all measures (except for slope and intercept). Although the application of the low pass filter led to an improvement of the agreement, the very good conformity of the EnMAP data to the upscaled information fall very short of being achieved. This emphasizes the value added by the use of hyperspectral data compared to multispectral data.

5 Conclusion and Outlook

Based on the data from the extensive field campaign, the validation proved that the LUT approach provides a robust and transparent method for parameter estimation from hyperspectral data, without requiring the use of in-situ data. However, the specification of the different selection criteria on which the final LUT setting was based, including the selection of the bands integrated in the analysis, the type and amount of artificial noise added, the cost function applied to identify the best fit between measured and modeled spectra, and the averaging method for the parameters retrieved from the best-fitting LUT spectra in order to reduce the ill-posed problem, had to be thoroughly considered. Further, the analysis conducted in this study showed that the different selection criteria exerted an influence on the estimation quality that varied strongly, for both LAI and chlorophyll content.

The analysis of the artificial noise, which was added to the modeled spectra to more accurately represent spectra as they are recorded by airborne and spaceborne sensors, led to the realization that it is not of decisive importance which *noise type* is chosen to be added to the simulated reflectances, but more so that some type of noise is added at all. Since both *inverse-multiplicative* and *inverse-combined* noise provided slightly more robust results, it seems reasonable to use one of these for future studies.

Another selection criterion resulting in only minor quality differences was the choice of the cost function. All four tested M-estimators led to a consistent identification of appropriate spectra. As a matter of fact, the mathematically simplest function, represented by the Laplace Distribution, performed best, possibly due to its lower susceptibility to outliers. Due to the slight differences in performance an unambiguous definition of an ideal cost function is, nevertheless, not possible.

By contrast, the integration of a number of multiple solutions, the choice of the method by which they are averaged, and the amount of noise added to the spectra were identified to exert a major impact on estimation quality. The consideration of a multiple number of solutions proved to be an efficient way to handle the ill-posed problem, since the parameters retrieved by the LUT inversion are thereby based not on a single, potentially faulty result, but on a selection of likely solutions. The use of the median rather than the mean as averaging method for the parameter combinations thus retrieved was clearly advantageous. This is attributable to the fact that the median is potentially less sensitive than the mean to outliers among all identified parameters. Further, it was found that adding noise to the simulated data, regardless

of the noise type, allows a more flexible identification of spectra and their corresponding input parameter setting, which was evidenced in distinctly higher accuracies.

Following the recommendation of RICHTER ET AL. (2012), the use of a coordinated set of various statistical measures supported the specification of the selection criteria named above. In consequence, it could be proved that the amount of noise and the number of solutions should both not be set too high, since this would lead to a sort of dilution. Especially when basing the input parameters on a Gaussian distribution, as is the case here, this would compensate for the potential of such a distribution aiming at the precise differentiation of parameter values.

In view of the hyperspectral capacity, it was shown that an increased number of available, and thus considered, spectral bands for the inversion contributed to the achievement of robust results relating to the estimation accuracy of both leaf area index and chlorophyll content, especially when compared to a multispectral band number as provided by Sentinel-2. This can be attributed to the improved precision of the curve fitting when a high number of bands, representing a quasi-continuous reflectance spectrum, are used. However, the estimation accuracy when applying both hyperspectral and multispectral band settings in particular depends on the availability of bands covering the SWIR. This fact may appear surprising, because LAI does not affect the reflectance in this spectral domain to a larger extent than in the VNIR region. In addition, chlorophyll content does not in the least influence the reflectance in the SWIR. However, the integration of this range, which is predominated by the water content, evidently limited the possible solutions and thus supported a more precise deduction of the vegetation parameters.

EnMAP, which meets these requirements by supplying a number of bands for a contiguous high-quality representation of the surface's reflectance, therefore enables an accurate multiseasonal analysis of vegetation parameters on a regional scale. By transferring the method, which proved to be consistent and robust for the estimation of vegetation parameters, to the scale of the satellite sensor, it was shown that an application of the LUT approach to the spaceborne data with its different spatial and spectral properties is possible.

A further increase in the estimation accuracy might result from the use of the wider spectral range of EnMAP, covering also the spectral region from 1700 nm to 2450 nm, which is referred to as SWIR 2. The effect of taking this range into account could not be analyzed with AVIS-3 data, thus a further examination should be the subject of future studies. As part of such investigations, the biophysical and biochemical parameters examined should be extended, including well-known properties, such as leaf water content, but also comparatively complicated parameters, which are difficult to grasp, e.g., the structural parameter N. This would, on the one hand, deepen the understanding of the nature and composition of radiative transfer models, such as the combined PROSAIL model, leading ultimately to their

improvement. On the other hand, such studies would allow a more detailed description of processes in vegetation canopies throughout the growing period, described by the phenological status of the plant, which currently is difficult to determine from remote sensing data alone. By supplying the high-quality data in the exceptionally temporal frequency of at least 23 days EnMAP has the potential to significantly advance the research in these fields.

6 Summary

With the imminent initiation of the hyperspectral satellite mission EnMAP, a powerful instrument for the generation of Earth Observation Data will become available. From 2017 onwards, EnMAP will, for the first time, enable the retrieval of multiseasonal hyperspectral observation series from space. For agricultural applications this offers the highly relevant opportunity of retrieving information on the seasonal development of vegetation parameters not only for single plots, but on a regional scale. The knowledge of the seasonal development of crop parameters represents a key product of agricultural information in the context of precision farming and is thus extremely valuable.

The purpose of this study was to investigate whether an analysis method for the retrieval of biophysical and biochemical parameters based on hyperspectral image data, developed and validated on an airborne scale, is transferable to the spaceborne scale corresponding to the future EnMAP mission. Two major subjects were defined in this regard: data supply and data analysis.

Since EnMAP data is not yet available, an alternative data basis had to be created using airborne imaging spectrometers and capturing the development of different crops within a growing season. As commercial airborne sensors suffer from a limited availability and are often cost-intensive, the Airborne Visible and Near Infrared Imaging Spectrometer (AVIS) was developed at the Department of Geography of the LMU Munich to achieve this goal. The third-generation sensor, AVIS-3, equipped with two camera systems covering VNIR and SWIR, was used to establish a multiseasonal database of a 12 km² sized study site dominated by agricultural use in Lower Bavaria, Germany. By that means, the database obtained encompassed recordings on four different dates within the growing period of 2012 and was complemented by two acquisitions from the airborne sensor HySpex, operated by the German Aerospace Center (DLR). As a result, six individual acquisitions were acquired which served as the basis for the development of an analysis algorithm by which vegetation parameters can be retrieved. Parallel to the airborne acquisitions, an extensive field campaign was conducted, during which more than 500 in-situ measurements of, in particular, leaf area index (LAI) and canopy chlorophyll content (CCC) of different crops were gathered, as these are very important variables for the monitoring of the current status of plant and canopy physiology.

Before the data was analyzed with a view to its potential for parameter retrieval, the spectral properties of AVIS-3 had to be characterized in the laboratory, followed by the preprocessing of the recorded image data. This included the processing steps of sensor calibration, geometric

correction and radiometric calibration to transform the measured grey values to reflectance values. The preprocessing resulted in 197 bands covering a spectral range from 477 to 1704 nm and a corresponding ground sampling distance of 4 m. In order to enable comparability, the HySpex data was spectrally and spatially resampled to correspond to the specifications of AVIS-3.

Since it was a goal of the study to investigate the transferability of an analysis method to the EnMAP scale, the acquired data served not only the evaluation of an appropriate estimation technique, but also the simulation of EnMAP data. By the use of the EnMAP-end-to-end-Simulator, called EeteS, developed and conducted by the GFZ German Research Centre for Geosciences in Potsdam, the airborne data was converted to simulated raw sensor data (DN) by its forward simulation module, with respect to the spectral and spatial properties of the hyperspectral imager onboard the satellite. Afterwards it was subjected to a simulated on-board calibration, followed by conversion to realistic reflectance values and a ground sampling distance of 30 m in its backward simulating tool.

Subsequently, the data obtained was used for the second aim of this study – the determination of a unified method enabling the retrieval of LAI and CCC from remote sensing data without requiring the input of in-situ information, thereby validated, however, for all data acquisitions in this study. This led to the investigation of physically based methods, such as the inversion of canopy reflectance models. Quite in contrast to empirical-statistical models, such as vegetation indices, which have to be calibrated against in-situ data if they are to be used for the derivation of actual vegetation variables, physically based methods can be applied without using in-situ data. Moreover, empirical-statistical methods have the disadvantage of a limited transferability and are sensitive to anisotropy effects resulting from a variable sun-sensor-target geometry within the airborne data, which, by contrast, are explicitly taken into account by physically based models. Consequently, the information on observer zenith and azimuth angles of AVIS-3 was stored in the image data for each pixel as additional bands, allowing the corresponding illumination geometry to be considered during the analysis.

The leaf optical properties model (PROSPECT5) and the canopy bidirectional reflectance model (4SAIL), combined in the PROSAIL model, were used for the physically based retrieval of land surface parameters. This model simulates realistic reflectance data for homogeneously vegetated surfaces and thus makes it most suitable for the application in an agricultural context. Based on various biophysical input parameters the model simulates corresponding reflectance spectra. The model had to be inverted since the parameters underlying the modeled spectra are the target variables of this study. There are several inversion techniques described in the literature, which differ in computation speed, robustness and performance. The most common inversion techniques for parameter retrieval are numerical optimization algorithms, artificial neural networks (ANNs) and look-up tables (LUTs). Due to its simplicity, transparency and robustness, the LUT approach was chosen for

this study. The 100 000 simulated spectra stored in the LUT, including the vegetation parameters by which they were produced, were generated by the PROSAIL model and were based on a specific range of input parameter combinations. To take the various illumination geometries into account, this step was repeated for several classes of different observer zenith and azimuth angles, as well as for the different sun position among all six flights, resulting in a LUT library including a total of 83 600 000 spectra. When applied to the image data, a cost function searched for the highest agreement between the measured signal and the spectra stored within the LUT. The underlying parameter combination of the best fitting modeled spectrum is, within this method, assumed to represent the biophysical variables to be retrieved in a physically meaningful way. However, model results are often ill-posed, which means that the solution found by the cost function might not correspond to the parameters which caused this reflectance in reality, since various input parameter combinations to the model can produce almost identical reflectance spectra. To counteract this problem, multiple solutions were considered and their corresponding input parameters averaged. In addition to the ideal number of considered solutions, further selection criteria influence the model accuracy, such as the averaging method, the choice of cost function as well as the amount of artificial noise added to the simulated reflectance data within the LUT, to provide more flexibility in finding the optimal solution. For a systematical evaluation of the ideal combination of the selection criteria, these were combined in different configurations, resulting in 17 640 individual inversion processes applied to the data and analyzed with regard to their performance.

In order to validate the estimation accuracy using the relevant in-situ measurements, a set of statistical measures was introduced (R^2, RMSE, RRMSE, NSE as well as slope and intercept of Theil-Sen regression), allowing an accurate identification of potential weaknesses in the retrieval quality. It was found that in particular the averaging method, the amount of noise and the number of considered solutions were of distinctive relevance to the model performance. Finally, a combination of LUT criteria was found that led to acceptable results for both leaf area index and canopy chlorophyll content.

In addition to the identification of the ideal model configuration, the value added by the use of the high number of bands supplied by hyperspectral data was examined. This was achieved by comparing the resulting accuracies of the LUT inversion by applying the full range of AVIS-3, excluding the bands affected by atmospheric water vapor absorption, to the accuracies resulting from the LUT inversion based on the band combination of the future multispectral Sentinel-2 mission. The comparison revealed that the use of a hyperspectral band setting led to a distinctly higher estimation accuracy than the multispectral band setting.

Consequently, it was shown that hyperspectral sensors hold the highest potential among the available remote sensing techniques to provide data for an accurate estimation of several biophysical parameters, with an analysis method which was proven to be both consistent and robust and applicable to multiseasonal datasets. In a final stage, the LUT inversion was

adapted to the bands of the simulated EnMAP data and validated against upscaled results of the airborne parameter estimation. Thus it was shown that the determined analysis method can be applied successfully to data supplied by the upcoming EnMAP mission.

7 Zusammenfassung (German)

Ab 2017 wird die hyperspektrale Satellitenmission EnMAP erstmals hochwertige Erdbeobachtungsdaten bereitstellen, die eine Ableitung regelmäßiger multisaisonaler Informationen aus dem All ermöglichen wird. Für landwirtschaftliche Anwendungen bietet dies die Möglichkeit, aus diesen Daten relevante Informationen über die saisonale Entwicklung von einzelnen Vegetationsparametern auf regionaler Ebene abzuleiten. Kenntnisse über die die Entwicklung dieser Parameter stellen ein wertvolles Schlüsselprodukt zur landwirtschaftlichen Informationsbereitstellung dar, gerade im Kontext der sogenannten Präzisionslandwirtschaft.

Das Ziel dieser Studie war es zu untersuchen, ob eine Analysemethode zur Ableitung biophysikalischer und biochemischer Blatt- und Bestandesparameter, die auf der Auswertung flugzeuggetragener hyperspektraler Sensordaten basiert, auf eine Skala entsprechend der EnMAP-Mission übertragen werden kann. In diesem Zusammenhang wurden demnach zwei vorrangige Ziele definiert: Datenbereitstellung und Datenanalyse.

Da EnMAP-Daten noch nicht verfügbar sind, musste anhand flugzeuggetragener abbildender Spektrometer eine alternative Datenbasis geschaffen werden, welche die Entwicklung landwirtschaftlicher Kulturen innerhalb einer Wachstumsperiode adäquat wiedergeben kann. Tatsächlich aber sind kommerzielle abbildende Spektrometer sehr kostenintensiv oder nur unregelmäßig verfügbar, was schließlich zur Entwicklung des abbildenden Spektrometers AVIS (Airborne Visible and Near Infrared Imaging Spectrometers) am Institut für Geographie der LMU München führte. AVIS, mittlerweile in der dritten Generation und mit zwei Kamerasystemen ausgestattet, diente daher für die Generierung einer multisaisonalen Datenbasis eines 12 km² großen und landwirtschaftlich geprägten Untersuchungsgebietes in Neusling, Niederbayern. So konnten während der Wachstumsphase 2012 insgesamt vier Datenakquisitionen durchgeführt werden, ergänzt durch zwei weitere Aufnahmen des flugzeuggetragenen Sensors HySpex, welches vom Deutschen Zentrum für Luft- und Raumfahrt betrieben wird. Die insgesamt sechs Aufnahmen dienten als Grundlage zur Entwicklung und Validierung eines Analysealgorithmus zur Ableitung von Vegetationsparametern. Parallel zu den Datenakquisitionen aus der Luft wurde eine umfangreiche Feldkampagne mit mehr als 500 Messungen durchgeführt, bei der der Fokus auf die Aufnahme von Blattflächenindex (engl. leaf area index, LAI) und Chlorophyllgehalt lag, da diese wichtige Größen für das Monitoring des aktuellen Zustands der Vegetation und der Bestandesphysiologie sind.

Bevor die Hyperspektraldaten aber hinsichtlich ihres Potentials zur Parameterabschätzung analysiert werden konnten, mussten die spektralen Eigenschaften von AVIS-3 im Labor charakterisiert und die gewonnen Bilddaten vorprozessiert werden. Dies umfasste folgende Verarbeitungsschritte: Sensorkalibrierung, geometrische Korrektur sowie radiometrische Kalibrierung, bei der die gemessenen Grauwerte in spektrale Reflektanzen umgewandelt wurden. Die Prozessierung der Daten resultierte schließlich in einer spektralen Abdeckung von 477 bis 1704 nm in 197 Kanälen und einer geometrischen Auflösung von 4 m pro Pixel. Um eine Vergleichbarkeit der HySpex-Daten mit den AVIS-3-Daten zu gewährleisten, wurden erstere entsprechend den räumlichen und spektralen Spezifikationen von AVIS-3 angepasst.

Da es ein Ziel der Studie war die Übertragbarkeit eines Analyseverfahrens auf die EnMAP-Skala zu untersuchen, dienten die Daten nicht nur für die Erprobung eines entsprechenden Schätzverfahrens, sondern auch zur Simulation künstlicher EnMAP-Daten. Hierfür wurde das Simulationstool „EeteS“ (EnMAP-end-to-end-Simulator) des GeoForschungszentrum GFZ Potsdam zurande gezogen, welches aus den Flugzeugdaten simulierte Rohdaten von EnMAP berechnete. Dabei wurden insbesondere die spektralen und räumlichen Eigenschaften des Satellitensensors berücksichtigt. Die Rohdaten wurden dann einer simulierten On-board-Kalibrierung unterzogen und anschließend entsprechend einer atmosphärischen und geometrischen Korrektur in realistische Reflektanzwerte und einer geometrischen Auflösung von 30 m konvertiert.

Die aufbereitenden Daten konnte anschließend für das zweite Ziel der Studie verwendet werden – der Definierung einer einheitlichen Methode zur Ableitung von LAI und Chlorophyllgehalt aus Fernerkundungsdaten ohne auf in-situ Messungen angewiesen zu sein, diese wurden lediglich zur Validierung eingesetzt. Dies führte zur Untersuchung physikalisch-basierter Methoden wie der Invertierung von Bestandesreflexionsmodellen. Im Gegensatz zu empirisch-statistischen Methoden, wie beispielsweise Vegetationsindizes, die erst gegen in-situ Messungen kalibriert werden müssen um biophysikalische Parameter abzuleiten, sind physikalisch-basierte Methoden unabhängig von in-situ Messungen. Darüber hinaus haben empirisch-statistische Methoden den Nachteil, dass sie kaum übertragbar sind und des Weiteren empfindlich auf Anisotropieeffekte reagieren, die sich aus einer variable Sonnen-Ziel-Sensor Geometrie bei flugzeuggetragenen Aufnahmen ergeben. Physikalisch-basierte Modell hingegen berücksichtigen diese ausdrücklich. Infolgedessen wurden Zenit- und Azimutwinkel des Sensors, gemessen für jedes aufgenommene Pixel, als zusätzliche Kanäle in den Daten abgespeichert, so dass die entsprechende Beleuchtungsgeometrie bei der Analyse berücksichtigt werden konnte.

Als physikalisch-basierte Methode zur Abschätzung von Vegetationsparameter diente das optische Blattflächen Modell PROSPECT5, sowie das bidirektionale Reflexionsmodell SAIL4, kombiniert zu PROSAIL. Dieses ist in der Lage realistische Reflektanzen für

homogene Oberflächen zu simulieren und eignet sich daher insbesondere für eine Anwendung in einem landwirtschaftlichen Kontext. Das Modell simuliert Reflexionsspektren nach Eingabe verschiedener Blatt- und Bestandesparameter. Da diese Eingabeparameter das eigentliche Ziel darstellen, musste das Modell invertiert werden. Hierfür werden in der Literatur verschiedene Methoden beschrieben, die sich in Rechengeschwindigkeit, Stabilität und Leistung unterscheiden. Die häufigsten Inversionstechniken sind dabei numerische Optimierungsalgorithmen, künstliche neuronale Netze (engl. artificial neural network, ANN) und Look-Up Tabellen (LUT). Infolge seiner Einfachheit, Robustheit und Transparenz wurde der LUT Ansatz für diese Studie gewählt. Basierend auf spezifischen Parameterkombinationen simulierte PROSAIL 100 000 verschiedene Reflexionswerte, die zusammen mit ihren Eingabeparametern im LUT gespeichert wurden. Um variierender Beleuchtungsgeometrien Rechnung zu tragen, wurde dieser Schritt für mehrere Klassen verschiedener Zenit- und Azimutwinkel des Sensors sowie für die unterschiedlichen Sonnenpositionen zwischen den sechs Flügen mehrfach wiederholt, was schließlich zu einer Bibliothek von Look-Up Tabellen geführt hat, in der insgesamt 83 600 000 Spektren abgespeichert sind. Bei Anwendung der Tabelle auf die Bilddaten suchte eine Kostenfunktion die größte Übereinstimmung zwischen dem gemessenen Spektrum eines Pixels und den Spektren aus der Look-Up Tabelle. Dabei wird angenommen, dass die zugrunde liegende Parameterkombination des am besten passenden modellierten Reflexionsspektrums die gesuchten Variablen repräsentiert. Allerdings sind die Modellergebnisse oftmals mathematisch schlecht gestellt (engl. ill-posed), das heißt dass die identifizierte Lösung den tatsächlichen Parametern nicht entsprechen muss. Dies ist zurückzuführen auf das Modell, das bei Eingabe verschiedener Parameterkombination nahezu identische Reflexionsspektren erzeugen kann. Um diesem Problem entgegenzuwirken, wurde eine multiple Anzahl der jeweils besten Übereinstimmungen für die Ableitung berücksichtigt und die entsprechenden Eingabeparameter gemittelt. Neben der gesuchten idealen Anzahl berücksichtigter Lösungen beeinflussen weitere Auswahlkriterien die Modellgenauigkeit, darunter die Methode zur Mittelung, die Wahl der Kostenfunktion und der Anteil von künstlichem Rauschen, das den modellierten Spektren hinzugefügt wurde, um ein erhöhte Flexibilität bei der Suche der optimalen Lösung zu ermöglichen. Für eine systematische Auswertung der idealen Kombination von Auswahlkriterien wurden diese in verschiedenen Konfigurationen kombiniert, was insgesamt zu 17 640 individuellen Inversionsprozessen geführt hat, die auf die Daten angewendet wurden und anschließend entsprechend ihrer Leistungsfähigkeit untersucht worden sind.

Um die Schätzgenauigkeit des Modells mittels der entsprechenden in-situ Messungen präzise validieren zu können, wurde ein Set statistischer Maße verwendet (R^2, RMSE, RRMSE, NSE, sowie Steigung und Schnittpunkt der Theil-Sen Regression), das es erlaubt potentielle Schwachstellen in der Schätzungsqualität nachweisen zu können. Auf diese Weise zeigte sich,

dass insbesondere die Mittelungsmethode, die Menge von künstlichem Rauschen sowie die Anzahl der berücksichtigten Spektren entscheidenden Einfluss auf die Performance des Modells haben. Schließlich konnte eine Kombination identifiziert werden, die es erlaubt sowohl Blattflächenindex als auch Chlorophyllgehalt ausreichend genau abzuschätzen.

Neben der Identifizierung der idealen Modellkonfiguration wurde ebenso die Anzahl der spektralen Kanäle untersucht, die bei der Inversion berücksichtigt werden. Um den potentiellen Mehrwert der Hyperspektraldaten zu überprüfen, wurde das Ergebnis der Inversion, welches auf dem gesamten Spektrum der zur Verfügung stehenden Kanäle abzüglich der von Wasserdampfabsorption betroffenen basiert, verglichen mit einer reduzierten Inversion, die auf den Spektralkanälen der zukünftigen multispektralen Sentinel-2 Mission basiert. Der Vergleich zeigte, dass die Verwendung der Vielzahl hyperspektraler Kanäle eine deutlich höhere Schätzgenauigkeit erzielt, als wenn lediglich eine multispektrale Auswahl berücksichtigt wird.

In der Folge wurde gezeigt, dass bei den zur Verfügung stehenden Fernerkundungstechniken hyperspektrale Sensoren das größte Potential aufweist Daten bereitzustellen, die eine Ableitung biophysikalischer Parameter ermöglichen. Es zeigte sich, dass der untersuchte Ansatz eine einheitliche und robuste Analysemethode darstellt, die für eine Anwendung auf multisaisonale Daten geeignet ist. Zu guter Letzt wurde die LUT Inversion entsprechend der simulierten EnMAP Daten angepasst und das Ergebnis gegen jenes validiert, welches auf der Auswertung der flugzeuggetragenen Daten basiert. Dabei konnte bewiesen werden, dass die definierte Analysemethode erfolgreich auf die zukünftigen EnMAP Daten angewendet werden kann.

8 References

ALLEN, W. A., GAUSMAN, H. W., & RICHARDSON, A. J. (1970): Mean effective optical constants of cotton leaves. *JOSA, 60*(4), 542-547.

ALLEN, W. A., GAUSMAN, H. W., & RICHARDSON, A. J. (1973): Willstätter-Stoll theory of leaf reflectance evaluated by ray tracing. *Applied Optics, 12*(10), 2448-2453.

ALLEN, W. A., GAUSMAN, H. W., RICHARDSON, A. J., & THOMAS, J. R. (1969): Interaction of isotropic light with a compact plant leaf. *JOSA, 59*(10), 1376-1379.

ANDRIEU, B., BARET, F., JACQUEMOUD, S., MALTHUS, T., & STEVEN, M. (1997): Evaluation of an improved version of SAIL model for simulating bidirectional reflectance of sugar beet canopies. *Remote Sensing of Environment, 60*(3), 247-257.

ATKINSON, P. M., & TATNALL, A. R. L. (1997). Introduction neural networks in remote sensing. *International Journal of Remote Sensing, 18*(4), 699-709.

ATZBERGER, C. (2004): Object-based retrieval of biophysical canopy variables using artificial neural nets and radiative transfer models. *Remote Sensing of Environment, 93*(1), 53-67.

ATZBERGER, C., JARMER, T., SCHLERF, M., KÖTZ, B., & WERNER, W. (2003): Retrieval of wheat biophysical attributes from hyperspectral data and SAILH+ PROSPECT radiative transfer model. In *Proceedings of the 3rd EARSeL Workshop on Imaging Spectroscopy* (pp. 473-482).

BACH, H. (1995): *Die Bestimmung hydrologischer und landwirtschaftlicher Oberflächenparameter aus hyperspektralen Fernerkundungsdaten*. Münchner Geographische Abhandlungen, Reihe B, Band 21.

BACH, H., MAUSER, W., & SCHNEIDER, K. (2003): The use of radiative transfer models for remote sensing data assimilation in crop growth models. *Precision Agriculture, J. Stafford, A. Werner (ed.), ISBN, 487063621*, 35-40.

BACOUR, C., BARET, F., BEAL, D., WEISS, M., & PAVAGEAU, K. (2006): Neural network estimation of LAI, fAPAR, fCover and LAI×C_{ab}, from top of canopy MERIS reflectance data: Principles and validation. *Remote Sensing of Environment, 105*(4), 313-325.

BARET, F., & BUIS, S. (2008): Estimating canopy characteristics from remote sensing observations: review of methods and associated problems. In *Advances in Land Remote Sensing* (pp. 173-201). Springer Netherlands.

BARET, F., & FOURTY, T. (1997): Estimation of leaf water content and specific leaf weight from reflectance and transmittance measurements. *Agronomie*, *17*(9-10), 455-464.

BARET, F., & GUYOT, G. (1991). Potentials and limits of vegetation indices for LAI and APAR assessment. *Remote Sensing of Environment*, *35*(2), 161-173.

BARET, F., HAGOLLE, O., GEIGER, B., BICHERON, P., MIRAS, B., HUC, M., BERTHELOT, B., NIÑO, F, WEISS, M., SAMAIN, O., ROUJEAN, J. L. & LEROY, M. (2007): LAI, fAPAR and fCover CYCLOPES global products derived from VEGETATION: Part 1: Principles of the algorithm. *Remote Sensing of Environment*, *110*(3), 275-286.

BARET, F., JACQUEMOUD, S., GUYOT, G., & LEPRIEUR, C. (1992): Modeled analysis of the biophysical nature of spectral shifts and comparison with information content of broad bands. *Remote Sensing of Environment*, *41*(2), 133-142.

BARNSLEY, M. J., SETTLE, J. J., CUTTER, M. A., LOBB, D. R., & TESTON, F. (2004): The PROBA/CHRIS mission: A low-cost smallsat for hyperspectral multiangle observations of the earth surface and atmosphere. *Geoscience and Remote Sensing, IEEE Transactions on*, *42*(7), 1512-1520.

BAUMGARTNER, A., GEGE, P., KÖHLER, C., LENHARD, K., & SCHWARZMAIER, T. (2012): Characterisation methods for the hyperspectral sensor HySpex at DLR's calibration home base. In *SPIE Remote Sensing* (pp. 85331H-85331H). International Society for Optics and Photonics.

BLACKMER, T. M., SCHEPERS, J. S., VARVEL, G. E., & WALTER-SHEA, E. A. (1996): Nitrogen deficiency detection using reflected shortwave radiation from irrigated corn canopies. *Agronomy Journal*, *88*(1), 1-5.

BOREL, C. C., GERSTL, S. A., & POWERS, B. J. (1991): The radiosity method in optical remote sensing of structured 3-D surfaces. *Remote Sensing of Environment*, *36*(1), 13-44.

BOUSQUET, L., LACHÉRADE, S., JACQUEMOUD, S., & MOYA, I. (2005): Leaf BRDF measurements and model for specular and diffuse components differentiation. *Remote Sensing of Environment*, *98*(2), 201-211.

BRAKKE, T. W., & SMITH, J. A. (1987): A ray tracing model for leaf bidirectional scattering studies. *International Geoscience and Remote Sensing Symposium* (IGARSS 1987), Ann Arbor, MI, *18-21 May 1987, pp. 643-648.*

BRÉDA, N. J. (2003). Ground-based measurements of leaf area index: a review of methods, instruments and current controversies. *Journal of Experimental Botany*, *54*(392), 2403-2417.

CAMPBELL, G. S. (1986): Extinction coefficients for radiation in plant canopies calculated using an ellipsoidal inclination angle distribution. *Agricultural and Forest Meteorology*, *36*(4), 317-321.

CEROVIC, Z. G., OUNIS, A., CARTELAT, A., LATOUCHE, G., GOULAS, Y., MEYER, S., & MOYA, I. (2002): The use of chlorophyll fluorescence excitation spectra for the non-destructive in-situ assessment of UV-absorbing compounds in leaves. *Plant, Cell & Environment*, *25*(12), 1663-1676.

CLEVERS, J. G. P. W., & VERHOEF, W. (1993): LAI estimation by means of the WDVI: A sensitivity analysis with a combined PROSPECT-SAIL model. *Remote Sensing Reviews*, *7*(1), 43-64.

COCKS, T., JENSSEN, R., STEWART, A., WILSON, I., & SHIELDS, T. (1998): The HyMapTM airborne hyperspectral sensor: the system, calibration and performance. In *1st EARSeL Workshop on Imaging Spectrometry* (pp. 37-42).

COLLINS, W. & CHANG, S.-H. (1990): Commercial spectroscopy with the geophysical research imaging spectrometer (geris). In *Proceedings of the Technical Symposium on Optical Engineering and Photonics in Aerospace Sensing*, vol. 1298, pp. 61–72, Society of Photo-Optical Instrumentation Engineers (SPIE)

COMBAL, B., BARET, F., WEISS, M., TRUBUIL, A., MACE´, D.,PRAGNE`RE, A., ET AL. (2002): Retrieval of canopy biophysical variables from bidirectional reflectance using prior information to solve the ill-posed inverse problem. *Remote Sensing of Environment*, 84, pp. 1– 15.

CORSON, M. R., KORWAN, D. R., LUCKE, R. L., SNYDER, W. A., & DAVIS, C. O. (2008): The hyperspectral imager for the coastal ocean (HICO) on the international space station. In *Geoscience and Remote Sensing Symposium (IGARSS), 2008 IEEE International* (Vol. 4, pp. IV-101). IEEE.

CURRAN, P. J. (1989): Remote sensing of foliar chemistry. *Remote Sensing of Environment*, *30*(3), 271-278.

CURRAN, P. J. (1994). Imaging spectrometry. *Progress in Physical Geography*, *18*(2), 247-266.

CUTTER, M. & LOBB, D. (2004, June): Design of the compact high-resolution imaging spectrometer (CHRIS), and future developments. In *Proc. 5th Intl. Conf. Space Opt* (p. 41).

DANSON, F. M., & ALDAKHEEL, Y. Y. (2000): Diurnal water stress in sugar beet: Spectral reflectance measurements and modelling. *Agronomie*, *20*(1), 31-39.

DARVISHZADEH, R., ATZBERGER, C., SKIDMORE, A., & SCHLERF, M. (2011): Mapping grassland leaf area index with airborne hyperspectral imagery: a comparison study of statistical approaches and inversion of radiative transfer models. *ISPRS Journal of Photogrammetry and Remote Sensing*, *66*(6), 894-906.

DARVISHZADEH, R., MATKAN, A. A., & AHANGAR, A. D. (2012): Inversion of a radiative transfer model for estimation of rice canopy chlorophyll content using a lookup-table approach. *Selected Topics in Applied Earth Observations and Remote Sensing, IEEE Journal of, 5*(4), 1222-1230.

DARVISHZADEH, R., SKIDMORE, A., SCHLERF, M., & ATZBERGER, C. (2008): Inversion of a radiative transfer model for estimating vegetation LAI and chlorophyll in a heterogeneous grassland. *Remote Sensing of Environment, 112*(5), 2592-2604.

DATT, B. (1998): Remote Sensing of Chlorophyll a, Chlorophyll b, Chlorophyll a+b, and Total Carotenoid Content in Eucalyptus Leaves. *Remote Sensing of Environment, 66*(2), 111-121.

DEERING, D. W., & HARLAN, J. C. (1974): *Monitoring the vernal advancement and retrogradation (greenwave effect) of natural vegetation* (p. 371). Texas A & M University, Remote Sensing Center.

DURBHA, S. S., KING, R. L., & YOUNAN, N. H. (2007): Support vector machines regression for retrieval of leaf area index from multiangle imaging spectroradiometer. *Remote Sensing of Environment, 107*(1), 348-361.

FERET, J. B., FRANÇOIS, C., ASNER, G. P., GITELSON, A. A., MARTIN, R. E., BIDEL, L. P., USTIN, S. L., LE MAIRE, G. & JACQUEMOUD, S. (2008): PROSPECT-4 and 5: Advances in the leaf optical properties model separating photosynthetic pigments. *Remote Sensing of Environment, 112*(6), 3030-3043.

FERNANDES, R., & G LEBLANC, S. (2005): Parametric (modified least squares) and non-parametric (Theil–Sen) linear regressions for predicting biophysical parameters in the presence of measurement errors. *Remote Sensing of Environment, 95*(3), 303-316.

FONTENLA, J., WHITE, O. R., FOX, P. A., AVRETT, E. H., & KURUCZ, R. L. (1999): Calculation of solar irradiances. I. Synthesis of the solar spectrum. *The Astrophysical Journal, 518*(1), 480.

FOURTY, T., BARET, F., JACQUEMOUD, S., SCHMUCK, G., & VERDEBOUT, J. (1996): Leaf optical properties with explicit description of its biochemical composition: direct and inverse problems. *Remote Sensing of Environment, 56*(2), 104-117.

GAO, J. (2006): *Canopy chlorophyll estimation with hyperspectral remote sensing* (Doctoral dissertation, Kansas State University).

GARABEDIAN, P. (1964): *Partial Differential Equations*. Wiley. New York.

GAUSMAN, H. W., ALLEN, W. A., CARDENAS, R., & RICHARDSON, A. J. (1970): Relation of light reflectance to histological and physical evaluations of cotton leaf maturity. *Applied Optics, 9*(3), 545-552.

GITELSON, A. A., & MERZLYAK, M. N. (2003): Relationships between leaf chlorophyll content and spectral reflectance and algorithms for non-destructive chlorophyll assessment in higher plant leaves. *Journal of Plant Physiology*, *160*(3), 271-282.

GITELSON, A. A., ZUR, Y., CHIVKUNOVA, O. B., & MERZLYAK, M. N. (2002): Assessing Carotenoid Content in Plant Leaves with Reflectance Spectroscopy. *Photochemistry and Photobiology*, *75*(3), 272-281.

GLENN, E. P., HUETE, A. R., NAGLER, P. L., & NELSON, S. G. (2008): Relationship between remotely-sensed vegetation indices, canopy attributes and plant physiological processes: what vegetation indices can and cannot tell us about the landscape. *Sensors*, *8*(4), 2136-2160.

GOEL, N. S. (1988): Models of vegetation canopy reflectance and their use in estimation of biophysical parameters from reflectance data. *Remote Sensing Reviews*, *4*(1), 1-212.

GOEL, N. S., & STREBEL, D. E. (1984): Simple beta distribution representation of leaf orientation in vegetation canopies. *Agronomy Journal*, *76*(5), 800-802.

GOETZ, A.F.H., VANE, G., SOLOMON, J. & ROCK, B.N. (1985): Imaging spectrometry for earth remote sensing. *Science, 228*, 1147-1153.

GOVAERTS, Y. M., & VERSTRAETE, M. M. (1998): Raytran: A Monte Carlo ray-tracing model to compute light scattering in three-dimensional heterogeneous media. *Geoscience and Remote Sensing, IEEE Transactions on*, *36*(2), 493-505.

GOVAERTS, Y. M., JACQUEMOUD, S., VERSTRAETE, M. M., & USTIN, S. L. (1996): Three-dimensional radiation transfer modeling in a dicotyledon leaf. *Applied Optics*, *35*(33), 6585-6598.

GOVENDER, M., CHETTY, K., & BULCOCK, H. (2007). A review of hyperspectral remote sensing and its application in vegetation and water resource studies. *Water SA*, *33*(2), 145-151.

GOWER, J. F. R., BORSTAD, G. A., ANGER, C. D., & EDEL, H. R. (1992): CCD-based imaging spectroscopy for remote sensing: the FLI and CASI programs. *Canadian Journal of Remote Sensing*, *18*, 199-199.

GREENBLATT, G. D., ORLANDO, J. J., BURKHOLDER, J. B., & RAVISHANKARA, A. R. (1990): Absorption measurements of oxygen between 330 and 1140 nm. *Journal of Geophysical Research: Atmospheres* (1984–2012), 95(D11), 18577-18582

HACK, H., BLEIHOLDER, H., BUHR, L., MEIER, U., SCHNOCK-FRICKE, U., WEBER, E., & WITZENBERGER, A. (1992): Einheitliche Codierung der phänologischen Entwicklungsstadien mono- und dikotyler Pflanzen. Erweiterte BBCH-Skala, Allgemein. *Nachrichtenblatt des deutschen Pflanzenschutzdienstes*, *44*(12), 265-270.

HANK T., FRANK, T., BACH, H., SPANNRAFT, K. & MAUSER, W. (2013): Assessing the required temporal frequency of optical EO acquisitions for agricultural information systems. In: *RapidEye Science Archive – From Basics to Service*, edited by Borg, E., Daedelow, H. & Johnson, R (GITO, Berlin).

HANK, T. B. (2008): *A biophysically based coupled model approach for the assessment of canopy processes under climate change conditions* (Doctoral dissertation, LMU).

HANK, T., BACH, H., SPANNRAFT, K., FRIESE, M., FRANK, T., & MAUSER, W. (2012): Improving the process-based simulation of growth heterogeneities in agricultural stands through assimilation of earth observation data. In *Geoscience and Remote Sensing Symposium (IGARSS), 2012 IEEE International* (pp. 1006-1009). IEEE.

HANK, T., MARZAHN, P., SCHLENZ, F., & MAUSER, W. (2010a): Assessing Moisture Conditions of Heterogeneous Land surfaces through Hyperspectral Analysis of Water Absorption Features. In *Proc. Hyperspectral Workshop*.

HANK, T., MAUSER, W. & GEBHARDT, T. (2010b): Entwicklung, Kalibrierung und Erprobung eines neuen kosteneffizienten abbildenden Spektrometers für umweltrelevante Forschungsanwendungen , Publikationen der Deutschen Gesellschaft für Photogrammetrie, Fernerkundung und Geoinformation, Band 19 , 423-432.

HAPKE, B. W. (1981): Bi-directional reflectance spectroscopy 1. Theory. *Journal of Geophysical Research*, 86, 3039-3054

HODÁŇOVÁ, D. (1985): Leaf optical properties. In *Photosynthesis during Leaf Development* (pp. 107-127). Springer Netherlands.

HOLST, G.C. (1998): *CCD Arrays, Cameras, and Displays.* 2nd edition. JDC Publishing, Winter Park, Florida, USA.

ITTEN, K. I., DELL'ENDICE, F., HUENI, A., KNEUBÜHLER, M., SCHLÄPFER, D., ODERMATT, D., SEIDEL, F., HUBER, S., SCHOPFER, J., KELLENBERGER, T., BÜHLER, Y., D'ODORICO, P., NIEKE, J., ALBERTI, E. & MEULEMAN, K. (2008). Apex – the hyperspectral ESA airborne prism experiment. *Sensors*, *8*(10), 6235-6259.

JACQUEMOUD, S., & BARET, F. (1990): PROSPECT: A model of leaf optical properties spectra. *Remote Sensing of Environment*, *34*(2), 75-91.

JACQUEMOUD, S., & USTIN, S. L. (2001): Leaf optical properties: A state of the art. In *8th International Symposium of Physical Measurements & Signatures in Remote Sensing* (pp. 223-332).

JACQUEMOUD, S., BACOUR, C., POILVE, H., & FRANGI, J. P. (2000): Comparison of four radiative transfer models to simulate plant canopies reflectance: Direct and inverse mode. *Remote Sensing of Environment*, *74*(3), 471-481.

JACQUEMOUD, S., BARET, F., ANDRIEU, B., DANSON, F. M., & JAGGARD, K. (1995): Extraction of vegetation biophysical parameters by inversion of the PROSPECT+ SAIL models on sugar beet canopy reflectance data. Application to TM and AVIRIS sensors. *Remote Sensing of Environment*, *52*(3), 163-172.

JACQUEMOUD, S., USTIN, S. L., VERDEBOUT, J., SCHMUCK, G., ANDREOLI, G., & HOSGOOD, B. (1996). Estimating leaf biochemistry using the PROSPECT leaf optical properties model. *Remote Sensing of Environment*, *56*(3), 194-202.

JACQUEMOUD, S., VERHOEF, W., BARET, F., BACOUR, C., ZARCO-TEJADA, P. J., ASNER, G. P., FRANCOIS, C., & USTIN, S. L. (2009): PROSPECT+ SAIL models: A review of use for vegetation characterization. *Remote Sensing of Environment*, *113*, S56-S66.

JANESICK, J. R. (2001): *Scientific Charge-coupled Devices* (Vol. 117). Bellingham, WA: SPIE press

JONES, H. G., & VAUGHAN, R. A. (2010). *Remote Sensing of Vegetation: Principles, Techniques, and Applications*. Oxford, UK: Oxford University press.

KAUFMAN, Y. J. (1985): The atmospheric effect on the separability of field classes measured from satellites. *Remote Sensing of Environment*, *18*(1), 21-34.

KAUFMANN, H., FÖRSTER, S., WULF, H., SEGL, K., GUANTER, L., BOCHOW, M., HEIDEN, U., MUELLER, A., HELDENS, W., SCHNEIDERHAN, T., LEITÃO, P.J., VAN DER LINDEN, S., HILL, J., BUDDENBAUM, H., MAUSER, W., HANK, T., KRASEMANN, H., RÖTTGERS, R., OPPELT, N. & HEIM, B. (2012): *Science Plan of the Environmental Mapping and Analysis Program (EnMAP)*, Deutsches GeoForschungsZentrum GFZ, Scientific Technical Report, 63 pp

KELLY, R. L., & PALUMBO, L. J. (1973): Atomic and Ionic Emission Lines below 2000 Angstroms-Hydrogen through Krypton. *NRL Report, No. 7599.*

KIMES, D. S., KNYAZIKHIN, Y., PRIVETTE, J. L., ABUELGASIM, A. A., & GAO, F. (2000): Inversion methods for physically-based models. *Remote Sensing Reviews*, *18*(2-4), 381-439.

KUBELKA, P., AND MUNK, F. (1931): Ein Beitrag zur Optik der Farbanstriche, Ann. Techn. Phys., 11:593-601.

KUUSK, A. (1985): The hot spot effect of a uniform vegetative cover. *Soviet Journal of Remote Sensing*, *3*(4), 645-658.

KUUSK, A. (1991): The hot spot effect in plant canopy reflectance. In *Photon-Vegetation Interactions* (pp. 139-159). Springer Berlin Heidelberg.

LANDGREBE, D. A. (1999): Some fundamentals and methods for hyperspectral image data analysis. In *BiOS'99 International Biomedical Optics Symposium* (pp. 104-113). International Society for Optics and Photonics.

LARGE, E. C. (1954): Growth stages in cereals illustration of the Feekes scale. *Plant Pathology*, *3*(4), 128-129.

LAVERGNE, T., KAMINSKI, T., PINTY, B., TABERNER, M., GOBRON, N., VERSTRAETE, M.M., VOSSBECK, M., WIDLOWSKI, J.-L., GIERING, R. (2007): Application to MISR land products of an RPV model inversion package using adjoint and Hessian codes. *Remote Sensing of Environment, 107*(1), 362-375.

LE MAIRE, G., FRANCOIS, C., & DUFRENE, E. (2004). Towards universal broad leaf chlorophyll indices using PROSPECT simulated database and hyperspectral reflectance measurements. *Remote Sensing of Environment*, *89*(1), 1-28.

LELONG, C. C., BURGER, P., JUBELIN, G., ROUX, B., LABBÉ, S. & BARET, F. (2008): Assessment of unmanned aerial vehicles imagery for quantitative monitoring of wheat crop in small plots. *Sensors*, *8*(5), 3557-3585.

LEONENKO, G., LOS, S. O., & NORTH, P. R. (2013): Statistical Distances and Their Applications to Biophysical Parameter Estimation: Information Measures, M-Estimates, and Minimum Contrast Methods. *Remote Sensing*, *5*(3), 1355-1388.

LI, X., & STRAHLER, A. H. (1985): Geometric-optical modeling of a conifer forest canopy. *Geoscience and Remote Sensing, IEEE Transactions on*, (5), 705-721.

LI, X., & STRAHLER, A. H. (1992): Geometric-optical bidirectional reflectance modeling of the discrete crown vegetation canopy: Effect of crown shape and mutual shadowing. *Geoscience and Remote Sensing, IEEE Transactions on*, *30*(2), 276-292.

LI-COR, INC. (2010): *LAI-2200 Plant Canopy Analzyer, Instruction Manual*. Lincoln, NE.

MAIER, S. W., LÜDEKER, W., & GÜNTHER, K. P. (1999): SLOP: A revised version of the stochastic model for leaf optical properties. *Remote Sensing of Environment*, *68*(3), 273-280.

MAKOWSKI, D., HILLIER, J., WALLACH, D., ANDRIEU, B., & JEUFFROY, M. H. (2006): Parameter estimation for crop models. *Working with dynamic models. Evaluation, analysis, parameterization and applications, Elsevier, Amsterdam*, 101-150.

MARKWELL, J., OSTERMAN, J. C., & MITCHELL, J. L. (1995): Calibration of the Minolta SPAD-502 leaf chlorophyll meter. *Photosynthesis Research*, *46*(3), 467-472.

MERONI, M., COLOMBO, R., & PANIGADA, C. (2004): Inversion of a radiative transfer model with hyperspectral observations for LAI mapping in poplar plantations. *Remote Sensing of Environment*, *92*(2), 195-206.

MERONI, M., ROSSINI, M., GUANTER, L., ALONSO, L., RASCHER, U., COLOMBO, R., & MORENO, J. (2009): Remote sensing of solar-induced chlorophyll fluorescence: Review of methods and applications. *Remote Sensing of Environment*, *113*(10), 2037-2051.

MERZLYAK, M. N., & GITELSON, A. (1995): Why and What for the Leaves Are Yellow in Autumn? On the Interpretation of Optical Spectra of Senescing Leaves (Acerplatanoides L.). *Journal of Plant Physiology*, *145*(3), 315-320.

MINOLTA (1989): *SPAD-502 Owner's manual. Industrial meter division*. Minolta Corp., Ramsey, N.J.

MONJE, O. A., & BUGBEE, B. (1992): Inherent limitations of nondestructive chlorophyll meters: a comparison of two types of meters. *HortScience*, *27*(1), 69-71.

NELDER, J. A., & MEAD, R. (1965). A simplex method for function minimization. *The Computer Journal*, *7*(4), 308-313.

NICODEMUS, F. E. (1970): Reflectance nomenclature and directional reflectance and emissivity. *Applied Optics*, *9*(6), 1474-1475.

NICODEMUS, F. E., RICHMOND, J. C., HSIA, J. J., GINSBERG, I. W., & LIMPERIS, T. (1977): Geometrical considerations and nomenclature for reflectance, Natl. *Bur. Stand. Rep., NBS MN-160*.

NUMERICAL ALGORITHMS GROUP (2012): Keyword Index: Quasi-Newton. *NAG Library Manual, Mark 23*.

OLSEN, D., DOU, C., ZHANG, X., HU, L., KIM, H. & HILDUM, E. (2010): Radiometric calibration for AgCam. *Remote Sensing*, *2*(2), 464-477.

OPPELT, N. (2002). *Monitoring of plant chlorophyll and nitrogen status using the airborne imaging spectrometer AVIS* (Doctoral dissertation, LMU).

OPPELT, N., & MAUSER, W. (2007): The Airborne Visible/Infrared Imaging Spectrometer Avis: Design, Characterization and Calibration. *Sensors*, *7*(9), 1934-1953.

OTTERMAN, J., & WEISS, G. H. (1984): Reflection from a field of randomly located vertical protrusions. *Applied Optics*, *23*(12), 1931-1936.

PEARLMAN, J. S., BARRY, P. S., SEGAL, C. C., SHEPANSKI, J., BEISO, D., & CARMAN, S. L. (2003): Hyperion, a space-based imaging spectrometer. *Geoscience and Remote Sensing, IEEE Transactions on*, *41*(6), 1160-1173.

PEDRÓS, R., GOULAS, Y., JACQUEMOUD, S., LOUIS, J., & MOYA, I. (2010): FluorMODleaf: A new leaf fluorescence emission model based on the PROSPECT model. *Remote Sensing of Environment*, *114*(1), 155-167.

PINTER, P. J., HATFIELD, J. L., SCHEPERS, J. S., BARNES, E. M., MORAN, M. S., DAUGHTRY, C. S., & UPCHURCH, D. R. (2003): Remote sensing for crop management. *Photogrammetric Engineering and Remote Sensing*, *69*(6), 647-664.

PRESS, W.H., FLANNERY, B.P., TEUKOLSKY, S.A. & VETTERLING, W.T. (1986): Numerical Recipes, *Cambridge University Press,* New York, 274-312.

PRICE, J. C., & BAUSCH, W. C. (1995): Leaf area index estimation from visible and near-infrared reflectance data. *Remote Sensing of Environment*, *52*(1), 55-65.

RICHTER, K., ATZBERGER, C., HANK, T. B., & MAUSER, W. (2012): Derivation of biophysical variables from Earth observation data: validation and statistical measures. *Journal of Applied Remote Sensing*, *6*(1), 063557-1.

RICHTER, K., ATZBERGER, C., VUOLO, F., WEIHS, P., & D'URSO, G. (2009): Experimental assessment of the Sentinel-2 band setting for RTM-based LAI retrieval of sugar beet and maize. *Canadian Journal of Remote Sensing*, *35*(3), 230-247.

RIVERA, J. P., VERRELST, J., LEONENKO, G., & MORENO, J. (2013): Multiple Cost Functions and Regularization Options for Improved Retrieval of Leaf Chlorophyll Content and LAI through Inversion of the PROSAIL Model. *Remote Sensing*, *5*(7).

ROUJEAN, J. L., LEROY, M., & DESCHAMPS, P. Y. (1992): A bidirectional reflectance model of the Earth's surface for the correction of remote sensing data. *Journal of Geophysical Research: Atmospheres (1984–2012)*, *97*(D18), 20455-20468.

SCHANDA, E. (1986): *Physical Fundamentals of Remote Sensing.* Springer Verlag, Berlin, Heidelberg.

SCHLERF, M., ATZBERGER, C., HILL, J., BUDDENBAUM, H., WERNER, W., & SCHÜLER, G. (2010): Retrieval of chlorophyll and nitrogen in Norway spruce (Picea abies L. Karst.) using imaging spectroscopy. *International Journal of Applied Earth Observation and Geoinformation*, *12*(1), 17-26.

SEGL, K., GUANTER, L., ROGASS, C., KUESTER, T., ROESSNER, S., KAUFMANN, H., SANG, B., MOGULSKY, V. & HOFER, S. (2012): EeteS—The EnMAP end-to-end simulation tool. *Selected Topics in Applied Earth Observations and Remote Sensing, IEEE Journal of, 5*(2), 522-530.

SOLOMON, J., & ROCK, B. (1985): Imaging spectrometry for earth remote sensing. *Science*, *228*, 1147-1153.

STAENZ, K. (2009): Terrestrial imaging spectroscopy–some future perspectives. In *Proceedings of 6th EARSeL Workshop on Imaging Spectroscopy, Tel-Aviv, Israel* (pp. 16-19).

SUITS, G. H. (1972): The calculation of the directional reflectance of a vegetative canopy. *Remote Sensing of Environment*, *2*, 117-125.

TANRE, D., DESCHAMPS, P. Y., DUHAUT, P., & HERMAN, M. (1987): Adjacency effect produced by the atmospheric scattering in thematic mapper data. *Journal of Geophysical Research: Atmospheres (1984–2012)*, *92*(D10), 12000-12006.

TANRE, D., HERMAN, M., & DESCHAMPS, P. Y. (1981): Influence of the background contribution upon space measurements of ground reflectance. *Applied Optics*, *20*(20), 3676-3684.

TERASHIMA, I., & SAEKI, T. (1983): Light environment within a leaf I. Optical properties of paradermal sections of Camellia leaves with special reference to differences in the optical properties of palisade and spongy tissues. *Plant and Cell Physiology*, *24*(8), 1493-1501.

TUCKER, C. J., & GARRATT, M. W. (1977): Leaf optical system modeled as a stochastic process. *Applied Optics*, *16*(3), 635-642.

UDDLING, J., GELANG-ALFREDSSON, J., PIIKKI, K. & PLEIJEL, H. (2007): Evaluating the relationship between leaf chlorophyll concentration and SPAD-502 chlorophyll meter readings. *Photosynthesis Research, 91,* 37-46.

VANE, G., & GOETZ, A. F. (1988): Terrestrial imaging spectroscopy. *Remote Sensing of Environment*, *24*(1), 1-29.

VANE, G., GOETZ, A. F., & WELLMAN, J. B. (1984): Airborne Imaging Spectrometer: A new tool for remote sensing. *Geoscience and Remote Sensing, IEEE Transactions on*, (6), 546-549.

VANE, G., GREEN, R. O., CHRIEN, T. G., ENMARK, H. T., HANSEN, E. G., & PORTER, W. M. (1993): The airborne visible/infrared imaging spectrometer (AVIRIS). *Remote Sensing of Environment*, *44*(2), 127-143.

VAPNIK, V. (1995): *The Nature of Statistical Learning Theory*. New York: Springer-Verlag.

VERGER, A., BARET, F., & CAMACHO, F. (2011): Optimal modalities for radiative transfer-neural network estimation of canopy biophysical characteristics: Evaluation over an agricultural area with CHRIS/PROBA observations. *Remote Sensing of Environment, 115*(2), 415-426.

VERHOEF, W. (1984): Light scattering by leaf layers with application to canopy reflectance modeling: the SAIL model. *Remote sensing of Environment, 16*(2), 125-141.

VERHOEF, W. (1985): Earth observation modeling based on layer scattering matrices. *Remote Sensing of Environment, 17(2)*, 165-178.

VERHOEF, W. (2002): Improved modelling of multiple scattering in leaf canopies: The model SAIL++. In *Proceedings of the First Symposium on Recent Advances in Quantitative Remote Sensing, Torrent, Spain* (pp. 11-20).

VERHOEF, W., & BACH, H. (2003): Simulation of hyperspectral and directional radiance images using coupled biophysical and atmospheric radiative transfer models. *Remote Sensing of Environment, 87*(1), 23-41.

VERHOEF, W., & BACH, H. (2007): Coupled soil–leaf-canopy and atmosphere radiative transfer modeling to simulate hyperspectral multi-angular surface reflectance and TOA radiance data. *Remote Sensing of Environment, 109*(2), 166-182.

VERHOEF, W., JIA, L., XIAO, Q., & SU, Z. (2007): Unified optical-thermal four-stream radiative transfer theory for homogeneous vegetation canopies. *Geoscience and Remote Sensing, IEEE Transactions on, 45*(6), 1808-1822.

VERRELST, J., RIVERA, J. P., LEONENKO, G., ALONSO, L., & MORENO, J. (2014): Optimizing LUT-Based RTM Inversion for Semiautomatic Mapping of Crop Biophysical Parameters from Sentinel-2 and-3 Data: Role of Cost Functions. *Geoscience and Remote Sensing, IEEE Transactions on, 52*(1), 257-269.

VOGELMANN, T.C. (1989): Penetration of light into plants. *Photochemistry and photobiology, 50*(6), 895-902.

VUOLO, F., ATZBERGER, C., RICHTER, K., D'URSO, G., & DASH, J. (2010): Retrieval of biophysical vegetation products from RapidEye imagery. *International Society for Photogrammetry & Remote Sensing*, 281-286.

WAINWRIGHT, J., & MULLIGAN, M. (EDS.). (2005). *Environmental Modelling: finding simplicity in complexity*. Wiley. com.

WANG, Q., WU, C., LI, Q., & LI, J. (2010): Chinese HJ-1A/B satellites and data characteristics. *Science China Earth Sciences, 53*(1), 51-57.

WEISS, M., BARET, F., MYNENI, R. B., PRAGNÈRE, A., & KNYAZIKHIN, Y. (2000): Investigation of a model inversion technique to estimate canopy biophysical variables from spectral and directional reflectance data. *Agronomie, 20*(1), 3-22.

WEISS, M., TROUFLEAU, D., BARET, F., CHAUKI, H., PREVOT, L., OLIOSO, A., BRUGUIER, N. & BRISSON, N. (2001). Coupling canopy functioning and radiative transfer models for remote sensing data assimilation. *Agricultural and Forest Meteorology, 108*(2), 113-128.

WIDENHORN, R., BLOUKE, M. M., WEBER, A., REST, A. & BODEGOME, E. (2002): Temperature dependence of dark current in a CCD. *Proceedings of SPIE Vol. 4669 (2002), Sensors and Camera Systems for Scientific, Industrial, and Digital Photography Applications*, pp. 193-201.

WIDLOWSKI, J. L., TABERNER, M., PINTY, B., BRUNIQUEL-PINEL, V., DISNEY, M., FERNANDES, R., ... & XIE, D. (2007): Third Radiation Transfer Model Intercomparison (RAMI) exercise: Documenting progress in canopy reflectance models. *Journal of Geophysical Research: Atmospheres (1984–2012), 112*(D9).

WOOD, C. W., REEVES, D. W., & HIMELRICK, D. G. (1993): Relationships between chlorophyll meter readings and leaf chlorophyll concentration, N status, and crop yield: A review. In *Proceedings of the Agronomy Society of New Zealand* (Vol. 23, pp. 1-9).

ZADOKS, J. C., CHANG, T. T., & KONZAK, C. F. (1974). A decimal code for the growth stages of cereals. *Weed research, 14*(6), 415-421.

Internet References

INT 1: BAYERISCHES LANDESAMT FÜR UMWELT (2013): GeoFachdatenAtlas (Bodeninformationssystem Bayern)
URL: *http://www.bis.bayern.de/bis/initParams.do*, visited at Dec 18th 2013

INT 2: FLETCHER, K. (2012): Sentinel-2: ESA's Optical High-Resolution Mission for GMSE Operational services (ESA SP-1322/2 March 2012). ESA Communications, ESTEC, Netherlands.
URL: *http://esamultimedia.esa.int/multimedia/publications/SP-1322_2/*, visited at Dec 19th 2013

Appendix

A.1 LAI Estimation accuracy (NSE)

Noise type: **Additive**

Band selection: AVIS-3 full range

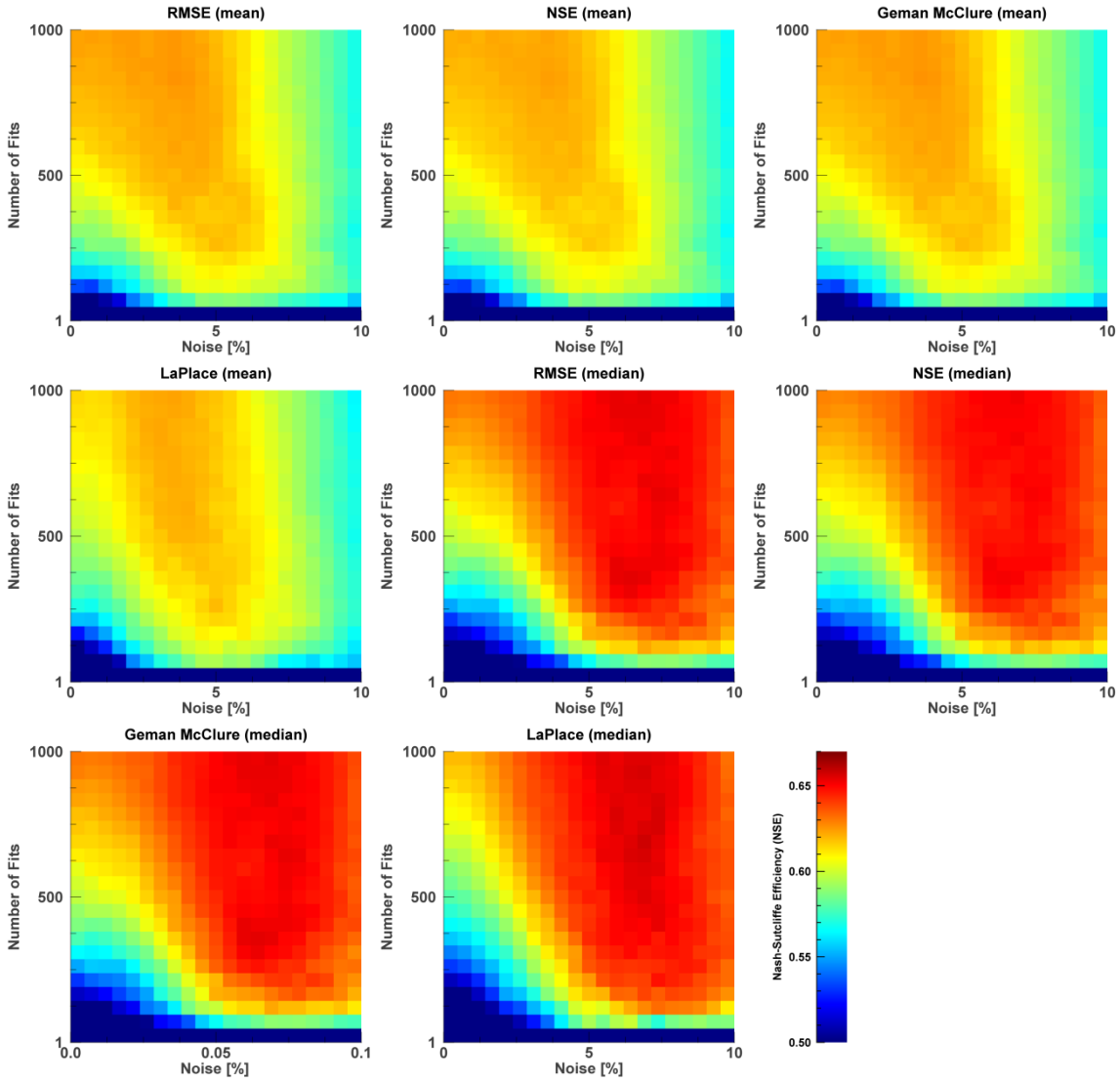

A.2 LAI Estimation accuracy (NSE)

Noise type: **Multiplicative**

Band selection: AVIS-3 full range

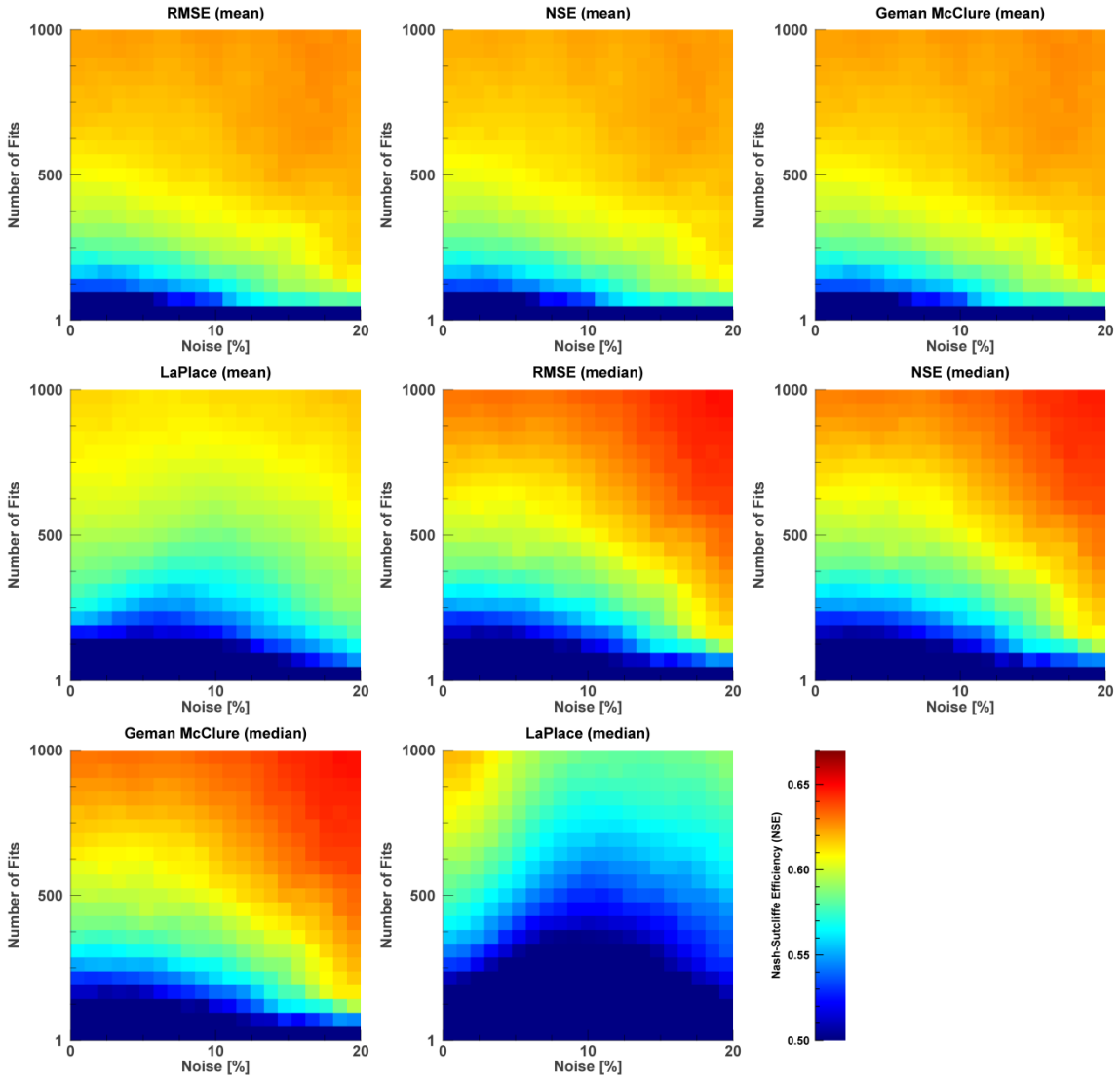

A.3 LAI Estimation accuracy (NSE)

Noise type: **Combined**

Band selection: AVIS-3 full range

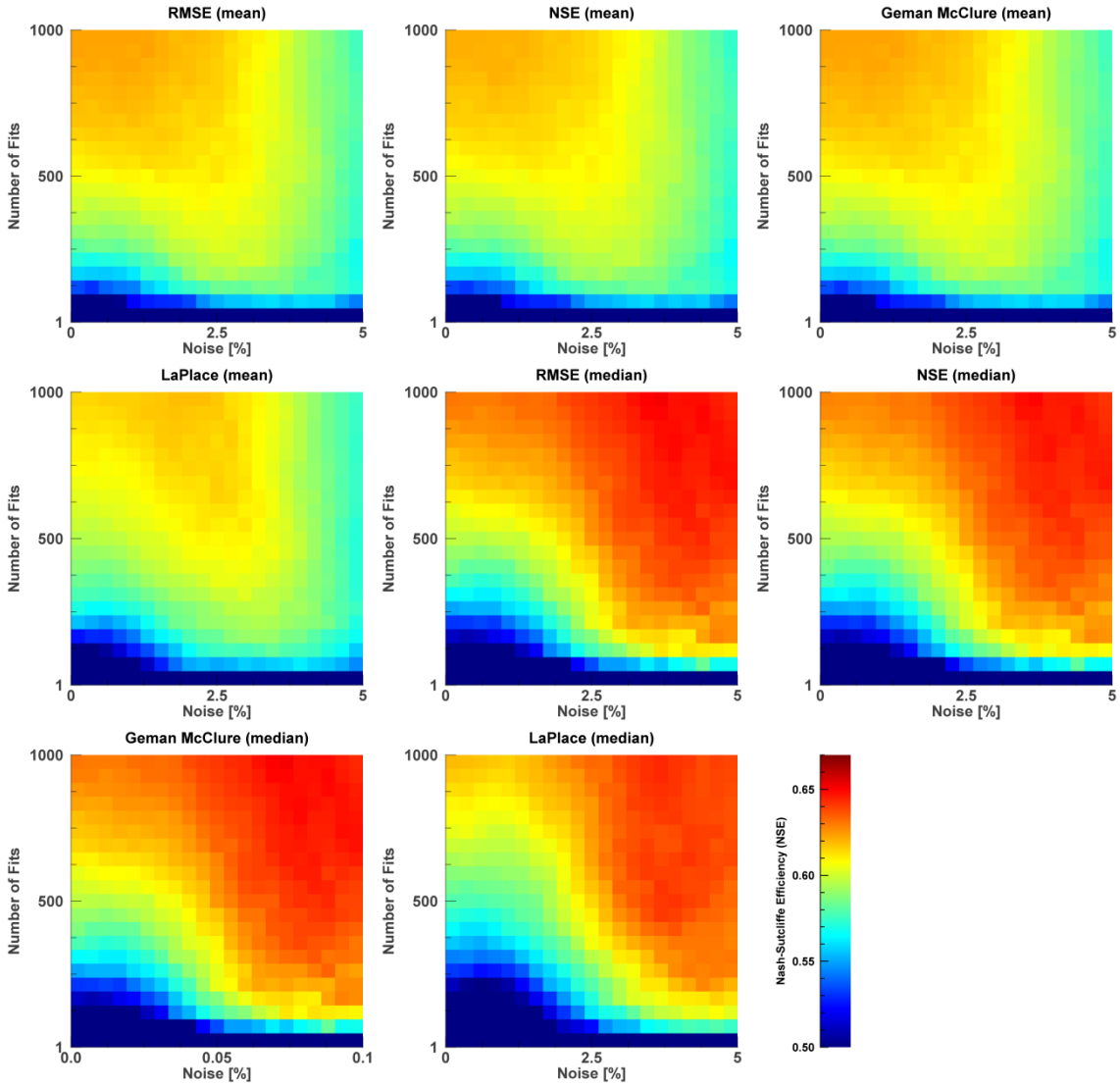

A.4 LAI Estimation accuracy (NSE)

Noise type: **Inverse-combined**

Band selection: AVIS-3 full range

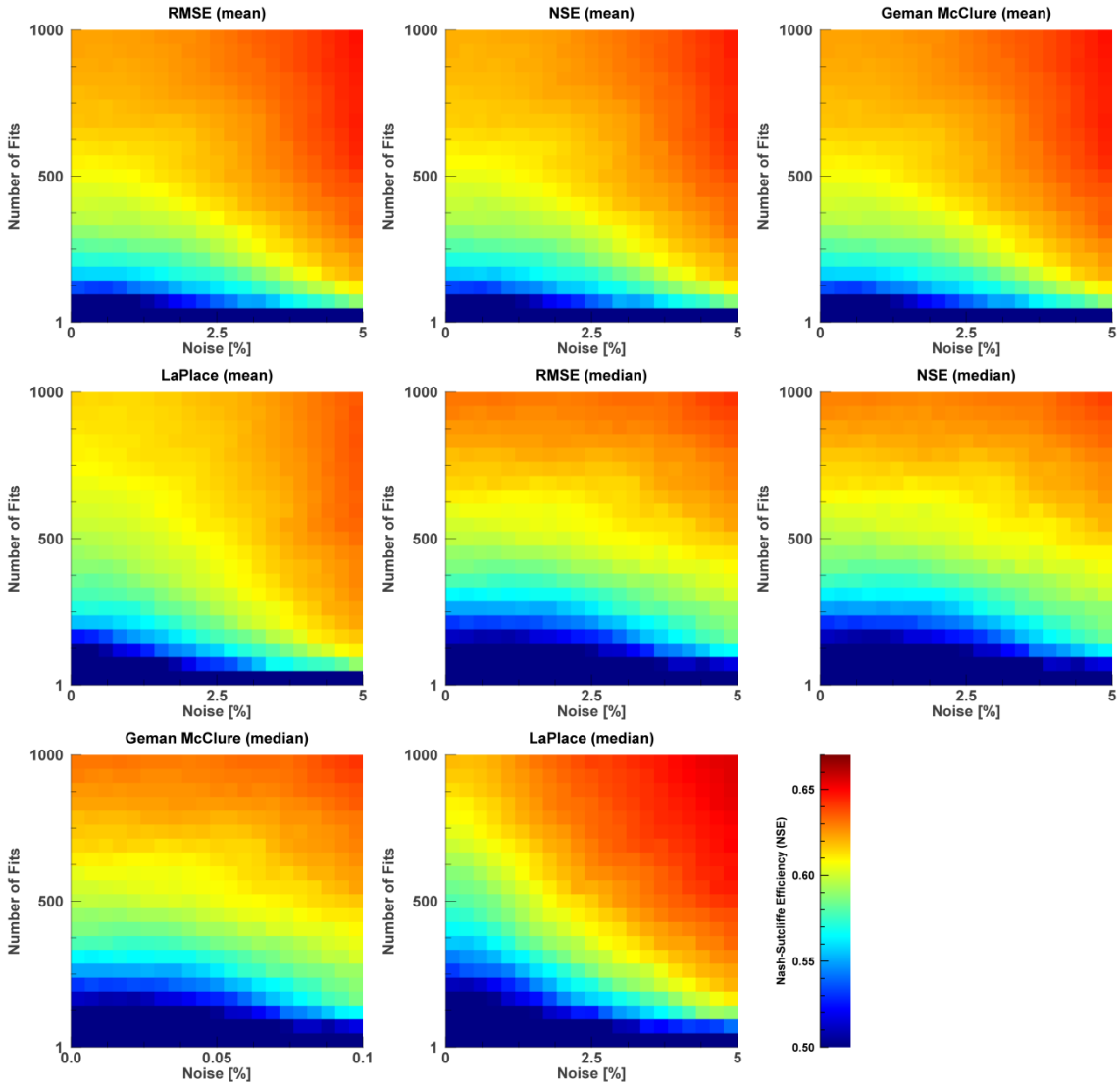

A.5 LAI Estimation accuracy (NSE)

Noise type: Inverse-multiplicative

Band selection: **AVIS-3 VNIR**

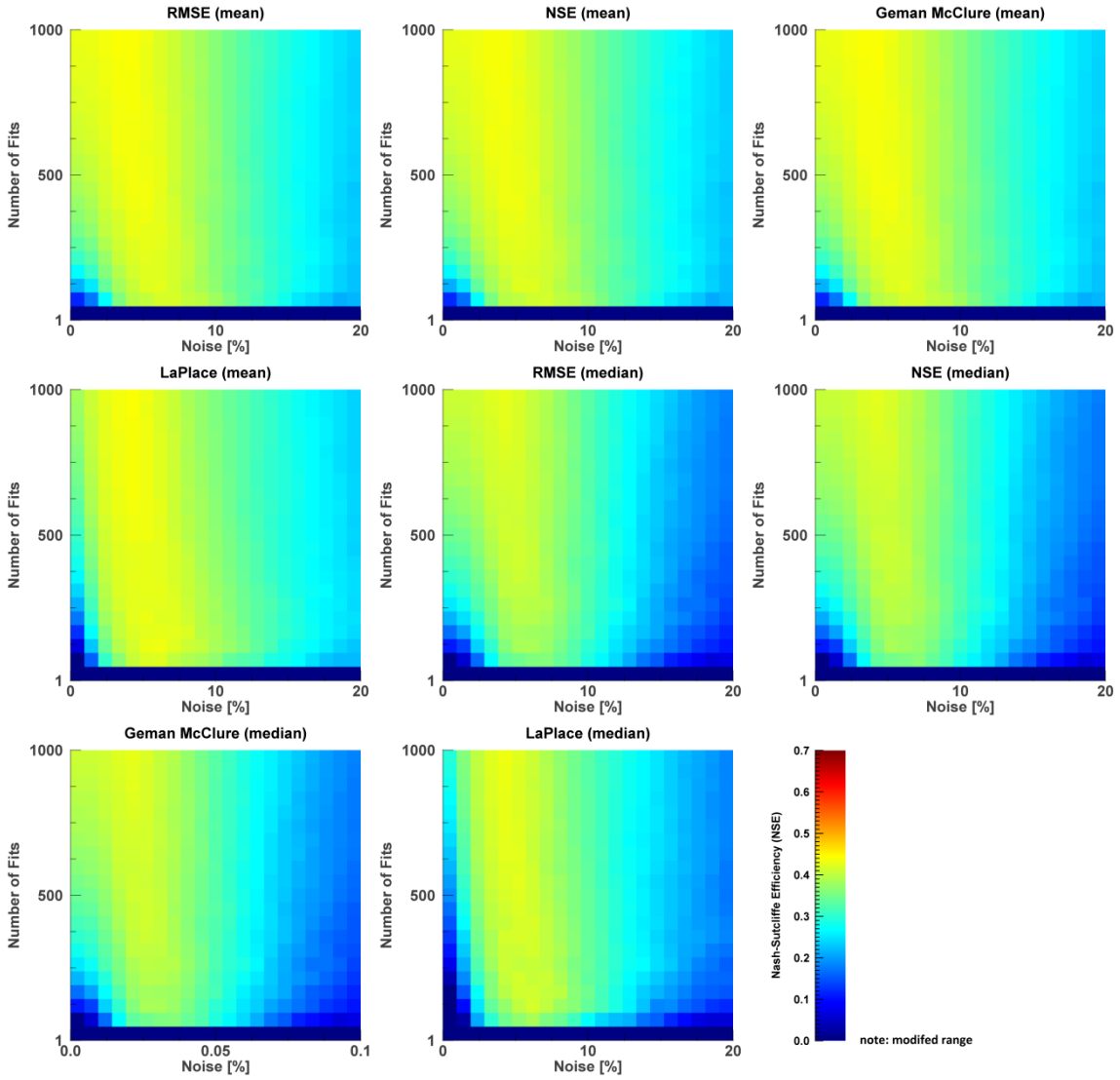

A.6 LAI Estimation accuracy (NSE)

Noise type: Inverse-multiplicative

Band selection: **Sentinel-2**

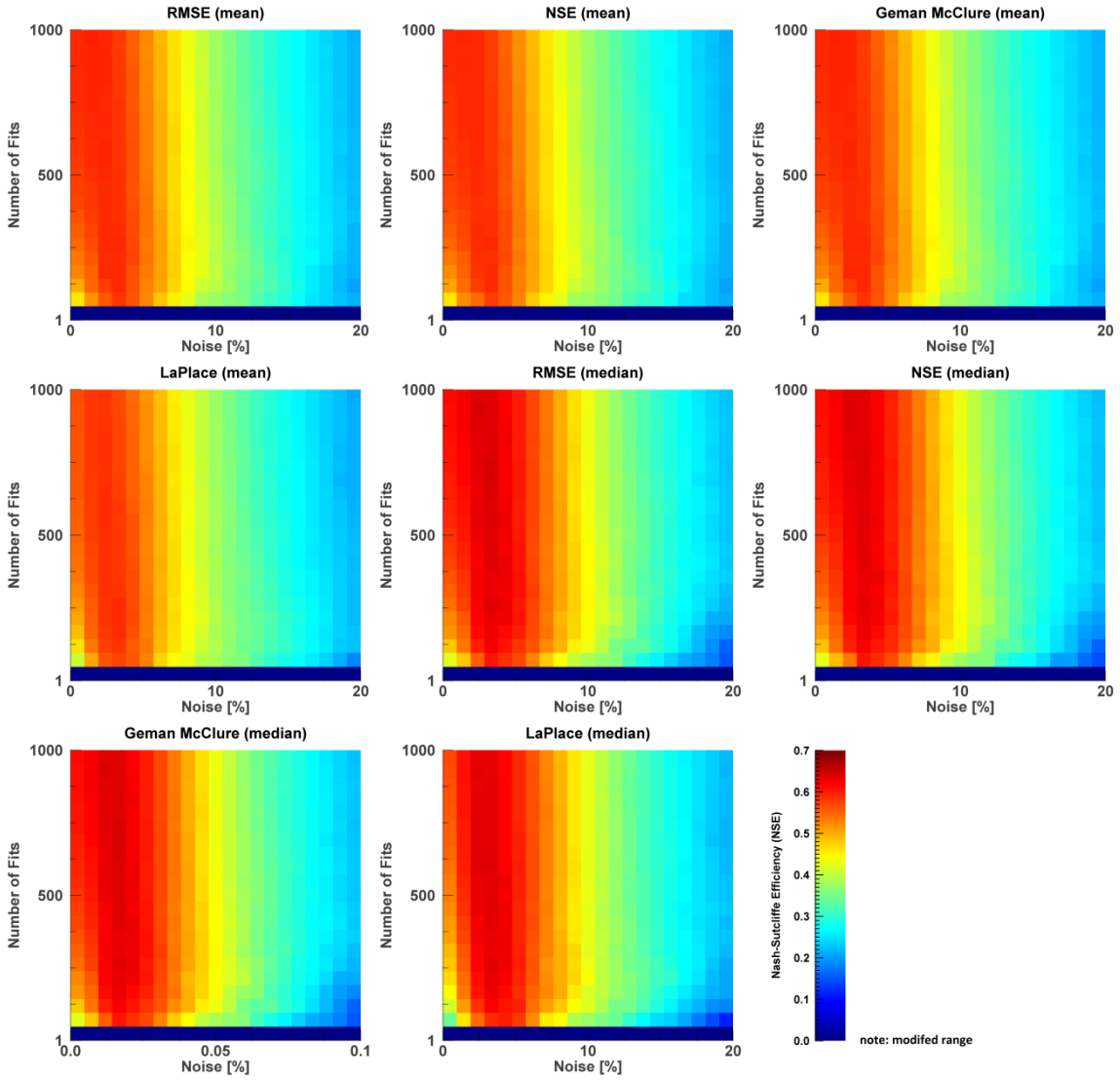

A.7 LAI Estimation accuracy (NSE)

Noise type: Inverse-multiplicative

Band selection: **Landsat TM**

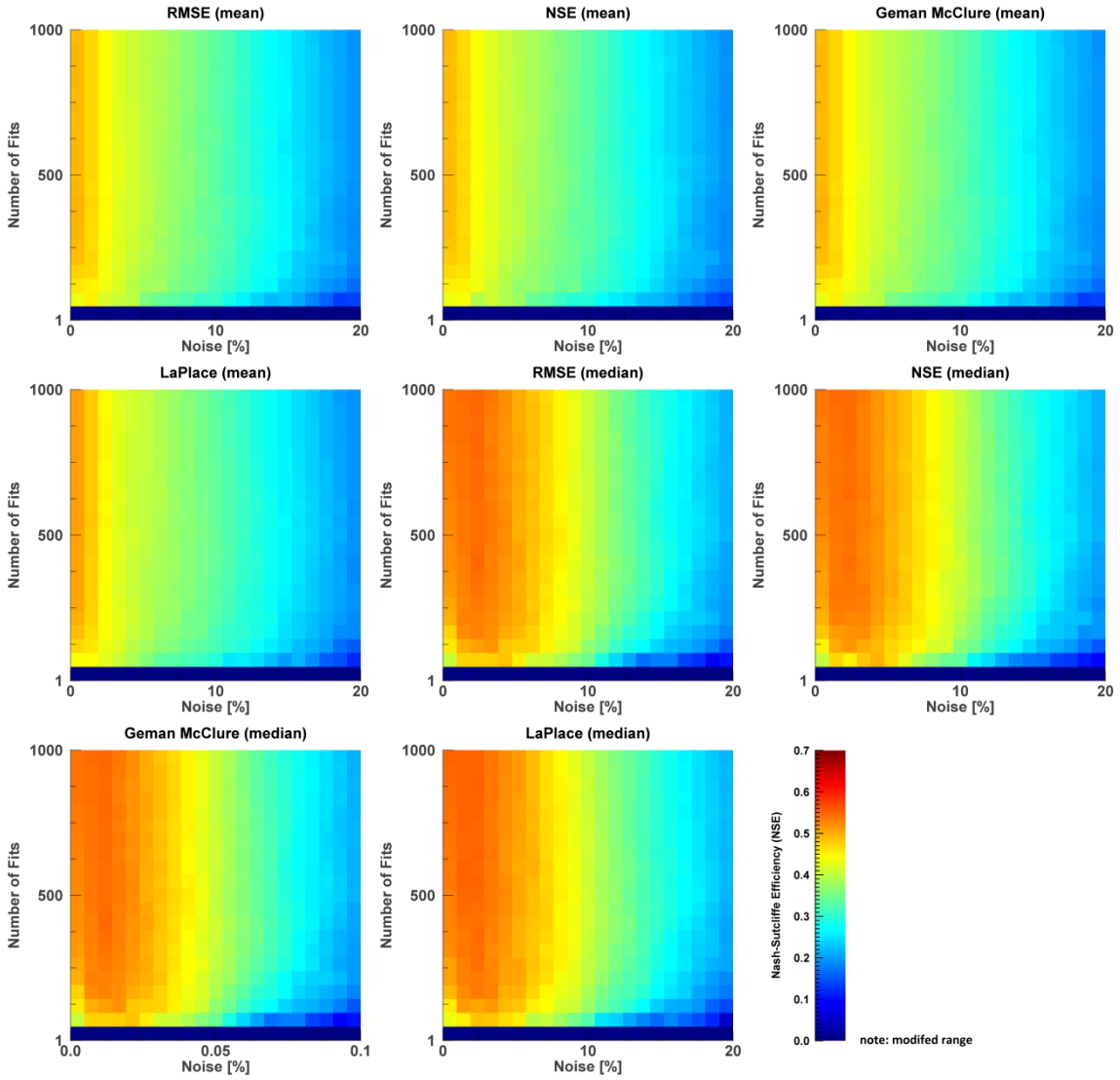

A.8 CCC Estimation Accuracy (NSE)

Noise type: **Inverse-multiplicative**

Band selection: **AVIS-3 full range**

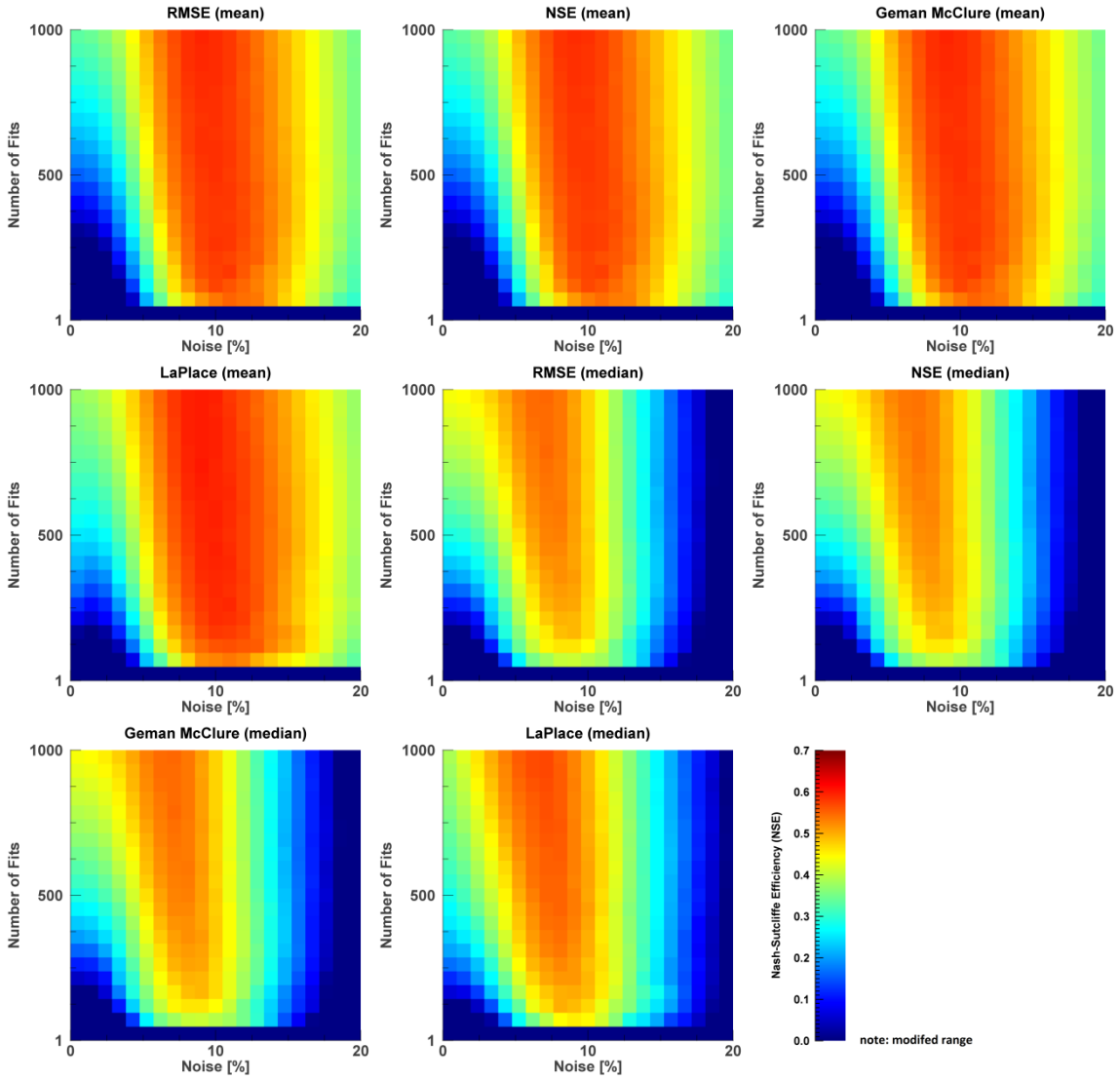

A.9 CCC Estimation Map

EnMAP | AVIS-3 (upscaled to 30 m)

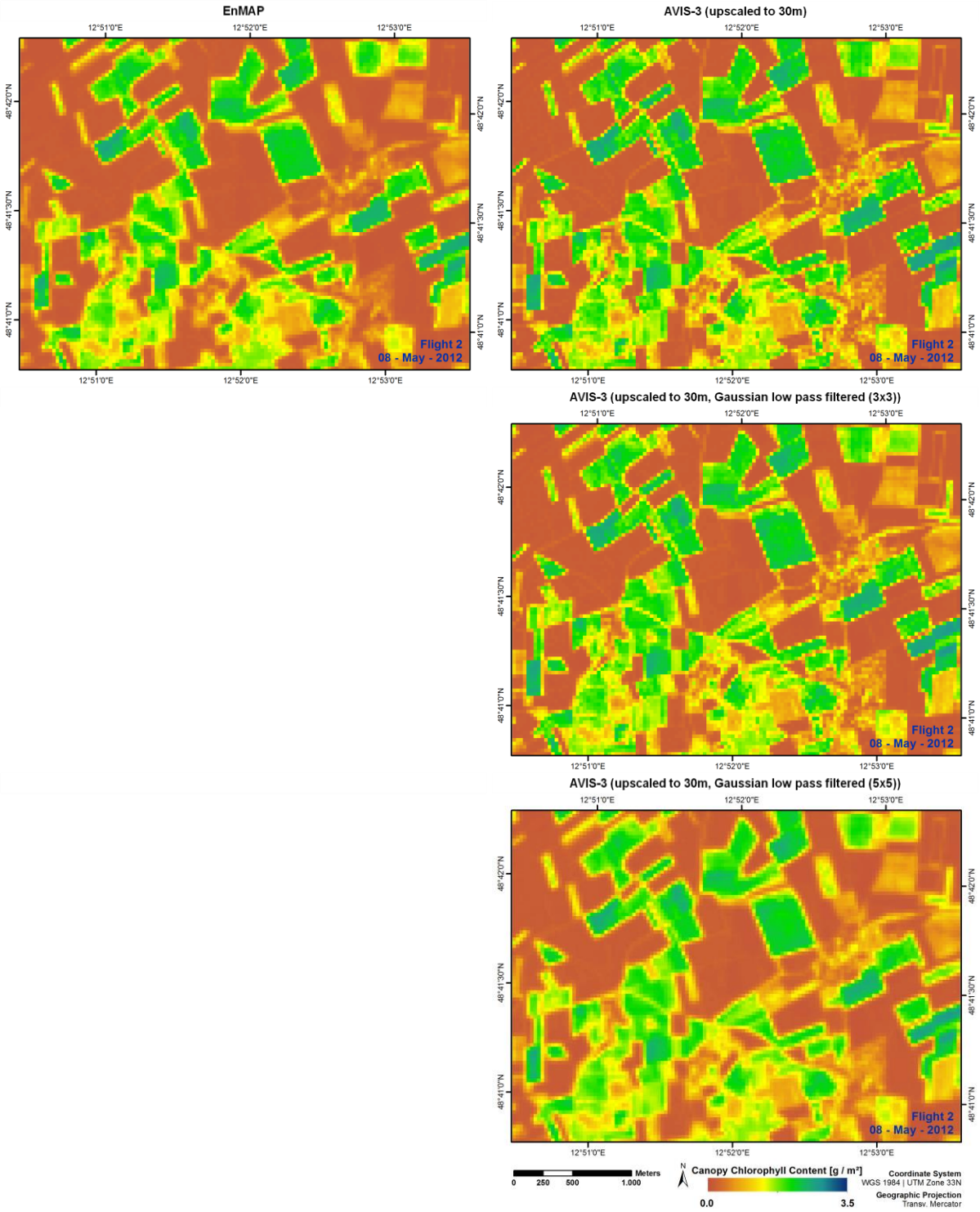

A.10 CCC Difference Map

EnMAP | AVIS-3 (upscaled to 30 m)

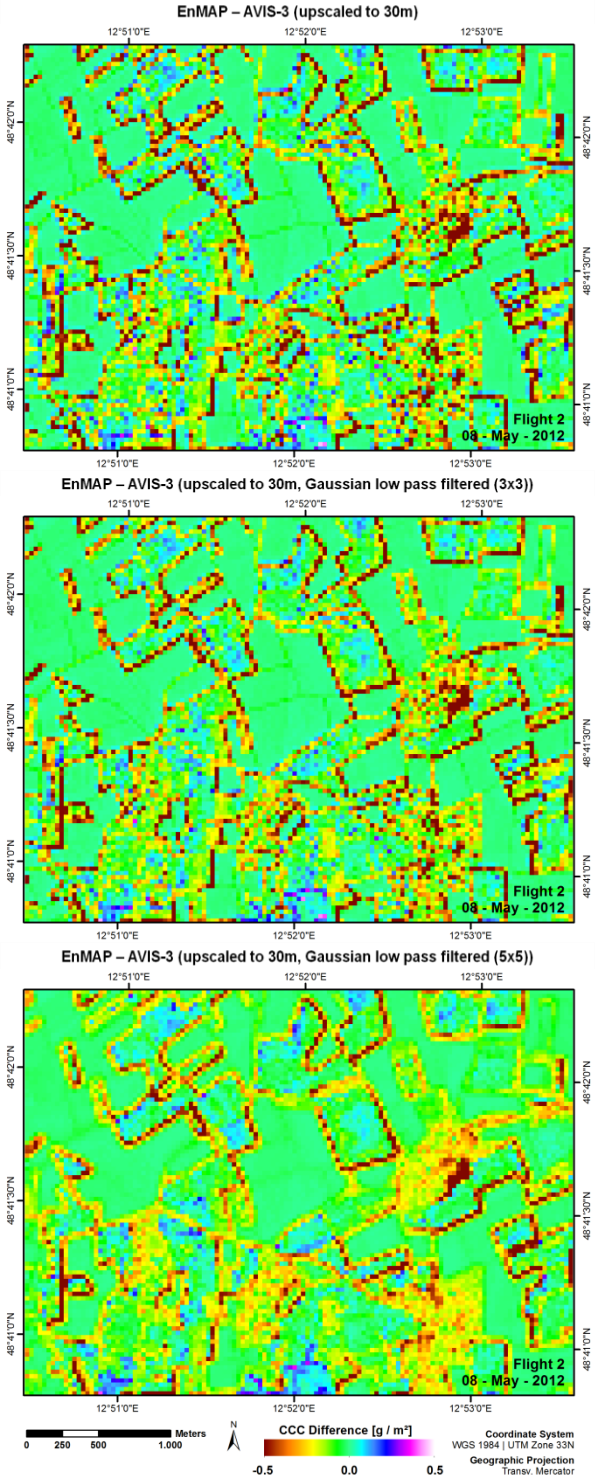

A.11 CCC Difference Map & Correlation

Sentinel-2 | AVIS-3 (upscaled to 30 m)